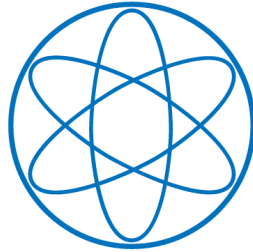


PHYSIK - DEPARTMENT



**Energy-Dependent Quenching
Factor Measurements of CaWO_4
Crystals at mK Temperatures
and
Detector Prototypes for Direct
Dark Matter Search with CRESST**

DISSERTATION

VON

Raimund Johann Strauß



TECHNISCHE UNIVERSITÄT MÜNCHEN

TECHNISCHE UNIVERSITÄT MÜNCHEN

Lehrstuhl E15 für Experimentalphysik und Astroteilchenphysik

**Energy-Dependent Quenching Factor
Measurements of CaWO_4 Crystals at mK
Temperatures**

and

**Detector Prototypes for Direct Dark
Matter Search with CRESST**

Raimund Johann Strauß

Vollständiger Abdruck der von der Fakultät für Physik der Technischen Universität München zur Erlangung des akademischen Grades eines

Doktors der Naturwissenschaften (Dr. rer. nat.)

genehmigten Dissertation.

Vorsitzender: Univ.-Prof. Dr. A. Ibarra

Prüfer der Dissertation:

1. Univ.-Prof. Dr. F. Freiherr von Feilitzsch (i.R.)

2. Hon.-Prof. Dr. S. Bethke

Die Dissertation wurde am 11.07.2013 bei der Technischen Universität München eingereicht und durch die Fakultät für Physik am 30.09.2013 angenommen.

Abstract

There is strong evidence that a significant amount of the matter in the Universe is not interacting electro-magnetically. Precision cosmology which was recently updated by the results of the PLANCK mission predicts 26.5% of the total mass-energy density of the Universe to be made up of such Dark Matter (DM) while only 4.9% is due to baryonic matter. Promising theoretical approaches suggest weakly interacting massive particles (WIMPs) beyond the well-established standard model of particle physics to account for the abundance of DM. Extensive efforts have been made to directly detect these hypothetical particles with earth-bound experiments via WIMP-induced nuclear recoils. While WIMP-nucleon cross-sections down to $2 \cdot 10^{-45} \text{ cm}^2$ (at a WIMP mass of $\sim 55 \text{ GeV}$) have been excluded, lately, several of these ultra-sensitive detectors gave indications for a possible existence of low-mass WIMPs ($\mathcal{O}(1\text{-}30 \text{ GeV})$).

The direct DM search experiment CRESST (Cryogenic Rare Event Search with Superconducting Calorimeters) which is located underground in the LNGS (Laboratori Nazionali del Gran Sasso) in Italy uses CaWO_4 as a “multi-material” target for WIMPs. The scintillating CaWO_4 crystals of $\sim 300 \text{ g}$ each are operated as phonon detectors at mK temperatures which allows a precise measurement of the total energy deposition of particle interactions. The corresponding scintillation light is detected simultaneously by a separate silicon-on-sapphire light detector also operated as a cryogenic detector. The main feature of such a two-channel CRESST detector module is the active background discrimination technique based on the different relative light yield (LY) for different kinds of particle interactions. It allows to separate the dominant e^-/γ -background (LY=1 per definition) from the signal region of nuclear-recoil events (typically 10-40 keV) with reduced LY due to light quenching. This reduction of the LY compared to electron recoils is the more pronounced the higher the mass number (A) of the recoiling nucleus. The quantification of this behaviour is realized by the introduction of Quenching Factors (QFs). With an exact knowledge of the QFs the recoiling nucleus can be identified on an event-by-event basis which allows to discriminate neutron-background and due to the A^2 -dependence of the coherent WIMP-nucleus scattering cross-section to disentangle the recoil composition (O, Ca and W) of a possible DM signal (WIMP-mass spectroscopy). The main part of this thesis addresses the precise measurement of the QFs of CaWO_4 at mK temperatures. The latest extensive scientific run of CRESST (run32) with an exposure of 730 kg-days shows an excess signal at high statistical significance ($> 4\sigma$) which could be a hint towards low-mass WIMPs. Known backgrounds alone, like neutrons, α -particles, e/γ induced recoils, and ^{206}Pb recoils from ^{210}Po decays on surfaces surrounding the crystals cannot explain this excess. However, rare processes (e.g. surface sputtering effects) that are correlated to the known backgrounds could mimic (part of) these intriguing signal events.

In the framework of this thesis, detector prototypes which allow to reduce the background level significantly have been designed and investigated in the CRESST test cryostat at LNGS. CaWO_4 crystals produced at the TU München (TUM) have been operated for the first time to study phonon properties, light output and radiopurity. An extensive analysis of the intrinsic α -contamination shows a total activity of typically $\sim 3 \text{ mBq/kg}$. In a dedicated measurement, the influence of the implantation of ^{222}Rn from air on the ^{206}Pb -recoil background in CRESST has been investigated. The results suggest that $\sim 28\%$ of the observed ^{206}Pb events in run32 are due to this process. To completely avoid surface-decay induced backgrounds, a novel detector design was developed here. A TUM-grown block-shaped CaWO_4 crystal of $\sim 250 \text{ g}$ is held by sticks made of CaWO_4 which together with a scintillating polymeric foil surrounding the detector establish a fully scintillating detector housing. α -particles of corresponding

^{210}Po decays produce additional scintillation light in these scintillating materials which shifts the ^{206}Pb recoil events out of the signal region. The functionality of such a veto and the influence of the CaWO_4 sticks on the performance of the phonon detector was successfully tested in a series of measurements in the test cryostat at LNGS. In addition, the light output of block-shaped crystals is increased by 48% compared to a similar crystal of the classic cylindrical CRESST design. Within the present thesis, two such novel detector modules with TUM-grown crystals were implemented into the CRESST setup for the next run.

At the accelerator of the Maier-Leibnitz Laboratorium (MLL) in Garching a dedicated neutron scattering facility to measure the QFs of CaWO_4 at mK temperatures was set up. Monoenergetic neutrons of ~ 11 MeV - produced in a nuclear reaction by a pulsed ^{11}B beam - scatter off an especially developed CRESST-like detector module operated in a dilution refrigerator and are detected by an array of liquid-scintillator modules at fixed scattering angles. In this way the scattering kinematics is fixed. The so-called triple coincidence technique allows to identify the recoiling nucleus in the CaWO_4 crystal by searching for neutron events with the correct time of flight between neutron production and detection and with a coincident nuclear recoil in the cryogenic detector module. The simultaneous measurement of the corresponding scintillation light determines the QFs. The experimental setup was optimized for the measurement of the QF of W (QF_{W}) which had not been measured before at mK temperatures with the required precision. For a scattering angle of 80° the identified W recoils are expected at a recoil energy of ~ 100 keV in the phonon detector. In total, three beamtimes of ~ 1 week each were performed and 158 W-events were separated with a signal-to-background ratio of $\sim 7 : 1$. A dedicated maximum-likelihood-analysis yields $QF_{\text{W}} = 0.0196 \pm 0.0022$.

With the knowledge of the QF of W an energy-dependent QF analysis of the entire nuclear recoil band up to 1800 keV has become possible. Therefore, a correlated maximum-likelihood fit was developed which includes the contributions of O, Ca and W (each with a Gaussian LY distribution) and the precision measurement of QF_{W} by the triple coincidence technique. The energy dependence of the QFs is parametrized in analogy to that of the electron recoil band with a constant component and an exponential rise (for the electron recoil band: exponential reduction) of the QFs towards lower recoil energies. The fit converges over the whole energy range and the data is fully described by the proposed parametrization. The resulting energy dependence of the QF of O is $\sim 6.1\%$ comparing recoils at 100 keV with recoils at 20 keV while for Ca it is only $\sim 1.5\%$. Phenomenological models predict that the energy dependence is indeed reduced the higher the mass of the recoiling nucleus involved. This motivates the assumption of a constant QF of W over the considered energy range from 20 to 250 keV. The final results for a recoil energy of 100 keV are $QF_{\text{O}} = 0.1212 \pm 0.0035$, $QF_{\text{Ca}} = 0.0667 \pm 0.0030$ and $QF_{\text{W}} = 0.0196 \pm 0.0022$.

Furthermore, a variation of the QF in the order of $\sim 10\%$ among different CaWO_4 crystals has been observed. The precision measurements of the QFs at the MLL allow to nicely describe the CRESST neutron-calibration data with energy-dependent QFs. The mean QFs averaged over the eight detector modules operated in run32 of CRESST at a recoil energy of 20 keV are $QF_{\text{O}}^{\text{cresst}} = 0.1124 \pm 0.0042$, $QF_{\text{Ca}}^{\text{cresst}} = 0.0595 \pm 0.0022$ and $QF_{\text{W}}^{\text{cresst}} = 0.0172 \pm 0.0022$.

In conclusion, the QFs of CaWO_4 were measured with unprecedented accuracy at mK temperatures and for the first time a clear energy dependence could be observed. This has significant influence on the Dark Matter analysis and the understanding of CRESST detectors. In addition, the novel detector design (using CaWO_4 sticks) developed in this thesis should lead to a significant reduction of surface backgrounds and help to clarify in the near future whether the observed signal excess in run32 of CRESST is due to unconsidered backgrounds or a true hint for Dark Matter.

Zusammenfassung

Es gibt überzeugende Hinweise darauf, dass ein beträchtlicher Teil der Materie im Universum nicht elektromagnetisch wechselwirkt. Die Kosmologie, welche im letzten Jahrzehnt - nicht zuletzt durch die kürzlich veröffentlichten Ergebnisse des PLANCK-Experiments - zu einer Präzisionswissenschaft wurde, sagt voraus, dass 26.5% der totalen Energie-Massendichte im Universum aus Dunkler Materie (DM) bestehen. Die baryonische Materie macht nur 4.9% davon aus. Vielversprechende Theorien deuten darauf hin, dass schwach wechselwirkende, massive Teilchen (WIMPs) jenseits der Standardmodells der Teilchenphysik diesen Überfluss an DM erklären könnten. Mit erheblichem Aufwand wird versucht, diese Teilchen mit erdgebundenen Experimenten über WIMP-Atomkern-Streuung nachzuweisen. Während WIMP-Nukleon-Wechselwirkungsquerschnitte größer als $2 \cdot 10^{-45} \text{ cm}^2$ (bei einer WIMP-Masse von $\sim 55 \text{ GeV}$) bereits ausgeschlossen sind, geben einige der ultra-sensitiven Detektoren Hinweise auf die Existenz von WIMPs niedriger Masse ($\mathcal{O}(1\text{-}30 \text{ GeV})$).

Das Experiment CRESST (Cryogenic Rare Event Search with Superconducting Calorimeters), welches im Untergrundlabor des LNGS (Laboratori Nazionali del Gran Sasso) in Italien aufgebaut ist, benutzt CaWO_4 -Kristalle zum Nachweis von WIMPs. Die szintillierenden Kristalle mit einer Masse von jeweils $\sim 300 \text{ g}$ werden als Phonondetektoren bei mK-Temperaturen betrieben, welche es erlauben die totale Energiedeposition einer Teilchenwechselwirkung zu messen. Das zugehörige Szintillationslicht wird gleichzeitig mit einem separaten kryogenen Lichtdetektor (Silizium auf Saphir) nachgewiesen. Solch eine Zweikanalauslese der Detektoren ermöglicht eine aktive Untergrunddiskriminierung von verschiedenen Teilchenwechselwirkungen mittels deren unterschiedlicher relativer Lichtausbeute (LY). Der dominante e^-/γ -Untergrund (per Definition bei LY=1) kann somit von der Signalregion der Kernrückstöße unterschieden werden. Die Reduktion von LY im Vergleich zu Elektronrückstößen ist umso stärker, je höher die Massenzahl (A) des Rückstoßkerns ist. Dieser Effekt wird durch die Einführung von sogenannten Quenching-Faktoren (QF) quantifiziert. Die genaue Kenntnis des QFs eines jeden Rückstoßkerns erlaubt dessen Identifizierung auf einer Einzelereignis-Basis und damit eine Diskriminierung von Neutronenuntergrund und die Aufschlüsselung der Zusammensetzung der Kernrückstöße an O, Ca und W durch ein mögliches WIMP-Signal. Dabei geht man üblicherweise von kohärenter WIMP-Nukleon-Streuung aus (direkt proportional zu A^2). Der Hauptteil dieser Arbeit befasst sich mit der präzisen Messung der QFs von CaWO_4 bei tiefen Temperaturen (mK). Die neuesten CRESST-Ergebnisse der letzten Messkampagne (run32) mit einer Exposition von 730 kg-Tagen zeigen einen Signalüberschuss von hoher statistischer Signifikanz ($> 4\sigma$), welcher nicht mit den bekannten Untergründen (Neutronen, α , e^-/γ und ^{206}Pb) vereinbar ist und auf die Existenz von WIMPs niedriger Massen hindeuten könnte. Jedoch könnten auch seltene Prozesse (wie z.B. Oberflächen-Sputtereffekte), die mit den bekannten Untergründen korreliert sind, dieses Signal (oder Teile davon) erklären.

Im Rahmen dieser Arbeit wurden Detektorprototypen entwickelt, die es erlauben, die oben genannten Untergründe maßgeblich zu reduzieren, und im CRESST-Testkryostaten im Untergrundlabor des LNGS getestet. An der TU München produzierte CaWO_4 -Kristalle wurden zum ersten Mal als CRESST-Detektoren betrieben und auf Phononeigenschaften, Lichtausbeute und radioaktive Reinheit untersucht. Dabei wurde eine intrinsische α -Kontamination von $\sim 3 \text{ mBq/kg}$ gemessen. Außerdem ergab eine spezielle Messkampagne, dass $\sim 28\%$ aller in run32 beobachteten ^{206}Pb -Rückstöße durch ^{222}Rn -Implantation aus Luft verursacht worden sein könnten. Um solche Oberflächenereignisse vollständig zu unterdrücken, wurde in dieser Arbeit ein neues Detektordesign entwickelt: ein quaderförmiger Kristall ($\sim 250 \text{ g}$) wird dabei

von CaWO_4 -Stäben gehalten, welche - zusammen mit einer szintillierenden Polymerfolie, die den Detektor umgibt - ein komplett szintillierendes Detektorgehäuse bilden. α -Teilchen von ^{210}Po -Zerfällen produzieren zusätzliches Szintillationslicht, das die ^{206}Pb -Rückstoßereignisse aus der Signalregion entfernt. Die Funktionsweise eines solches Vetos wurde erfolgreich im Testkryostaten geprüft. Außerdem wurde gezeigt, dass dieses Detektordesign sich exzellent als Phonondetektor eignet und dass die Quaderform des Kristalls zu einer erhöhten Lichtausbeute führt (48% mehr Licht im Vergleich zu einem Zylinder). Daraufhin wurden im Rahmen dieser Arbeit zwei solcher Module realisiert und in den CRESST-Aufbau integriert.

Im Beschleunigerlabor des Maier-Leibnitz-Laboratoriums (MLL) in Garching wurde ein Neutronenstreuexperiment speziell zur Messung der QFen von CaWO_4 aufgebaut. Monoenergetische Neutronen mit einer Energie von 11 MeV, welche in einer durch einen gepulsten ^{11}B -Strahl induzierten Kernreaktion produziert werden, streuen dabei an einem CRESST-ähnlichen Detektormodul in einem Entmischerkryostaten und werden von Flüssigszintillator-Detektoren bei festem Streuwinkel nachgewiesen. Mit Hilfe der sogenannten Dreifach-Koinzidenztechnik kann der Rückstoßkern identifiziert werden. Durch die simultane Messung des Licht- und Phononkanals kann der entsprechende QF bestimmt werden. Das Experiment wurde auf die Messung des QF von W optimiert, welcher mit den Daten von ~ 3 Wochen Strahlzeit und einem Signal-zu-Untergrund Verhältnis von $\sim 7 : 1$ zum ersten Mal mit hoher Präzision und bei tiefen Temperaturen (mK) gemessen werden konnte. Eine speziell entwickelte Maximum-Likelihood-Analyse liefert $QF_W = 0.0196 \pm 0.0022$.

Mit der so erlangten Kenntnis des QF von W wird eine energieabhängige Analyse der gesamten Kernrückstoßbänder bis zu einer Energie von 1800 keV möglich. Dafür wurde ein korrelierter Maximum-Likelihood-Fit entwickelt, der die Beiträge von O, Ca und W jeweils mit einer Gaußkurve beschreibt und außerdem den präzise gemessenen QF von W verwendet. Eine mögliche Energieabhängigkeit der QFen wurde in Analogie zum Elektronrückstoßband durch eine Konstante und einem exponentiellen Anstieg (für das Elektronrückstoßband: exponentieller Abfall) hin zu kleinen Energien parametrisiert. Der Fit konvergiert über den gesamten Energiebereich und die Daten werden vollständig von der gewählten Parametrisierung beschrieben. Die Energieabhängigkeit des QF von O beträgt $\sim 6.1\%$, wenn man 20 keV und 100 keV Rückstöße vergleicht, während diese für Ca nur $\sim 1.5\%$ beträgt. Phänomenologische Modelle sagen voraus, dass die Energieabhängigkeit tatsächlich umso schwächer ist, je höher die Masse des Rückstoßkerns ist. Die Annahme eines konstanten QF von W im Energiebereich von 20 bis 250 keV ist damit gerechtfertigt. Die Ergebnisse bei einer Rückstoßenergie von 100 keV sind $QF_O = 0.1212 \pm 0.0035$, $QF_{\text{Ca}} = 0.0667 \pm 0.0030$ und $QF_W = 0.0196 \pm 0.0022$. Darüberhinaus wurde eine Variation der QFen von $\sim 10\%$ zwischen verschiedenen CaWO_4 -Kristallen beobachtet. Trotzdem können die Neutronenkalibrationsdaten von CRESST-Detektoren sehr gut durch die gemessenen energieabhängigen QFen beschrieben werden. Die QFen - gemittelt über die acht Detektormodule, die in CRESST-run32 eingesetzt wurden - belaufen sich bei einer Rückstoßenergie von 20 keV auf $QF_O^{\text{cresst}} = 0.1124 \pm 0.0042$, $QF_{\text{Ca}}^{\text{cresst}} = 0.0595 \pm 0.0022$ und $QF_W^{\text{cresst}} = 0.0172 \pm 0.0022$.

Die QFen von CaWO_4 wurden mit noch nie da gewesener Präzision bei mK-Temperaturen gemessen, wodurch zum ersten Mal eine klare Energieabhängigkeit beobachtet werden konnte. Dies hat erheblichen Einfluss auf die DM-Analyse und das Verständnis von CRESST-Detektoren. Zusätzlich wurden neue, komplett szintillierende Detektormodule entwickelt, in denen der Kristall von CaWO_4 -Stäben gehalten wird. Diese sollten den Untergrund von Oberflächenereignissen maßgeblich unterdrücken und dabei helfen, in naher Zukunft aufzuklären, ob der Signalüberschuss in run32 durch unberücksichtigten Untergrund zu erklären ist oder ob es sich um einen tatsächlichen Hinweis auf Dunkle Materie handelt.

Contents

1	Dark Matter	1
1.1	Evidence for Dark Matter in the Universe	1
1.2	The WIMP Scenario	4
1.3	Direct Detection of WIMPs	7
1.4	Direct Dark Matter Experiments and Recent Results	11
2	The CRESST Experiment	15
2.1	CaWO ₄ Crystals as Target for Dark Matter	15
2.2	Working Principle of Cryogenic CRESST Detectors	16
2.2.1	Phonon and Light Detectors	16
2.2.2	Phonon-Light Technique	18
2.2.3	Surface Background Discrimination	20
2.2.4	Cryogenic Detector Model	21
2.3	Experimental Setup	23
2.3.1	Shielding Against Background	23
2.3.2	The Cryostat	26
2.3.3	Data Acquisition and Electronics for Detector Operation	26
2.4	First Extensive Dark Matter Run (run32)	28
2.4.1	Results	28
2.4.2	Backgrounds	29
2.5	Preparations for the Upcoming Dark Matter Run (run33)	33
3	Detector Prototypes for the CRESST Experiment	41
3.1	The CRESST Test Cryostat at Gran Sasso	41
3.2	Data Analysis of Cryodetectors	41
3.2.1	Standard Event Fit and Calibration	42
3.2.2	Phonon-Anti-Quenching	45
3.2.3	Cuts and Live-Time Determination	47
3.2.4	Parametrization of Recoil Bands	48
3.2.5	Determination of the Light Output of Crystals	50
3.3	First Test of TUM-Grown CaWO ₄ Crystals	51
3.3.1	Performance as Cryogenic Detector	53
3.3.2	Light Output and Resolution	54
3.4	Radon-Exposure Measurement	57
3.5	New Detector Holder Concept Based on CaWO ₄ Sticks	65
3.5.1	The Challenge of a Fully-Scintillating Detector Housing	65

3.5.2	Basic Idea and Working Principle	67
3.5.3	Realization	69
3.5.4	Detector Performance at the CRESST Test Cryostat	70
3.5.5	Light Output and Resolution	77
3.6	Radiopurity of Self Grown Crystals	81
3.6.1	α Analysis	82
3.6.2	Results and Discussion	85
3.7	Implementation of Prototype Detectors in the CRESST Setup	88
4	Quenching Factor (QF) Measurements of CaWO_4	93
4.1	Definition of QFs and Relevance for the CRESST Experiment	93
4.2	Phenomenological QF Model	95
4.3	Previous QF Measurements	97
4.4	Working Principle of Quenching Factor Measurements	98
4.5	Experimental Setup: The CRESST Scattering Facility	103
4.5.1	Accelerator Setup	103
4.5.2	Cryogenic Setup	104
4.5.3	Liquid-Scintillator Detectors	108
4.5.4	Data Acquisition	108
4.6	Data Analysis Overview	110
4.7	Results of the Cryodetector Measurement	112
4.8	QF Measurements using the Triple Coincidence Technique	116
4.8.1	Triple Coincidence Search	117
4.8.2	Maximum-Likelihood-Analysis	122
4.8.3	Results for the QF of W	126
4.9	Energy-Dependent QF Analysis of CaWO_4 at mK Temperatures	128
4.9.1	Independent Fits of the Nuclear Recoil Bands	128
4.9.2	Basic Considerations for a Energy-Dependent QF Analysis	128
4.9.3	Correlated Likelihood Fit for the Energy-Dependent QF Analysis	131
4.9.4	Results of the Energy-Dependent QF Analysis	132
4.10	Application of QFs to CRESST Detector Modules	136
5	Summary and Outlook	145
A	Background Gamma Lines	151
B	Technical Drawings of Novel Detector Holder	155
C	The MLL Accelerator as a Neutron Source	167
C.1	Ion Production and Acceleration	168
C.2	Pulsed Ion Beam	168
C.3	Neutron Production	169
C.4	Mounting of the Cell and Beam-Monitoring System	172
D	Cryogenic Setup of the Scattering Facility	173
	Bibliography	184

Chapter 1

Dark Matter

1.1 Evidence for Dark Matter in the Universe

Evidence for Dark Matter (DM) becomes visible on **the scale of galaxies**. The measurement of the orbital velocities of stars at various distances from the galactic center indicates the existence of a large amount of non-luminous matter. According to Newtonian dynamics the orbital velocities of stars and gas is given by

$$v(r) = \sqrt{\frac{GM(r)}{r}} \quad (1.1)$$

where $M(r)$ is the total mass within the distance r from the center and G the gravitational constant. Therefore, outside the optical disc (with radius $r = R$) of a galaxy the stars' orbital velocities should fall according to

$$v(r) = \sqrt{\frac{GM(R)}{r}} \propto \frac{1}{\sqrt{r}}. \quad (1.2)$$

In contrast to this expectation, in most galaxies a rather flat velocity distribution - even far beyond the visible matter (galactic disk) - is measured as, e.g., shown in figure 1.1 for the galaxy NGC 6503 [1]. Assuming a spherical parametrization of the mass $M(r) = 4\pi \int \rho(r)r^2 dr$ with $\rho(r)$ being the mass density, the nearly constant orbital velocities imply the existence of a dominant DM halo with $M(r) \propto r$ and $\rho(r) \propto \frac{1}{r^2}$ until far beyond the radius of the visible part of the galaxy.

A crucial issue concerning a direct detection of DM is the knowledge of its local density at the position of the Earth which can be derived from measurements of the rotation curves of our galaxy, the Milky Way. Despite uncertainties in the velocity distribution of DM and the mass density distributions of the galactic bulge, the DM density can be constrained within $0.2\text{-}0.8 \text{ GeV/cm}^3$ [2]. The average velocity of DM is thereby assumed to be $v_0 \approx 270 \text{ km/s}$.

Observations of **galaxy clusters**, e.g., the COMA cluster by F. Zwicky in the 1930ies [3], provided similar evidence for the existence of Dark Matter in addition to the visible mass. The observed velocities of the galaxies are too large to hold them together in clusters only by their mutual gravitation. Calculations based on the virial theorem which relates kinetic and potential energy give the following approximate relation [2]

$$k_B T \approx (1.3 - 1.8) \text{ keV} \left(\frac{M_r}{10^{14} M_\odot} \right) \left(\frac{1 \text{ Mpc}}{r} \right) \quad (1.3)$$

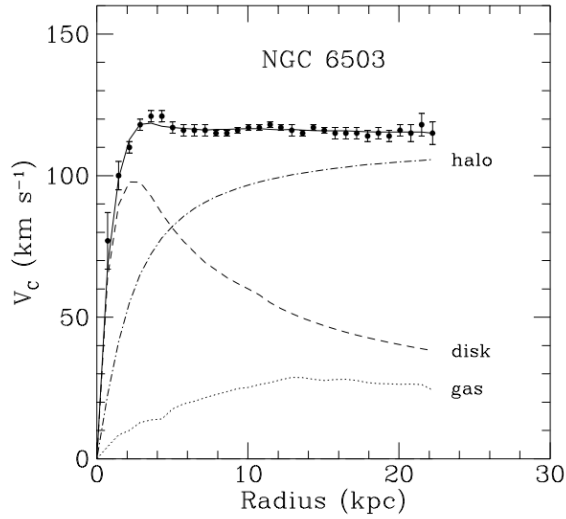


Figure 1.1: Orbital velocities of objects of the galaxy NGC 6503 [1]. The rotational curve is basically flat beyond a radius of 5 kpc. This is not consistent with the visible matter of the galaxy alone (disk, gas) but a significant contribution of non-luminous matter (halo), called Dark Matter, is necessary.

where T is the temperature - which can be determined experimentally - when the dynamics within the cluster is described by an ideal gas and M_r is the enclosed mass within a radius r . For typical baryonic masses and dimensions of galaxy clusters a temperature of 1.3-1.8 keV is expected while ~ 10 keV is measured. This can be checked by weak gravitational lensing. The results suggest a significant contribution of DM which exceeds the visible matter by a factor of ~ 5 .

The Bullet Cluster [4] which characterizes the region of a unique merger of two galaxy clusters is the most illustrative evidence for DM. Due to the collision, the visible part (X-ray measurement) is strongly deformed while the centers of gravity (measured by gravitational lensing) of both clusters passed through each other and are clearly spatially separated from the centers of the baryonic matter, as shown in figure 1.2. This is a strong indication that the majority of the matter therein is not visible.

The observations of the **cosmic microwave background** (CMB) radiation released at the time of decoupling about 380.000 years after the Big Bang, actually turned cosmology into a quantitative science and allowed to precisely determine the parameters of the standard cosmological concordance model, the Λ CDM model [2]. According to the observations of A. Penzias and R. Wilson [5] the CMB is isotropic on large scales and turned out to be a perfect black-body radiator with a temperature of $T = 2.726$ K [6]. However, the existence of fluctuations in the CMB radiation on smaller scales was found for the first time by the satellite missions COBE [7] and WMAP [8] the results of which were recently updated by the third-generation experiment PLANCK [6]. The fluctuations observed on a level of $< 10^{-5}$ (see figure 1.3) were the seeds for the large-scale structures which fill the present Universe. Apart from minor deviations at intermediate scales [6], the data can very well be fitted to the Λ CDM model [2] which describes the Universe being dominated by the gravitationally repul-

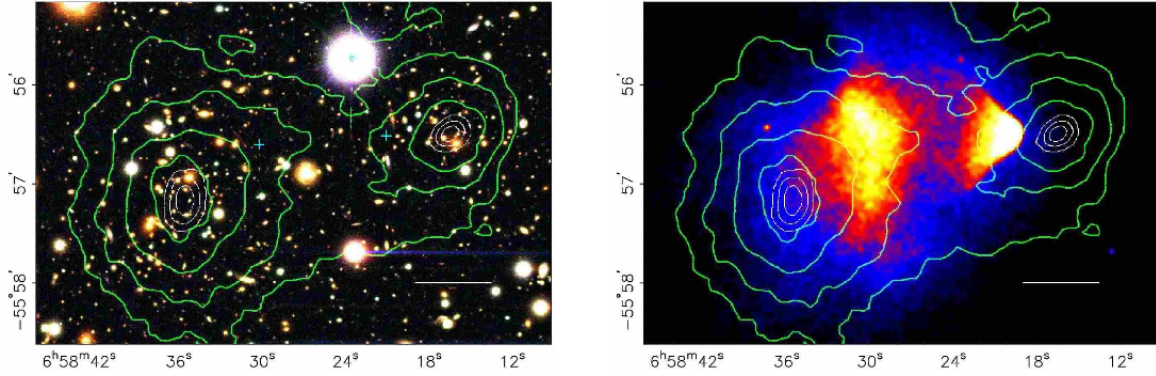


Figure 1.2: Left: Optical image of the merging cluster 1E0657-558, commonly called “Bullet Cluster”. Right: X-ray picture of the same region. In both panels, the white horizontal bar corresponds to a distance of 200 kpc, the “+”-signs (left) and the color coding (right) indicate the centers of the visible mass (at $\sim -55^\circ 56.5'$, $\sim 6\text{h}58^m 31^s$ and $\sim 6\text{h}58^m 20^s$) and the green contours are the results of gravitational-lensing measurements. The significant spatial separation of the baryonic matter from the gravitational centers is a strong indication for the existence of DM [4].

sive, widely unknown Dark Energy (Λ) and the non-relativistic, cold Dark Matter (CDM). The Hubble constant, one of the fundamental cosmological parameters which describes the expansion rate of the Universe was determined with high precision:

$$H_0 = (67.4 \pm 1.4) \text{km s}^{-1} \text{Mpc}^{-1} = h \cdot 100 \text{km s}^{-1} \text{Mpc}^{-1} \quad (1.4)$$

Within the standard cosmological model the energy contents Ω_i of the Universe are commonly expressed by

$$\Omega_i = \frac{\rho_i}{\rho_{\text{crit}}}, \quad (1.5)$$

the fraction of the energy density ρ_i normalized by the critical density $\rho_{\text{crit}} = 3H_0/(8\pi G)$ (G being the gravitational constant). If the total density ρ_{tot} of the Universe has the value of the critical density, galactic velocities would vanish at infinite times. For $\rho_{\text{tot}} > \rho_{\text{crit}}$ the Universe would collapse while it would be ever expanding for $\rho_{\text{tot}} < \rho_{\text{crit}}$ [9]. The data of the Planck mission, however, is consistent with a spatially flat Universe ($\Omega_{\text{tot}} = 1$) on a percent level and gives precise measurements of the relic densities of baryonic matter $\Omega_b h^2$ and cold DM $\Omega_\chi h^2$:

$$\Omega_b h^2 = 0.02205 \pm 0.00028 \quad (1.6)$$

$$\Omega_\chi h^2 = 0.1199 \pm 0.0027. \quad (1.7)$$

Thus, the data suggests the following contributions to the total mass-energy density of the Universe ($\Omega_{\text{tot}} \sim 1.0$): Cold Dark Matter ($\Omega_\chi \sim 0.265$) is ~ 5 times more abundant than baryonic matter ($\Omega_b \sim 0.049$) and the contribution of the cosmological constant Λ ($\Omega_\Lambda = 0.685^{+0.018}_{-0.016}$) is dominant.

Since there is compelling evidence for Dark Matter over a wide range of length scales in the Universe there is only little room for modified gravitational theories as, e.g., the MOND

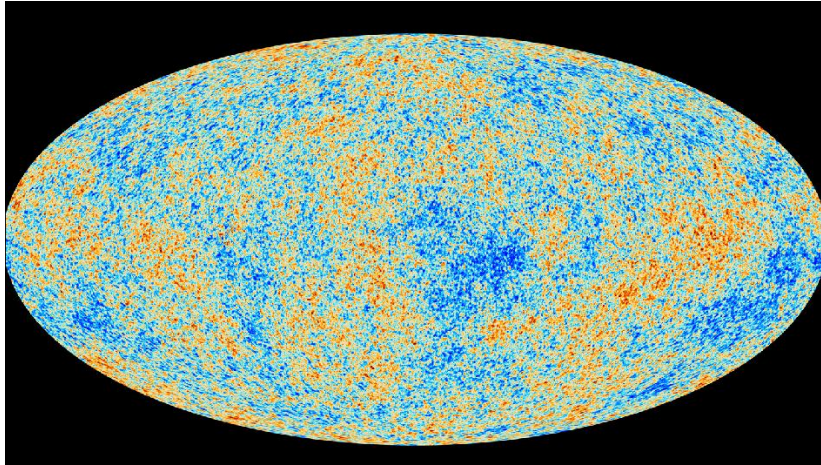


Figure 1.3: Sky map of the cosmic-microwave background (CMB) measured by the Planck mission. The plot shows the results of the analysis using the Planck instruments at different frequencies (30-857 GHz) with an angular resolution of $5'$ [6].

(MODified Newtonian Dynamics) theory [1] which is an attempt to explain the observations without DM, only with baryonic matter. Nevertheless, only a direct detection in earth-bound experiments would be the final proof for the existence of DM.

1.2 The WIMP Scenario

Due to the compelling evidence on various scales in the Universe it is impossible to describe the observations, as e.g., the CMB data without cold Dark matter and, thus, without massive, non-relativistic and electrically neutral particles beyond the standard model of particle physics. In general, for a stable Dark Matter (DM) particle naturally existing in the present Universe energy conservation (decay only into lighter particles) and gauge symmetry (e.g. conservation of electric charge) have to be valid [9]. For example, electrons are stable for the trivial reason that there is no lighter particle with the same electric charge (the gauge invariance of electromagnetism is exact), whereas protons do not have to be necessarily stable as there is no gauge symmetry of the baryon number. Therefore, there are long-standing attempts to search for a possible proton decay [10].

There is no room to explain the total abundance of DM present in the Universe with standard-model particles as, firstly, a possible DM particle obviously cannot carry any electric charge - otherwise it would already have been detected. Secondly, neutrinos which would in principle be a natural candidate are widely ruled out to account for the major part of DM:

- Neutrinos are not abundant enough to sufficiently explain the DM in the Universe. From thermodynamics in the early Universe and the freeze out of relativistic particles from thermal equilibrium follows for the relic density of neutrinos [11]

$$\Omega_\nu h^2 = \sum_{i=1}^3 \frac{m_i}{94\text{eV}} \quad (1.8)$$

where m_i is the mass of the i -th neutrino flavour. The best upper limit from laboratory experiments on the electron-neutrino mass is $m_\nu < 2.05\text{eV}$ (95% C.L.) [12]. For the

relic density of neutrinos follows

$$\Omega_\nu h^2 < 0.07 \quad (1.9)$$

assuming that all three neutrino flavours have similar masses.

- Additionally, observations of the CMB (see chapter 1.1) [8] set an even tighter constraint on the relic density of neutrinos to $\Omega_\nu h^2 < 0.0067$ (95% C.L.) which implies - assuming mass degeneration - a neutrino mass of $m_\nu < 0.23$ eV.
- Neutrinos being relativistic particles, also called hot DM, are strongly disfavoured over cold DM relics concerning structure formation. Below the free-streaming length (~ 40 Mpc) neutrinos would destroy fluctuations of the mass density which is against the obvious existence of small-scale structure in the present Universe [13].

This shows that new physics beyond the standard model of particles is necessary to solve the DM enigma. Due to the considerations above, a hypothetical DM particle must be of a new particle species carrying a certain quantum number which is strictly conserved. The lightest among these particles would therefore be stable. In many supersymmetric models an additional Z_2 symmetry¹ is introduced with an additional “charge”

$$R = (-1)^{3(B-L)+2s}, \quad (1.10)$$

called R -parity, where B is the baryon number, L is the lepton number and s is the spin of the corresponding particle. Ordinary standard-model particles ($R = +1$) have a supersymmetric partner with $R = -1$ and R -parity conservation is assumed. The lightest supersymmetric particle (LSP) would be stable and therefore constitute an excellent candidate for a DM particle. Such particles are commonly referred to as WIMPs (Weakly Interacting Massive Particles). Due to the multiplicative quantum number R the neutralinos can only be produced and annihilated in pairs. The most popular WIMP candidate is the neutralino

$$\chi = N_1 \tilde{\gamma} + N_2 \tilde{Z}_0 + N_3 \tilde{H}_1^0 + N_4 \tilde{H}_2^0 \quad (1.11)$$

as LSP in the so-called minimal supersymmetric standard model (MSSM) where $\tilde{\gamma}$ is the photino (supersymmetric partner of the photon), \tilde{Z}_0 the zino (supersymmetric partner of the Z_0 -boson) and the higgsinos $\tilde{H}_1^0, \tilde{H}_2^0$, the supersymmetric partners of the neutral scalar Higgs bosons. The coefficients N_i are normalized such that $\sum_{i=1}^4 |N_i|^2 = 1$ [9].

A possible DM scenario would be the following: In the time immediately after the Big Bang when thermal energies were sufficiently high, large numbers of supersymmetric particle pairs were produced. The cooling due to the expansion of the Universe caused heavier particles to freeze out of the thermal equilibrium. Successively, these particles decayed into the stable LSP, e.g., the neutralino and could still exist at present. If the mass of the considered particles is sufficiently large ($\mathcal{O}(1-1000)$ GeV) they could constitute the main contribution to the DM abundance. If the supersymmetric particles were interacting on the electroweak scale with ordinary matter in the early Universe they have been non-relativistic when freezing out and their relic density can be calculated as [2]

$$\Omega_\chi h^2 \simeq \frac{3 \cdot 10^{-27} \text{ cm}^3 \text{ s}^{-1}}{\langle \sigma v \rangle} \quad (1.12)$$

¹ Z_2 stands for a discrete multiplicative group with two elements: +1 and -1 [11].

with $\Omega_\chi h^2$ being the relic cold DM density and $\langle\sigma v\rangle$ the total, thermally averaged WIMP annihilation cross section times the relative velocity [14]. Assuming $\Omega_\chi h^2 \simeq 0.12$ as measured by Planck (see equation 1.7) gives: $\langle\sigma v\rangle \simeq 2.5 \cdot 10^{-26} \text{ cm}^3 \text{ s}^{-1}$. For weak interaction of WIMPs it follows that $\langle\sigma v\rangle \approx G_F^2 m_\chi^2$ assuming the WIMP mass m_χ being smaller than the Z_0 -mass [15] and hence

$$\Omega_\chi h^2 \simeq 3 \left(\frac{m_\chi}{\text{GeV}} \right)^{-2}. \quad (1.13)$$

This means, that the annihilation cross section required to be consistent with the cosmological parameters measured by Planck (see section 1.1) is remarkably close to the electroweak interaction cross section for reasonable WIMP masses in the GeV range.

This often called ‘‘WIMP miracle’’ might just be a coincidence, however, it suggests that DM might interact at the electro-weak scale. Thereby, it might be possible to detect these particles in earthbound experiments. Due to extensive theoretical studies [16] the LSP became a well-motivated WIMP candidate for the detection of which an enormous experimental effort has been made.

There are generally three different methods for the detection of DM:

- **Accelerator searches:** At particle accelerators, like the LHC (CERN) with its full design energy of 14 TeV the main experiments ATLAS [17] and CMS [18] can discover signals which point towards new particles beyond the standard model. Of course, even if a particle is found which fulfils all requirements for a WIMP it is not proven to be the DM particle existing in the present Universe. The demonstration that the lifetime of the new particle discovered is longer than the age of the Universe is impossible in such an experiment [11]. Nevertheless, the general mass scale of such a new class of particles would be of utmost interest for the entire research field.
- **Indirect searches:** As mentioned above, WIMPs could annihilate with each other and create standard model particles. In particular, the production of antiparticles might be detectable with a good signal-to-background ratio due to the large baryon asymmetry in the Universe. There are dedicated experiments searching for an excess of positrons and anti-protons in the galactic halo. WIMPs could also annihilate into γ -rays which would unlike charged particles point back to the site where the reaction took place. The annihilation rate can be written as [2]

$$\Gamma_{\chi\chi} \propto n_\chi^2 \sigma_{\chi\chi} v \quad (1.14)$$

where n_χ is the number density of WIMPs, $\sigma_{\chi\chi}$ the WIMP annihilation cross section and v the relative velocity. Therefore, regions where an enhanced DM density is expected as, e.g., the galactic center are in the focus of Earth-bound and satellite γ -ray telescopes (typical energies GeV-TeV). Also high-energy neutrinos could be a tracer for WIMP annihilation. For example, due to the quadratic rise of $\Gamma_{\chi\chi}$ with the WIMP density high-energy neutrinos (\gg MeV) could be created preferentially in the center of the sun and unlike other particles would easily escape. Large Earth-bound neutrino telescopes [19] search for such an excess signal from the direction of the sun. For more detailed information about the extensive field of indirect DM detection refer to [2] and references therein.

- **Direct searches:** Probably the most promising technique to detect DM is to look for interactions of WIMPs with ordinary matter such as, e.g., elastic nuclear scattering, in

Earth-bound detectors. A mathematical description of such interactions (chapter 1.3) and an overview of experimental approaches (chapter 1.4) are presented in this work.

Apart from WIMPs there is a huge variety of alternative, well-developed DM models, such as e.g., axions, gravitinos, superWIMPs, non-thermal DM, decaying DM, sterile neutrinos, Q-balls [11]. A detailed description of these models, however, is beyond the scope of this work and the interested reader is directed to an extensive review [2].

1.3 Direct Detection of WIMPs

There is evidence for Dark Matter (DM) on all scales of the Universe including our own galaxy which implies that DM should also be present in the solar system and DM particles should traverse the earth with the typical galactic velocities. Direct DM experiments search for WIMP-induced nuclear recoils by using a variety of techniques (see chapter 1.4). Here, a mathematical description of the scattering mechanism is given. For more details see, e.g., [20, 21].

The velocity of the WIMPs is mainly given by the velocity of the DM particle relative to the Earth-bound target (in average: $v_0 \sim 230 \text{ km s}^{-1}$) and a Maxwellian velocity distribution f according to

$$f(\mathbf{v}, \mathbf{v}_e) = e^{-(\mathbf{v}-\mathbf{v}_e)^2/v_0^2} \quad (1.15)$$

with the velocity \mathbf{v} of the DM particle and the velocity of the Earth \mathbf{v}_e with respect to the galactic rest frame. As described in chapter 1.1, the local mass density of DM derived from rotation curves is $\rho_\chi = 0.2 - 0.8 \text{ GeV/cm}^3$. The differential particle density can be written as [20]

$$dn = \frac{1}{k} \frac{\rho_\chi}{m_\chi} f(\mathbf{v}, \mathbf{v}_e) d^3\mathbf{v} \quad (1.16)$$

where m_χ is the mass of the WIMP and k is normalized such that $\int_0^{v_{\text{esc}}} dn = \frac{\rho_\chi}{m_\chi}$ (v_{esc} is the galactic escape velocity). The differential rate can be expressed by

$$dR = \frac{N_A}{A} \sigma_0 v dn \quad (1.17)$$

with $N_A = 6.02 \cdot 10^{26} \text{ kg}^{-1}$ being the Avogadro number, A the atomic mass number and σ_0 the WIMP-nucleus cross-section. Under the approximation of $v_{\text{esc}} = \infty$ and $v_e = 0$ the total rate can be written as

$$R_0 = 0.054 \left(\frac{100}{A} \right) \left(\frac{100 \text{ GeV}}{m_\chi} \right) \left(\frac{\sigma_0}{1 \text{ pb}} \right) \left(\frac{\rho_\chi}{0.4 \text{ GeV cm}^{-3}} \right) \left(\frac{v_0}{230 \text{ km s}^{-1}} \right) \text{ kg}^{-1} \text{ d}^{-1}. \quad (1.18)$$

Assuming typical parameters in this equation only **very low event rates** are expected. An additional challenge for direct detection are the **low-energy recoils** ($\mathcal{O}(10 \text{ keV})$) induced by WIMPs. For elastic scattering of WIMPs on a nucleus of mass number A the recoil energy E_R of the nucleus is given by

$$E_R = E \frac{4\mu^2}{m_\chi m_N} (1 - \cos \Theta) / 2 \quad (1.19)$$

where $\mu = m_\chi m_N / (m_\chi + m_N)$ is the reduced mass, Θ the scattering angle in the center-of-mass system, E the energy of the WIMP and m_N the mass of the nucleus. In the following,

the mass of the nucleon m_N is approximately expressed by $m_N \approx A \cdot m_p$ (m_p is the proton mass). The maximal recoil energy ($\Theta = 180^\circ$) for a WIMP of $m_\chi = 100$ GeV, e.g., on tungsten ($A \sim 184$) is $E_R \sim 38$ keV. Isotropic scattering in $\cos \Theta$, namely, $dR(\cos \Theta)/d \cos \Theta = 0$ gives for the differential rate

$$\frac{dR(E)}{dE_R} = \int_{E_{\min}}^{E_{\max}} \frac{1}{E \cdot r} dR(E) \quad (1.20)$$

with $r = 4\mu^2/(m_\chi m_N)$ and $E_{\min} = E_R/r$ being the minimal WIMP energy which can give a recoil energy of E_R . The maximal energy that can produce a recoil of energy E_R is determined by $E_{\max} = m_\chi v_{\max}^2/2$ where v_{\max} is the maximal WIMP velocity [20]. An approximate calculation ($v_{\text{esc}} = \infty$, $v_e = 0$) yields

$$\frac{dR(E_R)}{dE_R} = \frac{R_0}{E_0 \cdot r} e^{-\frac{E_R}{E_0 \cdot r}} \quad (1.21)$$

with the mean WIMP energy $E_0 = \frac{1}{2} m_\chi v_0^2$ which shows the characteristic exponential energy spectrum towards lower recoil energies due to the Maxwellian velocity distribution of the DM particles in the galactic halo.

Due to the finite size of a target nucleus an additional multiplicative correction, the so-called Helm form factor [22] has to be considered. If the momentum transfer from the WIMP to the nucleus $q = (2Am_p E_R)^{1/2}$ increases such that the wavelength h/q is no longer large in comparison to the effective nuclear radius r_n the Helm form factor F which is a function of the dimensionless factor qr_n/\hbar becomes relevant. According to [20] this quantity can be approximated as

$$\frac{qr_n}{\hbar} = 6.92 \cdot 10^{-3} A^{1/2} E_R^{1/2} (a_n A^{1/3} + b_n) \quad (1.22)$$

with E_R in units of keV and a_n , b_n to parametrize the effective nuclear radius $r_n = a_n A^{1/3} + b_n$ in units of fm. A commonly used approximation of the corrected cross section is

$$\sigma_{\text{corr}} = \sigma_0 \cdot e^{-\frac{1}{3} \left(\frac{qr_n}{\hbar} \right)^2} \quad (1.23)$$

which, however, is only valid for small momentum transfers $qr_n < 3$ [20].

For the interaction cross section one has to distinguish between spin-independent and spin-dependent scattering depending on the target material. Here, as for CaWO_4 - the detector material used in the CRESST experiment - only 2.4% of the nuclei [23] have net spin, just the spin-independent case is considered in the following. If spin-independent interactions on neutrons and protons are assumed to be similar, the scattering amplitudes add up in phase for sufficiently low momentum transfers ($qr_n < 1$) which results in a coherent cross section $\sigma_0 \propto A^2$. However, the coherence is broken for higher momentum transfers which is accounted for by the nuclear Form factors. Concretely, assuming a coherent electro-weak interaction that would be valid in the non-relativistic regime for heavy Dirac neutrinos as description of the WIMP-nucleus interaction cross section $\sigma_{0,\nu}$ it would be dependent also on the proton number Z and the Weinberg angle Θ_W :

$$\sigma_{0,\nu} = \frac{G_F^2}{8\pi\hbar^4} \mu^2 \cdot ((A - Z) + (1 - 4 \sin \Theta_W) \cdot Z)^2 \sim (A - Z)^2 \quad (1.24)$$

since $(1 - 4 \sin \Theta_W) \approx 0.08$ [20]. Nevertheless, both dependencies, $\sigma_0 \propto A^2$ and $\sigma_0 \propto (A - Z)^2$ enable a convenient comparison of experimental results originating from different target nuclei.

As the experimentally measured quantity will always be a superposition of the WIMP-nucleon cross section and the astrophysically determined WIMP density at the Earth, namely $\sigma_0 \cdot \rho_\chi$, the usual convention adopted by the DM-search community for the (spin-independent) scattering cross section of a single nucleon is [21]

$$\sigma_0^{(\text{nucleon})} = \frac{\mu_p^2}{\mu_N^2} \frac{\sigma_0}{A^2} = \left(\frac{1 + m_\chi / (A m_p)}{1 + m_\chi / m_p} \right)^2 \frac{\sigma_0}{A^2} \quad (1.25)$$

where μ_p and μ_N is the reduced mass of a proton and a nucleus, respectively, for the interaction with a WIMP of mass m_χ under the assumption $\sigma_0 \propto A^2$. Commonly, the DM density is fixed at $\rho_\chi = 0.3 \text{ GeV cm}^{-3}$.

In conclusion, the following mostly quite challenging characteristics of WIMP interaction in Earth-bound detectors have to be considered:

- Very **small event rates** are expected for elastic scattering of WIMPs as shown in equation 1.18 due to the extremely small WIMP-nucleon cross sections. The current best upper limit for $\sigma_0^{(\text{nucleon})}$ is $2 \cdot 10^{-9} \text{ pb}$ at $m_\chi \sim 55 \text{ GeV}$ [24]. Therefore, only single scatters which are uniformly distributed in the detector are expected. Due to the extremely low event rates ($\lesssim 0.1/\text{kg}/\text{day}$ [25]) experiments aiming at the detection of DM must be well shielded against ambient radioactivity which can mimic WIMP interactions. Therefore, such detectors are installed in underground laboratories and only ultra-pure materials are used for detector construction and shieldings.
- For typical WIMP masses and velocities and elastic scattering of WIMPs on nuclei (see equation 1.19), **nuclear recoils of low energies** (in the order of 10 keV) are expected which requires extremely sensitive detectors with excellent background-suppression capabilities.
- Due to the Maxwellian velocity distribution an **exponential energy spectrum** decreasing towards higher energies is expected (see figure 1.4) which unfortunately is similar to most background-induced event classes (see, e.g., [25]). Therefore, in many second-generation experiments (see chapter 1.4) apart from the channel that measures the total energy deposition in a detector a second channel (e.g. light or ionization) which is sensitive to the kind of particle interaction is recorded. This allows an active event-by-event background discrimination of the - in most cases - dominant γ -induced electron-recoil background.
- Due to the usually assumed A^2 dependency of the coherent spin-independent scattering cross section a possible claim for the discovery of a DM particle can be cross-checked using information provided by different target materials from various direct-detection experiments (see chapter 1.4). At present, this **multi-material target approach** is only realized in the CRESST experiment (see chapter 2) which uses CaWO_4 crystals as target.
- The annual motion of the Earth around the Sun causes an **annual modulation** of the Earth velocity with respect to the galactic rest frame:

$$v_e = (244 + 15 \sin(2\pi t)) \text{ km s}^{-1} \quad (1.26)$$

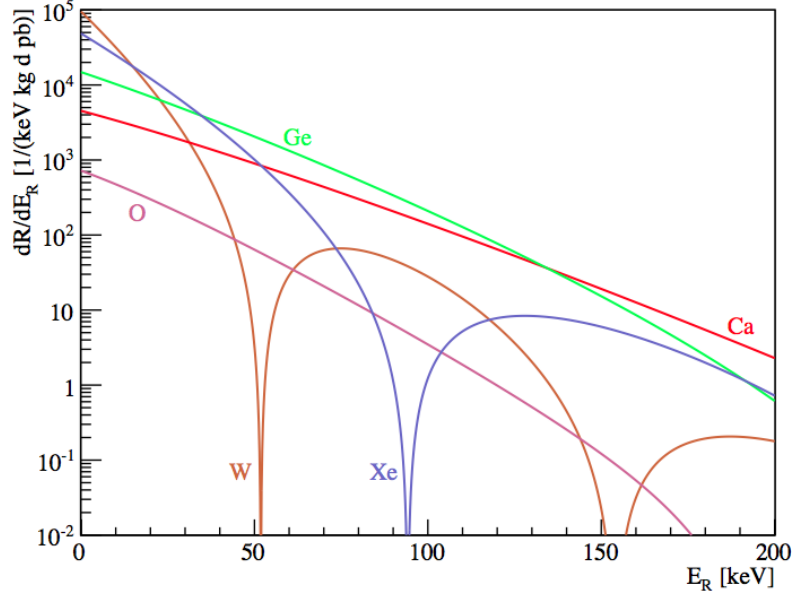


Figure 1.4: Differential rates assuming a WIMP mass of $m_\chi = 100$ GeV, a WIMP-nucleon cross section of $\sigma_0^{(\text{nucleon})} = 1$ pb and taking Helm form factors [20] into account which cause a decrease of the rate (e.g. for W at $E_R \sim 50$ keV). Picture from [27].

where t [years] is the time from March 2nd [20]. This effect of $\sim 6\%$ in velocity modulation converts into a $\sim 3\%$ modulation in rate which can be approximated in differential form by

$$\frac{dR(v_e, v_{\text{esc}} = \infty)}{dE_R} = c_1 \frac{R_0}{E_0 \mu} e^{-c_2 \frac{E_R}{E_0 \mu}} \quad (1.27)$$

where c_1 and c_2 are fitting constants (dependent on t) in the order of unity [20]. The detection of this modulation effect with the correct phase and amplitude could be a hint for the existence of WIMPs [26].

- In principle, there is also a diurnal variation of the expected WIMP signal due to the rotation of the Earth. However, to exploit such a signal the direction of the DM particles has to be resolved. Up to now, there is no experimental technique available with the required sensitivity.

Illustration and Comparison of Results: As far as backgrounds are sufficiently reduced or rejected, direct DM search experiment can probe DM-particle interactions. The results are commonly displayed in the WIMP-nucleon cross section versus WIMP-mass plane as shown in figure 1.5. A positive signal interpreted as DM would allow to constrain a certain region in this parameter space. In absence of a signal, upper limits for the WIMP-nucleon cross section $\sigma_0^{(\text{nucleon})}$ as defined in equation 1.25 can be given. The shape of those curves depends on the sensitivity of the individual detector for the considered WIMP-mass m_χ and is influenced by the following factors:

- The interaction rate is highest if m_χ has the same mass as the recoiling target nucleus $\sim A m_p$ and decreases for lower and higher values of the WIMP mass. It is governed by the reduced mass μ .
- The rate is directly proportional to the flux of DM particles $\Phi_\chi = \frac{\rho_\chi}{m_\chi}$ (see equation 1.18). Therefore, the sensitivity is the lower the higher the value of m_χ .
- The energy threshold of the detector which is usually in the order of 1-10 keV significantly reduces the sensitivity at $m_\chi \lesssim 10$ GeV. Since the expected WIMP-induced recoil spectrum is less energetic for lower values of m_χ a smaller fraction of the signal is “sampled”.

1.4 Direct Dark Matter Experiments and Recent Results

In this chapter selected detection techniques and experiments for the direct detection of Dark Matter (DM) are briefly presented. For a more complete view refer, e.g., to the recent review [28] and the references contained therein.

Scintillation Detectors: The light output of scintillating crystals by WIMP-induced nuclear recoils is exploited in several DM experiments. The DAMA/LIBRA experiment [26] located in the underground laboratory of the Laboratori Nazionali del Gran Sasso (LNGS) in Italy uses ~ 250 kg of Tl-doped NaI crystals to search for an annual modulation of the WIMP-nucleon interaction. In the total exposure of 1.17 ton-years corresponding to 13 annual cycles a modulation amplitude of (0.0116 ± 0.0013) counts/kg/keV/day is observed for single detector hits in the energy region of 2-6 keV with high significance (8.9σ C.L.) [26]. As explained in chapter 1.3, such a results is consistent with Dark Matter made of WIMPs within a mass range of $m_\chi \sim 1 - 10$ GeV (see figure 1.5), however, a background origin of this signal is not completely ruled out.

Other experiments are on their way to probe this WIMP claim such as the KIMS experiment [29] using Tl-doped CsI crystals and the DarkIce project [30] using NaI crystal in the infrastructure of the IceCube experiment [31] at South pole. The latter is particularly interesting, as a seasonally related background would be shifted by ~ 6 month due to the location on the southern hemisphere.

Ionization Detectors: Apart from early experiments based on ionization Si/Ge detectors [40, 41] recently the CoGeNT experiment located in the Soudan underground laboratory using p-type point-contact Ge detectors [36] with an energy threshold as low as 0.5 keV should be mentioned here. Apart from an excess signal which - if interpreted as a DM signal - would point towards low-mass WIMPs of 7-9 GeV [42] a hint (2.8σ C.L.) for an annual modulation of the signal [43] has been found. The preferred parameter space is depicted in figure 1.5 and 1.6.

Phonon-Ionization Detectors: The EDELWEISS experiment [33] located in the Laboratoire Souterrain de Modane and the CDMS (Cold Dark Matter Search) experiment [34] installed in the Soudan underground laboratory are using cryogenic Ge (in case of CDMS also Si) detectors operated at mK temperatures. This allows a very precise measurement of the heat (phonons) produced by particle interaction such as nuclear recoils induced by WIMPs.

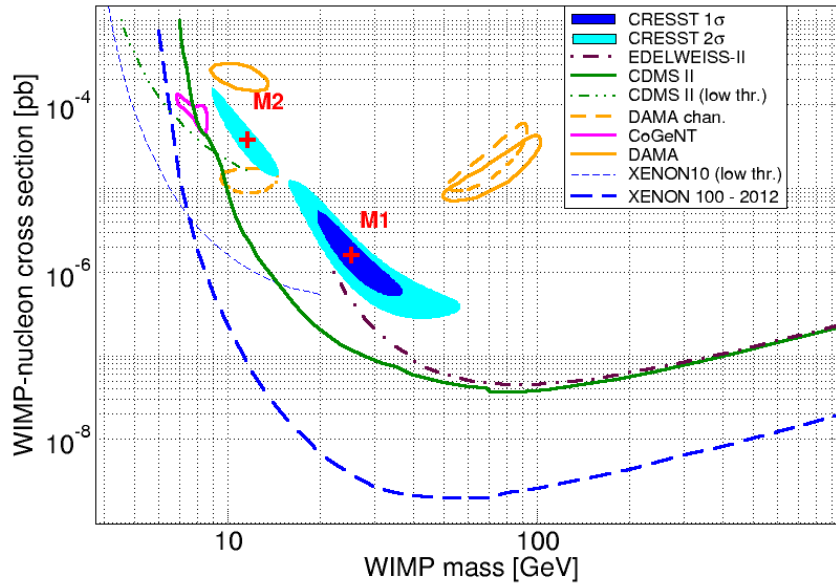


Figure 1.5: WIMP-nucleon cross section versus WIMP-mass plot with the latest results of the leading direct Dark Matter experiments described in chapter 1.4. The tension between the best upper limits from XENON [24, 32], EDELWEISS [33], and CDMS [34, 35] and the possible hints for WIMPs by CRESST [25], DAMA [26] and CoGeNT [36] is clearly visible. The recent results of CDMS using Si detectors is shown in figure 1.6.

By simultaneously measuring the ionization those detectors allow to discriminate electron recoils and surface background which significantly increases the sensitivity. And indeed, these experiments set stringent limits on the WIMP-nucleon scattering cross section (see figure 1.5) with the highest sensitivity at $m_\chi \sim 70$ GeV. In addition, due to a low-threshold analysis of their detectors both experiments give tighter constraints in the low-mass WIMP region below ~ 10 GeV [35, 39]. Very recently, the CDMS collaboration published WIMP-search data with Si detectors [37]. Three background events that are not consistent with background (background-only probability: 0.19%) are observed within an exposure of 140 kg-days. If interpreted as WIMP signal, the best fit suggests a WIMP mass $m_\chi = 8.6$ GeV at a cross section of $\sigma_0^{(\text{nucleon})} = 1.9 \cdot 10^{-5}$ pb (see figure 1.6).

Liquid Noble Gas Detectors: The XENON100 experiment [24] uses a dual-phase liquid Xe time-projection chamber to search for rare interactions. A particle-interaction induced scintillation signal (S1) is recorded by an array of photomultipliers (PMTs) installed in the liquid phase of Xe (present mass ~ 62 kg) and the simultaneously produced charge is drifted along an electric field to the interface between the liquid and the gaseous phase. A second, delayed scintillation signal is produced there and detected by an additional array of PMTs installed above the gaseous phase. The combination of both signals and the drifting time is used to discriminate backgrounds. In addition, the position of the particle interaction in the detector volume can be reconstructed which enables a surface-event rejection. Presently, the data of the XENON100 experiment with an exposure of ~ 7.6 ton-days [24] set the world-best exclusion limit on the WIMP-nucleon scattering cross-section: $\sigma_0^{(\text{nucleon})} = 2 \cdot 10^{-9}$ pb at

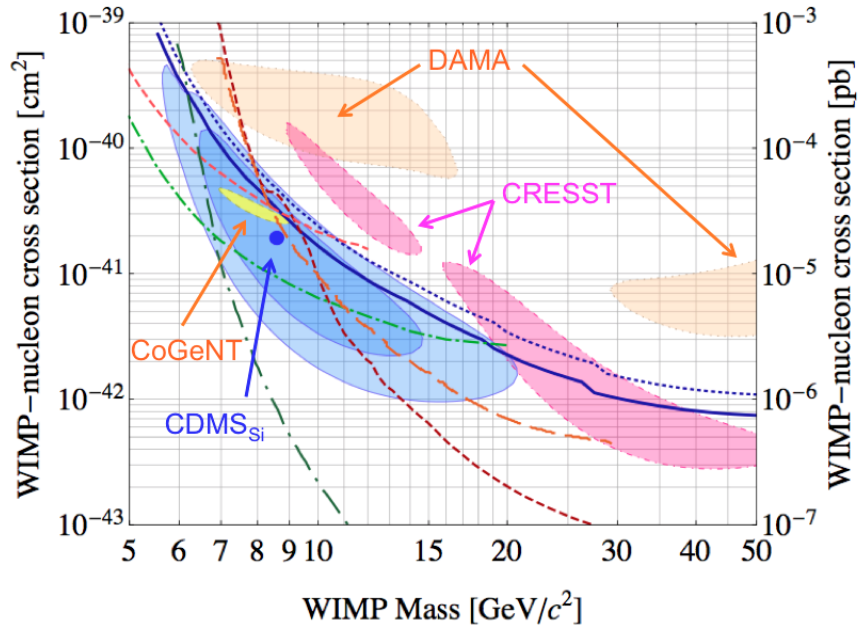


Figure 1.6: WIMP-nucleon cross section versus WIMP-mass plot of the low-mass region [37]. The following limits are shown in the plot: dotted blue, CDMS(Si) [37]; full blue, CDMS(Si) combined data [38]; dashed-dark red, CDMS(Ge) [34]; dashed-light red, CDMS(Ge) low threshold [35]; long-dashed orange, EDELWEISS low threshold [39]; long-dashed-dotted green, XENON100 [24]; dashed-dotted green, XENON10 S2-only [32]. The regions of positive DM signals if interpreted as WIMP scatters are directly indicated by arrows and explained in the text.

$m_\chi \sim 55 \text{ GeV}$.

In addition, the LUX (Large Underground Xenon) detector [44], a dual-phase Xe detector based on the XENON100 technique with a larger target mass ($\sim 370 \text{ kg}$) is under construction. Detectors based on liquid Ar, DEAP-3600 [45] at SNOLAB and DarkSide [46] in the LNGS are under construction and will, in the future, help to clarify the tensions between different experimental results especially in the low-mass WIMP region.

Phonon-Scintillation Detectors: The second phase of the CRESST experiment which is located in the LNGS in Italy uses scintillating CaWO_4 crystals operated as phonon detectors at mK temperatures to search for WIMPs. The setup, performance and results of CRESST are described in detail in chapter 2. In the data of the last run (2009-2011) with an exposure of $\sim 730 \text{ kg-days}$ an excess signal above the rather high background contributions has been observed with high significance ($> 4\sigma \text{ C.L.}$). If those events are interpreted as WIMP-scatters they would point towards WIMPs of $m_\chi = 11.6 \text{ GeV}$ and $m_\chi = 25.3 \text{ GeV}$, respectively (see figure 1.5 and 1.6).

Considering possible hints for Dark Matter concentrated in the low-mass WIMP region of $m_\chi \sim 5 - 20 \text{ GeV}$ by DAMA/LIBRA, CoGeNT, CDMS(Si) and CRESST, and the stringent limits by XENON, EDELWEISS and CDMS(Ge) down to $\sigma_0^{(\text{nucleon})} = 2 \cdot 10^{-9} \text{ pb}$ serious tensions arise (see figure 1.5). However, the clustering of WIMP claims within roughly one order of magnitude in WIMP mass $m_\chi \sim 10 \text{ GeV}$ and cross section $\sigma_0^{(\text{nucleon})} \sim 10^{-4} \text{ pb}$ might indicate that the edge of a discovery is reached. Many of the mentioned experiments have data to be published or are currently taking data which will hopefully clarify the situation in the near future.

Furthermore, projected ton-scale experiments like XENON1ton [47] and EURECA [48, 49] which is proposed to be a merger between the CRESST and EDELWEISS type experiments will probably reach sensitivities which will finally be limited mainly by coherent neutrino-nucleus scattering of neutrinos emitted by the Sun and of atmospheric neutrinos [50].

Chapter 2

The CRESST Experiment

The **C**ryogenic **R**are **E**vent **S**earch with **S**uperconducting **T**hermometers (CRESST) experiment aims at the direct detection of **W**eakly **I**nteracting **M**assive **P**articles (WIMPs). In this chapter, the experimental approach, the setup and the latest results of CRESST are presented and, in particular, an outlook regarding the upcoming experimental run is given.

2.1 CaWO_4 Crystals as Target for Dark Matter

CRESST features scintillating CaWO_4 single crystals as target material. In the standard detector design cylindrical crystals of 40 mm in diameter and height and a mass of ~ 300 g are used. The intrinsic luminescence centers WO_4^{2-} give rise to **scintillation** with a maximum light emission at a wavelength of ~ 420 nm and a typical decay times of $\mathcal{O}(10 \mu\text{s})$ at room temperature. The mean light yield of $\sim 20\,000$ photons per MeV of deposited energy by, e.g., a particle interaction is enhanced by a factor of ~ 1.8 at mK temperatures where the decay times also significantly extend to $\sim 400 \mu\text{s}$ [51, 52]. The light output of the transparent crystals with a refractive index of $n = 1.92$ strongly depends on the surface conditions such as roughness. This is illustrated in figure 2.1 and discussed in great detail in chapter 3.



Figure 2.1: Picture of standard CRESST-size CaWO_4 crystals under UV-light irradiation. The front surface of the left crystal is polished (bevelled edges) while the right one is roughened which visibly homogenizes and enhances the light output through this surface.

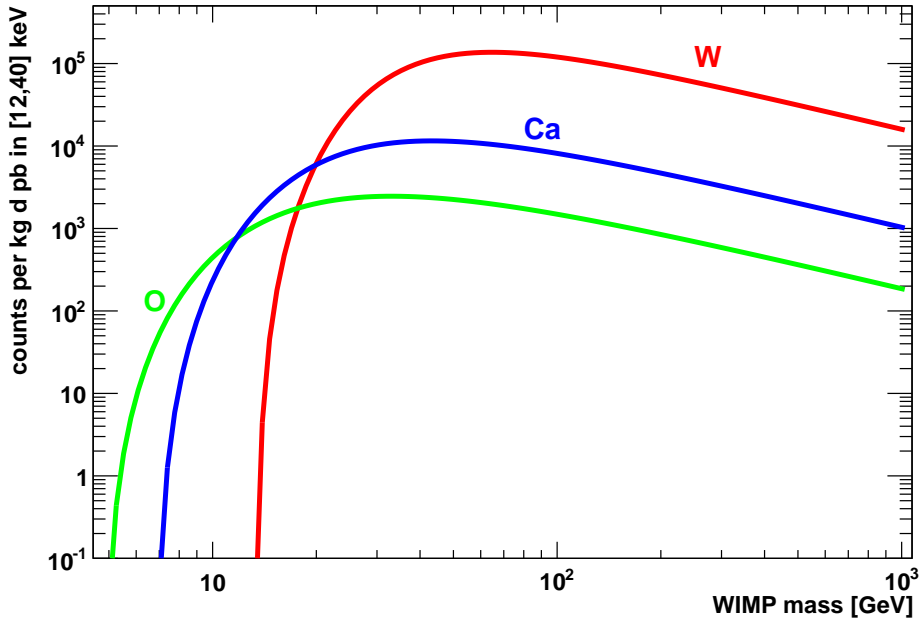


Figure 2.2: Contribution of the three constituents of CaWO_4 to the total expected rate of WIMP interactions as a function of the WIMP mass. The rate is calculated according to equation 1.21 with an assumed WIMP-nucleon cross section of 1 pb in the sensitive energy range of a typical CRESST detector (12-40 keV).

As widely observed in common scintillating materials [53] the light output of highly ionizing particles such as alphas and recoiling nuclei is reduced due to **light quenching** (see chapter 4). The effect is the stronger the higher the proton number Z of the interacting particle. For this reason different kind of particles can be identified and discriminated against each other.

Assuming coherent WIMP scattering off nuclei, due to its $\propto A^2$ dependency on the mass number A of the target nucleus (see chapter 1.3) the scattering cross section is strongly enhanced for W ($A \approx 184$). Nevertheless, also the lighter constituents in CaWO_4 namely O ($A \approx 16$) and Ca ($A \approx 40$) become relevant especially for lower WIMP masses $m_\chi \lesssim 10$ GeV. In figure 2.2 this effect is illustrated for a typical detector with a sensitive energy range between 12 and 40 keV: While the expected WIMP-induced recoils for $m_\chi > 30$ GeV are completely dominated by W recoils, the momentum transfer (see equation 1.19) of lower WIMP masses on W is not sufficient to induce detectable signals (due to the finite threshold of the detectors) which are, therefore, strongly suppressed for $m_\chi < 10$ GeV. Due to the unique feature of having three nuclei in the same target material, a so-called **multi-material target**, CRESST detectors are sensitive to a large range of possible WIMP masses.

2.2 Working Principle of Cryogenic CRESST Detectors

2.2.1 Phonon and Light Detectors

CRESST detectors based on scintillating CaWO_4 crystals are designed and operated to simultaneously exploit two different signals:

- The **total energy deposition** by a particle interaction in the crystal is measured by the produced heat in terms of phonons. Therefore, the crystals are operated as cryogenic phonon detectors at mK temperatures.
- A small part of the total deposited energy ($\mathcal{O}(1\%)$) is converted into **scintillation light** which is measured by a second, separate cryogenic light detector.

The ~ 300 g CaWO_4 target crystal, called the **phonon detector**, is equipped with a transition-edge-sensor (TES) which consists of a thin W-film of $6\text{ mm} \times 8\text{ mm}$ evaporated onto the crystal or evaporated onto a CaWO_4 carrier which is then glued onto the crystal (composite design) [54]. The temperature is adjusted such that the detector is stabilized in the steep transition (width $\sim\text{mK}$) between the superconducting and normal-conducting state of the W-film in the $10 - 20\text{ mK}$ range. Phonons induced by a particle interaction uniformly fill the crystal and thermalize in the TES. This heats up the sensor and the corresponding temperature change results in a significant variation of the TES resistance (see figure 2.3) which is amplified and read out by a SQUID (Superconducting Quantum Interference Device) [55]. The detector relaxes back to the equilibrium state via a weak thermal coupling to the heat bath by a Au-bond wire. This results in electronic pulses with typical decay times of 10-100 ms and with an amplitude proportional to the deposited energy. Typically, energy thresholds as low as $\lesssim 1\text{ keV}$ and a dynamic range extending to $\mathcal{O}(10\text{ MeV})$ are reached with these devices. To increase the light output the base surface opposite to the side carrying the TES is roughened.

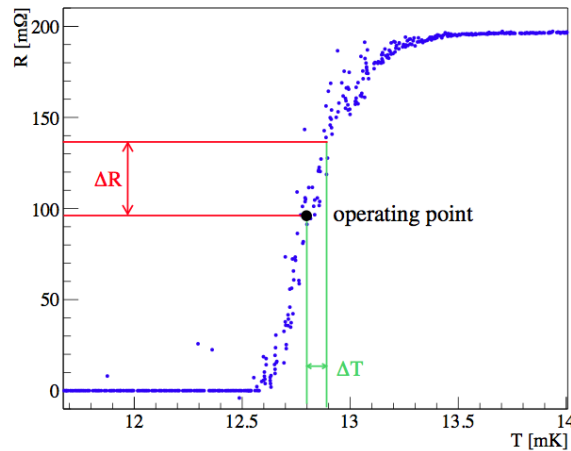


Figure 2.3: Transition from the superconducting to the normal-conducting state for a typical W-TES as used for CRESST detectors. The temperature is typically stabilized in the most linear part of the transition (operating point). A small rise in temperature ΔT (green) causes a significant change of the resistance ΔR (red) which is read out by a SQUID circuit [55].

The separate cryogenic **light detector** consists of a sapphire disc of 40 mm in diameter and 0.46 mm thickness with a $1\ \mu\text{m}$ Si layer grown onto one side - so-called silicon-on-sapphire (SOS) - to absorb the optical scintillation photons from the CaWO_4 crystal. In some cases, pure Si discs are used. Photon-induced phonons, like in the phonon detector, are detected in a W-TES of about $1.5\text{ mm} \times 2\text{ mm}$ which produces electronic pulses corresponding to the amount of detected light. Due to the small mass of $\sim 2.3\text{ g}$, an optimized TES with Al phonon

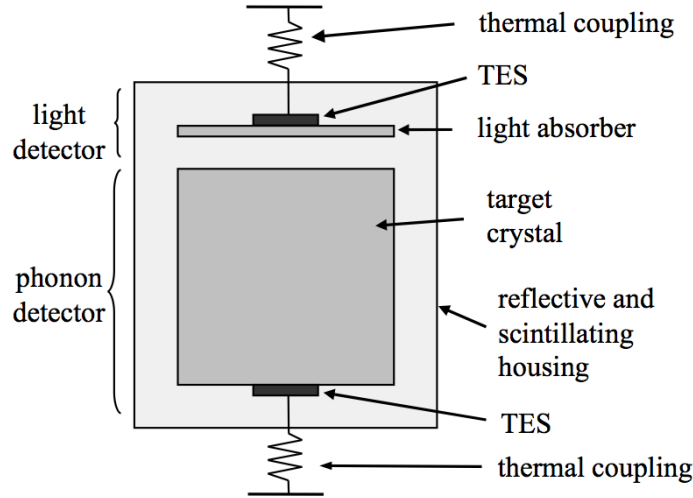


Figure 2.4: Scheme of a CRESST detector module consisting of a CaWO_4 phonon detector and a separate light detector which are surrounded by a reflective and scintillating foil [25].

collectors and an extremely weak thermal coupling the light detectors are sensitive to light energies of $\mathcal{O}(10\text{ eV})$ [56].

Both detectors are housed in a so-called **detector module** supported by a structure made of NOSV copper [57] which is radio-pure and suited for low-temperature operation [23]. A scheme of a CRESST detector module is shown in figure 2.4 and a picture of an opened module (as operated in run32 of CRESST) is shown in figure 2.5. The detectors themselves are held by bronze clamps which remain flexible at mK temperatures and which are coated by a reflective material (e.g. Ag, Al) to avoid light losses. Seemingly a technical detail these clamps holding the CaWO_4 crystal are crucial for the functionality of the detectors (see chapters 2.4.2 and 3.5). The crystal is surrounded by a reflective and scintillating polymeric foil (VM2002 [23]) to increase the light collection and to guide the scintillation light to the light detector. The fact that this foil is also scintillating under particle radiation is crucial for surface background rejection (see chapter 2.2.3)

2.2.2 Phonon-Light Technique

Due to the two simultaneously operated cryogenic detectors, both, the deposited energy E_r and the corresponding scintillation light E_L can be used to characterize the particle interaction. As described in chapter 2.1, light quenching observed in CaWO_4 crystals offers the possibility to identify the kind of particle interacting. The relative light output, commonly called light yield LY is defined as

$$LY \propto \frac{E_L}{E_r}. \quad (2.1)$$

Accordingly, for highly ionizing particle a reduced light yield compared to electron recoils is expected from quenching. In practice, the heavier the interacting nucleus the lower the light yield. In a simplified view, the LY_x of an interaction of a particle x is constant with the

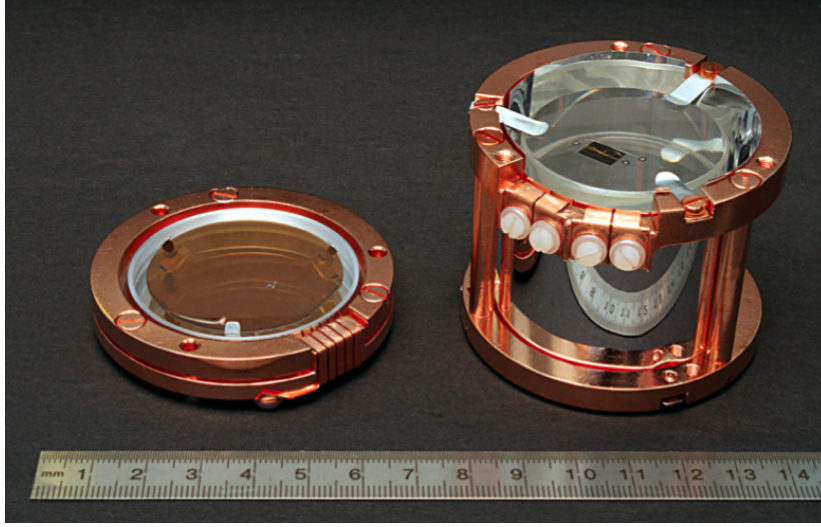


Figure 2.5: Picture of an opened CRESST detector module as operated in run32. Left: A silicon-on-sapphire light detector with the W TES on the upper side. Right: CaWO_4 target crystal with the W TES enclosed by the reflective and scintillating polymeric foil. Both detectors are held by silver-coated bronze clamps. The upper side of the phonon detector is covered by polymeric foil while the light detector which faces the roughened side of the CaWO_4 crystal is mounted at the bottom.

deposited energy and can be quantified by **Quenching Factors** QF_x :

$$QF_x \sim \frac{LY_\gamma}{LY_x}. \quad (2.2)$$

The schematic plot in figure 2.6 in which the light yield is plotted against the total energy deposition illustrates how CRESST data is commonly displayed.

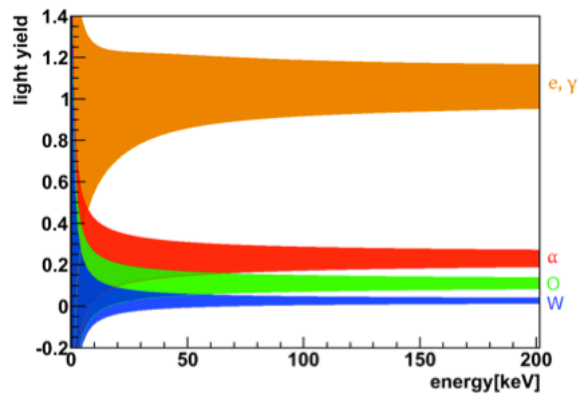


Figure 2.6: Scheme of how CRESST data is commonly displayed: the light-yield plot in which the light yield is plotted against the recoil energy. Horizontal bands related to different particle interactions arise.

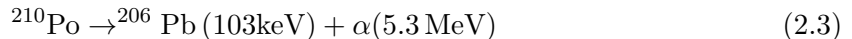
In such a light-yield plot horizontal bands of a certain width related to the finite detector res-

olution arise, obviously, the lower the higher the mass of the interacting particle. This allows to actively discriminate the dominant e^-/γ background from the nuclear-recoil bands (O, Ca and W) which form the region-of-interest (ROI) for WIMP search (typically 12-40 keV). If the resolution of the light detector is sufficient, even the individual nuclear-recoil bands can be disentangled which gives rise to an identification of backgrounds (e.g., α s, neutrons) and in case of a positive signal a determination of the WIMP-mass (see chapter 2.1).

The precise knowledge of the Quenching Factors (QFs) is crucial for the analysis of CRESST detectors and is the main topic of this thesis: for the first time the QFs of all three constituents have been measured at mK temperatures with the required precision and an energy-dependence has been observed (see chapter 4).

2.2.3 Surface Background Discrimination

α decays on the surface of the CaWO_4 and on surrounding surfaces (e.g. clamps, foil) constitute a dangerous background for DM search, in particular that of ^{210}Po which is a daughter nucleus of ^{238}U :



Due to momentum conservation the reaction products undergo a back-to-back (180°) emission which implies that either the high-energetic α particle or the ^{206}Pb nucleus hits the CaWO_4 target crystal and deposits energy in the phonon detector. α radiation in the MeV range is generally no problem as the energy regime is far off the ROI for DM search. However, **energy-degraded α 's** that decay at some implantation depth in surrounding material, e.g., in the clamps and lose a significant fraction of their energy therein can leak into the ROI (see overlap of α and nuclear-recoil bands in figure 2.6).

In turn, if **^{206}Pb nuclei** interact in the crystals - due to light quenching - only a small fraction of the deposited energy is converted into scintillation light. The QF of Pb is similar to that of W and ^{206}Pb recoils cannot be separated unambiguously from possible (heavy-) WIMP-induced W recoils. Of course, most of the surface decays will deposit an energy close to the full energy of $\sim 103\text{keV}$ in the crystal which is off the ROI. However, similar to degraded alphas the ^{206}Pb nuclei can lose some energy already in surrounding materials and leak down to lower energies (see figure 2.7).

Most of such events, nevertheless, can be **vetoed due to the scintillating foil** surrounding the crystal. α particles of MeV energies produce scintillation photons which typically deposit an energy of $\mathcal{O}(1\text{keV})$ in the phonon detector. This corresponds to the typical light output of 100 keV electron-recoil events which clearly shifts the ^{206}Pb events out of the nuclear-recoil band. Thereby, all ^{206}Pb events from the surface of the crystal as well as from the surface of the foil are efficiently vetoed. Strongly degraded α particles from the foil, obviously, lose energies of $\mathcal{O}(5\text{MeV})$ therein and produce light. Thereby they are shifted out of the ROI.

In conclusion:

- ^{210}Po decays occurring on the surface of the CaWO_4 crystal are generally no problem for DM search as they always deposit at least 103 keV in the phonon detector. Additionally, in case of the α particle escaping the crystal additional light is produced in the foil.
- Potentially dangerous ^{210}Po decays in the foil surrounding the detectors are efficiently vetoed as - for all possible low-energy events in the crystal - the α deposits an energy of $\mathcal{O}(5\text{MeV})$ in the foil which causes scintillation light.

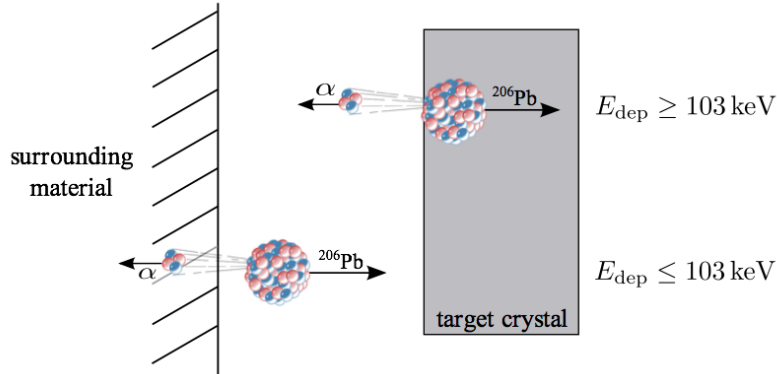


Figure 2.7: Illustration of ^{210}Po decays occurring on the surface either of the crystal or of surrounding material. Depending on the implantation depth the particles involved can loose energy in the corresponding material which influences the deposited energy in the phonon detector. If the surrounding material is scintillating (as, e.g., the foil) low-energetic ^{206}Pb recoil are vetoed by additionally produced light [25].

- Non-scintillating surfaces, such as the (silver-coated) bronze clamps holding the crystal, are critical. Degraded ^{206}Pb and strongly degraded α 's are not vetoed and can deposit energies < 103 keV in the phonon detector.

Indeed, in run32 of CRESST (see chapter 2.4) a ^{210}Po (surface-) contamination was the dominant background source. For technical reasons the clamps could not be covered with scintillating material which would establish an efficient veto similar to that of the foil.

In this thesis, an alternative CRESST-detector design was developed which features a fully scintillating detector housing (see chapter 3.5).

2.2.4 Cryogenic Detector Model

The formation of a pulse after a particle interacting in a CRESST detector is described by a model for cryogenic detectors in detail [58]. Here, only a brief overview according to [23] is given.

After a particle interaction, high-frequency acoustic phonons with up to about half the Debye frequency $f_{\text{Debye}}/2$ are produced in the absorber crystal. The Debye temperature of CaWO_4 is $\Theta_{\text{Debye}} \approx 250$ K [59] which leads to a phonon frequency of $f_{ph} = f_{\text{Debye}}/2 = k_B T/2 \approx 2$ THz. This corresponds to an energy $E = hf_{ph} \approx 8$ meV which is large compared to the energies of **thermal phonons** in the absorber crystal $E_{ph,t} = k_b T \approx 1 \mu\text{eV}$ (at typical operational temperatures of $T \sim 10$ mK). These high-frequency phonons are called **non-thermal phonons** which than decay within a few milliseconds decreasing their frequency to ~ 300 GHz.

Within $\sim 10 \mu\text{s}$ after the particle interaction, the phonons spread throughout the crystal and fill it uniformly. The fraction ϵ of the produced non-thermal phonons that enter the thermometer are efficiently absorbed by the electrons in the metallic film (e.g. W). Due to the strongly interacting electrons the phonons are quickly thermalized which heats up the thermometer. This gives rise to the fast signal component which is mathematically described

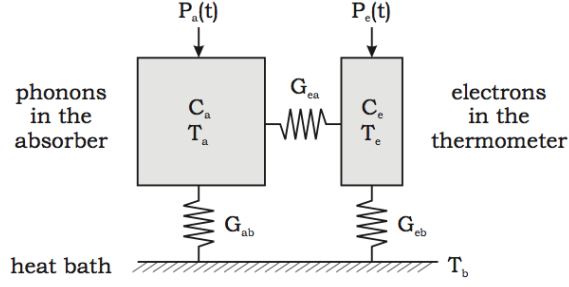


Figure 2.8: Simplified thermal model for cryogenic detectors. C_a and C_e are the heat capacities of the phonon system in the absorber crystal and of the electron system in the thermometer, respectively. T_a and T_e are the corresponding temperatures. The systems are thermally coupled to each other and to the heat bath of temperature T_b (quantified by the heat conductance G). $P_a(t)$ and $P_e(t)$ are the power inputs of non-thermal phonons into absorber crystal and thermometer, respectively. Illustration from [23].

by a time-dependent power input of high-frequency phonons into the thermometer:

$$P_e(t) = \Theta(t)\epsilon\frac{\Delta E}{\tau_n}e^{-t/\tau_n} \quad (2.4)$$

where $\Theta(t)$ is a step function, ΔE is the energy deposited by the incident particle and τ_n is the life-time of the non-thermal phonons in the system. Hence, the initial power input into the thermometer is $P_0 = \epsilon\Delta E/\tau_n$. The remaining fraction $(1 - \epsilon)$ thermalizes at the crystal surface which leads to a power input directly into the thermal phonon system of the absorber:

$$P_a(t) = \Theta(t)(1 - \epsilon)\frac{\Delta E}{\tau_n}e^{-t/\tau_n} \quad (2.5)$$

An illustration of a simplified thermal model for cryogenic detectors is shown in figure 2.8. Therein, the absorber (heat capacity C_a , temperature T_a) and the thermometer (C_e , T_e) are thermodynamical systems which are thermally coupled by the conductance G_{ea} and thermally linked to the heat bath (G_{ab} , G_{eb}) of temperature T_b . Prior to the power inputs $P_e(t)$ and $P_a(t)$ both systems are in thermal equilibrium with the heat bath ($T_a(t=0) = T_e(t=0) = T_b$). The thermal system can be described by two coupled differential equations [58] and solved for the temperature change in the thermometer $\Delta T_e(t) = T_e(t) - T_b$:

$$\Delta T_e(t) = \Theta(t)\left[\underbrace{a_n(e^{-t/\tau_n} - e^{-t/\tau_n})}_{\text{non-thermal component}} + \underbrace{a_t(e^{-t/\tau_t} - e^{-t/\tau_n})}_{\text{thermal component}}\right], \quad (2.6)$$

where τ_n is the life-time of the non-thermal component, τ_t is the thermal relaxation time of the absorber and τ_{in} the intrinsic relaxation time of the thermometer¹. The thermal response of the thermometer is converted into an electrical pulse due to the change in resistance with temperature. The pulses are described by two components: a_n is the amplitude of the non-thermal component and a_t the amplitude of the thermal component. Often the ratio of the

¹The sign of a_n is inverted compared to the definition in [58], however, matches the convention of the CRESST data analysis and the analysis performed in chapter 3 in the present thesis.

non-thermal component and the total amplitude a_{tot} is used for a characterization of the pulse shape:

$$\frac{a_n}{a_{tot}} = \frac{a_n}{a_t + |a_n|} \quad (2.7)$$

The three considered time constants are sufficient to explain the observed pulses of CRESST detectors.

The ratio τ_n/τ_{in} which controls the sign of the ratio a_n/a_t (or a_n/a_{tot}) classifies the two different operation modes of the detector:

- **Calorimetric Mode:** If $\tau_{in} \gg \tau_n$ ($a_n/a_t > 0$) the phonons flow into the thermometer faster than out of it. The thermometer integrates the power input into the thermometer $P_e(t)$ and thus measures the total energy of the absorbed high-energy phonons. The amplitude of the non-thermal component is proportional to the energy ΔE deposited by the particle and in this case dependent on the heat capacity of the thermometer C_e : $a_n \approx \epsilon \Delta E / C_e$. In the calorimetric mode, τ_n describes the rise time of both pulse components, τ_t the decay time of the thermal component and τ_{in} the decay time of the non-thermal component.

Due to an extremely weak thermal coupling to the heat bath and the small size of the absorber the light detectors operated in CRESST commonly work in the calorimetric mode. Typical values of the time constants are: $\tau_n \sim 1$ ms, $\tau_t \sim 50$ ms and $\tau_{in} \sim 10$ ms. Usually the non-thermal component dominates ($a_n : a_t \sim 10 : 1$).

- **Bolometric Mode:** If $\tau_{in} \ll \tau_n$ ($a_n/a_t < 0$) the phonons flow out of the thermometer faster than into it. The thermometer measures the flux of the non-thermal phonons and the amplitude of the non-thermal component is given by

$$a_n \approx -\frac{P_0}{G_{ea} + G_{eb}} \propto \Delta E \quad (2.8)$$

with the thermal couplings of the thermometer to the absorber G_{ea} and the heat bath G_{eb} . Hence, also in the bolometric mode the amplitude a_n is proportional to the energy ΔE deposited by the incident particle. τ_{in} and τ_n are the rise times and τ_n and τ_t the decay times of the non-thermal and thermal component, respectively.

The phonon detectors operated in CRESST work in the bolometric mode. Typical values of the times constants are: $\tau_n \sim 30$ ms, $\tau_t \sim 120$ ms and $\tau_{in} \sim 3$ ms. Same as for CRESST light detectors, the non-thermal component dominates ($a_n : a_t \sim 10 : 1$).

2.3 Experimental Setup

2.3.1 Shielding Against Background

In order to reach the sensitivities necessary for the detection of Dark Matter particles the reduction of the background level is crucial. **Cosmic radiation** is a strong source of background at sea level which is composed of muons ($\sim 45\%$), γ -rays ($\sim 35\%$), electrons/positrons ($\sim 20\%$) and to a small fraction of protons ($< 1\%$) with a total flux of $\sim 10^3 \text{ m}^{-2} \text{ s}^{-1}$ [23].

Environmental radiation is the second source of radioactivity originating from the natural decay chains of ^{235}U , ^{238}U and ^{232}Th , the biologically widespread isotope ^{40}K and radioactivity produced by mankind in nuclear reactions (mainly ^{137}Cs and ^{90}Sr). Most materials

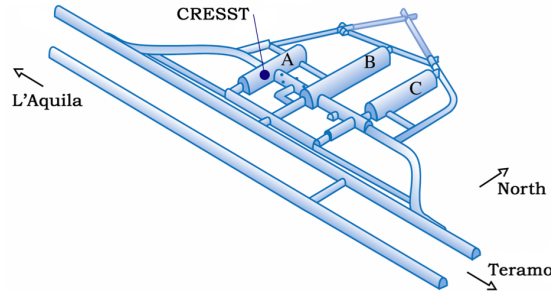


Figure 2.9: Overview of the Laboratori Nazionali del Gran Sasso (LNGS) of the INFN (Istituto Nazionale per Fisica Nucleare) in central Italy. At about halfway of the 10 km long highway tunnel through the Gran Sasso mountain three experimental halls of ~ 200 m length each are excavated. The CRESST experiment is located in hall A.

contain such radioactive isotopes to some extent.

Therefore, firstly, the experiment has to be well-shielded against cosmic and environmental radiation and, secondly, only extremely radio-pure materials should be present in the vicinity of the detectors.

The CRESST experiment is hence installed in the underground facility of the Laboratori Nazionali del Gran Sasso (LNGS) of the INFN (Istituto Nazionale per Fisica Nucleare) in central Italy (see figure 2.9) with a rock overburden corresponding to 3500 m of water equivalent. The cosmic-muon flux is reduced by ~ 6 orders of magnitude to a level of $\sim 1 \text{ m}^{-2} \text{ h}^{-1}$ with a mean energy of $\sim 320 \text{ GeV}$ [60]. The remaining components of the cosmic rays are completely suppressed. However, the remaining muons can induce backgrounds in the following ways:

- Directly passing through the detector and depositing energy therein (stopping power $\sim 2 \text{ MeV cm}^2 \text{ g}^{-1}$, e.g., in Cu).
- Production of secondary particles in surrounding materials via delta electrons.
- Production of neutrons or γ s by muon-induced interactions and spallation in surrounding material.
- Stopping of muons in the detector or surrounding material.

To reject most of the remaining muon-induced background an active muon veto (plastic scintillator) is installed around the detector volume of CRESST (see figure 2.10).

To shield against environmental γ -rays (flux $\sim 1 \text{ cm}^{-2} \text{ s}^{-1}$ at the experimental site [61]) a Pb layer of 20 cm in thickness is installed around the detectors. To reduce the intrinsic contamination by up to 5 orders of magnitude compared to conventional Pb, Boliden [10] and Roman [62] Pb was used. In between the detectors and the Pb shield an additional 14 cm thick layer of Cu (total mass 10 tons) is installed. It is made of ultra-pure OF01 copper from the Norddeutsche Affinerie [23].

Concerning **neutrons**, there are basically two sources at the underground site:

- Fast neutrons ($\gtrsim 10 \text{ MeV}$) induced by cosmic muons in the rock or in materials surrounding the detectors (e.g., Cu, Pb).

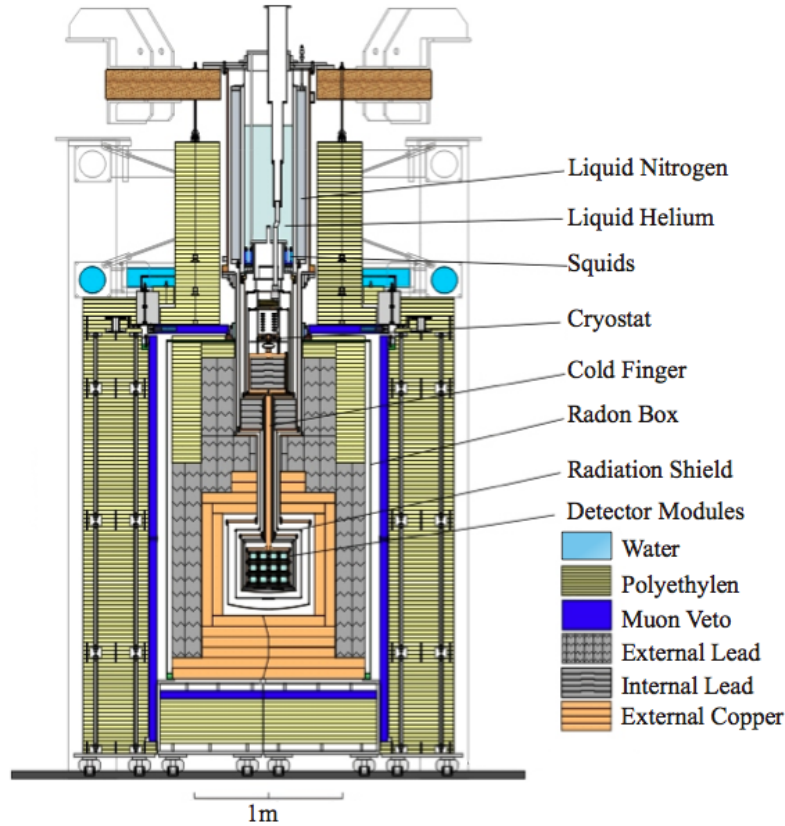


Figure 2.10: Scheme of the CRESST setup with the main components indicated. The experimental volume where the detectors are installed is surrounded by different layers of shieldings. The low-temperatures required for the operation of CRESST detectors are provided by a dilution refrigerator. Picture from [27].

- Neutrons from (α, n) reactions with energies of $\lesssim 10$ MeV in the concrete walls of the laboratory (flux $\mathcal{O}(30 \text{ m}^{-2} \text{ h}^{-1})$).

Therefore, the experimental volume is shielded by a 45 cm thick layer of polyethylene (PE) which moderates the neutrons below the threshold of CRESST detectors. It is installed outside of the muon-veto panels (see figure 2.10). Muon-induced neutrons produced in the inner Pb and Cu shieldings (muon missed by the muon veto) and (α, n) neutrons from material inside of the PE shield, however, are not moderated sufficiently. Hence, for the next run of CRESST an additional (inner) PE shield was installed directly around the detector volume (see chapter 2.5). The noble gas **radon** is produced in the natural decay chain of ^{238}U with a half-life of 3.8 days. ^{222}Rn is washed out or diffuses out of the rock which surrounds the experimental halls and has a high content of ^{238}U . The ^{222}Rn -induced α rate in air is thus measured to be $50 - 100 \text{ Bq m}^{-3}$ in the underground laboratory. If this contaminated air reaches the inner shieldings it can be implanted on any surface and successive α and β decays induce backgrounds. This is avoided by a container around the Pb shielding which is constantly flushed by clean nitrogen gas, the so-called radon box.

Radon implantation into surfaces of the detector modules from air (e.g., during mounting) might play a significant role concerning α and nuclear-recoil background and will be discussed

extensively in chapter 2.4.2 and 3.4.

2.3.2 The Cryostat

CRESST detectors are operated at mK temperatures which are provided by a $^3\text{He}/^4\text{He}$ dilution refrigerator. The cryostat itself is placed at a distance of ~ 1.5 m above the detector volume (see figure 2.10). This arrangement allows to sufficiently shield the cryostat which is commercially available and does not fulfil the requirements in terms of radiopurity. The detectors are thermally coupled to the dilution refrigerator by a 1.3 m long cold finger made of ultra-pure copper. This allows to almost completely enclose the detector volume by the Cu, Pb and PE shieldings described in chapter 2.3.1. At the bottom end of the cryostat additional layers of ultra-pure Pb are installed.

A commercial Oxford 1000S $^3\text{He}/^4\text{He}$ dilution refrigerator with a base temperature of ~ 5 mK is pre-cooled by the cryogenic liquids nitrogen² (~ 77 K) and helium (~ 4 K). A further refrigeration is achieved by pumping on a ^4He bath (1K-pot) and the dilution of ^3He and ^4He in the mixing chamber [63].

Around the detectors, cylindrical thermal shields made of ultrapure copper with a total thickness of ~ 1.2 cm are installed at room temperature (300 K), 77 K, 4 K, 600 mK and 80 mK. The detector volume (so-called detector carousel) also made of ultrapure copper provides a volume of 24 litres and space for up to 33 standard-sized CRESST detectors which are arranged in 12 three(two)-storied towers. The carousel is mechanically decoupled by custom-made bronze springs [23] to reduce mechanical disturbances (microphonics) and thermally coupled by copper wires. At the present design state, the cryostat is equipped with 36 readout channels allowing to operate 18 (2-channel) CRESST modules which make up a total target mass of ~ 5 kg.

2.3.3 Data Acquisition and Electronics for Detector Operation

In this chapter a brief overview of the electronics used for the readout and the operation of CRESST detectors is given. For more details see [23, 27, 64].

Front-End Electronics: The cryogenic detectors used in CRESST are equipped with transition-edge-sensors (TESs) which are operated in the transition from the superconducting to the normal-conducting state. The TESs are biased by a constant current I_0 (detector bias) of typically $\sim 10 \mu\text{A}$. In a parallel branch to the TES (see figure 2.11), two shunt resistors of $20 \text{ m}\Omega$ each are connected in series to the input coil of a **SQUID** (Superconducting Quantum Interference Device) [55]. Hence, a temperature change in the TES causes a resistance change and a magnetic flux in the input coil. The flux is measured and amplified by the SQUIDs which in the case of CRESST are dc SQUIDs from Supracon immersed into the He bath at 4 K [65, 66]. The SQUIDs are operated in the so-called flux-locked-loop mode by means of a feedback loop, realized by the so-called feedback coil [23]. This widely linearizes the output signal which is given by the current through the feedback coil.

Additionally, every CRESST detector is equipped with a heater structure evaporated onto or in the vicinity of the TES which consists of a **Au film** that maintains its ohmic resistance at

²In the present setup cold nitrogen gas of ~ 77 K evaporated from liquid nitrogen is constantly flushed through the nitrogen dewar (see figure 2.10). This has advantages in terms of microphonics.

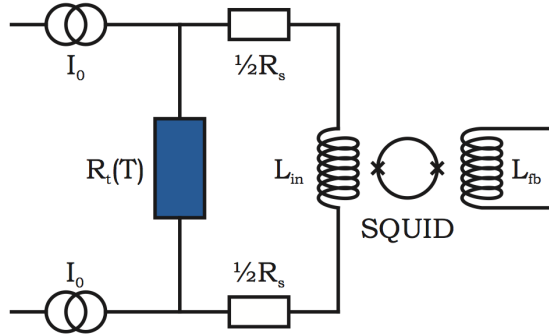


Figure 2.11: SQUID readout scheme of CRESST detectors. The TES is constantly biased by a current I_0 of typically $\sim 10 \mu\text{A}$. In the parallel branch to the TES ($R_t(T)$), two shunt resistors of $1/2R_s = 20 \text{ m}\Omega$ each are connected in series to the superconducting input coil of the SQUID. A temperature change in the detector induces a change in resistance in the TES ($R_t(T)$) and hence to a magnetic flux through the input coil L_{in} of the SQUID. The flux is measured and amplified by a SQUID. The current through the feedback coil L_{fb} gives the output signal (see text) [23].

mK temperatures. A current can be applied through the Au film which causes a temperature change of the TES and the detector.

Back-End Electronics: The operation of the SQUID and the supply of the currents for detector bias and heaters are provided by custom-made electronics at room temperature [66]. A VME-based data acquisition system is used to record the response of the detectors. A trigger unit sends signals to 16-bit transient digitizers which sample the pulses at a typical rate of 25 kHz ($40 \mu\text{s}$ time base) and a total sample length of 164 ms (for details see [23]). Additionally, VME-based digital-to-analog converters (DACs) and pulse generators are used for the stabilization and calibration of the detectors:

- The DACs allow to apply a constant current through the Au-heater structure of each detector. This is to regulate the temperature of the TES and stabilize it in the transition. Onto this so-called heater bias, electrical pulses with typical decay times of $\sim 10 \text{ ms}$ are applied by the pulse generators. For stabilization, **control pulses** are injected into the Au films. Thereby, the voltage is sufficient to completely drive the detector out of the transition. The amplitude of the response of the control pulses which is sampled by the transient recorders and evaluated in real-time by software is sensitive to the operating point (see figure 2.3). The control-pulse amplitude serves as an input parameter for a software-based PI control of the operational temperature by adjusting the heater current. Typically, control pulses every $\sim 3 \text{ s}$ are sufficient to stabilize the detectors with the required precision.
- **Test pulses** of various amplitudes are injected into the Au films every $\sim 30 \text{ s}$ in order to calibrate the detectors over a wide energy range (from $\sim 10 \text{ keV}$ up to $\sim 1 \text{ MeV}$). This is, in particular, important for low energies where radioactive calibration sources are not practical for CRESST. Furthermore, the test pulses are also used to monitor the

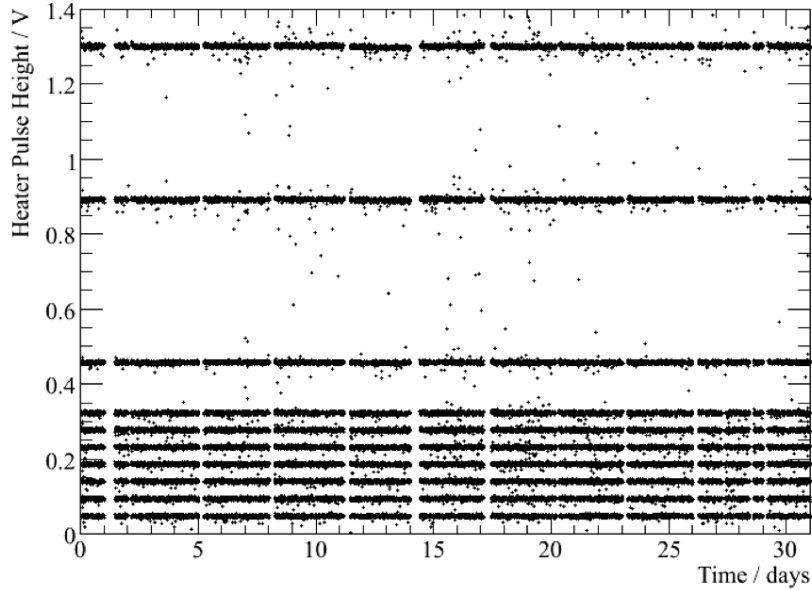


Figure 2.12: The response of heater pulses (test pulses) of various amplitudes injected into the Au film of a CRESST detector is plotted versus time. The detector can be calibrated over a wide energy range (typically from ~ 10 keV to ~ 1 MeV). The excellent long-term stability of the detector response can be seen. The time gaps indicate periods in which the detector was not active, e.g., due to liquid He refills. Picture from [23].

detector response over time as shown in figure 2.12. In case of drifts of the operating point with time, the pulse height can be corrected [27].

2.4 First Extensive Dark Matter Run (run32)

2.4.1 Results

Run32 was the first extensive Dark Matter (DM) run of CRESST with a net exposure of 730 kg-days taking data between June 2009 and April 2011 [25]. In total, 18 detector modules of ~ 300 g each were operated out of which 8 were used for the DM analysis.

In figure 2.13 the results of one CRESST detector module (Ch51) with a total exposure of 88.5 kg-days is shown. The acceptance region (highlighted in orange) for WIMP interactions covers the three nuclear-recoil bands of CaWO_4 to have a maximal sensitivity to a wide range of possible WIMP masses (see chapter 2.1). The lower threshold is defined such that 1 leakage event from the electron-recoil band is expected per detector module in the whole data set. The acceptance region is restricted to recoil energies below 40 keV as above this threshold no significant contribution of WIMP scatters are expected for CaWO_4 (see figure 1.4).

In the whole data set of ~ 730 kg-days a total of 67 events has been observed, originating from the 8 detector modules considered in the data analysis. Despite rather large background contributions (α , neutrons, ^{206}Pb recoils, e^-/γ) an excess signal with an exponential spectrum towards lower recoil energies remains. A dedicated maximum-likelihood analysis including energy and light-yield information of the 8 detector modules, the known background contri-

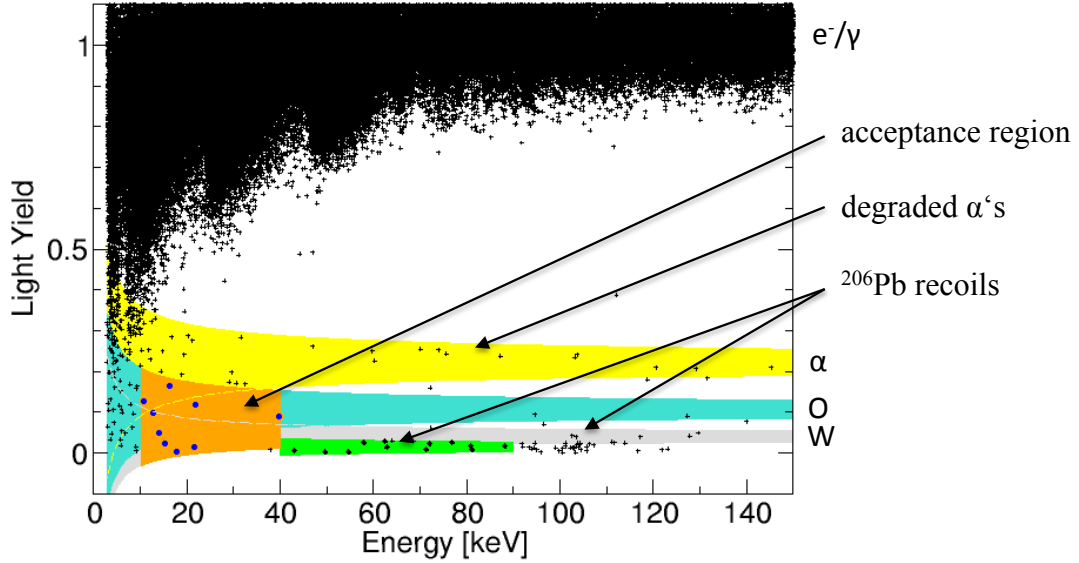


Figure 2.13: Light-yield plot of the full data acquired with one detector module (ch51, Rita/Steven) during CRESST run32. The nuclear-recoil bands of O and W (Ca in-between is not shown) and the α band are depicted. The acceptance region (orange) covers all three nuclear-recoil bands (O, Ca and W) typically between 12-40 keV (see text). The background contributions observed in run32 are indicated by arrows.

butions, and data from γ and neutron-calibration campaigns was performed. The results of this analysis which also includes the interpretation of the excess signal as WIMP interactions are listed in table 2.1. Due to the strong overlap of the nuclear recoil bands (O, Ca and W) in the acceptance region (typically from $\gtrsim 12$ to 40 keV) two maxima of the likelihood function (M1 and M2) are found with different recoil compositions. If interpreted as signals from a DM particle, M1 (M2) suggests a WIMP-mass of 25.3 GeV (11.6 GeV) at a WIMP-nucleon scattering cross section of 1.6 ± 10^{-6} pb (3.7 ± 10^{-5} pb) with a statistical significance on a 4.7σ (4.2σ) confidence level. The corresponding contours in the WIMP-parameter space are depicted in figures 1.5 and 1.6 and compared with results of other direct DM search experiments.

In conclusion, the observed signal excess cannot be explained with the known backgrounds alone. However, background contributions are rather large and additional correlated background sources could be present (discussed in chapter 2.4.2). Therefore, the main goal for the next DM run of CRESST is to significantly reduce the known background which will hopefully clarify whether the excess signal is a true hint for Dark Matter.

Details regarding the preparation of the next run are discussed in chapter 2.5.

2.4.2 Backgrounds

e^-/γ Background: The dominant background contribution is due to the intrinsic e^-/γ contamination of the CaWO_4 crystals themselves at a rate of $\sim 0.1 \text{ kg}^{-1} \text{ s}^{-1}$. External γ 's are measured at a rate of $\sim 1 \text{ kg}^{-1} \text{ h}^{-1}$.

Although e^-/γ events can be well discriminated from nuclear recoils via light quenching

		M1	M2
backgrounds	e^-/γ	8.00 ± 0.05	8.00 ± 0.05
	α	$11.5^{+2.6}_{-2.3}$	$11.2^{+2.5}_{-2.3}$
	n	$7.5^{+6.3}_{-5.5}$	$9.7^{+6.1}_{-5.1}$
	^{206}Pb	$15.0^{+5.2}_{-5.1}$	$18.7^{+4.9}_{-4.7}$
signal	counts	$29.4^{+8.6}_{-7.7}$	$24.2^{+8.1}_{-7.2}$
	m_χ [GeV]	25.3	11.6
	σ_{WN} [pb]	$1.6 \cdot 10^{-6}$	$3.7 \cdot 10^{-5}$
	C.L.	4.7σ	4.2σ
composition	O [%]	~ 7	~ 52
	Ca [%]	~ 25	~ 48
	W [%]	~ 69	-

Table 2.1: Final results of the analysis of CRESST run32 with a net exposure of ~ 730 kg-days [25]. The maximum-likelihood analysis includes all known backgrounds, however, an excess signal is observed on a statistically significant level ($> 4\sigma$). If interpreted as a Dark Matter signal the corresponding parameters, i.e., the WIMP mass and the WIMP-nucleon cross section can be calculated (best-fit points are shown). Due to the strong overlap of the three nuclear-recoil bands (O, Ca and W) and the finite resolution of the light detector two likelihood maxima (M1 and M2) with different recoil compositions arise. The confidence level (C.L.) of the statistical significance is also listed.

with a rejection power of up to $\sim 10^{-5}$, the lower boundary of the acceptance region is fixed by the expected leakage from the e^-/γ band and can therefore vary from crystal to crystal. Hence the radiopurity of the CaWO_4 crystals is crucial for the achievable threshold of CRESST detectors. Due to the expected exponential WIMP spectrum (see equation 1.20) the sensitivity would be increased significantly if the intrinsic contamination was reduced.

Neutron Background: Two classes of neutrons are considered in the likelihood analysis:

- Free neutrons that are emitted by spontaneous fission of heavy elements or (α, n) reactions on light nuclei from material inside the PE shielding, basically the Pb and Cu shields. According to Monte Carlo simulations only a negligible background of $10^{-3} \text{ kg}^{-1} \text{ day}^{-1}$ [67] is expected in the acceptance region. This source of background is considered in the analysis [25]. Therefore, also the information from various neutron-calibration campaigns is included.
- Fast neutrons ($\gtrsim 10 \text{ MeV}$) can be induced by muons in the experimental setup or in the surrounding material (e.g. rock). Since the active muon veto is not 100% efficient a small fraction of muons might be missed and could induce neutrons which are not sufficiently shielded by the Cu and Pb shieldings. High-energetic neutrons generated outside the PE shielding may penetrate the PE shielding and reach the detectors. Both classes can be studied by analysing the detector response of the neutrons induced by muons that are tagged by the muon veto [25].

α Background: As shown in figure 2.13 degraded α events occur at energies < 150 keV in the α band. Since typical α decays induce particles with discrete energies in the MeV range (e.g. ^{210}Po at ~ 5.3 MeV) the observed event must originate from decays at some depth in the material ($\sim 1 \mu\text{m}$). A rather flat recoil-energy spectrum is observed for the degraded α 's up to MeV energies with a typical rate of $\mathcal{O}(10^{-3} \text{ keV}^{-1} \text{ kg}^{-1} \text{ day}^{-1})$. This pinpoints towards a homogeneously distributed bulk contamination in a surrounding material. The reflective and scintillating polymeric foil which covers most of the surrounding area of the CaWO_4 crystal can be excluded as background source. The energy loss of $\sim \text{MeV}$ of the α particle in the foil would induce additional scintillation light, which would shift the events far above the acceptance region (see chapter 2.2.3). A non-negligible contamination of ^{210}Pb ($6.9 \pm 0.9 \text{ Bq/kg}$) was indeed found in the non-scintillating bronze clamps holding the crystals. The corresponding α decays of ^{210}Po (see decay scheme of the ^{238}U chain in figure 3.38 in chapter 3.6) are supposed to be responsible for the degraded α 's observed. The origin of the contamination ($\sim 20 \text{ mBq/kg}$) is most probably due to a contamination during the production cycle of the bronze material. Possibly, also graphite which was found in cracks of the surface of the clamps plays an essential role.

As will be discussed in the following, an additional ^{210}Po contamination in the Ag-surface layer must be present.

^{206}Pb Background: During CRESST run32 a population of low light-yield events ($\lesssim LY_W$, see figure 2.13) at an energy of about 103 keV with a tail towards lower energies was observed. These recoil events are identified as ^{206}Pb recoils from ^{210}Po decays (see equation 2.3) which, however, cannot be explained by the bulk contamination in the clamp material alone, which - as mentioned above - is the source for degraded α 's. Since heavy ions like ^{206}Pb only have a range of the order of 10 nm in typical solid materials there must be an additional ^{210}Po contamination present in the Ag-surface layer of the clamps. Figure 3.17 in chapter 3.4 shows a histogram of the total ^{206}Pb -recoil background observed during CRESST run32 in all 8 detector modules. In total, 246 events were recorded between 40 and 107 keV in the Pb band. This corresponds to a mean rate of $\sim 0.3 \text{ kg}^{-1} \text{ day}^{-1}$. The leakage into the acceptance region was quantified by an exponential towards lower energies as shown in figure 3.17 [25]. The origin of the contamination is not definitely clarified. Two possible scenarios have been discussed:

- One possibility is that a ^{210}Po contamination was introduced during the coating of the bronze clamps with Ag (electrochemical deposition). In this case or in the case of any other direct ^{210}Po contamination, the rate of ^{206}Pb recoils is supposed to drop with time according to the half-life $T_{1/2} = 138.4$ days of ^{210}Po .
- If radon implantation from air during assembly and mounting of the detectors and the successive decays to ^{210}Pb would be the source of the ^{206}Pb recoils observed, their rate should rise with time according to the half-life of 138.4 days since ^{210}Po has to be built up first (see chapter 3.4 for more details).

Indeed, hints for a time-dependence of the total ^{206}Pb -rate in all 8 detector modules operated in CRESST run32 can be found. The rate $R(t)$ of ^{206}Pb -recoil events around the peak of full energy deposition (~ 103 keV) using the interval from 96 keV to 107 keV and ^{206}Pb -recoils events in the tail towards lower energies using the interval from 40 keV to 90 keV

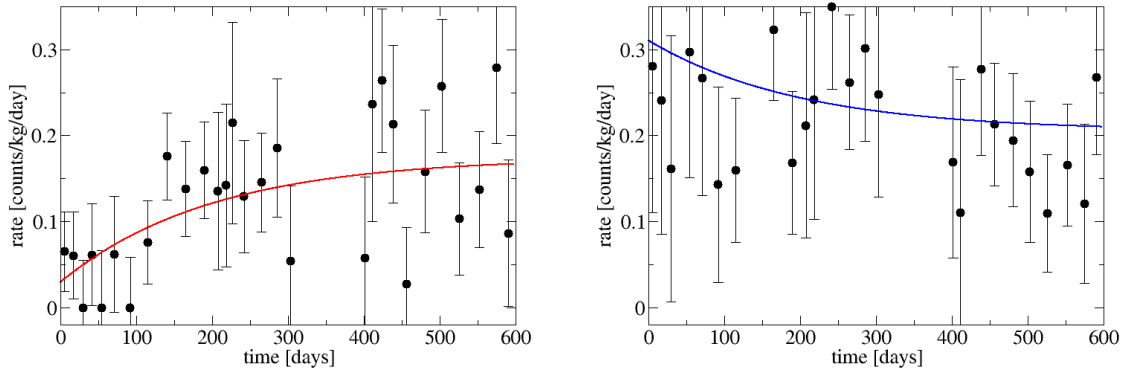


Figure 2.14: Left: Rate of ^{206}Pb events in the control region (40-90 keV) versus measuring time. The red line shows the best fit to the data under the assumption of an exponential behaviour with the half-life of ^{210}Po (138.4 days). The significant increase in rate over time clearly indicates that radon implantation from air during assembly and mounting of the detectors could contribute to the surface contamination. Right: Analog plot for the Pb-peak region (96-107 keV). In this case no significant time dependence of the ^{206}Pb -rate can be identified. The best fit shows a slight decrease which would point towards a dominant contamination of ^{210}Po in the Pb-peak. A detailed statistical analysis can be found in [68].

(control region³) are plotted against the measuring time in figure 2.14. Both data sets are fitted under the assumption of an exponential behaviour reflecting the life-time of ^{210}Po ($T_{1/2} = 138.4$ days):

$$R(t) = a \cdot e^{-b \cdot t / \tau} + c \quad (2.9)$$

with the fit parameters a , b and c . For the tail region, the significant increase in rate over time clearly indicates that radon implantation from air during assembly and mounting of the detectors could contribute to the surface contamination. For the peak region, no significant time dependence of the ^{206}Pb -rate can be identified. However, the best fit shows a slight decrease which would point towards a dominant contamination of ^{210}Po in the Pb-peak. Here, only the tendency of the time-dependent ^{206}Pb rates are discussed while a detailed statistical analysis can be found in [68].

In conclusion, this indicates that part of the ^{206}Pb recoils observed could be due to radon implantation from air which is further supported by a dedicated radon-exposure measurement performed within this work (see chapter 3.4). Hence for the next DM run of CRESST, extensive efforts were made to reduce the exposure of the detector modules (in particular the bronze clamps) to radon contaminated air (see chapter 2.5).

Unkonwn Backgrounds: Since the background level is rather large there might be somehow an additional background correlated to those listed in table 2.1. A possible sputtering of light nuclei (e.g. H, C) [69] induced by ^{210}Po decays on non-scintillating surfaces surrounding

³The control region of ^{206}Pb is defined from 40 to 90 keV in the Pb band. It is used to quantify the leakage of this background into the acceptance region. This is performed by an exponential with a decrease towards lower energies [25].

the crystals could explain (parts) of the excess events. However, the assumptions made in this study do not fully match the properties of the CRESST experiment.

Possibly also the very rare case of α decays on the surface of the foil where the alpha hits the non-scintillating bronze clamps and the ^{206}Pb nucleus sputters out light elements from the foil could contribute. The sputtered ions that reach the CaWO_4 crystal could induce low-energy signals $\mathcal{O}(10\text{ keV})$ with a light yield similar to that of the excess signals. However, this background should be correlated to the rate of ^{206}Pb recoils observed. To match the observed recoil-energy spectrum of the excess events a significant rise towards lower energies is required which is not observed for the ^{206}Pb events (see figure 2.7).

Ultimately, only a new experimental run with significantly improved background level will clarify the situation.

2.5 Preparations for the Upcoming Dark Matter Run (run33)

The preparations for the upcoming DM run of CRESST (run33) were recently finished (June 2013) and the cryostat is approaching its operational temperature of $\sim 10\text{ mK}$ at the moment of writing. During the last two years enormous efforts have been made to improve the detector modules and the experimental setup significantly. This was also a main issue of this thesis. In chapter 3 studies concerning the characterization of CRESST detectors and the development of an alternative detector design are presented.

Considering the results of CRESST run32 (see chapter 2.4) the three main goals for the upcoming DM run of CRESST were:

- Reduction of the background level - in particular - the contamination of the clamps.
- Increase of the target mass.
- Clarification of the excess signal observed in run32.

The majority of the detector modules (12 out of 18 available detector spots) were assembled in the standard CRESST detector design based on (non-scintillating) bronze clamps. Extensive studies showed [68] that it is not possible to cover these bronze clamps with scintillating material (e.g. plastic scintillator, polymeric foil). Any attempts failed as the phonon properties were not sufficient in most cases due to the occurrence of stress-relaxation events in the phonon detector (“light-only events”, described in chapter 3.5). Nevertheless, the suitability of the bare bronze clamps in terms of phonon properties and detector operation is well-known and has been tested extensively. With the following improvements we are convinced that the **standard CRESST detector design** is appropriate to fulfil the design requirements for run33.

- In the bronze material (CuSn_6) a contamination of ^{210}Pb was found at the level of $6.9 \pm 0.9\text{ Bq/kg}$ which caused a background of degraded α events. For run33 a new production cycle for CuSn_6 was set up at the Institut für Metallkunde at the RWTH Aachen [70]. Ultra-pure raw materials were used (activity $< 20\text{ mBq/kg}$) and every single production step was carefully controlled and monitored. Therefore, the bulk contamination of the bronze clamps should be reduced by $\lesssim 2$ orders of magnitude compared to run32.

- One possible source of the additional surface contamination of ^{210}Po is the electrochemical deposition process of the Ag layer onto the bare clamps. Therefore, for run33 a layer of ultra-pure Al was evaporated onto the clamps which provides a similarly good light reflection properties.
- There are strong indications (see chapter 2.4 and 3.4) that radon implantation from air could play an important role concerning surface background due to ^{210}Po . Therefore, the exposition to radon contaminated air during assembly should be kept as small as possible for the standard design with non-scintillating bronze clamps. At the experimental site of CRESST the mean radon contamination is $50\text{-}100\text{ Bg m}^{-3}$, while above ground $10\text{-}50\text{ Bg m}^{-3}$ are measured. Both strongly depend on environmental conditions. Fortunately, the CUORE experiment (located next to the CRESST experiment) [71] set up a dedicated facility which provides radon-filtered air and which manages to reduce the contamination by ~ 2 orders of magnitude. At the CRESST experimental site an air-tight container housing a clean-room facility to assemble the detector modules was installed and constantly flushed by this de-radonized air (see figure 2.15). Additionally, a tent was installed around the volume housing the detectors in the cryostat which is also flushed by the radon-pure air during mounting of the detectors.

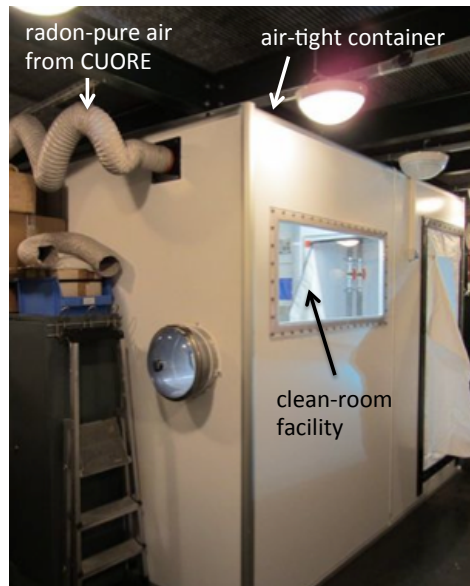


Figure 2.15: New clean-room facility at the experimental site of CRESST, which is constantly flushed by radon-filtered air from a dedicated air-purification facility of the CUORE experiment [71].

During the assembly and mounting of the detectors the α rate due to decays of ^{222}Rn was constantly $< 3\text{ Bq m}^{-3}$ (lower limit of radon monitor). The rate of ^{206}Pb recoils due to implantation of radon from air should hence be negligible for typical measuring times of ~ 2 years (see detailed calculation in chapter 3.4).

- To avoid possible rare sputtering events on the surface of the foil (see chapter 2.4.2) the polymeric foil was coated with parylene [72] which can be evaporated onto various

surfaces with a commercially available device. Parylene for which clean raw materials are available is transparent and well-scintillating (by a factor of ~ 2 more than the polymeric foil) and hence matches the requirements of reflectivity and scintillation. The exposition of the commercially available foil to radon cannot be controlled. If the foil is covered with clean parylene the “radon history” of the foil is reset and hence radon-induced background should become negligible. Half of the standard CRESST modules installed for run33 are equipped with parylene-coated foils (see table 2.2).

Backgrounds due to α decays on surfaces surrounding the CaWO_4 crystal can be completely rejected if all materials that have a direct line-of-sight to the crystal are made of scintillating material. While this is not possible with the standard design, three different approaches for an alternative detector design which provides a **fully-scintillating detector housing** have been developed and successfully tested:

- Two prototype modules of the so-called “K14-type” are installed in the setup for run33. A cylindrical CaWO_4 crystal of standard size (~ 40 mm in diameter and ~ 40 mm in height) is glued onto a CaWO_4 carrier of the same diameter and 7 mm in height. Both crystals are made out of the same raw ingot and have the right crystal orientation with respect to each other in order to avoid mechanical stress due to different thermal contraction. The lateral and the upper surface of the crystal are roughened while the base surface (adherend) and all surfaces of the carrier are polished (see figure 2.16). A standard CRESST TES is evaporated onto the carrier (see chapter 2.2.1). Both CaWO_4 crystals were grown in the crystal laboratory of the TUM (see also chapter 3) [73, 52]. The detector is held by standard bronze clamps which are covered with scintillating parylene only at the carrier (see figure 2.16). Possible relaxation events from these clamps into the carrier can be discriminated from events in the absorber crystal by different pulse shape.
- Another promising design is based on a silicon beaker as light detector and a “K14 type” crystal (see figure 2.16). The crystal is held by standard bronze clamps while the absorber crystal is completely immersed in the beaker [74]. This not only increases the light collection ($\sim 4\pi$ coverage) but also constitutes an efficient active veto against surface α decays. Due to 180° emission, in any case one of the particles hits the light detector which produces a large signal. Two such modules (called “beaker type”) are mounted in the setup of run33.
- A novel, fully scintillating detector design based on CaWO_4 sticks holding the absorber crystal was projected and developed within this thesis. Two such modules (also called “stick type”) were successfully tested and installed in the CRESST setup for run33. In this design TUM-grown block-shaped CaWO_4 crystals are held by CaWO_4 sticks and clamped from outside the detector housing by standard bare bronze clamps (see figure 2.16). In this way, the mechanical properties of the well-developed standard design are maintained while only scintillating materials are present inside the detector housing. Details about the design, measurements and results are given in chapter 3.5.

The main properties of the 18 detector modules installed in the setup of CRESST for run33 are listed in table 2.2. Figure 2.17 shows the mounted detector modules with a total mass of 5.12 kg mounted in the detector volume of the CRESST cryostat. The mass is roughly

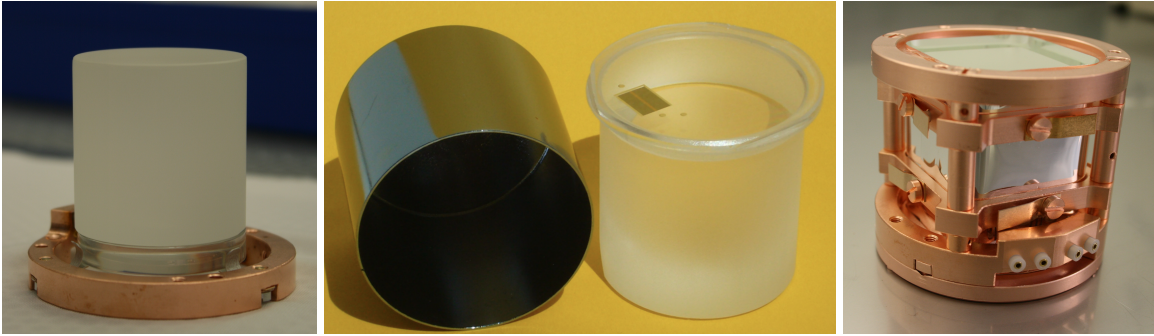


Figure 2.16: The three alternative detector designs which provide a fully-scintillating detector housing. Left: Cylindrical CaWO_4 crystal (roughened) glued onto a cylindrical, 7 mm thick CaWO_4 carrier (polished) onto which the TES is evaporated. The crystal is held only at the carrier by bronze clamps which are covered with scintillating parylene. Possible relaxation events from these clamps into the carrier can be discriminated from events in the absorber crystal by pulse shape (“K14 type”) Middle: Silicon beaker operated as light detector and a CaWO_4 crystal similar to the “K14-type” design. The crystal is immersed in the beaker which provides a full veto against surface decay events (“beaker type”). Right: Block-shaped CaWO_4 crystal held by CaWO_4 sticks which are clamped by bare bronze clamps from outside. Hence all materials inside the housing are scintillating (“stick type”). This design was developed in this thesis. For more details, see chapter 3.5.



Figure 2.17: Detector volume (“carousel”) of the CRESST experiment. The picture shows the fully mounted setup for CRESST run33. In total, 18 detector modules are mounted. Two of those are prototype detectors with a fully-scintillating detector design developed in this thesis (see chapter 3.5).



Figure 2.18: Inner PE shielding of ~ 3 cm thickness mounted in the inner vacuum vessel of the CRESST cryostat. The gaps in the PE allow to perform neutron calibrations with sources from outside the cryogenic part. The gaps are closed by an additional layer of PE at the outer part of the cryostat, however, still inside the Cu shielding. The outer PE parts can be removed for calibration during the experimental run.

doubled compared to run32.

In order to reduce a possible contribution of neutrons to the background observed in run32 an additional (inner) PE shielding was installed in the inner vacuum vessel (see chapter 2.3.2). The PE-layer of ~ 3 cm around the detector volume is particularly important for neutrons induced by muons (and missed by the active muon veto) in the Pb and Cu shieldings which are otherwise not sufficiently vetoed. A picture of the inner PE shielding is shown in figure 2.18. Gaps in the PE which can be closed from outside allow to perform neutron-calibration campaigns with sources.

In conclusion, with the improvements described above and the 18 detector modules mounted a net exposure of ~ 2 ton-days can be reached within a measuring time of two years. In case of the existence of low-mass WIMPs the upcoming run33 would undoubtedly either confirm the DM hypothesis with high statistical confidence or otherwise strengthen the limit⁴ for spin-independent WIMP-nucleon cross-section of $\sim 10^{-45}$ cm² at a WIMP mass of ~ 65 GeV (see figure 2.19).

⁴The sensitivity was calculated [75] under the assumption of zero backgrounds from degraded α 's, ^{206}Pb recoils and neutrons, and leakage from the e^-/γ band comparable to run32 which leads to similar lower boundaries of the acceptance regions. A net exposure of 2 ton-days was assumed.

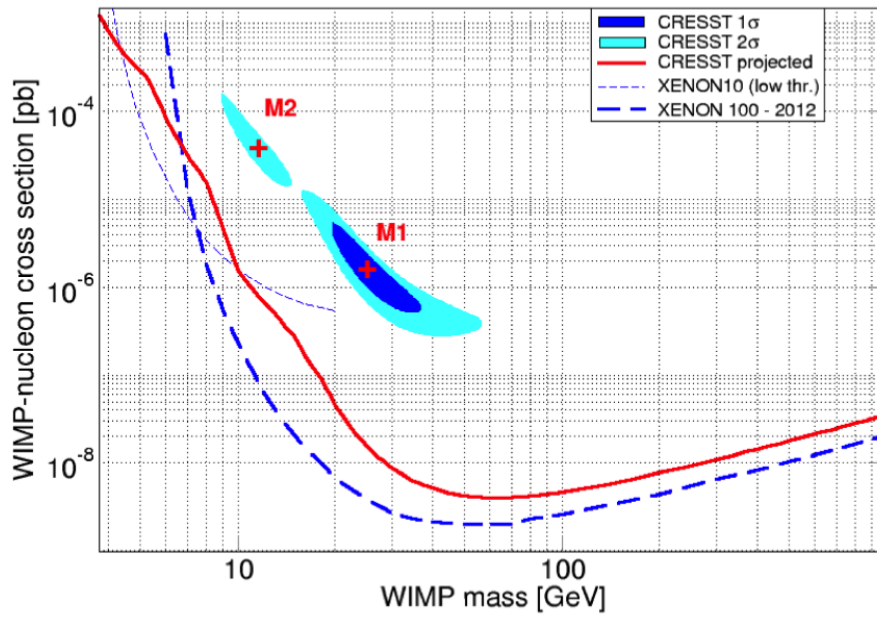


Figure 2.19: Exclusion plot with the results of CRESST run32 interpreted as WIMP signal (M1 and M2, see chapter 2.4) and the current best limit of XENON100 (blue dashed line) [24] and the low-threshold analysis of XENON10 (blue dotted line) [32] (see chapter 1.4). Under the assumption of significant reduction of the backgrounds (see text) for a measuring time of ~ 2 years and a target mass of 5.12 kg the projected sensitivity (red) for run33 can be calculated for the case that the signal excess observed in run32 was due to background [75].

crystal name	light output	mass [g]	T_c [mK]	light detector	foil	holder design
Rita(C)	131.0%	310	20.0	Steven	N	standard
Frederika(C)	146.0%	266	16.7	Gabriel	N	standard
VK35-Lise(C)	147.0%	306	19.5	Enrico	P	standard
Zora(C)	147.0%	302	17.0	Yoichiro	N	standard
Vk38-Anja(C)	137.0%	308	18.5	Claudius	P	standard
Daisy	97.0%	307	18.0	Donanld	N	standard
VK43	143.0%	304	18.0	Leon	P	standard
VK31	125.0%	307	18.0	Kurt	P	standard
VK32	121.0%	308	19.0	Anders	P	standard
VK33	117.0%	310	20.0	Franz	N	standard
Verena	108.0%	306	18.0	Q	N	standard
Wibke	100.0%	308	20.0	X	P	standard
TUM-29(C)	100.0%	299	22.5	Thomas	N	“K14-type”
TUM-38(C)	94.5.0%	299	15.5	Petrus	P	“K14-type”
VK27(C)	93.05%	197	18.5	Diogenes	N	“beaker-type”
VK28(C)	130.00%	194	20.5	Zam	N	“beaker-type”
TUM-40(C)	-	245	20.2	Michael	N	“stick-type”
TUM-45(C)	-	243	17.3	Oliver	N	“stick-type”

Table 2.2: Overview of the 18 detector modules installed for CRESST run33 with a total target mass of 5.12 kg. C indicates composite detectors. Foil type: N = normal, P = parylene coated. The light output is measured compared to the reference crystal Boris with a standardized technique at room temperature (see chapter 3). The light output of TUM-40 and TUM-45 is not directly comparable to the cylindrically-shaped crystals (see chapter 3).

Chapter 3

Detector Prototypes for the CRESST Experiment

3.1 The CRESST Test Cryostat at Gran Sasso

The measurements presented in this chapter were performed in the CRESST test cryostat which is located underground in the LNGS (Laboratori Nazionali del Gran Sasso) in central Italy, in a service tunnel close to the CRESST experiment (see figure 2.9). This facility which was set up between 2009 and 2011 provides the unique possibility to operate CRESST-size detector modules independent of the CRESST setup itself.

A MINIKELVIN 400-TOF $^3\text{He}/^4\text{He}$ -dilution refrigerator from Leiden Cryogenics B.V. [76] which reaches a base temperature of $\sim 7\text{ mK}$ is equipped with two SQUID-readout systems (Applied Physics 581H [77]). In the current setup [68], with an experimental volume of 190 mm in height and 90 mm in diameter one standard-size CRESST detector module can be operated under realistic measurement conditions similar to that of CRESST. The cryostat is surrounded by a 10 cm thick layer of ultra-pure Pb (total mass 4 tons) to shield against ambient γ -radiation and installed in a modified steel container as shown in figure 3.1. The electronics and gas-handling system are housed in the container while the infrastructure (e.g. pumps) for the cryogenic system are placed outside to avoid mechanical disturbances (microphonics). A VME-based data acquisition similar to the one used in the CRESST experiment (see chapter 2.3.3) is installed.

While cosmic-muon induced gamma background is negligible ($\sim 1\text{ muon/m}^2/\text{h}$) at the underground site and external radiation is efficiently shielded by the Pb layer, radioactive contaminations in the cryostat (e.g., thorium contamination in fiber-glass reinforced plastic parts) constitute the dominant γ -background source. The mean γ -rate below 200 keV is $\mathcal{O}(1000\text{ events/keV/kg/day})$ which is at least one order of magnitude higher than typical intrinsic contaminations in CaWO_4 . The neutron-background rate due to the absence of a PE shielding is $\mathcal{O}(10\text{ events/kg/day})$ above the typical discrimination threshold between electron and nuclear recoils (see figure 3.31).

3.2 Data Analysis of Cryodetectors

In this chapter, an overview of the basic methods for the analysis of cryogenic detectors as used in the framework of the CRESST experiment is presented. A more detailed description



Figure 3.1: The test cryostat installed in the underground laboratory of the LNGS in Italy. The facility is dedicated and optimized for the operation of one CRESST-detector module under realistic operational conditions. Left: The dilution refrigerator inside the Pb shielding. Right: Outside view of the container which houses the test cryostat.

of the data-analysis techniques used in the CRESST experiment are given in [27, 78, 23], herein, important aspects concerning the measurements performed within this thesis in the test cryostat at the LNGS are described in more detail.

3.2.1 Standard Event Fit and Calibration

In CRESST(-like) detector modules, the response of the phonon (CaWO_4 crystal) and the light detector (Silicon-on-Sapphire) is recorded simultaneously. To derive the energy information of both channels a so-called standard-event fit is applied by which a template pulse is fitted onto each event recorded. Simply using the pulse height of the individual events would overestimate the deposited energy as the maximum of the pulse would primarily be found where positive noise fluctuations occur. This would introduce a non-linearity to the energy spectrum as the pulse shape changes for different energies. Therefore, the template is built by summing up pulses (a few hundred), typically, from γ -events of sufficiently small energies where the response of the cryogenic detector is still linear. This is usually the case for phonon and scintillation events induced by 122 keV γ 's from a ^{57}Co source. Compared to using a single pulse as template, the summing results in a vanishing noise contribution to the standard event (by averaging). The following parameters are determined by the fit:

- The **baseline level** is adapted and - in case of pile-up - a falling exponential with the thermal decay time of the pulses is used to compensate the decaying baselines.
- The parameter corresponding to the deposited **energy** is derived by scaling the template to the individual pulse height.

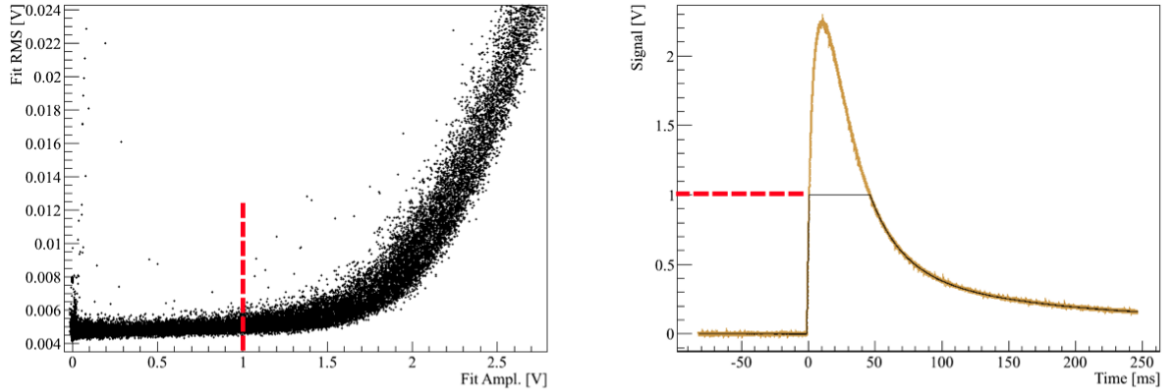


Figure 3.2: Illustration of the saturation effect of the pulse height for typical CRESST detectors and the need for a truncated standard-event fit. Left: The root-mean-square (rms) of every individual event versus the fitted amplitude. Above a certain amplitude (here: above 1V, typically corresponding to 100-200 keV) the rms value increases due to a changing pulse shape originating from non-linearities in the detector response. Right: A typical high-energy pulse (yellow) for which a truncated standard-event fit is applied (black line). The red dashed line indicates the truncation limit. Picture from [27].

- The template is shifted in time to find the correct **pulse onset**.

The root-mean-square (rms) which accounts for the deviation of every single pulse from the fitted template quantifies the quality of every individual fit [79]. In order to exclude parts of non-linear detector response at higher energy depositions a so-called **truncated** standard-event fit is applied. Only the linear parts of the transition-edge-sensor (see chapter 2.3.3) in which the pulse shape of the pulses is constant are used for fitting. For typical CRESST(-like) detectors the pulses start to saturate above 100-200 keV and therefore the truncation limit has to be chosen accordingly as illustrated in figure 3.2). In the left figure the rms of the individual pulses is plotted against the recoil energy. Above a certain amplitude (here: above 1V, typically corresponding to 100-200 keV) the rms value increases due to a changing pulse shape originating from non-linearities in the detector response. Therefore, a truncation limit is defined and only the linear parts of the pulse below that are taken into account (indicated by dashed red lines). Typical high-energetic events are shown in figures 3.2 (right) and 3.3. The observed correlation between the onset of the phonon pulse and the onset of the corresponding, simultaneously recorded scintillation-light pulse is crucial for the correct determination of the light amplitude. In particular for small light signals (e.g., for recoils of heavy nuclei) the light signal are below or only slightly above the baseline-noise level which makes it extremely difficult to directly derive the onset of the light pulses. A simultaneously fitted - so-called **correlated** standard-event fit (see figure 3.3) - of both, phonon and light pulses allows to determine the onset using the phonon pulse (which usually has a much higher signal-to-noise ratio). This fixes the position of the light pulse in time. Thereby, the resolution of the light channel is significantly increased. Since in this way there is no trigger threshold for the light detector the fit can also yield negative pulse heights if the amplitude of the light pulses is below the noise level.

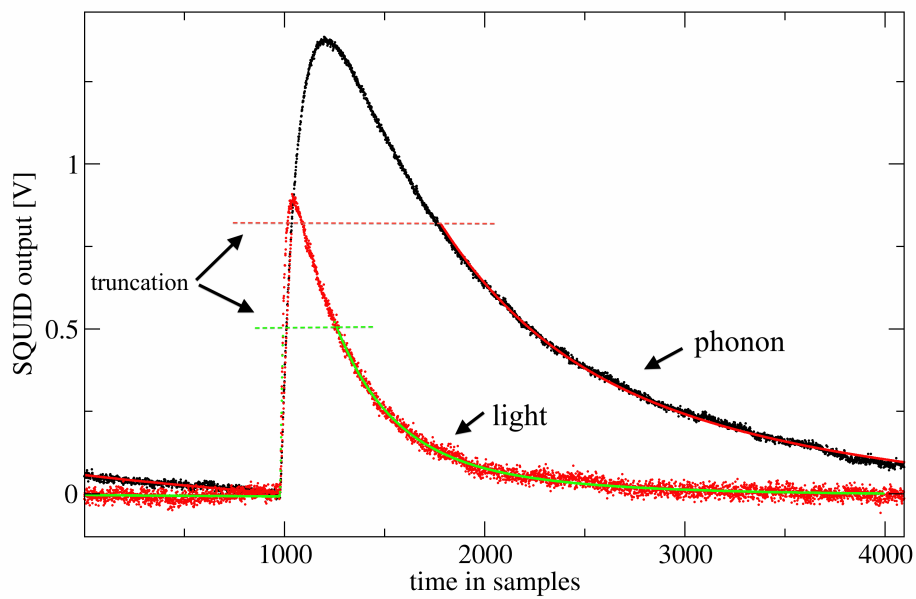


Figure 3.3: Phonon and light pulse from an electron recoil at an energy of ~ 122 keV acquired during run328 in the test cryostat at the LNGS. One sample corresponds to $40 \mu\text{s}$. The result of the correlated standard-event fit is also shown for both channels (phonon: red, light: green). Above the truncation limits (dashed lines), the pulses start to saturate. Therefore, only the linear parts of the pulses are used for the energy determination. The standard-event fit also accounts for decaying baselines originating from a previous pulse (pile-up) which can be seen in the first 1000 samples of the phonon pulse.

Calibration: Similar to the CRESST setup (see chapter 2.3.3), during the measurements in the test cryostat at the LNGS heater pulses (also called test pulses) are applied to both cryogenic detectors (light and phonon). Typically, every few seconds around 10 different voltages are injected via the heaters (gold strips evaporated onto the detectors) to obtain test pulses corresponding to the energies which are relevant for the individual measurement. Same as for particle-induced events these artificial pulses are sampled and fitted by a truncated standard-event fit. As the energy deposited by a test pulse is directly proportional to the square root of the applied voltage the fitted test pulse height can be used to linearise the detector response. Non-linearities remaining after the truncated standard-event fit can be compensated by a polynomial fit (typically of 2nd order) of the pulse height versus the injected voltage which is performed for different time periods during the measurement. Possible changes in the detector response with time are then accounted for by a spline fit¹ to the different calibrated test-pulse heights over the entire measuring time (drift correction), for more details see, e.g., [27].

The absolute energy scale is then fixed by a single γ calibration line which in most measurements performed within the CRESST collaboration is the 122 keV line of a ^{57}Co calibration source. In case of the light detector, by convention, the amount of scintillation light from electron recoil of 122 keV in the CaWO_4 crystal detected in the light channel is defined as 122 keV_{ee} (**electron-equivalent energy**). Therefore, the light yield (see chapter 2.2.2) of electron recoils of 122 keV is 1 per definition.

3.2.2 Phonon-Anti-Quenching

Usually the calibration of the phonon channel is performed with the help of γ -lines, however, it is commonly known that the energy scale of highly ionizing particles such as α -particles and ions is different [80]. As can be seen in figure 3.4 which shows a scatter plot acquired during run326 in the test cryostat, the energy of the intrinsic α lines of ^{147}Sm ($E_{\text{lit}} = 2233$ keV) and ^{180}W ($E_{\text{lit}} = 2516$ keV) observed at a reduced light yield (LY) of $LY \sim 0.22$ show up at higher phonon energies in comparison to the e^-/γ -band calibrated by the ^{208}Tl line at 2615 keV. This effect is commonly referred to as “phonon-anti-quenching” and can be expressed by

$$E_{\text{corr}} = (1 - a(1 - LY)) \cdot E_{\text{obs}} \quad (3.1)$$

where E_{obs} is the observed recoil energy, E_{corr} the corrected energy for the light yield LY and a describes the reduction of the visible phonon energy of γ -events compared to events at $LY = 0$. For a well calibrated spectrum (by γ sources), the constant a can be derived by

$$a = \frac{1}{1 - LY} \cdot \frac{1}{n} \sum_{i=1}^n 1 - \frac{E_{\text{lit},i}}{E_{\text{obs},i}} \quad (3.2)$$

where n indicates the number of available α -lines (here $n = 2$) with the corresponding energy from literature E_{lit} . The measurement (run326) shown in figure 3.4 yields $a = (8.4 \pm 0.5)\%$. There are several possible explanations for this effect:

- Due to light quenching of highly ionizing particles such as α 's compared to electron-recoil events a smaller part of the energy is converted into light. Assuming that the missing energy due to light production is the only reason for phonon-anti-quenching,

¹The function is interpolated by piecewise polynomials, so-called splines.

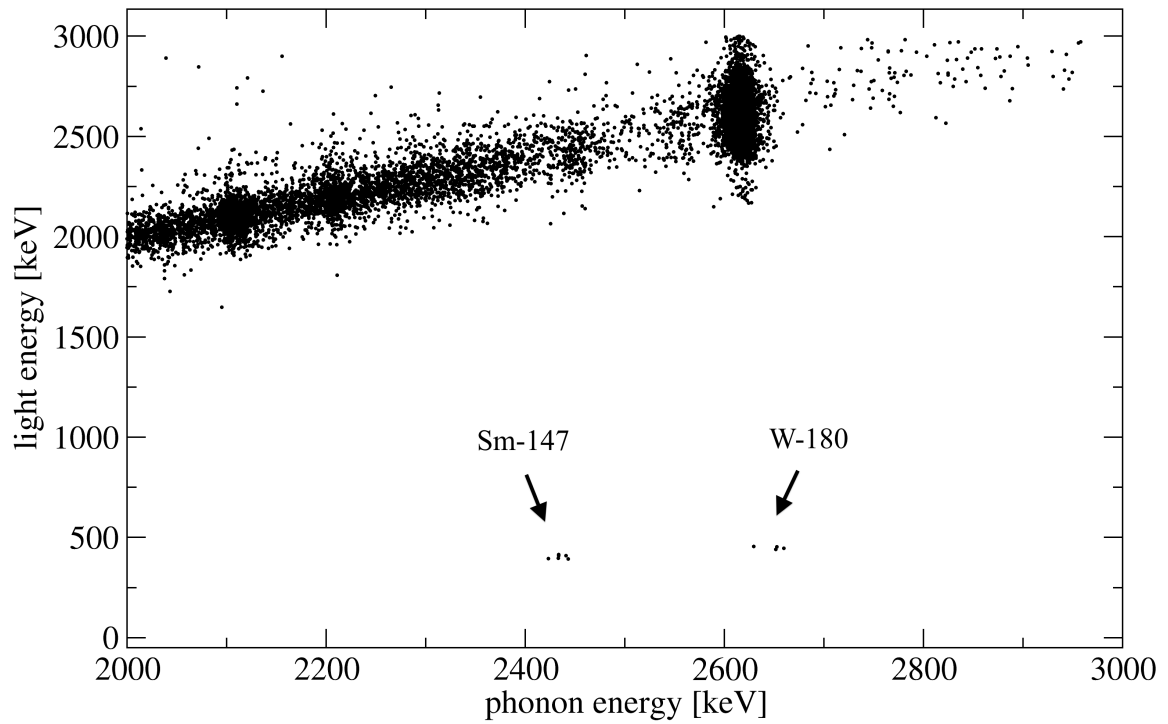


Figure 3.4: Scatter plot of data acquired in run326 in the test cryostat at Gran Sasso. The electron-recoil band is calibrated - in this case - by the dominant ^{208}Tl γ -line at 2615 keV. The intrinsic α -lines of ^{147}Sm ($E_{\text{lit}} = 2233$ keV) and ^{180}W ($E_{\text{lit}} = 2516$ keV) show up at higher recoil energies due to phonon-anti-quenching.

this measurement would suggest that $\sim 8.4\%$ of the total energy deposition in the CaWO_4 crystal is converted into scintillation light. While this is in agreement with a different approach to measure this effect [81] which gives $a = (9 \pm 5)\%$, there are studies dedicated to exclusively determine the fraction of produced light which suggest lower values of 3.9% [81] and $\sim 6\%$ [54].

- As the pulse shape of the phonon pulses of α and γ events slightly differs, there might be an influence on the determination of the pulse height which can lead to a wrong phonon-energy calibration of α interactions.

The measurements discussed above suggest that light quenching might not be the only reason for “phonon-anti-quenching”. Calibration effects which might even vary from crystal to crystal play a significant role. Fortunately, the effect can be quantified in most of the measurements with CRESST crystals by intrinsic α lines or, e.g., like done in the analysis of CRESST run32 additionally by the ^{206}Pb -recoil peak at 103 keV [25] in order to derive a individual calibration for different kinds of interacting particles in the CaWO_4 crystals.

3.2.3 Cuts and Live-Time Determination

For the analysis of cryogenic detectors, both, invalid pulses which are not caused by particle interactions such as, e.g., electronic noise and invalid pulses which are indeed caused by particles which can, however, not be sufficiently analysed have to be removed from the data. Therefore, these classes of invalid events have to be identified with dedicated selection algorithms, so-called “cuts”, which are well-established in CRESST for the analysis of cryogenic detectors [27, 78, 23]. These cuts and their efficiencies are crucial for the calculation of the live-time that corresponds to the periods during a measurement in which the detector is sensitive to particle interactions. Within this thesis, the live-time is in particular important for the analysis of the α -activity of CaWO_4 crystals (see chapter 3.6). In the following a brief overview of the most important cuts and their influence on the live-time is given. For further details see, e.g., [78]. At first, the data acquisition system used in CRESST and at the test cryostat itself introduce time periods in which the detectors are not sensitive to signal events (so-called dead time). To guarantee a sufficiently accurate energy determination the trigger is blocked for a certain period after each particle event. Furthermore during the injection of test and control pulses increases the dead time. The remaining time which is automatically calculated by the data-acquisition system is called t_{live} throughout this chapter.

The following cuts are applied during the data analysis process:

- **Removal of entire time periods:** Periods in which the detector operation is disturbed, e.g., by electronic noise or by mechanical interferences are completely removed from the data set. For the detectors used here, this is achieved by control pulses (see chapter 2.3.3) which stabilize the detectors and monitor their working points. Periods in which the control pulse height deviates significantly from the mean value are discarded. The fraction of the time t_{live} which is removed by this so-called stability cut [78] is described by $\epsilon_{\text{stability}}$.
- **Cuts on invalid pulses:** A variety of cuts especially developed and tuned to identify invalid event classes on a event-by-event basis are applied to the data. Each of these events reduce the total measurement only for the corresponding record length. The sum of these - denoted as t_{invalid} in this thesis - has to be subtracted from t_{live} .

- **Cuts for “quality control” of pulses:** Algorithms which discard part of possible signal events because the quality of the pulse is not sufficient or is only partially recorded have to be treated diversely. In this case, the fraction of the removed events - here called ϵ_{cuts} - has to be removed accordingly from t_{live} . The so-called rms-cut which evaluates the pulses’ quality by the rms value of the standard-event fit (see chapter 3.2.1) is one such example.

Unfortunately, the cut efficiencies are not completely understood. On the one hand, valid events might be misidentified by the “Cuts on invalid pulses” and, on the other hand, invalid events passing these cuts might be treated as valid pulses. To test the influence of the rms-cut on the live-time determination of the Dark-Matter analysis of CRESST (run32) a dedicated simulation of pulses has been performed which yields similar results [82]. A more sophisticated study regarding the efficiencies of all considered cuts is presently ongoing [83].

The results of the live-time determination for all measurements in the test cryostat carried out in this thesis are presented in table 3.3.

3.2.4 Parametrization of Recoil Bands

The data of both channels of a CRESST detector module which measures the phonon energy E_r and the light energy E_L are commonly displayed in so-called scatter plots in which the light energy E_L is plotted versus the total recoil energy E_r in the crystal. In this kind of illustration, bands with different slopes arise due to a certain light quenching corresponding to different kind of particle interactions. To describe the position and the width of the nuclear-recoil bands at lower light yield (LY), usually, the dominant electron-recoil band with a slope of ~ 1 (per definition) is parametrized by

$$E_L = (p_0 \cdot E_r + p_1 \cdot E_r^2) \cdot \left(1 - p_2 \exp\left(-\frac{E_r}{p_3}\right)\right) \quad (3.3)$$

where p_0 , p_1 , p_2 , and p_3 are fit parameters. In first order approximation the scintillator is linear (p_0), however, typically below ~ 100 keV the LY of electron recoils drops due to the “scintillator non-proportionality effect” [84] which is not yet fully understood and varies from crystal to crystal. The parameters p_2 and p_3 set the magnitude and the energy scales of the effect, respectively. At higher energies above $\mathcal{O}(100$ keV), additionally, a deviation from linearity is observed which is described by p_1 . This parameter varies among different crystals over one order of magnitude and in sign (see [27]). Thus, this effect might be non-physical and rather due to insufficient calibration of the light channel at higher energies (see further discussion in chapter 4.7).

The width of the electron/ γ band σ_γ is parametrized as follows

$$\sigma_\gamma(E_L) = \sqrt{S_0 + S_1 \cdot E_L + S_2 \cdot E_L^2}. \quad (3.4)$$

Thereby, S_0 accounts for the energy-independent baseline noise, S_1 for statistical uncertainties in the amount of photons produced and S_2 for higher-order fluctuations as, e.g. position dependencies in terms of light emission in the crystal [85].

A maximum-likelihood function is set up [27] to fit the acquired data points $(E_{r,i}, E_{L,i})$:

$$\mathcal{L}(E_{r,i}, E_{L,i}) = \frac{1}{\sqrt{2\pi}\sigma_\gamma(E_L(E_{r,i}))} \cdot \exp\left(-\frac{(E_{L,i} - E_L(E_{r,i}))^2}{2(\sigma_\gamma(E_L(E_{r,i})))^2}\right) \quad (3.5)$$

The free parameters are then determined by minimizing the negative logarithmic likelihood [86]

$$\mathcal{L}_{\text{tot}} = \sum_i -\ln \mathcal{L}(E_{r,i}, E_{L,i}) \quad (3.6)$$

For detectors operated in the CRESST setup, an additional event at $LY > 1$, so-called “excess-light events”, are observed and also considered in the likelihood function [27]. No significant distribution of such signals has been observed during measurements in the test cryostat.

Nuclear-Recoil Bands: The reduction of the relative light output of nuclear recoils compared to electron-recoil events is quantified by Quenching Factors²:

$$E_L^x = QF_x \cdot (L_0 E_r + L_1 E_r^2) \quad (3.7)$$

where E_L^x is the mean light energy of the recoiling nucleus x and the corresponding Quenching Factor QF_x . The non-proportionality effect has not been observed for nuclear recoils, therefore, it is not considered for the calculation of E_L^x (for a more extensive discussion see chapter 4.1). Accordingly, for the width of the nuclear recoil band the following equation holds:

$$\sigma_x(E_L^x, E_r) = \sqrt{(\sigma_{\gamma,L}(E_L^x))^2 + (QF_x \cdot \sigma_{\gamma,P}(E_r))^2}. \quad (3.8)$$

The total width of the electron/ γ -band $\sigma_\gamma(E_L)$ is a combination of the component accounting for the uncertainty of the light detector $\sigma_{\gamma,L}(E_L)$ and that of the phonon detector $\sigma_{\gamma,P}(E_r)$:

$$\sigma_\gamma(E_L, E_r) = \sqrt{(\sigma_{\gamma,L}(E_L))^2 + (\sigma_{\gamma,P}(E_r))^2}. \quad (3.9)$$

Using this equation, the width of the nuclear recoil band can be written as

$$\sigma_x(E_L^x, E_r) = \sqrt{(\sigma_\gamma(E_L^x))^2 + (QF_x - 1)^2 \cdot (\sigma_{\gamma,P}(E_r))^2}. \quad (3.10)$$

The contribution of the phonon channel $\sigma_{\gamma,P}(E_r)$ to the total resolution of the bands is determined by the width of the testpulses injected for calibration purposes (see chapter 3.2.1) or by the width of γ -calibration lines in the phonon spectrum. In good approximation - the phonon resolution plays a minor role compared to the resolution of the light channel - $\sigma_{\gamma,P}$ is kept constant over the entire energy range. Instead of $E_L \sim E_r$ for electron recoils, for nuclear recoils $E_L \sim QF_x \cdot E_r$ holds and, thus, the width of the quenched bands also has to be scaled with the corresponding Quenching Factor (see equation 3.8): $\sigma_{x,P} = QF_x \cdot \sigma_{\gamma,P}$. Switching to a different kind of illustration - the light-yield (LY) plot - in which the light yield $LY = E_L/E_r$ is plotted against the phonon energy the mean and the width of the quenched bands have to be transformed accordingly:

$$LY_x = QF_x \cdot (L_0 + L_1 E_r) \quad (3.11)$$

$$\sigma_x^{LY}(E_L^x, E_r) = \frac{\sigma_x(E_L^x, E_r)}{E_r}. \quad (3.12)$$

In figure 3.14, a typical LY plot with the acceptance bounds (80% C.L.) of the electron, α , O and Pb-recoil bands is shown.

²In chapter 3 the former assumption of energy-independent QFs is used ($QF_O = (10.4 \pm 0.5)\%$, $QF_{Ca} = (6.38_{-0.65}^{0.62})\%$, $QF_W = (3.91_{-0.43}^{0.48})\%$ [25]). As will be presented in chapter 4, an energy-dependence of the QFs has been measured for the first time within this thesis. This has significant influence on the Dark Matter analysis for CRESST, however, plays a minor role for the results of the measurements presented in chapter 3.

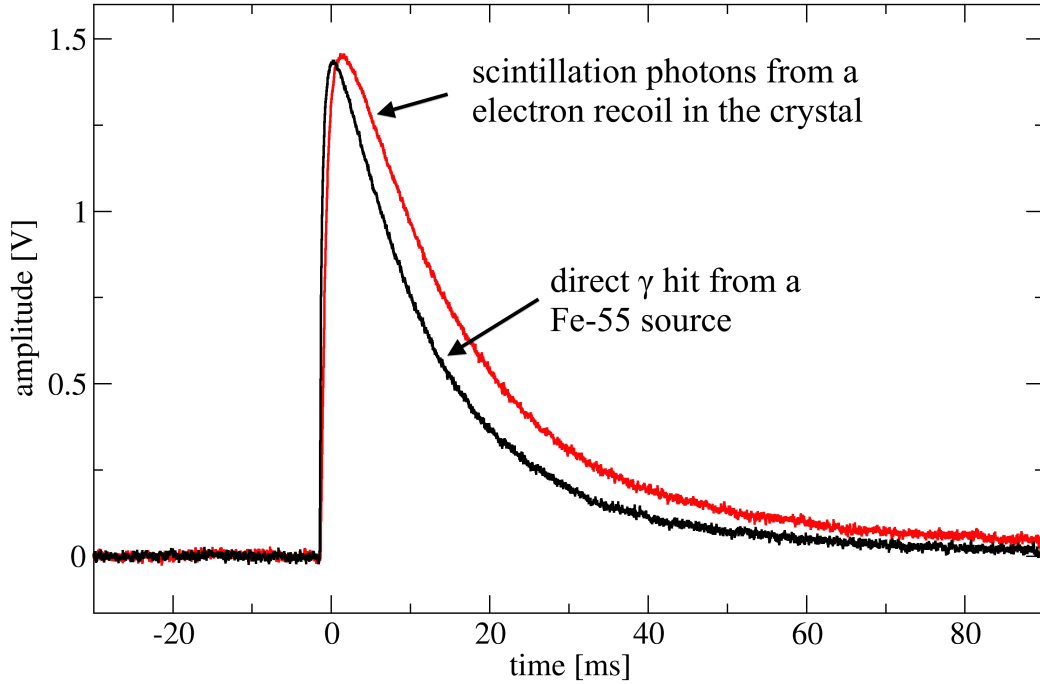


Figure 3.5: Comparison of the pulse shape of events in the light detector WII-136: Scintillation photons from a electron-recoil event in the CaWO_4 crystal and a direct X-ray hit from a ^{55}Fe source (~ 6 keV). Due to the slow scintillation time constant of CaWO_4 ($\sim 400 \mu\text{s}$) the crystal events have a slightly longer decay time.

3.2.5 Determination of the Light Output of Crystals

The scintillation light output of CaWO_4 crystals is of utmost importance for the sensitivity of a CRESST-detector module. In this thesis, CaWO_4 crystals produced at the crystal laboratory at TUM [73] have been operated in the test cryostat at Gran Sasso also to study their light output. To quantify the absolute light output of crystals a ^{55}Fe source was installed in direct line-of-sight to the silicon-on-sapphire (SOS) light detector.

Typical pulses of such direct γ -rays (X-rays of ~ 5.9 keV) are shown in figure 3.5 in comparison with an event originating from scintillation photons of an electron recoil in the CaWO_4 crystal. Due to the slow scintillation time constant of CaWO_4 ($\sim 400 \mu\text{s}$) the crystal events have a slightly longer decay time compared to the instantaneous energy deposition by X-rays in the light detector. These pulses cannot be fitted with the same template (see chapter 3.2.1) and have to be treated separately to derive the energy information. The light channel cannot be calibrated at energies below the X-rays of ^{55}Mn from a ^{55}Fe source at 5.90 keV (K_α) and at 6.49 keV (K_β). A typical spectrum is shown in figure 3.6.

The following assumptions are made in order to compare the energy scales of both kinds of interactions in the light detector which allows to determine the fraction of detected light from an energy deposition in the CaWO_4 crystal:

- The pulse height of the pulses is direct proportional to the energy deposited in the light detector. This is a good assumption, since the typical CRESST-light detectors are weakly coupled to the heat bath and are operated mainly in the “calorimetric mode”

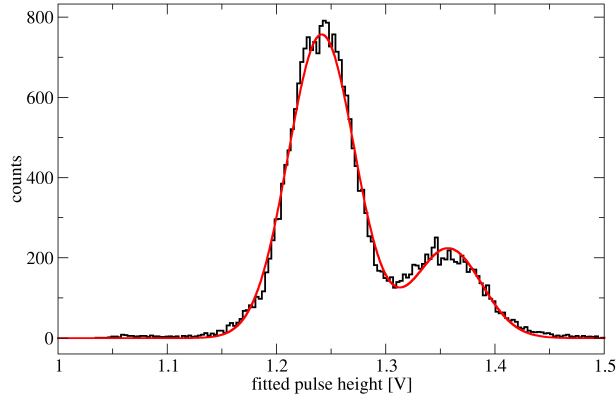


Figure 3.6: Spectrum of the pulse height derived by a truncated standard-event fit (fitted pulse height) of events from a ^{55}Fe source in the light detector (WII-136). The contributions of both X-ray lines of ^{55}Mn at 5.90 keV (K_α at 1.24 V) and at 6.49 keV (K_β at 1.36 V) can be resolved. The best fit to the spectrum is shown in red which yields the width of the X-ray lines as ~ 0.15 keV (1σ).

(see chapter 2.2.4). Hence the amplitude of the non-thermal phonons measures the total energy of the high-frequency phonons from a particle interaction in the detector [58].

- Pulses of direct hits in the light detector and pulses from scintillation photons equally saturate. The ratio of the pulse height and the pulse height derived by a truncated standard-event fit (fitted pulse height) allows to quantify the saturation effect. This effect is shown in figure 3.7 for light pulses originating from electron-recoil events in a CaWO₄ crystal.

The fraction f of the total energy deposition in the crystal which is detected in the light detector can be calculated as:

$$f = \frac{E_{\text{Mn},K_\alpha}}{E_\gamma(x)} \cdot \frac{PH_\gamma(x)}{x} \quad (3.13)$$

where x is the pulse height of the K_α line of ^{55}Mn with $E_{\text{Mn},K_\alpha} = 5.90$ keV from the ^{55}Fe source. $PH_\gamma(x)$ is the pulse height derived by a truncated standard event fit (fitted pulse height) corresponding to an event of pulse height x in the e^-/γ band and E_γ is the calibrated energy of an e^-/γ event of pulse height x .

3.3 First Test of TUM-Grown CaWO₄ Crystals

The crystal Rudolph VI was the first crystal which was produced by the crystal laboratory of TUM as a CRESST-size cylinder of 40 mm in diameter and 40 mm in height [52, 73]. Within the present thesis, this crystal was equipped for the operation as phonon detector and investigated in several measurements in the test cryostat at Gran Sasso.

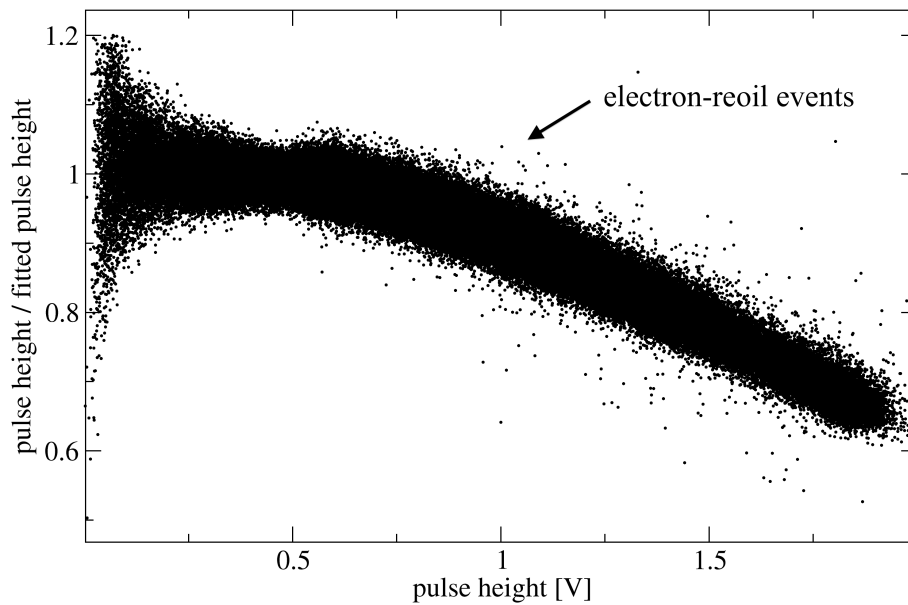


Figure 3.7: Saturation of the pulse height in the light detector WII-136 which was used in run326, run327 and run328 in the test cryostat at Gran Sasso. The ratio of the pulse height and the pulse height derived by a truncated standard-event fit (fitted pulse height) quantifies how much the energy of the recorded pulses is underestimated. Here, this ratio is plotted against the pulse height for electron-recoil events. Assuming similar saturation effects for direct hits in the light detector (e.g. X-rays from a ^{55}Fe source) and for scintillation-photons from the CaWO_4 crystal the energy deposition of both kinds of interactions in the light detector can be determined. This allows to measure the fraction of the total energy deposition in the CaWO_4 crystal which is detected as photons in the light detector.

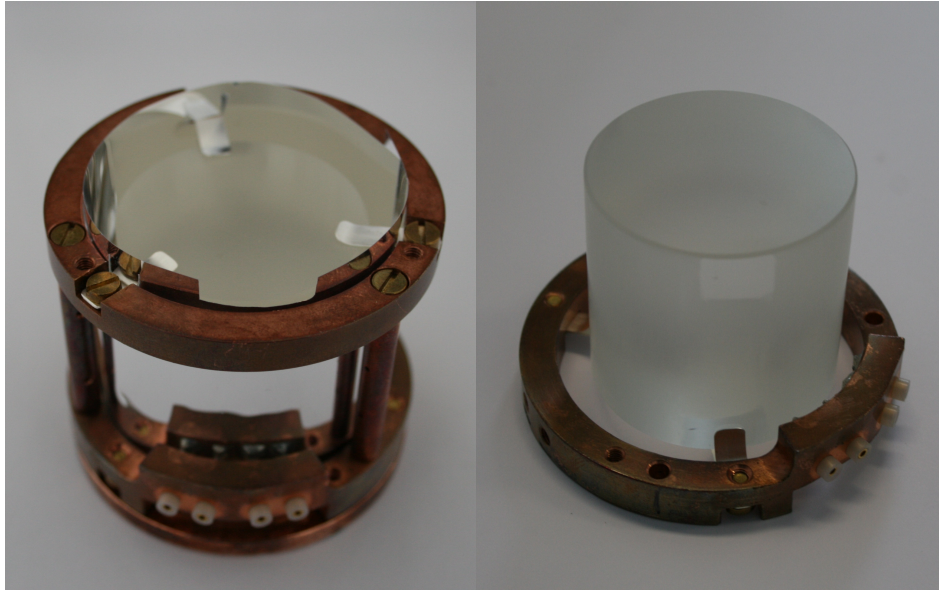


Figure 3.8: Left: Standard run32 CRESST detector holder with bronze clamps (coated with Al) holding the crystal Rudolph VI. Right: The TUM-grown crystal Rudolph VI in its second design state in which also the lateral surface was roughened with 600 SiC powder (see text). The spots where the bronze clamps are touching the crystal are left polished.

3.3.1 Performance as Cryogenic Detector

The raw CaWO_4 ingot produced in the crystal lab of TUM was annealed under pure O_2 flow in order to fill oxygen vacancies in the crystal's lattice which increases the absorption/scattering length of photons in the CaWO_4 crystal and raises the light output (at present typically by $\lesssim 50\%$) [51]. The following annealing procedure was applied: ramping up the temperature at a rate of $50^\circ/\text{h}$ to a maximum temperature of 1450°C , annealing for 72 h and ramping down analogously. Afterwards the CRESST-size cylinder Rudolph VI (also called TUM-27) was cut out and polished on all sides. Thereafter, the base surface facing the light detector was roughened with a silicon-carbide powder (600 SiC [51]). With this standard CRESST design the crystal showed a light output of $L = 98.7\%$ compared to the reference crystal Boris³ at room temperature [52].

The crystal was equipped with a standard CRESST-size tungsten transition-edge sensor (TES) with an Au strip (to establish the thermal link to the heat bath) evaporated onto a CaWO_4 carrier of $20\text{mm} \times 10\text{mm} \times 2.5\text{mm}$. Details about the dimensions and the production process of TESs are given, e.g., in [68]. The carrier was glued onto the polished base face of the cylindrically shaped crystal with the glue EPO-TEK [68]. Rudolph VI was then mounted into a standard run32 CRESST detector holder (see figure 3.8). Two measurement campaigns have then been performed with the crystal Rudolph VI at the test cryostat at Gran Sasso:

³A CRESST-size CaWO_4 crystal, called Boris, was defined as a reference crystal at the beginning of the CRESST activities. Its light output which was determined by a standardized method at room temperature is normalized to 100%.

- **run321:** First test of a TUM-grown crystal as phonon detector and determination of its light output with an exposure of 0.65 kg-days. For this measurement, only the side which faces the light detector was roughened, all other surfaces were kept polished.
- **run327:** In the second measurement campaign, the crystal was roughened on all surfaces except for the one where the TES is glued on and the spots where the bronze clamps touch (see figure 3.8). The latter is to prevent damage of the roughened surfaces by the clamps which could cause phonon-only events. With this measurement the influence of the roughening on the phonon detector performance and the light output has been studied. In addition, this extensive measurement of 3.41 kg-days has been used for the radon-exposure measurement presented in chapter 3.4.

The phonon detector was equipped with a silicon-on-sapphire (SOS) light detector (WII-131 in run321, WII-136 in all other runs) [68].

In order to study the phonon properties of the detector a template (standard event) pulse has been generated (from pulses of the electron-recoil band at $E_r \sim 122$ keV). The pulses can be described by the cryogenic detector model [58] presented in chapter 2.2.4. The template events and the best-fit results according to equation 2.6 are shown in figure 3.9. The thermal component ($\tau_t = 123.24 \pm 0.38$ ms) and the non-thermal component ($\tau_n = 25.52 \pm 0.04$ ms) as well as the ratio between the amplitude of the non-thermal component to the total amplitude ($a_n/a_{tot} = -0.843$) measured in run321 are well in agreement with the data of other phonon detectors operated in CRESST where crystals from commercial suppliers were used⁴. The additional roughening of the crystal has no significant influence on the pulse shape of the phonon pulses ($\tau_t = 125.66 \pm 0.38$ ms, $\tau_n = 22.70 \pm 0.06$ ms, $a_n/a_{tot} = -0.823$). Earlier concerns that the decay time of the thermal component would dramatically increase due to decay of non-thermal phonons on the roughened surfaces could not be confirmed. The phonon resolution of 2.45 keV ($1-\sigma$ C.L.) for run321 and 1.87 keV ($1-\sigma$ C.L.) for run327 measured by fitting the γ line at $E_r = 122$ keV are also comparable. In run321 the resolution suffered from detector instabilities which were worse compared to run327. The energy resolution of the phonon channel in run327 is similar to other comparable CRESST crystals and there is no indication of a worsening of the resolution due to additional roughening of crystal surfaces. In figure 3.10 the background-gamma spectrum of Rudolph VI is shown. Most of the background originates from contaminations in the cryostat (see chapter 3.1).

3.3.2 Light Output and Resolution

The light output of the scintillating crystals which is related to the resolution of the light channel is crucial for the background-suppression capability and thus for the sensitivity of a CRESST detector module. With the method described in chapter 3.2.5, a ^{55}Fe source installed in the direct line-of-sight of the light detector is used to determine the absolute amount of detected scintillation light. For run321 this method yields a light output of $L = 1.09\%$ of the total energy deposited in the CaWO_4 crystal (errors are discussed in chapter 3.2.5). Due to the roughening of the lateral surface in run327 the light output increases to $L = 1.31\%$. The resolution of the light channel can be determined by fitting the electron recoil band according to equation 3.4. The influence of the phonon-energy resolution is negligible for the energy range considered here. In figure 3.11 the fit results for the 1σ resolution of the

⁴The institute SRC Carat in Lviv, Ukraine is one of the current suppliers of CaWO_4 for CRESST.

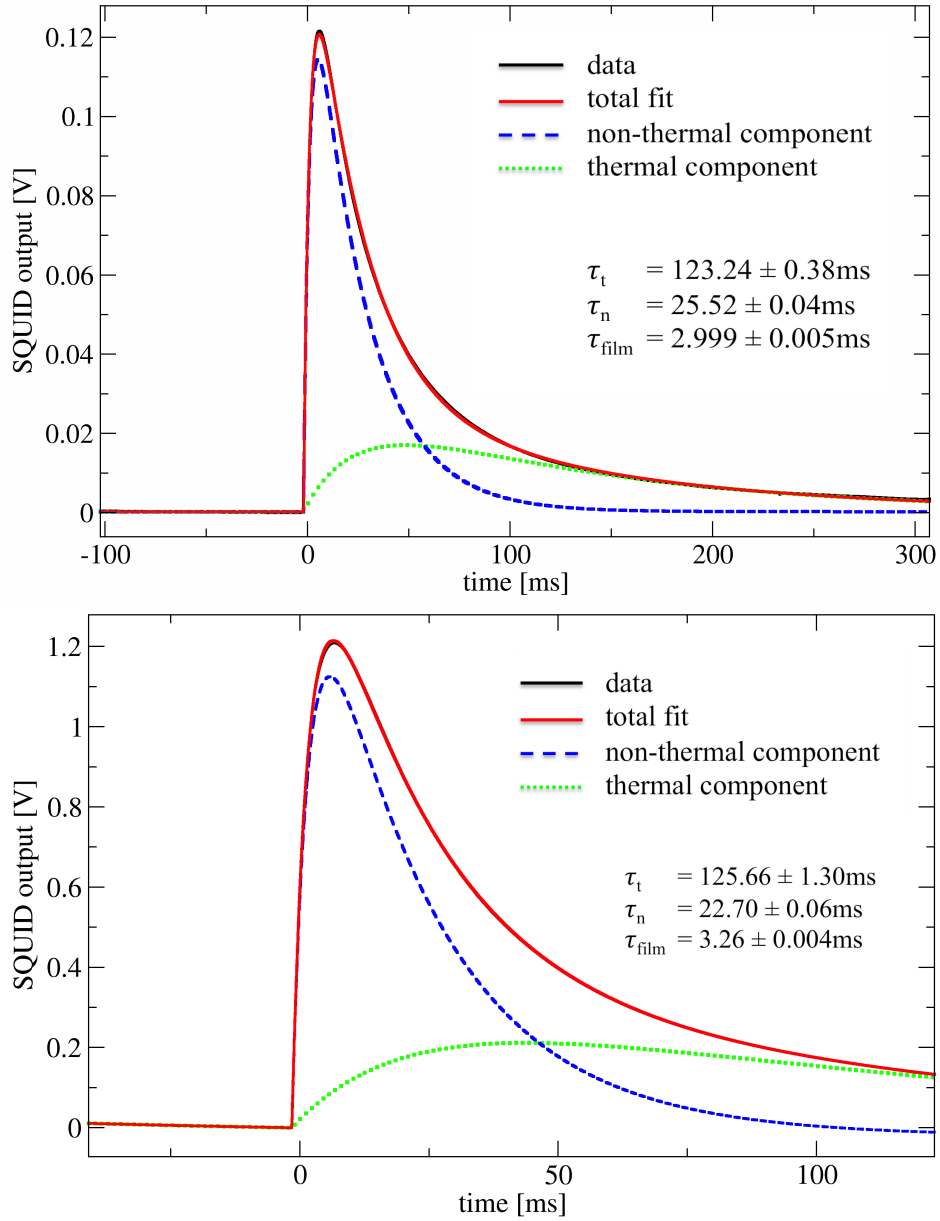


Figure 3.9: Top: Template of the phonon-detector pulses of run321 fitted according to equation 2.6. Bottom: Template of the phonon-detector pulses of run327 with corresponding fit. The additional roughening of the lateral surface of the crystal Rudolph VI (TUM-27) in run327 has no significant impact on the pulse shape of the phonon pulses. Note that the sample lengths of both measurements are different.

electron-recoil band of run321 and run327 are shown. The parameter S_0 is determined independently by the baseline noise, the parameters S_1 and S_2 were left free in the fit. The ratio $S_1^{\text{run321}}/S_1^{\text{run327}} = 1.244$ indicates an increased light output by $\sim 24\%$ for the roughened crystal which is well in agreement with the independent measurement using a ^{55}Fe source as

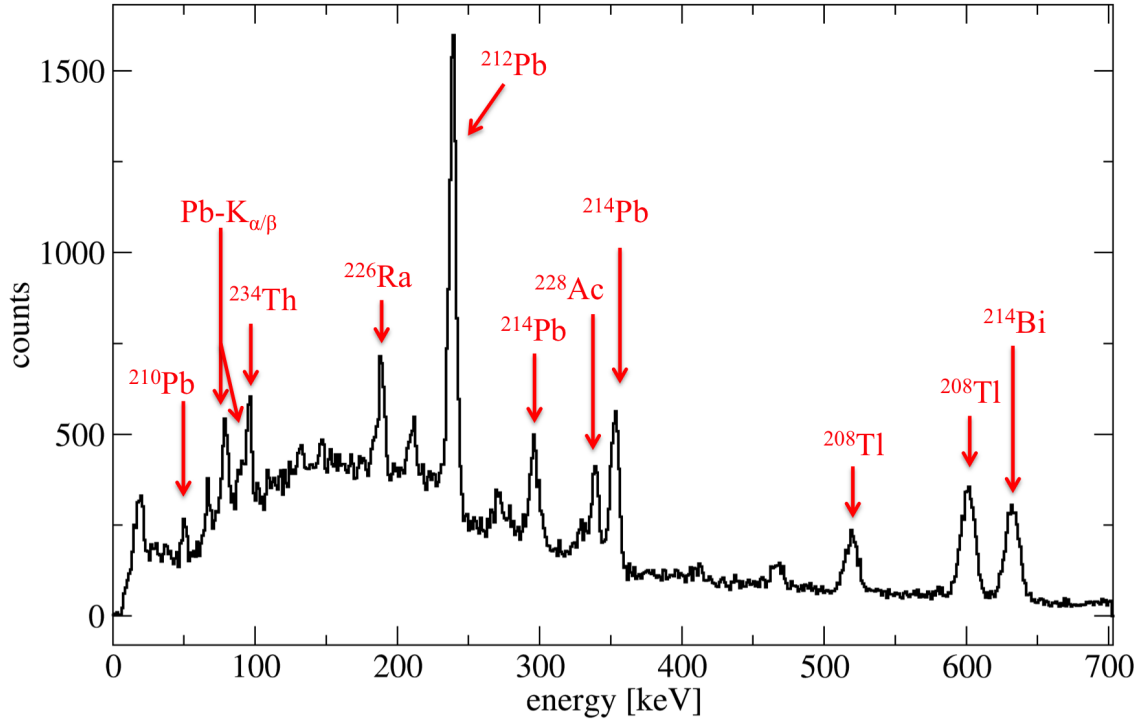


Figure 3.10: Background-gamma spectrum of the phonon detector Rudolph VI in its design state for run321 in the test cryostat at Gran Sasso. The gamma lines indicated in the plot are mainly due to contaminations in the Pb-shielding and in parts of the crystat. The continuous electron-recoil spectrum with a maximum at ~ 150 keV is correlated to cosmic muons which produce δ -electron induced Bremsstrahlung. A list of the visible γ lines are given in appendix XX.

described above. The parameter S_2 is proportional to the produced light and thus influenced, e.g., by position dependencies in the crystal. Such effects are significantly reduced in run327 due to the additional roughening: $S_2^{\text{run321}}/S_2^{\text{run327}} = 4.694$.

For illustration the linear ($S_1 \cdot E_L$) and quadratic ($S_2 \cdot E_L^2$) components of equation 3.4 are shown in figure 3.12. Above $E_L \sim 3$ keV_{ee} the resolution is dominated by the component $S_1 \cdot E_L$ which shows that besides the reduction of the baseline noise S_0 also the higher light output is crucial for the resolution in the region of interest for Dark Matter Search (typically 12 – 40 keV).

For the analysis of CRESST detectors the gaussianity of the recoil bands is essential. It was shown earlier [85] that due to position dependencies different areas of the crystal have a different light output. This effect is enhanced if absorption and scattering lengths are in the order of the dimensions of the crystal and becomes stronger the higher the more of the surface is polished. In extreme cases simulations and measurements showed that a double-peak structure in the light channel appears [85]. During run321 such an asymmetry in the light output has been observed which is illustrated in the case of the light-yield (LY) distribution of the ^{212}Pb peak in figure 3.13. The combination of absorption and scattering lengths of a similar TUM-grown CaWO_4 crystal (Jakob II) was measured to be ~ 10 cm at a wavelength

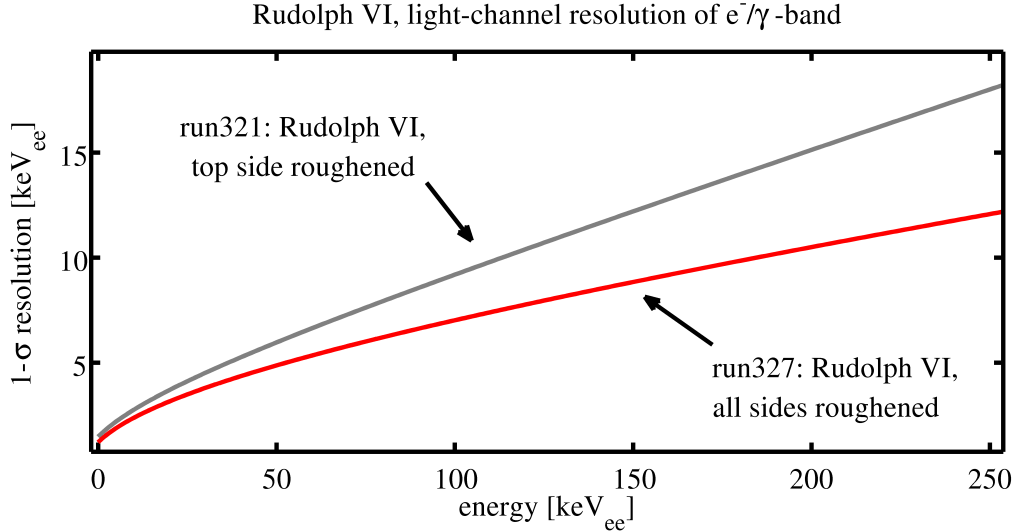


Figure 3.11: Best fits of the light-channel resolution of the e^-/γ -band measured for the TUM-grown CaWO_4 -crystal Rudolph VI at the test cryostat. In run321 only the side of the crystal facing the light detector was roughened, whereas in run327 all sides except for the side bearing the TES were roughened. The resolution was parametrized according to equation 3.4 where the parameter S_0 was determined independently by the baseline noise; only S_1 and S_2 were left free in the fit. The ratio $S_1^{\text{run321}}/S_1^{\text{run327}} = 1.244$ indicates an increased light output by $\sim 24\%$ for the roughened crystal (well in agreement with the independent measurement using a ^{55}Fe source). The ratio $S_2^{\text{run321}}/S_2^{\text{run327}} = 4.694$ shows that for run327 uncertainties which are proportional to the produced light (e.g., position dependencies in the crystal) are significantly decreased.

of 420 nm [52] compared to values of up to ~ 160 nm for commercially available crystals. Despite this fact, as shown in figure 3.13 for the crystal Rudolph VI the gaussianity of the light output can be achieved if the crystal is additionally roughened on the lateral surface.

In conclusion, by additional roughening of the lateral surfaces the crystal shows a higher light output (by $\sim 20\%$), better resolution (see figure 3.11) and a gaussian LY distribution while the phonon properties do not change significantly (summarized in table 3.3 in chapter 3.6). However, there are indications (see chapter 3.5.4) that the areas which are in contact with material holding the crystal (e.g. bronze clamps) should remain polished. Otherwise, damages on the roughened surface could cause phonon-only events which are a dangerous background for Dark Matter search.

3.4 Radon-Exposure Measurement

Among the different backgrounds observed in run32 of CRESST [25], contributions originating from α decays of ^{210}Po can be clearly identified. Decays may occur inside the crystal or in parts of the detector module which have a direct line-of-sight to the crystal. As discussed in detail in section 2.4.2, for decays which occur in the bulk of the CaWO_4 crystal both the α particle and the daughter nucleus (^{206}Pb) are detected whereas elsewhere in the module or on the crystal's surface only one decay product will hit the crystal and produce a phonon signal

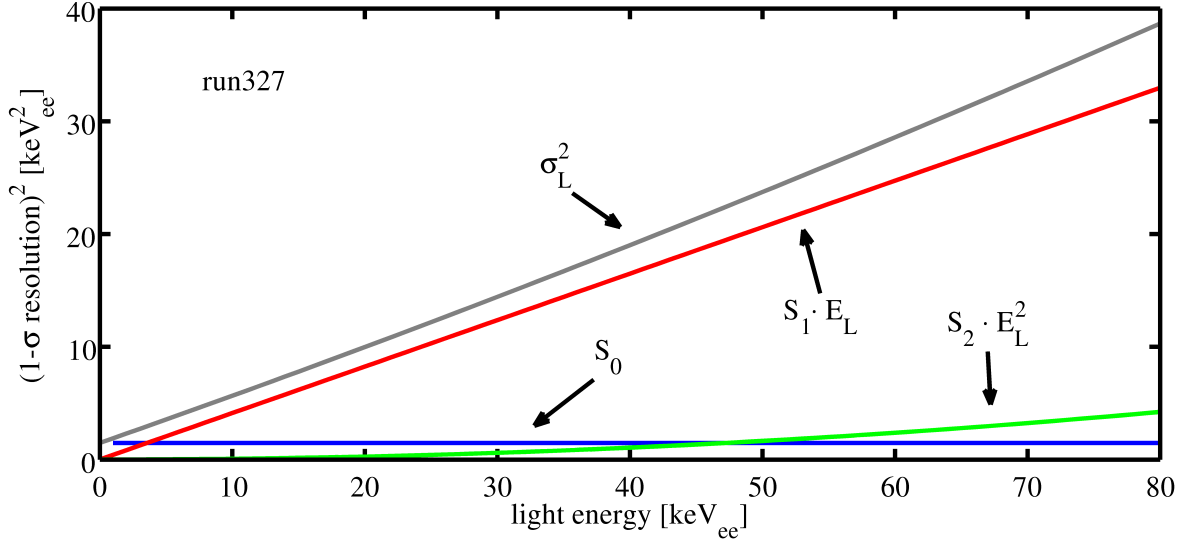


Figure 3.12: The best fit of the light resolution σ_L^2 of the e^-/γ -band in run327 is plotted together with its various components according to equation 3.4 versus the light energy E_L . Above $E_L \sim 3.5 \text{ keV}_{ee}$ the resolution is already dominated by the component S_1 which is directly proportional to the amount of detected light. At higher energies (here above $E_L \sim 625 \text{ keV}_{ee}$, not shown) the resolution is dominated by second-order effects, e.g., position dependencies of the light output of the crystal.

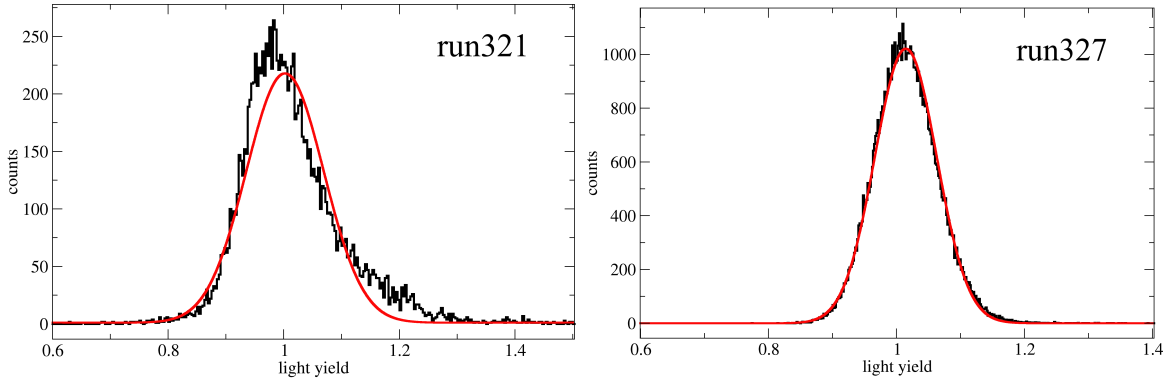


Figure 3.13: Gaussian fit to the LY distributions of the ^{212}Pb gamma peak at $E_r = 238.6 \text{ keV}$ of run321 and run327. Before the additional roughening (for run327) in the TUM-grown crystal Rudolph VI position dependencies occurred which resulted in an asymmetric LY distribution.

and scintillation light. Due to the isotropic 180° emission of the α and the corresponding ^{206}Pb particle half of such decays which take place on the surface of the bronze clamps holding the crystal occur as nuclear recoil events with a Quenching Factor (QF) of $\text{QF}_{Pb} = 2.35\%$ [25] close to the full recoil energy of 103 keV and - due to energy degradation in the clamp material - also at lower energies (see figure 2.13). The corresponding α particle is stopped in the non-scintillating clamp material and does not produce any signal. As this class of events can mimic

possible WIMP-induced tungsten recoils it is a dangerous kind of background for Dark Matter search. While the exact origin of the ^{210}Po contamination is unknown there are indications (see section 2.4.2) that ^{222}Rn implantation could contribute to this background, as all detector modules were exposed to air containing a certain amount of radon ($\mathcal{O}(100)\text{ Bq/m}^3$) prior to run32.

In the framework of this thesis a dedicated measurement to study the exact influence of radon implantation from air as a background source for the CRESST experiment has been carried out. For this purpose bronze clamps, identical to the ones used in run32 of CRESST, have been exposed intentionally to a strong radon source⁵ (mean rate $\bar{R}=2800\text{ Bq/m}^3$) for 110 days prior to a measurement in the test cryostat at Gran Sasso. The TUM-grown crystal Rudolph VI ($m = 305\text{ g}$) was mounted with these clamps in a standard CRESST module together with the light detector WII-136 and operated for a total runtime of 452.5 h (run327).

Figure 3.14 shows the result of this measurement where a prominent peak around a recoil energy of 103 keV is visible in the Pb-recoil acceptance band. After 11.2 days of measurement 10 events (after cuts) can be clearly identified as ^{206}Pb recoils within the 2σ bounds around a recoil energy of 103 keV. For the following quantitative analysis an original contamination of the clamps is neglected⁶. The observed neutron-induced oxygen recoils and the unexpected event distribution in and above the α band below 150 keV are discussed at the end of this section.

If the noble gas ^{222}Rn ($T_{1/2} = 3.82\text{ d}$) decays in the surroundings of the clamps' surfaces or the ^{222}Rn atoms (or their daughter atoms) stick to the surface, the daughter nuclei can be implanted into the material (illustrated in figure 3.15). The half-life of the successive daughter nuclei in the ^{238}U chain are short ($T_{1/2} \leq 26.8\text{ m}$) and can be considered as instantaneous compared to the long-lived ^{210}Pb with a half-life of $T_{1/2} = 22.4\text{ y}$. The successive β^- decay from ^{210}Bi to ^{210}Po is again short-lived ($T_{1/2} = 5.0\text{ d}$) and ^{210}Po itself decays with a half-life of $T_{1/2} = 138.4\text{ d}$. As the exact implantation mechanism and the implantation depth of the nuclei is strongly dependent on the roughness of the surface [87] and environmental conditions (such as e.g. humidity, dust concentration) it can not be calculated a priori. In the following the implantation process and the instantaneous decays are described quantitatively by the *effective implantation constant* α_1 . The relevant differential equations are

$$\frac{dN_{\text{Pb}^{210}}(t)}{dt} = \underbrace{-N_{\text{Pb}^{210}}\lambda_{\text{Pb}}}_{\text{decay}} + \underbrace{\alpha_1 R(t)}_{\text{Rn-exposure}} \quad (3.14)$$

$$\frac{dN_{\text{Po}^{210}}(t)}{dt} = \underbrace{-N_{\text{Po}^{210}}\lambda_{\text{Po}}}_{\text{decay}} + \underbrace{N_{\text{Pb}^{210}}\lambda_{\text{Pb}}}_{\text{build-up}} \quad (3.15)$$

$$\frac{dN_{\text{Pb}^{206}}(t)}{dt} = \underbrace{N_{\text{Po}^{210}}\lambda_{\text{Po}}}_{\text{build-up}} \quad (3.16)$$

where $N_{\text{Pb}^{210}}(t)$, $N_{\text{Po}^{210}}(t)$ and $N_{\text{Pb}^{206}}(t)$ are the number of atoms at a certain time t and λ_{Pb} , λ_{Po} are the decay constants of ^{210}Pb and ^{210}Po , respectively. $R(t)$ is the measured radon rate

⁵The setup consists of a limestone of the Gran Sasso mountain with a high intrinsic amount of ^{238}U . The stone is stored in a dedicated container inside of which a radon monitor constantly measures the radon level.

⁶A previous measurement with non-exposed clamps in the test cryostat and run32 data of CRESST supports this assumption.

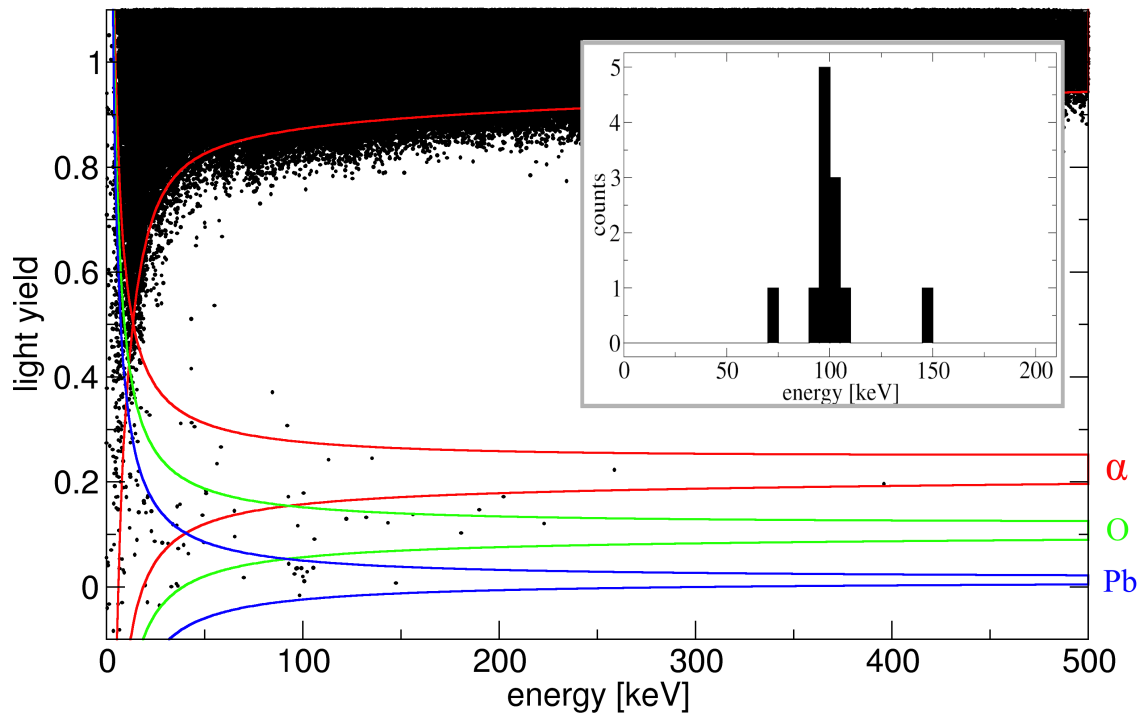


Figure 3.14: LY plot of run327 with a total runtime of 452.5 h. The 2σ acceptance bounds of α (red), oxygen (green) and lead (blue) events are shown. Around 103 keV a clear peak due to Rn-induced ^{206}Pb recoils is visible. Inset: Histogram of events inside the 2σ acceptance bounds of the lead band above 50 keV. Besides the 10 events accumulated around the full recoil energy, a degraded event at around 75 keV and an event at around 150 keV show up. The origin of the latter is not understood.

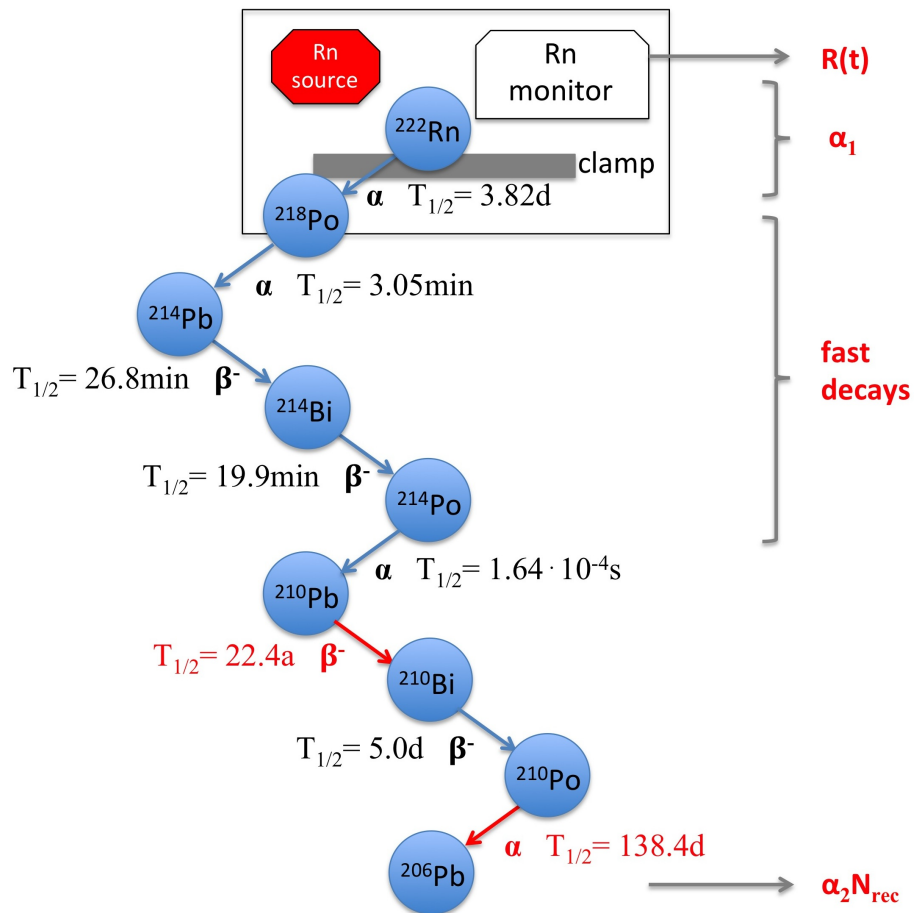


Figure 3.15: Illustration of the Rn-exposure measurement and the decay scheme of ^{222}Rn (part of the ^{238}U chain). The clamps are exposed to a Rn source inside a container in which a Rn monitor constantly measures the rate $R(t)$. Relevant for the calculation of the number of recoiling ^{206}Pb nuclei $N_{\text{rec}}(t)$ are only the decays of ^{210}Pb and ^{210}Po as all other reactions have short life times and can be considered as instantaneous. The effective constants α_1 and α_2 account for the unknown implantation processes into the clamps and geometric efficiencies of the detection, respectively.

inside the container of the radon source:

$$R(t) = \begin{cases} \bar{R}, & \text{for } t_0 \leq t \leq t_1 \\ 0, & \text{for } t > t_1 \end{cases} \quad (3.17)$$

where t_1 is the length of exposure to the radon source. Equations 3.14 and 3.15 can be solved analytically for the period of exposure:

$$N_{\text{Pb}^{210}}(t) = \alpha_1 \bar{R} \underbrace{\left[\frac{1}{\lambda_{\text{Pb}}} (1 - e^{-\lambda_{\text{Pb}} t}) \right]}_{C_1(t)}, \text{ for } t \leq t_1 \quad (3.18)$$

$$N_{\text{Po}^{210}}(t) = \alpha_1 \bar{R} \underbrace{\left[\frac{1}{\lambda_{\text{Po}} - \lambda_{\text{Pb}}} (e^{-\lambda_{\text{Po}} t} - e^{-\lambda_{\text{Pb}} t}) + \frac{1}{\lambda_{\text{Po}}} (1 - e^{-\lambda_{\text{Po}} t}) \right]}_{C_2(t)}, \text{ for } t \leq t_1 \quad (3.19)$$

With $C_1(t_1)$ and $C_2(t_1)$, the number of ^{210}Po atoms can be calculated for the period of measurement ($t > t_1$):

$$N_{\text{Po}^{210}}(t) = \alpha_1 \bar{R} \left[C_2(t_1) e^{-\lambda_{\text{Po}}(t-t_1)} + C_1(t_1) \frac{\lambda_{\text{Pb}}}{\lambda_{\text{Po}} - \lambda_{\text{Pb}}} (e^{-\lambda_{\text{Pb}}(t-t_1)} - e^{-\lambda_{\text{Po}}(t-t_1)}) \right] \quad (3.20)$$

Equation 3.16 can be solved:

$$\begin{aligned} N_{\text{Pb}^{206}}(t) &= \alpha_1 \bar{R} \left[C_1(t_1) \frac{1}{\lambda_{\text{Po}} - \lambda_{\text{Pb}}} (\lambda_{\text{Pb}} e^{-\lambda_{\text{Po}}(t-t_1)} - \lambda_{\text{Po}} e^{-\lambda_{\text{Pb}}(t-t_1)}) - C_2(t_1) e^{-\lambda_{\text{Po}}(t-t_1)} \right] \\ &= \alpha_1 \bar{R} \cdot C_3(t_1, t) \end{aligned} \quad (3.21)$$

with $N_{\text{Pb}^{206}}(t_1) = 0$. The actually measured number of ^{206}Pb -recoil events $N_{\text{rec}}(t)$ in the detector is lower due to the *effective geometrical constant* α_2 . This accounts for geometrical effects (e.g. solid-angle coverage of crystals, implantation depths) and for the fact that only one half of the decay events from the clamps are detected as lead recoils. With the measurement carried out at the test cryostat (run327) the combination of α_1 and α_2 the total effective constant α_{cresst} can be determined experimentally.

$$N_{\text{rec}}(t) = \alpha_2 N_{\text{Pb}^{206}}(t) = \alpha_1 \alpha_2 \bar{R} \cdot C_3(t_1, t) \quad (3.22)$$

$$\alpha_{\text{cresst}} = \alpha_1 \alpha_2 = \frac{N_{\text{rec}}(t)}{\bar{R} \cdot C_3(t_1, t)} \quad (3.23)$$

The clamps were exposed to a mean radon rate of $\bar{R} = 2800 \text{ Bq/m}^3$ for a period of $t_1 = 110$ days and during the measurement of 11.2 days (after cuts) 10 signal events have been observed which results in

$$\alpha_{\text{cresst}} = 0.135 \pm 0.043(\text{stat})_{-0.023}^{+0.034}(\text{syst})[s/d]. \quad (3.24)$$

The systematic error includes the uncertainty of the measurement of the radon rate. Further potential variations of α_{cresst} (e.g. due to different environmental conditions) are not considered here. Figure 3.16 (top) shows the evolution of $N_{\text{Po}^{210}}(t)$ and $N_{\text{rec}}(t)$ with time for the Rn-exposure and the measurement in the test cryostat (run327).

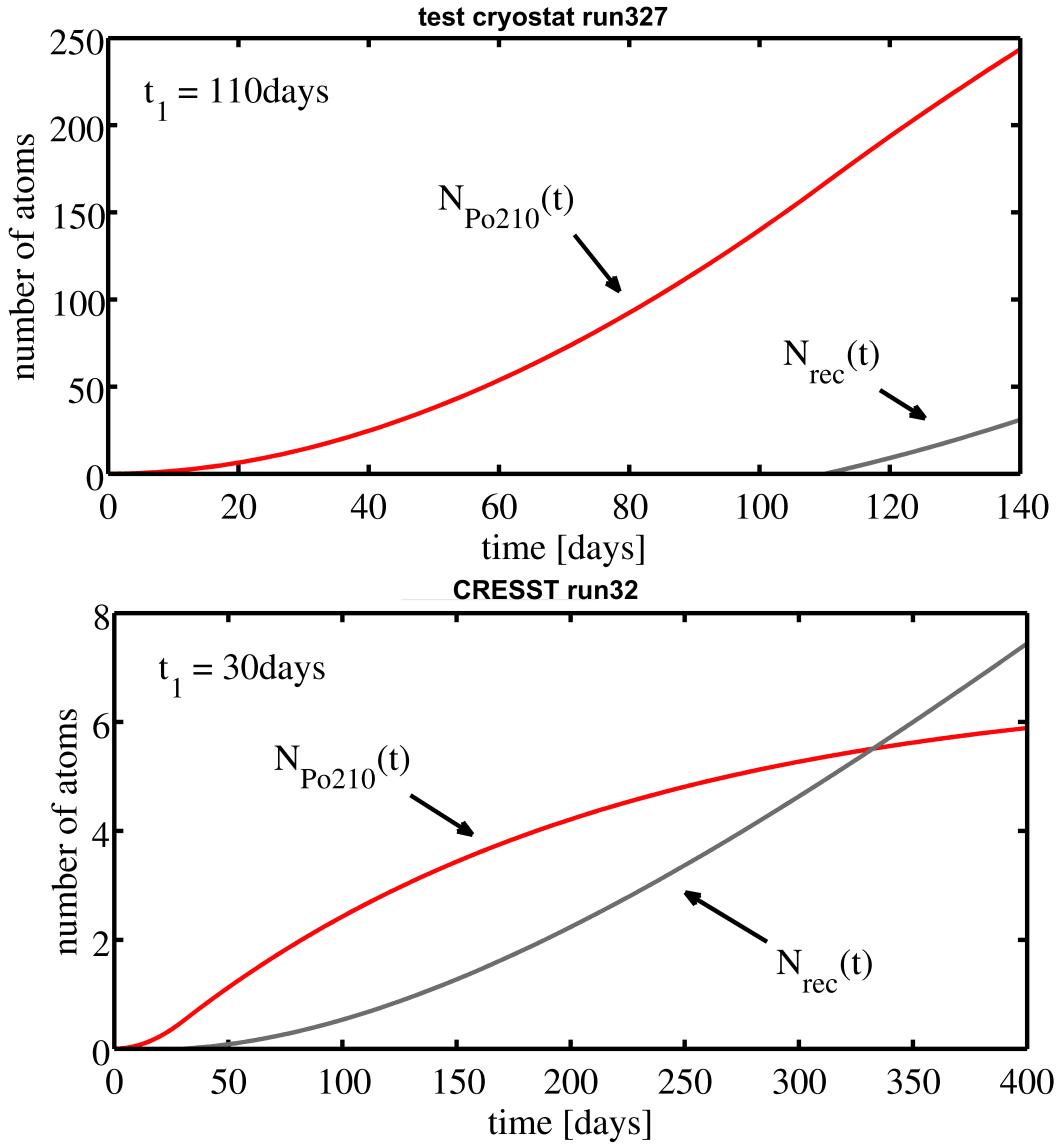


Figure 3.16: Top: Run327 at the test cryostat. Number of ^{210}Po atoms $N_{\text{Po}210}$ (red solid lines) and detected ^{206}Pb recoils N_{rec} (grey solid lines) in a typical detector module after an exposure of $t_1=110$ days to a Rn source with a mean Rn rate of $\bar{R}=2800\text{ Bq/m}^3$. Bottom: Run32 of the CRESST experiment. Expected number of ^{210}Po atoms and detected ^{206}Pb recoils (N_{rec}) in run32 after an assumed exposure of $t_1=30$ days to ambient Rn with a mean Rn rate of $\bar{R}=100\text{ Bq/m}^3$. This rate can be interpreted as an upper limit for the Rn-exposure of one module. For further details see text.

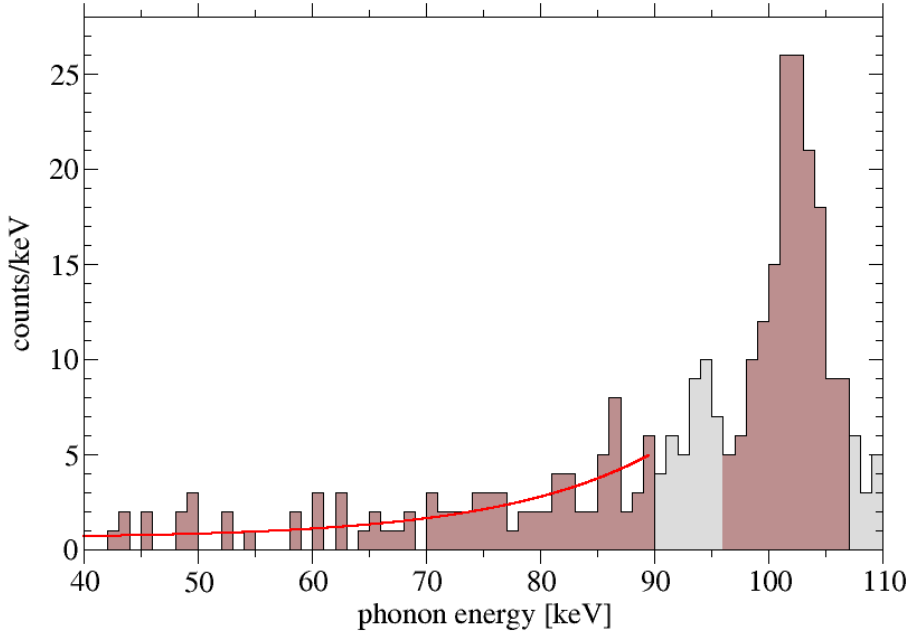


Figure 3.17: Events in the Pb acceptance region after an exposure of 730 kg-days in run32 of the CRESST experiment [25]. Highlighted are the Pb-reference region (40-90 keV) and the Pb-peak region (96-107keV). In total 157 (89) events have been observed in the peak (reference) region. The solid red line shows the best fit to the events in the reference region (see chapter 2.4.2).

Estimation of the Rn-induced ^{206}Pb background for run32 of CRESST: Under the assumption that α_{cresst} was the same for both, the radon exposure measurement described above as well as the exposure of the CRESST-detector modules in the Gran Sasso laboratory (LNGS) before run32 of CRESST, it is possible to estimate the number of events originating from radon-induced ^{210}Po decays (from the bronze clamps) in run32. During assembly and mounting the modules were exposed to air with a mean radon rate of $\bar{R} = 100 \text{ Bq/m}^3$ for $t_1 = 30$ days (both conservative assumptions).

The results are plotted in figure 3.16 (bottom). The number of ^{206}Pb events in the 2σ bounds around the full recoil energy of 103 keV during the measuring time of 305 days (after cuts, $t_2 = 335$ days) is expected to be

$$N_{\text{rec}}(t_2) = 5.5^{+3.1}_{-2.7} \text{ counts per module.} \quad (3.25)$$

This is the first quantitative study that demonstrates that radon-contaminated air can play an important role for the CRESST experiment if parts of the detector module are non-scintillating as in run32 (bronze clamps). In total, 157 events are observed in the ^{206}Pb -recoil peak in the 8 detector modules of run32 (see figure 3.17). The considerations above suggest 44^{+25}_{-22} of those events to be radon-induced recoils from the bronze clamps holding the crystal.

Estimation of the Rn-induced ^{206}Pb background for future runs of CRESST: For the upcoming run33 of CRESST an extensive radon-prevention system for assembly and

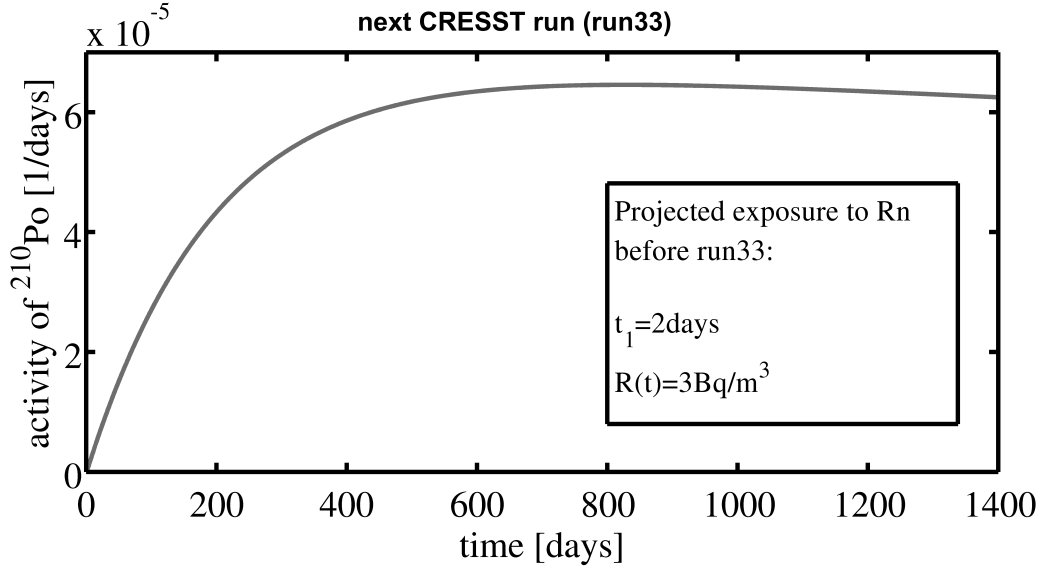


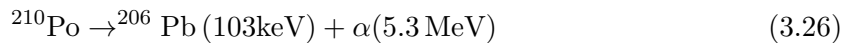
Figure 3.18: ^{210}Po -activity of one CRESST module for a scenario which is feasible with the newly developed Rn-prevention system at Gran Sasso: During assembly and mounting the module is exposed to air with a mean radon rate of $\bar{R}=3\text{Bq/m}^3$ for 2 days. The activity builds up with a time constant of $T_{1/2}(^{210}\text{Po})=138.4\text{d}$ and decreases again later with $T_{1/2}(^{210}\text{Pb})=22.4\text{a}$. The rate remains always well below $7\cdot 10^{-5}\text{d}^{-1}$ and only ~ 0.01 events are expected for a typical run with an exposure of ~ 300 days (after cuts).

mounting of the detector modules has been established (see section 2.5) at the Gran Sasso laboratory. Therefore, a significant reduction of the exposure to radon-contaminated air is technically feasible and it should be possible to mount the detectors under conditions where $\bar{R} < 3\text{Bq/m}^3$ for a maximum of 2 days. This reduces the expected number of recoils by more than two orders of magnitude; only $\sim 1\cdot 10^{-2}$ counts are expected per module within a typical measuring time (~ 300 days, after cuts) in the ^{206}Pb -recoil peak. For such a scenario the expected effective activity of ^{210}Po per detector module $A_{\text{Po}210} = \frac{dN_{\text{rec}}(t)}{dt}$ is shown in figure 3.18. $A_{\text{Po}210}$ corresponds to the rate of detected ^{206}Pb recoils in a typical CRESST detector module.

3.5 New Detector Holder Concept Based on CaWO₄ Sticks

3.5.1 The Challenge of a Fully-Scintillating Detector Housing

The likelihood analysis of run32 of CRESST [25] shows that the highest background contribution is due to ^{206}Pb recoils from ^{210}Po decays.



As already discussed in detail in section 2.4.2, in particular the events originating from contaminations on the surfaces of the non-scintillating bronze clamps can introduce a dangerous background for Dark Matter search. Due to an energy degradation in the clamp material, a leakage towards lower recoil energies is observed below the prominent peak of full energy

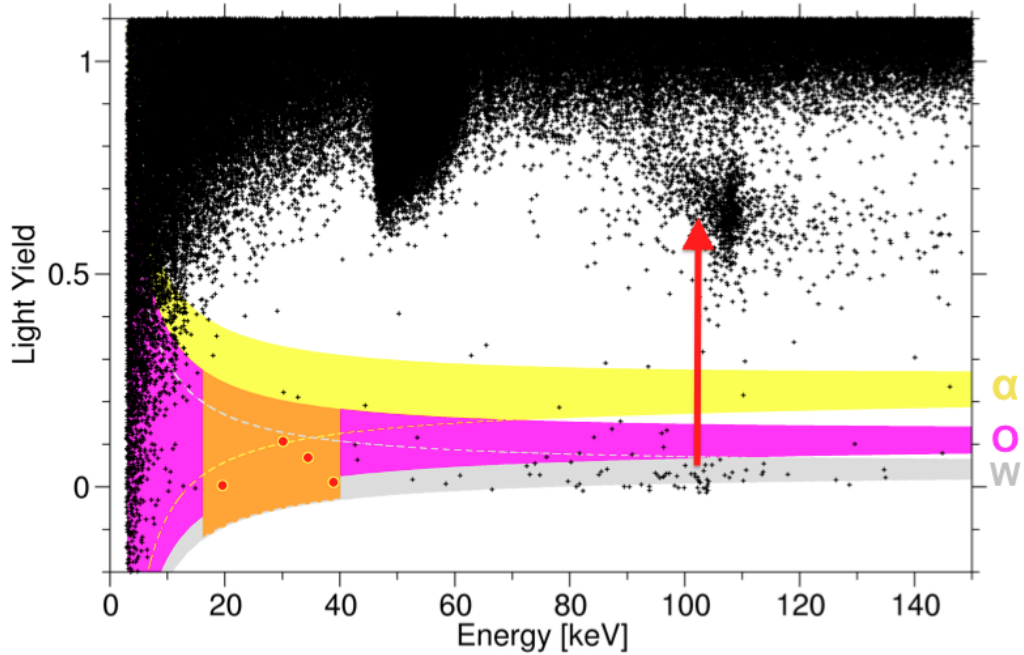


Figure 3.19: LY plot showing the full exposure (93.1 kg-days) of Channel 45 in run32 of CRESST [25]. Towards lower LY the α (yellow), oxygen (pink) and tungsten (gray) acceptance bounds (80%, 1.28σ) are shown and events lying in the region-of-interest (ROI) for Dark Matter search (here between 16.2 and 40 keV, orange) are highlighted in red. Slightly below the tungsten band a background contribution from ^{206}Pb recoils is visible around 103 keV with a tail towards lower energies. The additional light produced in the scintillating foil surrounding the crystal by the correlated α particle shifts the dominant part of the events out of the nuclear recoil bands (illustrated by red arrow).

deposition at ~ 103 keV. As shown in figure 3.19 only ^{206}Pb recoils where the corresponding α particle hits a scintillating surface (e.g. events from the surface of the foil surrounding the crystal) are vetoed. As this is not the case for events from the surface of the bronze clamps, these events appear slightly below the center of the tungsten (W) recoil band and the tail towards lower energies has a significant overlap with the region-of-interest (ROI) for Dark Matter search (typically 12-40 keV). Such a background significantly reduces the sensitivity of the detector especially to high-mass WIMPs (> 30 GeV) which are expected to scatter mainly off the heavy element W with a mass number of $A \sim 184$ (see section 2.1).

Although much effort is made to reduce the ^{210}Po contamination in the clamp material (see section 2.5) only a fully scintillating detector housing can completely avoid backgrounds from surface contaminations and shed light on the CRESST run32 results. Earlier attempts failed as not all requirements for a fully functional CRESST detector module could be fulfilled:

- **Mechanical stress** on CaWO_4 crystals causes relaxation events (so-called dark counts) which cannot be unambiguously distinguished from particle-induced events and do not produce any scintillation light. As these phonon-only signals have a strong overlap with the ROI, they have to be completely avoided. For the first time such events have been

observed in an early stage of the CRESST experiment (Al₂O₃ crystals were used) when fracture processes caused by tight clamping of the crystal induced a high signal rate [88]. These events had a tendency to cluster in time and a characteristic exponential energy spectrum $dN/dE \propto E^{-\beta}$ was observed ($\beta \approx 1.9$). Recently, several modifications of the standard bronze clamps avoiding non-scintillating surfaces have been tested by the CRESST collaboration. Neither the coverage of the bronze clamps with scintillating foil or scintillating glue [68] nor the introduction of plastic scintillator in contact with the crystal [82] have been successful in terms of detector operation. These studies suggest that plastic in contact with the target crystal or the bronze clamps causes stress relaxations due to tensions that build up when cooling these materials down to mK temperatures. In the standard CRESST design so far only blank bronze allowed an operation without relaxation events, as bronze is one of the few materials that maintains its flexibility at mK temperatures.

- Only **radiopure** material must be used.
- The **light collection and transportation** to the light detector has to be ensured.
- The **target mass** should be comparable to standard CRESST detectors (~ 300 g).
- The thermal coupling of the crystal via the holding structure (e.g. clamps) has to allow a bolometric operation of the detector.
- The clamps have to hold the crystal in a stable position, as the module has to be tilted during mounting.
- The **outer dimensions** of common CRESST holders have to be maintained to allow a proper mounting in the fixed geometry of the detector carousel (see section 2.3).

In the framework of this thesis a new, fully-scintillating detector design which fulfils the requirements above was designed, realized and successfully operated in the test cryostat. Two such modules were implemented into the CRESST setup of run33 that has started in June 2013.

3.5.2 Basic Idea and Working Principle

The technical basics of the newly developed detector design are illustrated in figure 3.20 and described in the following:

- To have only scintillating materials inside the detector housing sticks made out of CaWO₄ are used to hold the crystal. They are sharpened and polished on the side which touches the target crystal to provide a point-like contact. One stick of 4.0 mm in diameter (length: 8.2 mm) at the bottom and 8 sticks of 2.7 mm in diameter (length: 7.5 mm) at the four sides faces are fed through holes in the copper structure into the scintillating housing.
- To avoid stress on the crystals (see section 3.5.1) the well-established bronze clamps which maintain their flexibility also at mK temperatures are used outside of the housing to press the CaWO₄ sticks onto the target crystal.

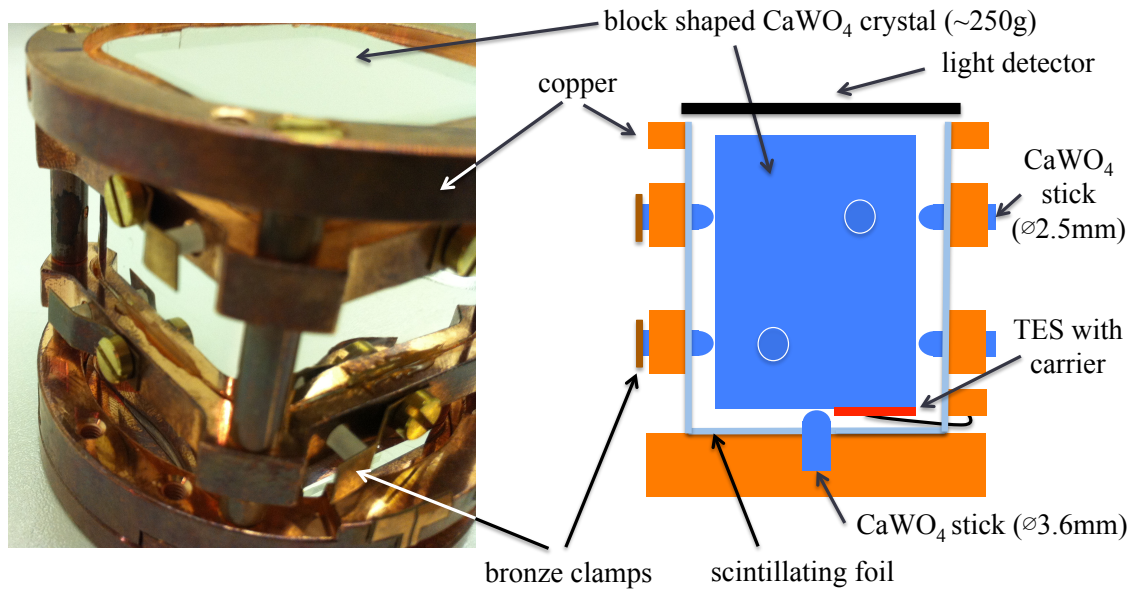


Figure 3.20: Right: Scheme of the new holder concept for CRESST detectors based on CaWO₄ sticks. The block-shaped crystal is held by eight sticks from the side (diameter 2.7 mm) and one stick from the bottom (diameter 4.0 mm) supported by bronze clamps placed outside the housing. Left: Picture of the prototype holder with the crystal Wilhelm mounted (opened module without light detector).

- The inner surface of the housing is completely covered by scintillating and reflective foil, except the holes where the sticks are fed through.
- The holder is designed for **block-shaped** crystals with typical dimensions of 32x32x40 mm³ and a total mass of $m \sim 250$ g.
- The holder structure is mostly redesigned (see chapter 3.5.3) but the outer dimensions are the same as those of the standard-CRESST detector holders.
- The upper copper ring is designed such that a standard CRESST light detector fits to the new phonon detector holder.

There are two major advantages compared to the run32-CRESST detector design:

- The detector housing is **completely scintillating**, i.e., on **all** surfaces that have a direct line-of-sight to the target crystal, α particles induce light emission which produces an additional signal in the light detector. This provides a full veto against all kinds of surface-decay events on the crystal and surrounding material.
- The holder is designed for **block-shaped crystals** which are expected to have a better light resolution [85]. This is confirmed by the measurements presented in chapter 3.5.5. In principle they also allow a higher packing density. This would increase the total mass in the available experimental volume and a better performance regarding the detection of multiple scatters of neutrons in different detector. Also the promising block-shaped crystal design was studied for the first time in form of a cryogenic detector within this thesis.

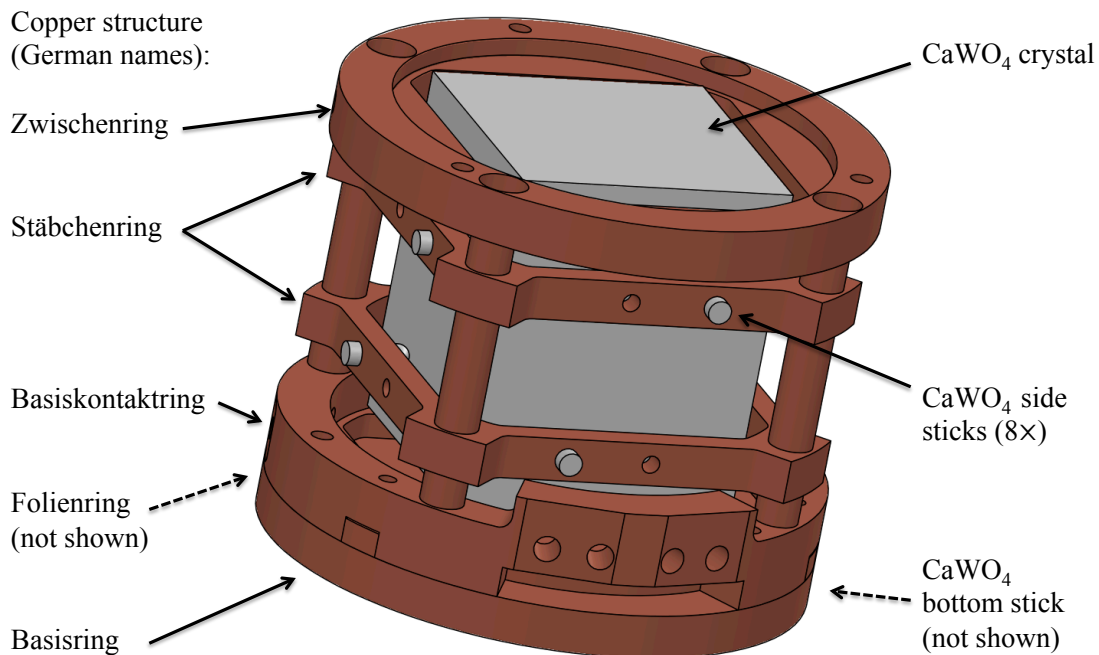


Figure 3.21: Technical drawing of the novel detector holder developed in this thesis. The copper parts (red) were modified with respect to the classic CRESST holder design to match the requirements of block-shaped crystals held by CaWO_4 (grey) sticks. The outer dimensions, however, are unchanged to allow an installation in the CRESST setup. Parts which cannot be seen directly in the drawing are indicated by dashed arrows (see figures 3.22 and 3.23). Not included in the picture are the bronze clamps that press the sticks onto the crystal, and the scintillating foil surrounding the CaWO_4 crystal (on the inner surfaces of the copper structure). Detailed technical drawings of the individual parts are presented in appendix B (technical drawings in German).

3.5.3 Realization

In this chapter technical aspects of the novel phonon-detector design are presented. A three-dimensional technical drawing of the prototype detector is shown in figure 3.21. The copper structure of the holder was modified such to match the requirements of block-shaped crystals held by CaWO_4 sticks (grey). The outer dimensions remain basically unchanged compared to the classic CRESST-module design with 62 mm in outer diameter and 51 mm in height in order to fit into the CRESST setup. The total mass of the detector holder including a $32 \times 32 \times 40 \text{ mm}^3$ block-shaped CaWO_4 crystal constitutes $\sim 595 \text{ g}$. The copper and CaWO_4 parts were machined in the workshop and crystal laboratory of TUM [73], respectively. Detailed technical drawings of the individual parts are given in appendix B.

Pictures of the CaWO_4 sticks as part of the novel phonon-detector holder are shown in figure 3.22. The bottom stick (4.0 mm in diameter, 8.2 mm in length) is mounted at the bottom plate (“Basisring”, see figure 3.21) and fixed by a bronze clamp while the eight side sticks (2.7 mm in diameter, 7.5 mm in length) are fed through holes in the copper structure (“Stäbchenring”,

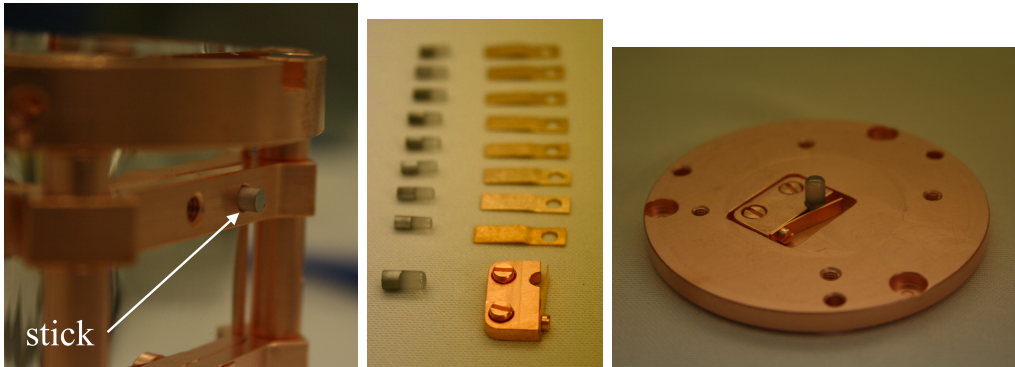


Figure 3.22: Left: Picture of the copper holder with a CaWO_4 stick in the hole of the copper holder without the corresponding bronze clamp. The outer surfaces of the sticks are coated with Al to prevent losses of light to the outside. Middle: Full set of CaWO_4 sticks, 8 side sticks of 2.7 mm diameter and 1 bottom stick of 4.0 mm in diameter, and the corresponding bronze clamps. Right: Bottom plate with the bottom CaWO_4 stick in its holder. In the final state, the bottom surface is completely covered by scintillating foil. In run326, a ^{147}Sm source was placed below the bottom surface in direct line-of-sight to the bottom stick in order to study the phonon response of recoil events occurring in the sticks (see chapter 3.5.4).

see figure 3.21). Standard bronze clamps (not shown in figure 3.22 left) are used to push the sticks onto the crystal. The outer parts of the side sticks are coated with pure Al to avoid light losses (thickness: 20 nm).

The mounted phonon-detector holder with the crystal TUM-40 mounted is shown in figure 3.23: The bonding wires for the readout (Al wires) and the thermal coupling (Au wire) of the TES are fed through comb-like slits in the reflective foil (top left). This design which was developed in the present thesis minimizes the holes in the foil and hence the non-scintillating area of the detector housing. The gap in the foil above the bonding wires is closed by a additional piece of scintillating foil attached to the “Folienring” (bottom left). The bottom plate is also fully covered by scintillating foil (top right).

3.5.4 Detector Performance at the CRESST Test Cryostat

In order to study the novel detector design based on CaWO_4 sticks and the performance of block-shaped crystals a series of measurement campaigns have been performed at the test cryostat at Gran Sasso. The following two campaigns are presented here in more detail:

- **run326:** The block-shaped crystal Wilhelm (TUM-40) of which all sides have been roughened except the one bearing the transition-edge-sensor (TES) was operated for the first time as phonon detector with a total exposure of 1.82 kg-days (after cuts). The crystal was held by CaWO_4 sticks manufactured in the crystal laboratory of TUM [73]. This run was also used for an extensive study of the α contamination of TUM-grown crystals as presented in chapter 3.6.
- **run328:** In a second design state the four side surfaces of the crystal Wilhelm were polished while the side facing the light detector remained roughened. In addition, the

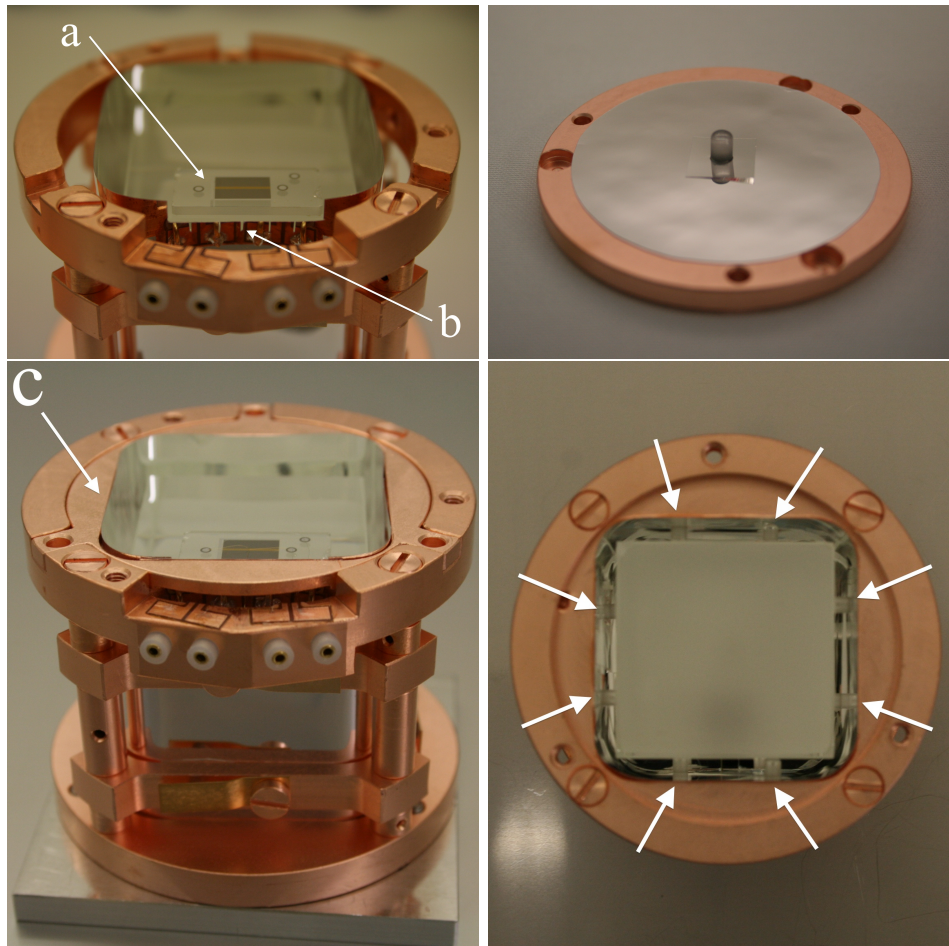


Figure 3.23: Pictures of the detector module with the crystal Wilhelm mounted. Top left: View onto the glued-on substrate bearing the TES (a). The small slits (b) in the scintillating foil are feed-throughs for the bonding wires. Bottom left: Additional copper ring (called “Folienring”, c) mounted for stabilization of the scintillating foil. Top right: Bottom plate with CaWO_4 stick covered with scintillating foil. This plate is mounted on the bottom side of the module, shown in the picture at the bottom left. Bottom right: Fully mounted detector module seen from the top where the light detector is later coupled to. The 8 side sticks (arrows) holding the crystal are also visible.

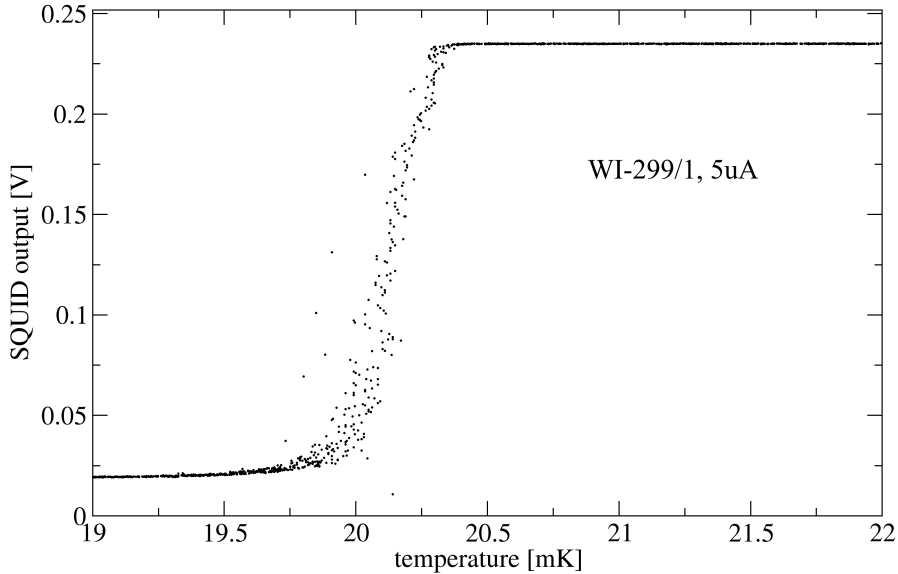


Figure 3.24: Transition curve from the normal-conducting to the superconducting state of the W-TES evaporated onto the carrier WI-299/1 which was glued onto the crystal Wilhelm. The transition curve was recorded before glueing with a bias current of $5 \mu\text{A}$. The transition temperature and width is $T_c = 20.2 \text{ mK}$ and $\Delta T_C \approx 1 \text{ mK}$, respectively.

tips of the sticks have been polished to obtain a spherical surface. The total exposure of this run was 1.60 kg-days (after cuts).

The crystal Wilhelm has been equipped with a CaWO_4 carrier on which a standard CRESST-size tungsten TES was evaporated. The transition curve of the TES with a transition temperature of $T_c = 20.2 \text{ mK}$ is shown in figure 3.24.

Phonon properties: In both experimental runs the performance of the phonon detector was satisfying. The decay times of the phonon pulses parametrized according to equation 2.6 in chapter 2.2.4 are comparable with CRESST detectors operated in standard detector holders. The fit results of all measurements are listed in table 3.3 in chapter 3.6. Exemplarily the parametrization of the phonon template in run326 is shown in figure 3.25. However, comparing the thermal decay times of both runs (run326: $\tau_t = 153.3 \text{ ms}$, run328: $\tau_t = 86.4 \text{ ms}$) the pulse shape is affected by the thermal coupling via the CaWO_4 sticks. In run328 the coupling via the CaWO_4 sticks is weaker because the polished surfaces on the sticks and the target crystal provide a point-like contact compared to the more undefined contact area with roughened surfaces in run326. This effect causes a change in the thermal decay time by a factor of ~ 2 while the ratio between the amplitude of the thermal component and the total amplitude of the pulses a_n/a_{tot} remains roughly unchanged. The phonon-energy resolution determined with the 122 keV gamma line of ^{57}Co is similar for both runs: $\sigma_{\text{run326}} = 1.45 \pm 0.01 \text{ keV}$ and $\sigma_{\text{run328}} = 1.52 \pm 0.02 \text{ keV}$.

Events in the CaWO_4 Sticks: During both measurement campaigns additional contributions of events show up at light yields (LY) > 1 above the electron recoil band. These

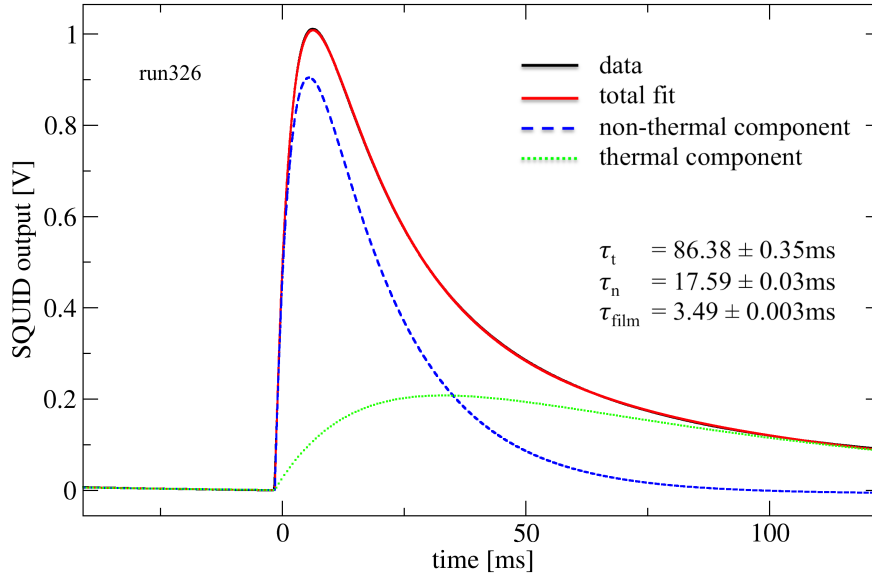


Figure 3.25: Phonon standard event of the crystal Wilhelm operated in the new holder based on CaWO₄ sticks in the test cryostat at Gran Sasso (run326). The template is fitted according to equation ?? and is plotted together with its individual components. The pulse shape is not significantly affected by the new holder concept.

events are referred to as recoil events in the CaWO₄ sticks. To a certain extent they can be separated from events in the bulk of the crystal by pulse-shape discrimination. To achieve this, for both, for electron recoils in the bulk and for electron recoils in the sticks a phonon template is generated and fitted to the full data set. The so-called relative root-mean-square⁷ (rms) difference

$$R_{\text{rel}} = \frac{r_{\text{bulk}} - r_{\text{stick}}}{r_{\text{bulk}} + r_{\text{stick}}} \quad (3.27)$$

individually calculated for every event with the rms of both fits r_{bulk} (for the bulk template) and r_{stick} (for the stick template) is a good parameter to quantify the pulse shape differences.

The two classes of events can be well discriminated as shown in figure 3.26 where R_{rel} is plotted against the phonon energy (energy scale of bulk events). For illustration, events which are clearly identified as events in the CaWO₄ sticks by pulse-shape discrimination on a confidence level of $> 3\sigma$ are plotted in a light yield (LY) plot in figure 3.27. Therein, the LY of electron recoils in the bulk of the crystal are normalized to 1. Besides electron/ γ events in the sticks at $LY \sim 20 - 30$ an additional class of events arises at $LY \sim 4$. The signals originate from a ¹⁴⁷Sm α source installed in the direct line-of-sight to the bottom CaWO₄ stick (see figure 3.22). The ¹⁴⁷Sm source provides a continuous α spectrum up to the full energy of 2233 keV [68] which allows to determine the energy scale of the stick events⁸ and quantify

⁷The root-mean-squared value describes the deviation of an acquired pulse from the fitted template and is explained in more detail in chapter 3.2.1.

⁸The energy scale of particle events in the CaWO₄ sticks was set by the endpoint of the continuous α spectrum of a ¹⁴⁷Sm source. To derive the energy scale of electron-recoil events in the sticks the phonon-anti-quenching effect (see section 3.2.2) has to be included. Thereby a similar behaviour was assumed for events in

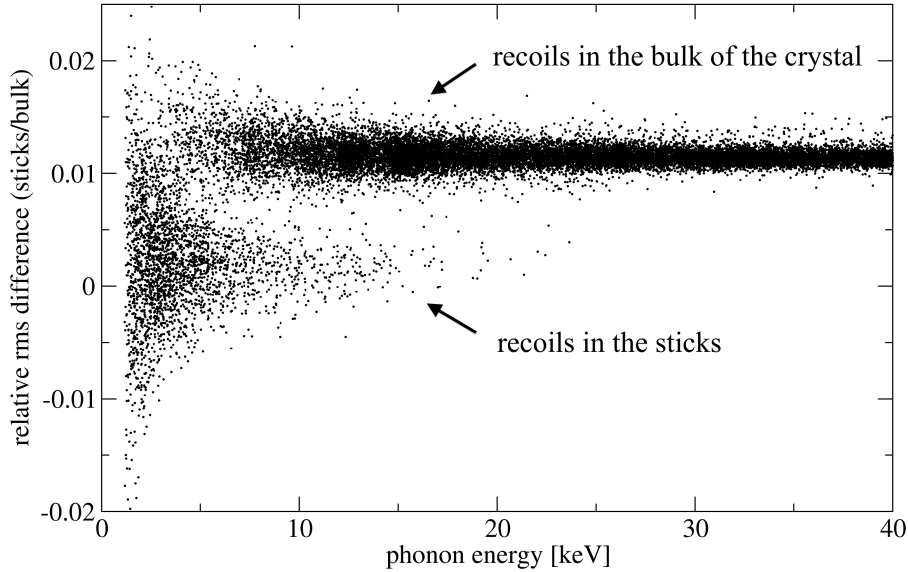


Figure 3.26: Relative root-mean-square (rms) difference R_{rel} (see equation 3.27) of two standard-event fits with a template from the e^-/γ -band of the CaWO_4 sticks holding the crystal and a template from the e^-/γ -band of the crystal's bulk. Clearly two bands arise as the pulse shape of the stick events (lower band) is different compared to that of bulk events (upper band).

the energy-degradation effect through the interface of the sticks to the CaWO_4 target crystal (so-called **phonon quenching**). The phonon Quenching Factor (pQF) which quantifies the reduction of the pulse height of stick events compared to bulk events of the same energy can be determined as $pQF_{\text{sticks}} = 96 \pm 6$. Dangerous nuclear recoils at the surface of the CaWO_4 sticks which are in the energy range of ~ 100 keV (discussed in detail in chapter 2.4.2) are thus far below the typical threshold of CRESST detectors ($E_{\text{th}} \gtrsim 10$ keV) and do not constitute a problem. The LY projection of the events clearly identified as stick events by pulse-shape discrimination are shown in figure 3.28. The distributions of the α and electron events are fitted by Gaussians. The center of the α contributions is found at a LY of $LY_{\alpha} = 4.16$ with a $1\text{-}\sigma$ width of $\sigma_{\alpha} = 0.43$. The nuclear recoil bands of the target crystal are thus separated by $\sim 9.4\sigma$ and no leakage therein is expected. For the electron recoils in the sticks two distinct distributions are visible, one at a mean of $LY_{e,\text{bottom}} = 19.32$ corresponding to events in the bottom stick and one at $LY_{e,\text{side}} = 27.24$ corresponding to events in the side sticks, both distributions have a width of $\sigma_e = 2.49$. Again no leakage is expected to the region of interest due to a 7.7σ separation from the nuclear-recoil bands ($LY \lesssim 0.1$) in the bulk of the crystal. As expected the pQF of the bottom stick is lower due to the tighter contact to the target crystal (the total weight of the target crystal rests onto the bottom stick). This is consistent with the fact that the energy spectrum of the bottom stick extends to higher energies ($E_{\text{max}} \approx 2000$ keV) compared to the one of the side sticks ($E_{\text{max}} \approx 2500$ keV). As the energy scale was calibrated with the α source at the bottom stick the pQF of the side sticks is even higher.

the bulk crystal and for events in the sticks.

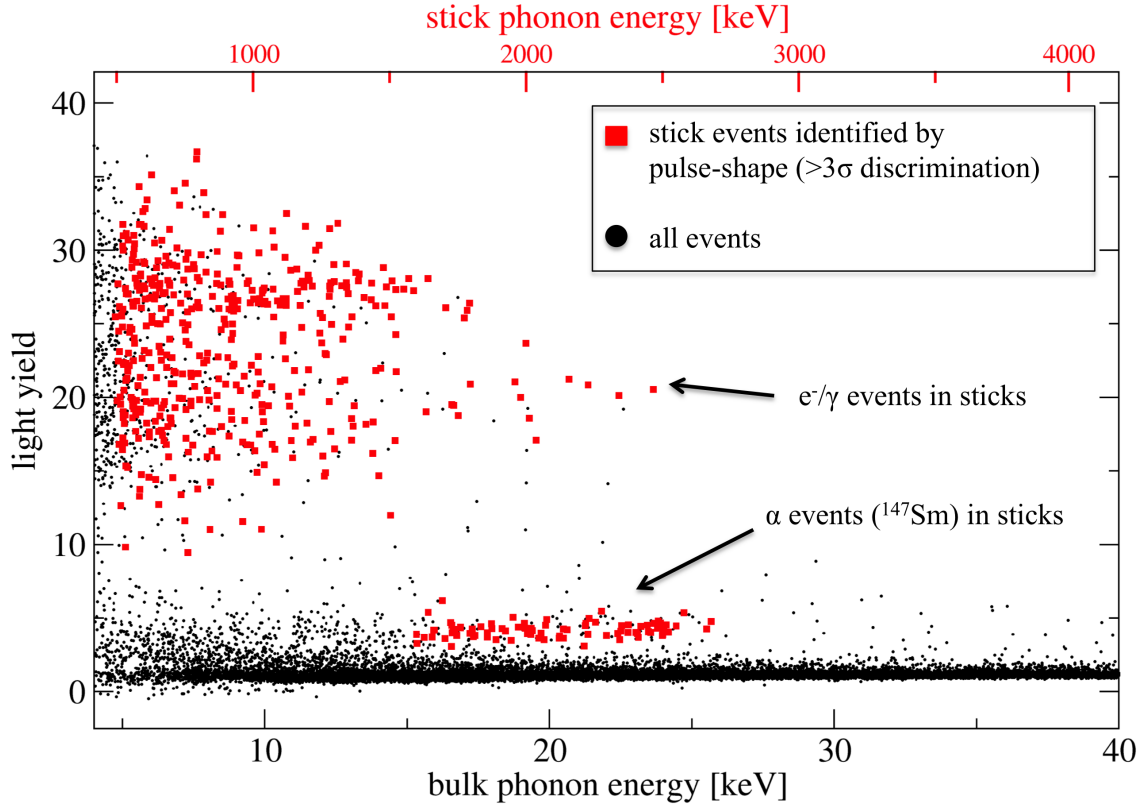


Figure 3.27: LY plot of the low-energy region of run326. Electron-recoil events in the bulk of the CaWO_4 crystal have been normalized to $LY = 1$. The red squares indicate events which are clearly ($\gtrsim 3\sigma$ discrimination) identified as events that occurred in the CaWO_4 sticks which hold the crystal. This is possible for electron recoil events down to 5 keV and for α events down to 15 keV. In order to calibrate the phonon energy of events in the CaWO_4 sticks, a ^{147}Sm source has been present at the bottom stick which provides a continuous α spectrum up to an energy of 2233 keV. The endpoint of this distribution visible at a LY of ~ 4.16 has been used to set the energy scale (top axis) of electron-recoil events in the CaWO_4 sticks (corrected for the phonon-anti-quenching effect, see chapter 3.2.2). The phonon signal of these events is highly degraded by a factor of $pQF_{sticks} = 96 \pm 6$ compared to events in the bulk CaWO_4 crystal.

In conclusion, phonon events occurring in the CaWO_4 sticks which are in point-like contact with the bulk CaWO_4 crystals are highly quenched ($pQF_{sticks} \sim 100$) and can be well separated from bulk events in case of α 's and γ 's by the higher LY. Dangerous nuclear recoils are not present in the energy range $\gtrsim 1000$ keV. Hence no background from events occurring in the CaWO_4 sticks is expected in the region-of-interest (ROI) for Dark Matter search (typically 12-40 keV).

Sensitivity for Dark Matter Search: The background contamination of the nuclear-recoil bands in the ROI for Dark Matter search is a crucial issue regarding the suitability of a new CRESST detector design. Dangerous backgrounds from nuclear recoils of surface α

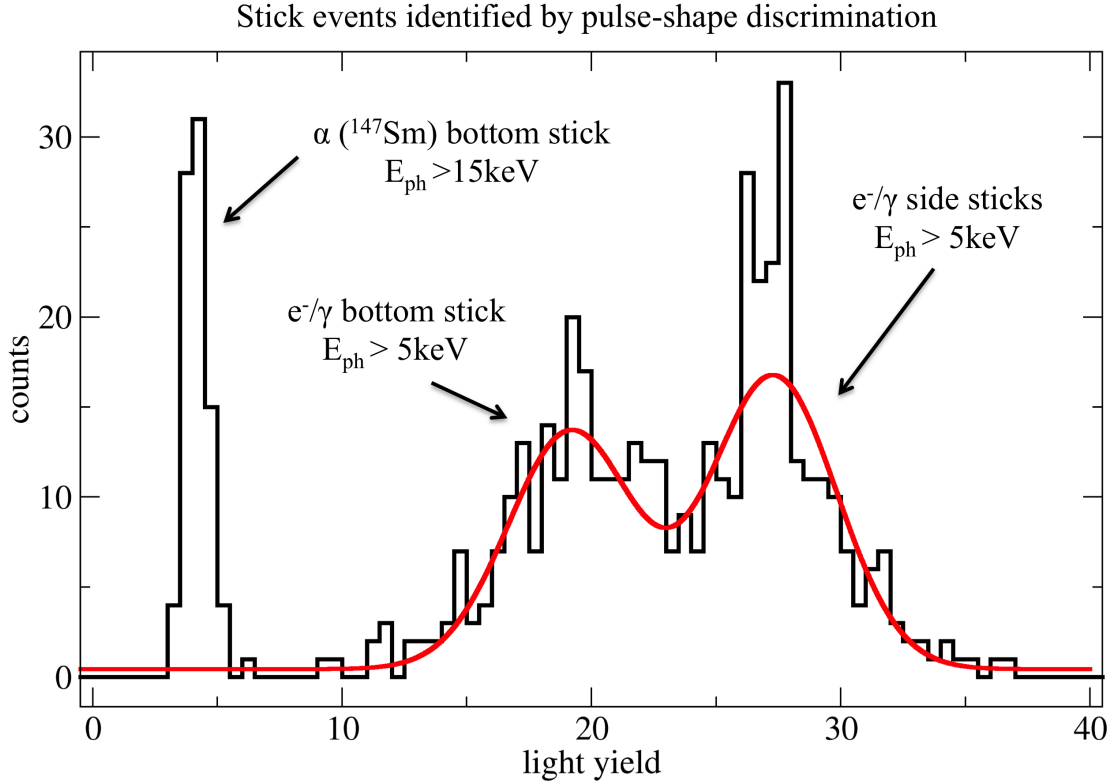


Figure 3.28: Histogram of the events which are clearly identified as events in the CaWO_4 sticks: α events from the ^{147}Sm source at a LY of $LY_\alpha = 4.16$ and electron events in the bottom ($LY_{e^-} = 19.32$) and side sticks ($LY_{e^-} = 27.24$). All contributions are far off ($> 7\sigma$) the nuclear recoil bands of the target crystal (at $LY \lesssim 0.1$).

decays (e.g. ^{206}Pb) are shifted out of the ROI due to the additional light produced by the corresponding α particle on the surfaces of the fully-scintillating detector holder. However, there have been concerns that relaxations of mechanical stress on the stick-crystal interface could cause phonon-only events (also called no-light events or dark counts) which would leak into the ROI. This was reported in an early stage of the CRESST experiment [88] where target crystals were held by sapphire spheres. These parasitic events extended to energies well above 100 keV and had a tendency to cluster in the time domain. The main reason for these stress relaxations was supposed to be the strong force which was applied to the crystals by a very tight clamping. The design proposed in this thesis instead uses the well-established flexible bronze clamps of the standard CRESST design to hold the CaWO_4 crystal and to compensate mechanical tensions e.g. due to temperature changes.

In both experimental runs performed with the crystal Wilhelm in the test cryostat at Gran Sasso a possible presence of such phonon-only events has been extensively studied. For kinematic reasons background-neutron events are visible mainly as oxygen recoils and reach energies of ~ 500 keV [25]. Thus the nuclear recoil events observed in experiments in the test cryostat should largely be consistent with oxygen scatters. As described in chapter 3.2.4 the acceptance bands for the individual recoiling nuclei can be calculated by using the corresponding QFs and the width of the electron recoil band. The LY plot of the total data set

of run326 is shown in figure 3.29 (top). Three events are observed at low LY which are not consistent with O scatters but with no-light events. A further study shows that these events occur preferably in unstable periods in which the setup is, e.g., mechanically disturbed from the outside. This has been tested by a more restrictive stability cut (see chapter 3.2) which accepts events within only $\pm 1\sigma$ around the mean of the measured control-pulse height instead of $\pm 3\sigma$ for the standard stability cut. Events which pass the rms cut (correct pulse shape) which, however, do not pass the stricter stability cut are shown in a LY plot in figure 3.29 (bottom). The events at low LY which are not consistent with neutron background show up preferably in this unstable period.

Furthermore, after dismounting the detector module damages of the crystal's (roughened) surface have been observed at the positions where the CaWO₄ sticks touched. A picture of the damaged area is shown in figure 3.30. Hence the CaWO₄ sticks could damage the crystal's surface during unstable periods in such a way that the resulting micro-fractures cause high-frequency phonons which in turn induce pulses similar to particle events (dark counts). To avoid damages of the crystal, for run328 all surfaces which touch the CaWO₄ sticks as well as the spherical tips of the sticks were polished. In this way, micro structures on the crystal's surface which could possibly be destroyed by mechanical disturbances are avoided. The results of run328 are presented in figure 3.31. Within an exposure of 1.60 kg-days (standard stability cut) which is comparable to that of run326 **no indications for no-light events were observed**. All events in the nuclear recoil bands are in perfect agreement with neutron-induced oxygen events.

A neutron rate of $13.1 \pm 2.8/\text{kg-days}$ has been observed for events above the discrimination threshold in the oxygen band⁹.

3.5.5 Light Output and Resolution

For the measurements with the block-shaped crystal Wilhelm in run326 and run328 the light output and resolution of the light channel has been determined according to the analysis method presented in chapter 3.3.2. The fraction of the deposited energy detected in the light detector was 1.62% in run326 where 5 sides were roughened and 1.58% in run328 where only the side facing the light detector was roughened. Hence no significant change in the light output is observed for the block-shaped crystal Wilhelm. The additional roughening seems to have less influence on the light output compared to when roughening the lateral surface of a cylindrically shaped CaWO₄ crystal (see chapter 3.3.2). Nevertheless, the block-shaped crystal design increases the fraction of light detected in a CRESSST detector module (at low temperatures) by $\sim 48\%$ compared to a cylindrical design (both crystal were roughened on one side). Instead, room-temperature measurements showed a more similar light output L compared to the reference crystal Boris (Rudolph VI: $L = 99\%$, Wilhelm: $L = 86\%$ [52]). This observation as well as similar growth conditions suggest that the properties of both crystals are comparable.

The resolutions of the electron-recoil band of both measurements parametrized according to equation 3.4 are illustrated in figure 3.32. The corresponding best fit values are listed in table 3.3 in chapter 3.6. The ratio of the parameter S_1 of both measurements is consistent with the determination of the light output using the ⁵⁵Fe source. The parameter S_2 is a factor of ~ 4 smaller for run328 which shows - similar to a cylindrically shaped crystal - that roughened

⁹In this case events are accepted as neutrons if they lie inside the 2σ acceptance bound of the oxygen-recoil band. The lower threshold is defined such that one leakage event from the e^-/γ band is expected.

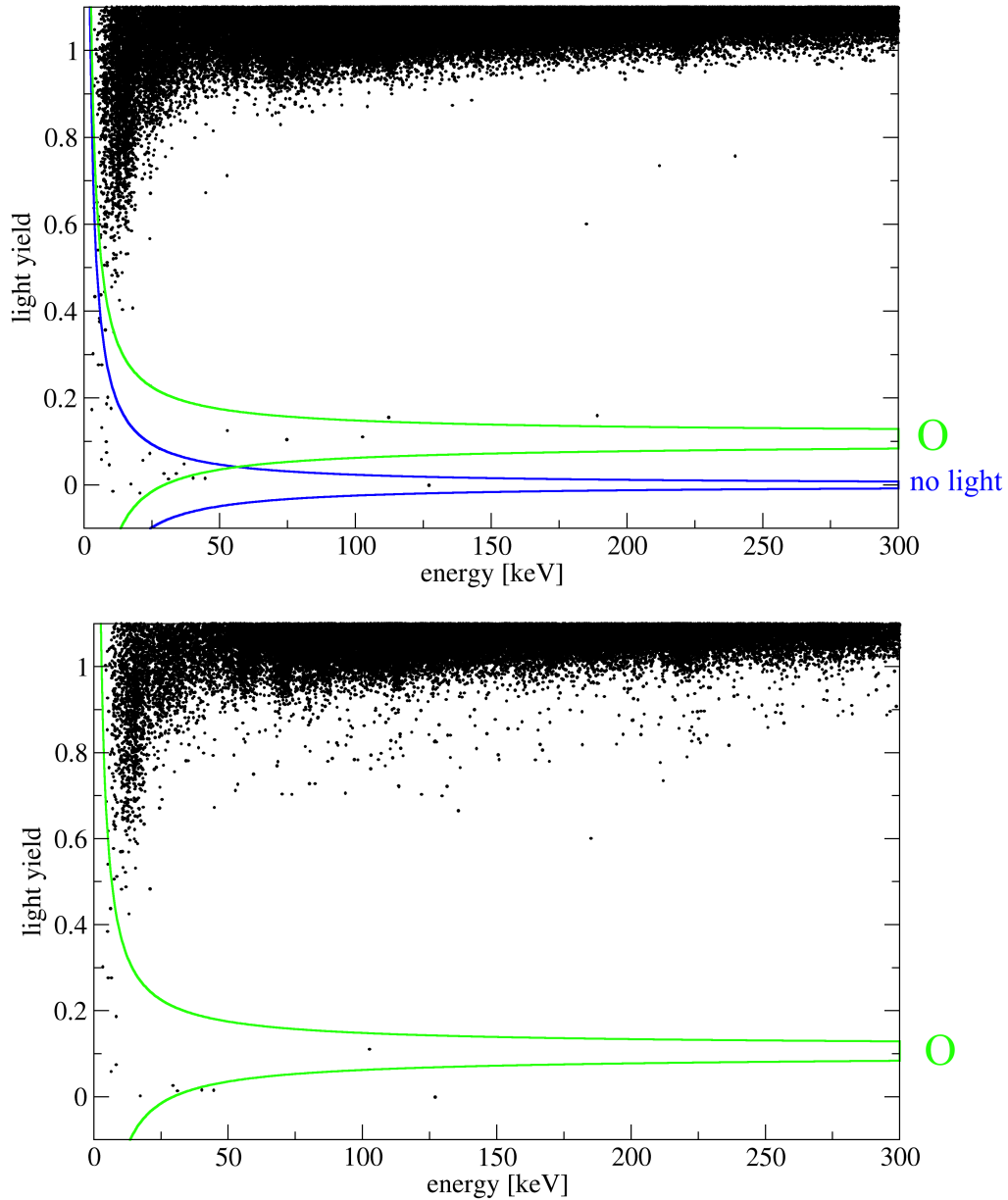


Figure 3.29: Illustration of the data acquired during run326. Top: LY plot of the total data set with the standard stability cut (exposure 1.82 kg.days). For kinematic reasons, background-neutron events are mainly visible in the oxygen band of which the 2σ acceptance bounds are depicted in green at a LY of ~ 0.1 . In addition, the 2σ acceptance bounds for no-light events are shown (blue). There are indications for events which are not consistent with neutron-induced oxygen scatters. Bottom: LY plot of events which do not pass a stricter stability cut (see text). This period of unstable conditions corresponds to an exposure of 0.78 kg.days. The events of the considered period occur during unstable periods (e.g. caused by mechanical disturbances in the surrounding of the cryostat) in which, however, the detector performance is still sufficient to analyse pulses (sufficient rms value, see text). Events which are not consistent with neutrons show up preferably in this data set. The possible source of such no-light events is discussed in the main text.

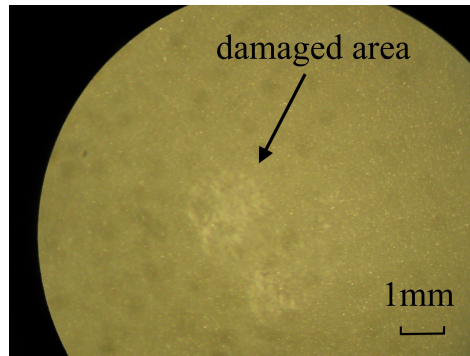


Figure 3.30: Picture (taken with a microscope) of the crystal surface of Wilhelm after run326 in the test cryostat at Gran Sasso. The position where one of the CaWO_4 side sticks touched is marked. It can be seen that the crystal surface at this area is damaged.

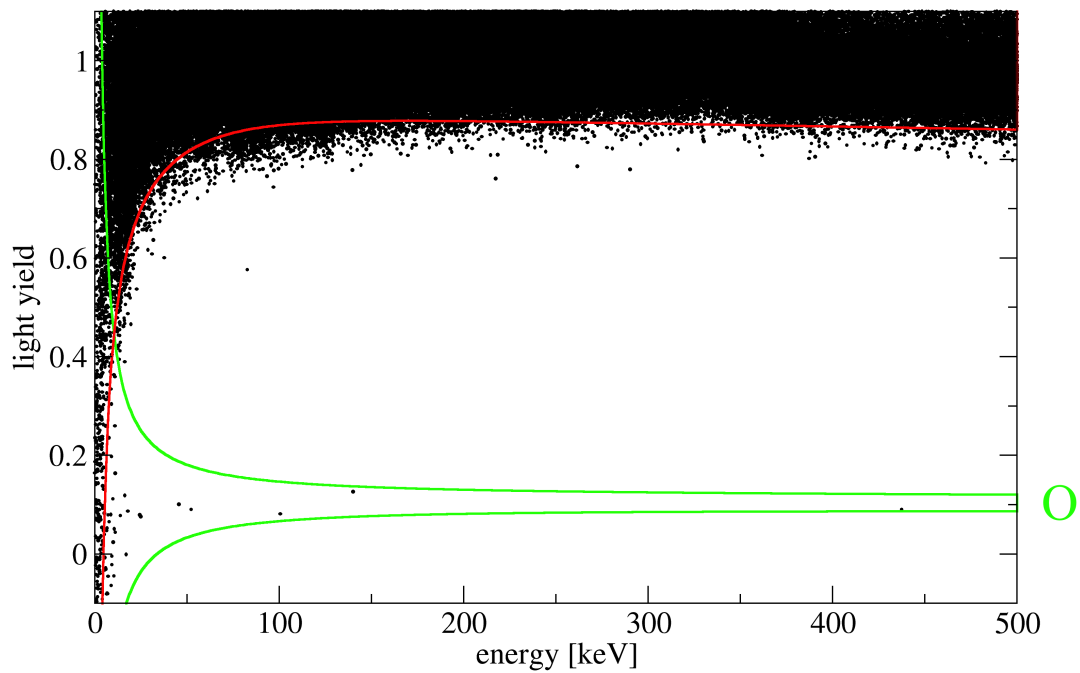


Figure 3.31: LY plot of the low-energy events acquired during run328 in the test cryostat at Gran Sasso. In red (green) the 2σ acceptance bounds of the e^-/γ (oxygen) recoil band are plotted. The observed 21 nuclear recoil events above the discrimination threshold (defined such that one leakage event from the electron-recoil band is expected) and inside the 2σ acceptance bounds for O are in perfect agreement with (background-) neutron induced oxygen recoils. In the total exposure of 1.60 kg-days no indications for no-light events are found.

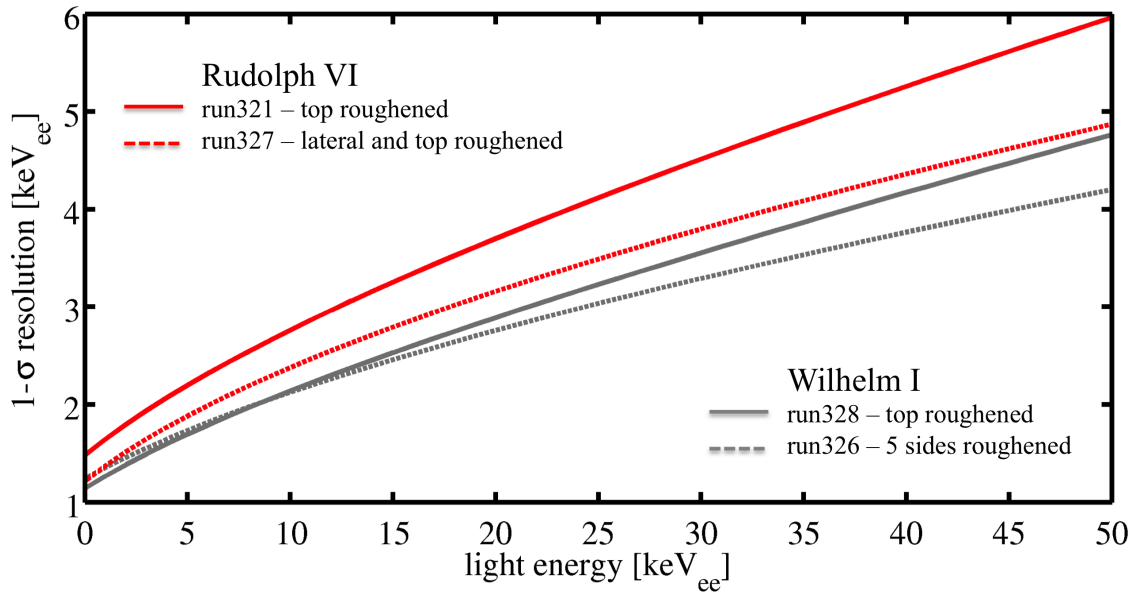


Figure 3.32: Comparison of the 1σ resolutions of the electron-recoil band of all measurements presented in chapter 3. The additional roughening of the block-shaped crystal Wilhelm hardly influences the light output of the crystal which results in a comparable resolution at energies smaller than $\sim 15 \text{ keV}_{ee}$. At higher energies, reduced position dependencies due to additional roughening of the surfaces improve the resolution in run 326. Over the entire energy range the resolution of the block-shaped crystal is better compared to the cylindrically-shaped crystal Rudolph VI. Only at very small light energies (typically $\lesssim 3 \text{ keV}_{ee}$) the baseline which depends on the measurement conditions becomes the dominant contribution (see figure 3.12).

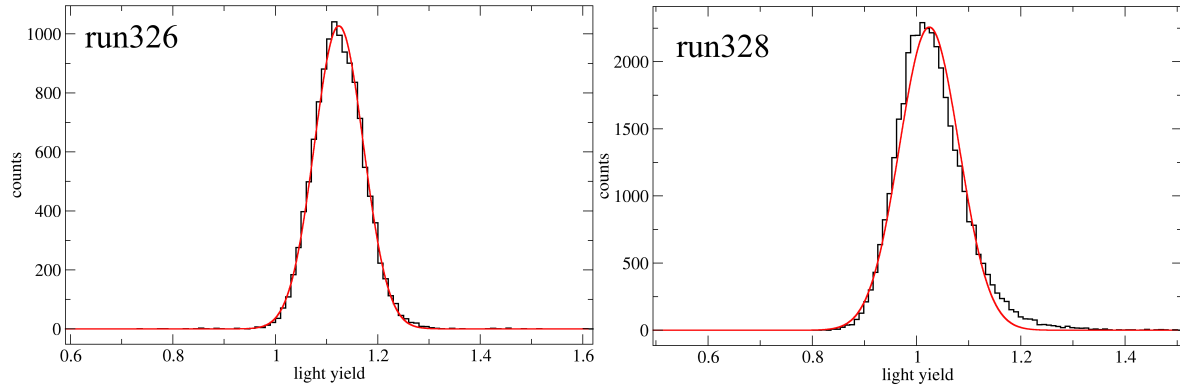


Figure 3.33: Gaussian fits to the LY distribution of the ^{212}Pb gamma peak at $E_r = 238.6$ keV. In run328 in which only the side of the TUM-grown crystal Wilhelm facing the light detector was roughened, position dependencies occurred. This results in an asymmetric LY distribution. In run326 in which five sides of the crystal were roughened, the electron recoil band is in good agreement with a Gaussian. For the block-shaped crystal, the asymmetry in the LY distribution is less pronounced than it is for the cylindrically shaped crystal investigated (see figure 3.13).

side surfaces reduce the position dependencies of the light collection.

As similar crystal quality is assumed for both crystals (Rudolph VI and Wilhelm) the results suggest that a block-shaped crystal with five sides roughened is the most promising design in terms of light output and resolution.

The uniformity of the light output of CaWO_4 crystals is crucial for the performance of CRESST detectors. Position dependencies in the light emission lead to a deviation of the Gaussian shape of the recoil bands. To study the influence of roughening concerning the gaussianity of the electron-recoil band (see chapter 3.3.2) the LY distribution of the ^{212}Pb γ peak at $E_r = 238.6$ keV has been studied in the data of run326 and run328. A tail to higher light yield (LY) can be observed in run328 where only one side was roughened but less pronounced compared to the cylindrically shaped crystal Rudolph VI (compare figures 3.13 and 3.33). This matches Monte-Carlo simulations [52] which suggest that cylindrically shaped crystals have higher position dependencies. By roughening the side surfaces of the crystal as done in run326, the LY distribution is in good agreement with a Gaussian.

3.6 Radiopurity of Self Grown Crystals

To study the radiopurity of CaWO_4 crystals in the test cryostat at Gran Sasso the best choice is to determine the α -particle interactions in the crystal. Unlike the γ background which in this setup is dominated by external radiation the α -background is mainly intrinsic and thus a good measure for the internal contamination. Over the entire energy range of a CRESST detector module ($\gtrsim 20$ keV) α events can be unambiguously separated from electron recoil events due to light quenching ($QF_\alpha \sim 0.22$).

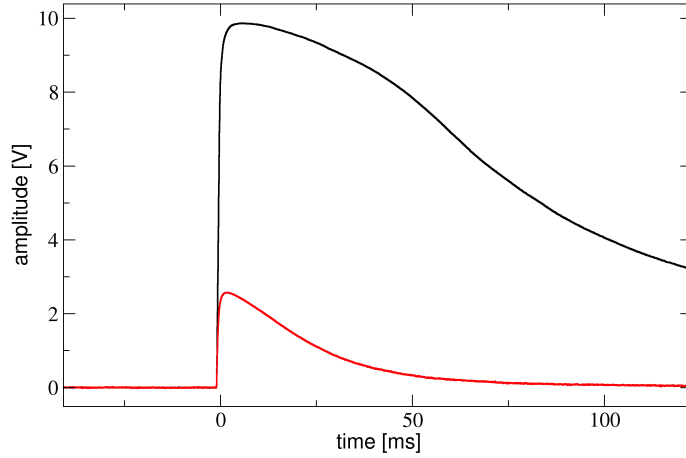


Figure 3.34: Phonon (black) and light (red) signal of a typical α -particle event with a recoil energy of ~ 5 MeV. The sample length of the data acquisition is too short to record the part (of the falling flank) of the phonon pulse where the response of the detector is linear. To use only the linear part of the pulses the truncation limit of the standard-event fit is typically ~ 1 V which corresponds to an energy deposition of ~ 100 keV. For the α pulses a higher truncation limit in a range in which the detector response is not strictly linear must be chosen, in this particular case ~ 5.5 V. The resulting non-linearity is compensated by calibration (see main text).

3.6.1 α Analysis

In addition to the data analysis of cryodetectors described in detail in chapter 3.2, there are several peculiarities concerning the analysis of α -particle interactions. The main difficulty is the determination of the pulse height of α events in the phonon channel as pulses strongly saturate which means that the range in which the response of the detector is linear ($E_r \leq 100$ keV) is usually by far exceeded. In addition, the sample length of the data acquisition in most cases is too short to record the part (of the falling flank) of the pulse in which the response of the detector is linear (see figure 3.34). Therefore, a higher truncation limit of $E_r \sim 500$ keV) has to be chosen for the standard-event fit (see chapter 3.2). The emerging non-linearity in the pulse-height spectrum has to be compensated by calibration.

In the following, the data of run326 acquired at the CRESST test cryostat at Gran Sasso is used exemplarily for the crystals produced in the crystal laboratory of the TUM [73]. The decay constant of the thermal component of the phonon pulses ($\tau_t = 86.4$) is a factor of ~ 1.5 smaller due to a stronger thermal coupling compared to other experimental runs (see table 3.3). This run is most suited for a detailed α analysis since a larger part of the pulse is recorded within the available sample length. The phonon channel is calibrated by gamma lines from gamma sources (^{57}Co) and by background γ -lines (see table 3.1). In contrast to the standard analysis, the calibration was not performed with test pulses (see chapter 3.2) since this heater pulses are commonly usable only up to energies of ~ 1 MeV. With the help of γ -calibration lines the phonon channel can be calibrated up to energies of $E_r \sim 2.6$ MeV. The calibration points can be fitted by a polynomial (in this case a 2nd order polynomial). In a first step, the effect of phonon-anti-quenching (see chapter 3.2.1) is corrected and the

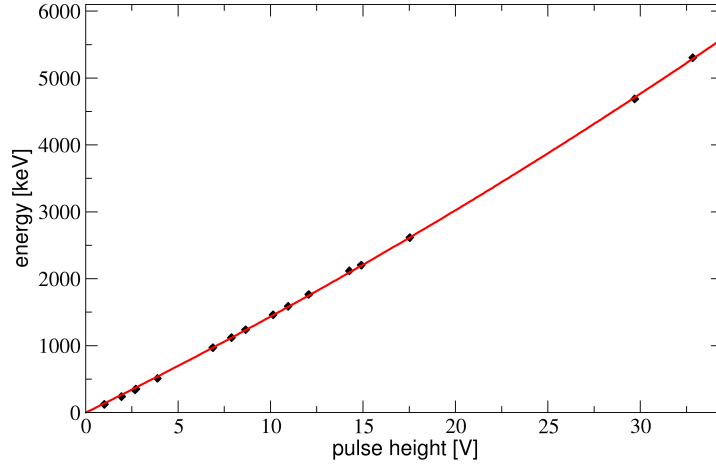


Figure 3.35: Calibration curve (2nd-order polynomial) of the phonon channel in run326. The gamma lines used for calibration are listed in table 3.1. The two lines above $E_r = 4000$ keV correspond to the identified α lines of ^{230}Th ($E_\alpha = 4687$ keV) and ^{210}Po ($E_\alpha = 5304$ keV). The effect of phonon-anti-quenching (see chapter 3.2) has been corrected.

polynomial is extrapolated to the high-energy α region ($E_r = 3 - 10$ MeV). Thereby, the energy scale is roughly set which allows an identification of the prominent α lines. In run326 the α lines of ^{230}Th ($E_\alpha = 4687$ keV) and ^{210}Po ($E_\alpha = 5304$ keV) are identified and are also used as calibration points. In figure 3.35 the calibration curve (2nd order polynomial) including all gamma lines and the two prominent α lines are shown. The gamma and α region are nicely described by the polynomial which demonstrates also the large dynamic range of CRESST detectors (from ~ 1 keV up to ~ 10 MeV).

In figure 3.36 a scatter plot of the full data set of run326 is presented. The phonon channel is calibrated with the method described above while the light channel is calibrated by the standard method using test pulses as described in chapter 3.2. For high phonon energies $E_r > 3000$ keV the ratio of light to phonon energy (=LY) remains roughly constant at the Quenching Factor (QF) expected for α events ($QF_\alpha \sim 0.2$). This demonstrates that the calibration of the phonon and the light channel is correct and proves the proper identification of the α lines.

Once clearly identified the activity of an individual α line A_α (or the total α activity) can be calculated by the following formula:

$$A_\alpha = \frac{N}{m \cdot t_{\text{live}}} \quad (3.28)$$

where N is the number of α counts in the individual peak at the 2σ C.L. (or total number of α counts), m is the mass of the crystal and t_{live} is the live-time of the measurement (see chapter 3.2.3).

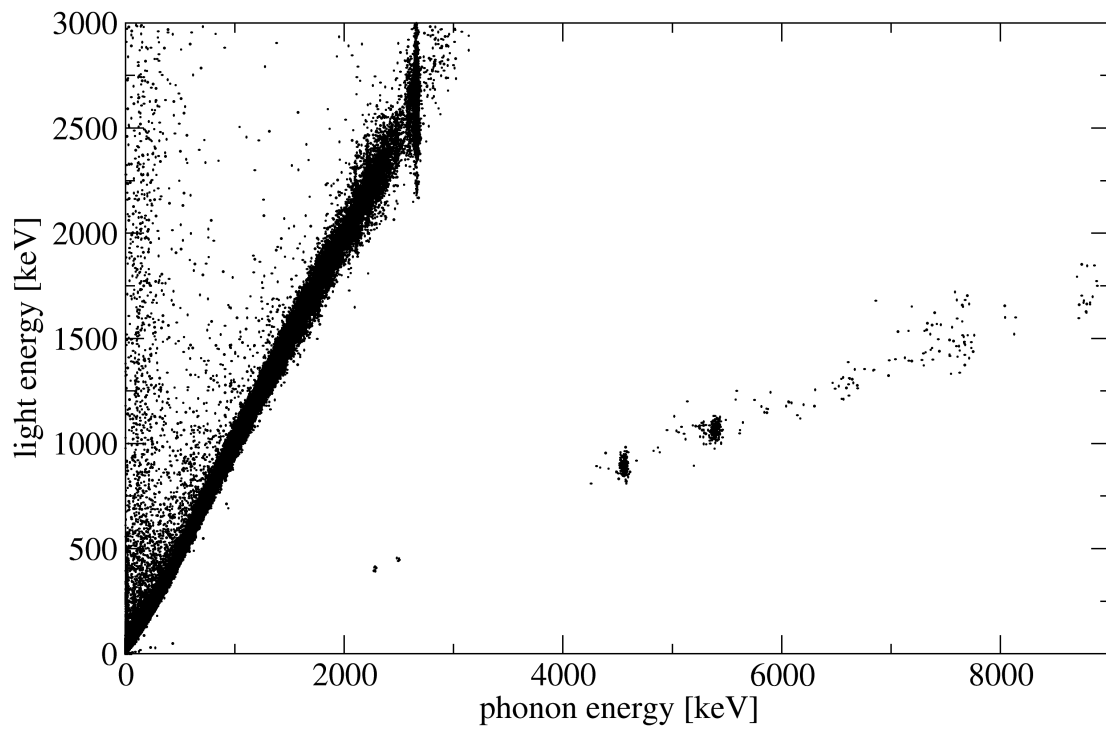


Figure 3.36: Scatter plot of the crystal Wilhelm operated in run326 at the test cryostat at Gran Sasso with a total exposure of 1.82 kg-days (after cuts). The electron recoil band and the α band can be clearly separated due to light quenching. The α region in the MeV regime is nicely described by a constant Quenching Factor $QF_{\alpha} \sim 0.2$.

γ emitter	energy [keV]	α emitter	total energy [keV]
^{57}Co	122.1	^{147}Sm	2233
^{212}Pb	238.6	^{180}W	2516
^{228}Ac	338.3	^{230}Th	4687
^{214}Pb	351.9	^{210}Th (ext)	5201
e^-e^+	510.7	^{210}Po (int)	5304
^{208}Tl	583.1		
^{228}Ac	969.1		
^{214}Bi	1120		
^{214}Bi	1238		
^{40}K	1461		
^{228}Ac	1588		
^{214}Bi	1765		
^{214}Bi	2118		
^{214}Bi	2204		
^{208}Tl	2615		

Table 3.1: Selected γ lines used for the calibration of the phonon detector (Wilhelm) for the analysis dedicated to the study of the α contamination. In addition, the dominant α -lines which are visible in the presented measurements in the test cryostat are listed. The most abundant crystal-intrinsic contributions of ^{230}Th and ^{210}Po (int) were used for calibration.

3.6.2 Results and Discussion

As described in chapter 3.6.1, run326 is particularly suited for an α analysis. For this run it is possible to disentangle individual α -lines while for all other measurements only the total α activity between 1.5 and 7 MeV can be derived. According to equation 3.28 the total activity is calculated for Rudolph VI (run321, run327) and for Wilhelm (run326, run328) and the results are presented in table 3.3. The mean value for the total α -activity A_α for Rudolph VI is $A_\alpha = 1.37 \pm 0.17$ mBq/kg and $A_\alpha = 2.93 \pm 0.27$ mBq/kg for Wilhelm. The higher value of the latter is most probably due to the fact that Wilhelm was grown in a later production cycle with the residual CaWO_4 melt of earlier growths (containing a higher concentration of impurities) remaining in the crucible [52].

Using the analysis method described in chapter 3.6.1, the individual α lines can be disentangled for run326. A spectrum of the α -region between 2 and 9 MeV is shown in figure 3.37. The activities of the contaminations which can be identified unambiguously (^{147}Sm , ^{180}W , ^{230}Th , ^{210}Po internal and external)¹⁰ are listed in table 3.2 for the TUM-grown CaWO_4 crystal Wilhelm and for selected commercial CaWO_4 crystals operated in the CRESST experiment [89]. The α -lines of ^{230}Th and ^{210}Po dominate the spectrum with a fraction of $\sim 31\%$ and $\sim 33\%$ of the total activity, respectively. Besides the main peak of internal ^{210}Po (int) decays, a minor contribution of surface ^{210}Po decays on the CaWO_4 and surfaces surrounding the detector (ext) where the energy of the recoiling ^{206}Pb nucleus (103 keV) is not detected in the phonon

¹⁰The intrinsic α activity due to ^{180}W decays are a good cross-check for the performed α analysis. With the half-life $T_{1/2} = (1.8 \pm 0.2) \cdot 10^{18}$ mBq/kg of ^{180}W (measured within the framework of CRESST [??]) the ^{180}W α -activity of CaWO_4 crystals (isotopic abundance 0.13%) can be calculated: $A_\alpha = 0.033$ mBq/kg. The activity determined herein is in nice agreement with the calculated value as well as with measurements of other CaWO_4 crystals (see table 3.2).

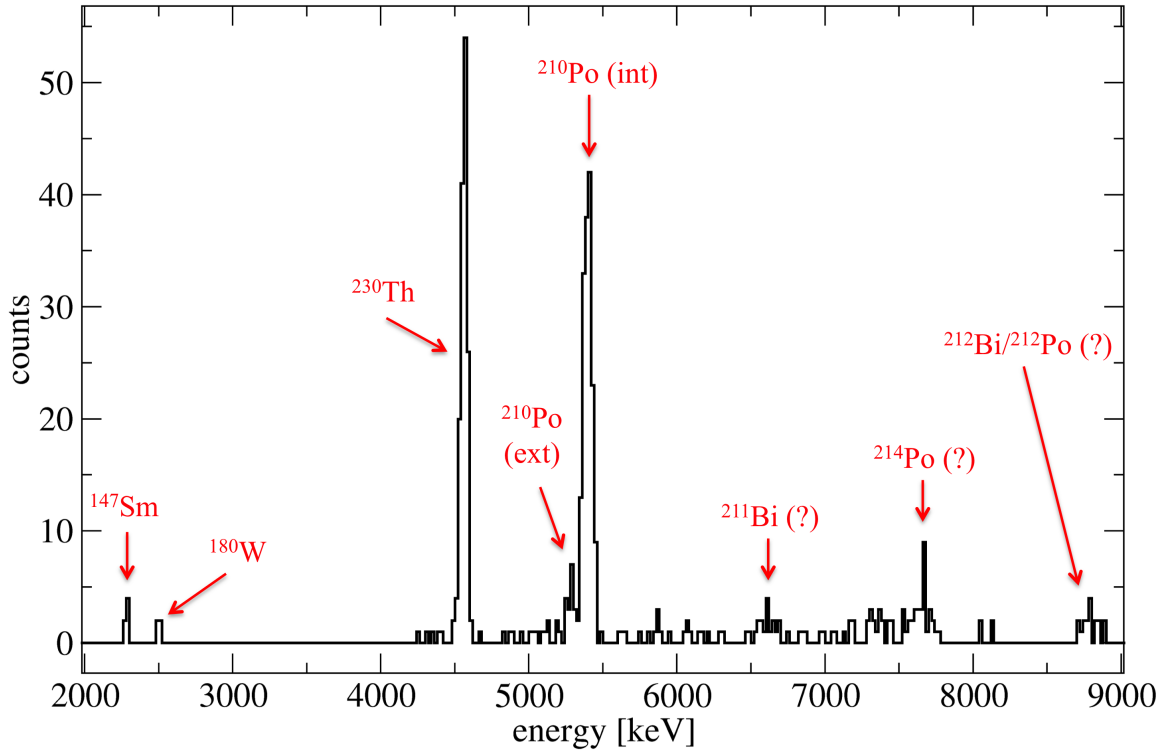


Figure 3.37: α spectrum of Wilhelm in run326 with a total exposure of 1.82 kg-days (after cuts). α decays of ^{230}Th ($E_\alpha=4687$ keV) and ^{210}Po ($E_\alpha=5304$ keV) completely dominate the spectrum which demonstrates that the ^{238}U chain is not in equilibrium (see text). External α decays of ^{210}Po where only the α particle and not the ^{206}Pb nucleus (103 keV) is detected show up in the spectrum. A contamination of ^{147}Sm ($E_\alpha=2233$ keV) and natural ^{180}W ($E_\alpha=2516$ keV) as well as indications for additional contributions of the ^{235}U and ^{232}Th decay chains are also visible. The individual activities are listed in table 3.2.

channel and only the α -particle is visible. ^{230}Th and ^{210}Po are part of the natural decay chain of ^{238}U which is illustrated in figure 3.38. Since the α -decays immediately following the decay of the long-lived ^{230}Th ($T_{1/2} = 7.54 \cdot 10^4$ a) do not show a significant contribution to the spectrum, the dominant ^{210}Po peak cannot be explained by the natural decay series of ^{238}U being in equilibrium. The decay chain must be broken. There are several possibilities to interpret this observation:

- It is very likely that the chain is already broken in the raw materials (CaCO_3 , WO_3) for the growth of CaWO_4 due to a prior chemical purification.
- If in the raw materials the ^{238}U -chain would be in equilibrium, however, Pb-nuclei (in this case ^{210}Pb) might preferably be integrated into the crystal lattice during the growth process.
- A contamination of ^{210}Po could be introduced during handling of the raw materials or the production process of the CaWO_4 crystals.

crystal		Daisy	Zora	Rita	Wilhelm
^{147}Sm	A_α [mBq/kg]	0.850 ± 0.011	0.17 ± 0.01	0.090 ± 0.003	0.038 ± 0.016
	counts	6288	192	674	6
^{180}W	A_α [mBq/kg]	0.031 ± 0.007	0.031 ± 0.01	0.031 ± 0.002	0.025 ± 0.013
	counts	229	58	232	4
^{230}Th	A_α [mBq/kg]	0.080 ± 0.003	5.83 ± 0.06	1.08 ± 0.01	0.95 ± 0.08
	counts	589	11022	8036	149
$^{210}\text{Po}(\text{int})$	A_α [mBq/kg]	0.109 ± 0.004	0.74 ± 0.02	2.506 ± 0.018	1.02 ± 0.08
	counts	809	1399	18 690	161
$^{210}\text{Po}(\text{ext})$	A_α [mBq/kg]	0.068 ± 0.003	-	0.094 ± 0.004	0.09 ± 0.02
	counts	504	-	698	16
total	A_α [mBq/kg]	2.38 ± 0.02	29.68 ± 0.06	10.21 ± 0.04	3.05 ± 0.26
	counts	17 589	237 245	76 138	480

Table 3.2: Activities of prominent α lines in different CaWO_4 crystals: Rita, Daisy [89] and Zora [82] from commercial suppliers and the crystal Wilhelm produced in the crystal lab at TUM. The α lines of Wilhelm have been derived by the data of run326 in the test cryostat at Gran Sasso.

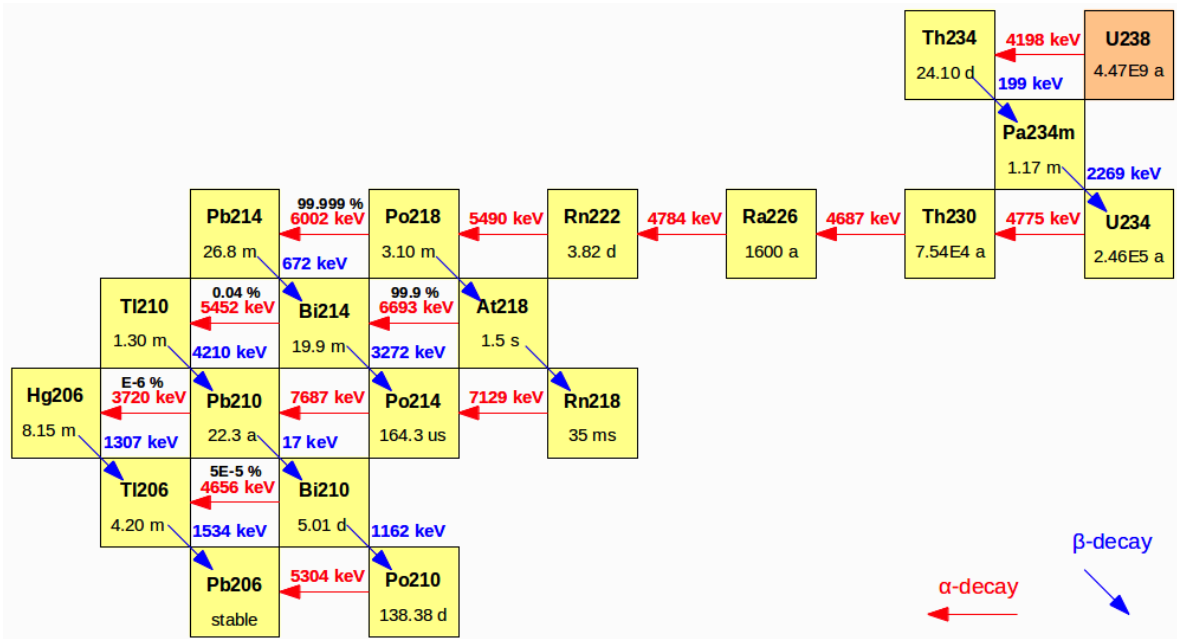


Figure 3.38: Decay chain of the mother nuclide ^{238}U (“uranium series”). Picture from [89]

- During production and storage of the raw materials (powder), ^{222}Rn implantation from air could play an important role and enhance the amount of ^{210}Pb significantly¹¹.

The measurement of the α activity of the crystal Wilhelm suggests that for the CaWO_4 crystals produced in the crystal lab of TUM a large fraction of the total activity ($\sim 65\%$) is concentrated on two single α -lines (^{230}Th and ^{210}Po decays). Therefore, e.g., improvements concerning radiopurity and Rn-prevention might significantly influence the amount of ^{210}Po and thus largely reduce the total activity of the crystals. Furthermore, it would be advantageous to reuse crystalline CaWO_4 material (from former growth processes) for crystal growth due to the segregation of impurities in every growth [52]. This is confirmed by the results of the total α activity of Rudolph VI which was grown in an earlier production cycle compared to Wilhelm.

Since several TUM-grown crystals are implemented in the CRESST setup (see chapter 2.5 and 3.7) and are likely to be operated for 1-2 years, the intrinsic α and β -contamination can be measured precisely and also subdominant α -lines might then be resolved. The influence of the raw-materials and the growth process on the individual contaminations can be studied in more detail. In particular, the rate dependence of ^{210}Po decays with time can be studied in a long CRESST run:

- The rate would be constant if the ^{210}Po is in equilibrium with ^{210}Pb .
- The rate would increase with the half-life of ^{210}Po ($T_{1/2} = 138.4$ d) if the contamination is induced by ^{222}Rn implantation (see also chapter 3.4) or ^{210}Pb .
- The rate would decrease with $T_{1/2} = 138.4$ d if the contamination is introduced by ^{210}Po itself.

3.7 Implementation of Prototype Detectors in the CRESST Setup

Two of the detector modules based on CaWO_4 sticks which have been designed, developed, successfully commissioned and implemented in the CRESST setup for the upcoming experimental Dark Matter run (run33) within this thesis. The results of the extensive studies which have been performed in terms of detector operation and performance (see chapter 3.5) has influenced the final design of the detector module which is described in the following:

- To avoid damages of the crystal surface at the interface with the CaWO_4 sticks which can cause phonon-only events and mimic particle-induced signals, the surface of the crystal as well as the spherical tips of the sticks were polished. It was shown in chapter 3.5.4 that no indications for such dangerous background events (possibly induced by mechanical disturbances) have been observed for polished crystal surfaces.
- However, the light resolution was reduced for the design with only one side roughened (run328). At high light energies ($\gtrsim 15 \text{ keV}_{ee}$) the resolution was worse due to position dependencies regarding the light emission (see figure 3.32). Those uncertainties were particularly visible in a deviation from gaussianity in the light yield (LY) for the electron-recoil band (see figure 3.33).

¹¹After being shipped to TUM the raw materials are constantly flushed with pure nitrogen gas. However, radon implantation from air could play a significant role before.





crystal		Rudolph VI (TUM-27)		Wilhelm (TUM-40)	
					
volume	$V[\text{mm}^3]$	$40 \times 20^2 \pi$		40x32x32	
mass	$m[\text{g}]$	305		246	
measurement		run321	run327	run328	run326
rough surfaces		top	top+lateral	top	5 sides
light output		1.09%	1.31%	1.58%	1.62%
resolution	$S_0[\text{keV}_{\text{ee}}^2]$	2.19(f)	1.47(f)	1.30(f)	1.54(f)
	$S_1[\text{keV}_{\text{ee}}]$	0.504	0.412	0.303	0.291
	S_2	$3.01 \cdot 10^{-3}$	$6.61 \cdot 10^{-4}$	$2.60 \cdot 10^{-3}$	$6.32 \cdot 10^{-4}$
position	$p_0[\text{keV}^{-1}]$	1.13	1.00	1.00	1.01
	$p_1[\text{keV}^{-2}]$	0(f)	$4.62 \cdot 10^{-5}$	$9.80 \cdot 10^{-5}$	$4.55 \cdot 10^{-5}$
	p_2	0.282	0.140	0.681	0.563
	$p_3[\text{keV}]$	267	6.61	7.19(f)	7.18
pulse shape	a_n/a_{tot}	-0.84	-0.82	-0.86	-0.81
	$\tau_t[\text{ms}]$	123.2	125.7	153.3	86.4
	$\tau_n[\text{ms}]$	25.5	22.7	26.8	17.6
	$\tau_{\text{film}}[\text{ms}]$	2.99	3.26	3.82	3.49
livetime	$t_{\text{measured}}[\text{h}]$	105.3	452.5	218.9	267.6
	$t_{\text{live}}[\text{h}]$	85.7	398.5	196.6	229.2
	$t_{\text{invalid}}[\text{h}]$	3.3	41.9	8.8	8.9
	$\epsilon_{\text{cuts}}[\%]$	21.6	22.2	13.3	13.6
	$\epsilon_{\text{stability}}[\%]$	21.2	3.0	5.0	6.6
	$t_{\text{final}}[\text{h}]$	50.9	269.1	154.6	177.6
exposure	$E[\text{kg-days}]$	0.65 ± 0.03	3.41 ± 0.35	1.60 ± 0.07	1.82 ± 0.07
α counts	N_α	74	420	389	480
α activity	$A_\alpha[\text{mBq/kg}]$	1.31 ± 0.10	1.42 ± 0.23	2.81 ± 0.28	3.05 ± 0.26

Table 3.3: Summary of physical and geometrical properties of the crystals Rudolph VI (TUM-27) and Wilhelm (TUM-40) in the measurement campaigns performed at the test crystal at Gran Sasso within this thesis. The parameters are explained in more detail in the main text in which also - if relevant for the analysis - uncertainties are discussed.

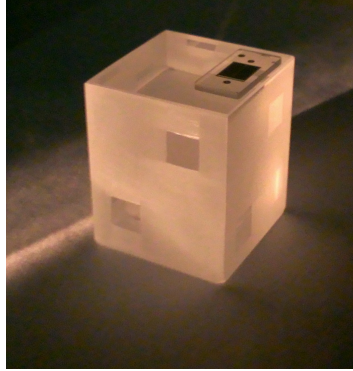


Figure 3.39: The crystal Wilhelm (TUM-40) in the final design state for the implementation in the CRESST setup for run33. The crystal has been roughened with a silicon-carbide powder (600 SiC [51]) on all surfaces except the one bearing the TES and the quadratic areas (7mm x 7mm) where the CaWO_4 sticks touch the crystal.

Hence for the final design only the quadratic areas around the positions where the sticks touch (7mm x 7mm) are polished. The remaining part of the side surfaces were roughened. A picture of the crystal Wilhelm in its final design state is shown in figure 3.39.

The measurements in the test cryostat at Gran Sasso showed that the newly developed detector design presented here fulfils all requirements for a CRESST detector module concerning light output, phonon properties, radiopurity and mechanical constraints for the installation in the CRESST setup. Furthermore, it provides a full veto against surface- α decays due to a fully scintillating detector housing (see chapter 3.5).

In addition to the extensively tested crystal Wilhelm (TUM-40) another CaWO_4 crystal of similar size and performance, called “Türkenlouis” (TUM-45) has been chosen for the second prototype detector. Both crystals were grown in the crystal laboratory of the TUM [73]. Table 3.4 summarizes their properties. Although radon-induced events can be fully rejected with this detector design the two modules were assembled in the recently installed clean room at Gran Sasso using the radon-filtered air (see chapter 2.5). The fully mounted modules are shown in figure 3.40. Equipped with a CRESST silicon-on-sapphire (SOS) light detector both prototype detectors can be treated like standard CRESST modules and were installed in the three-storied towers of the detector volume (see chapter 2.3).

At the moment of writing the cryostat is cooling down to its base temperature of ~ 5 mK and the transition-edge-sensors of the phonon detectors TUM-40 and TUM-45 as well as their corresponding light detectors (Michael and Oliver) already have reached their superconducting state. They will start taking data soon for a projected period of ~ 2 years.

crystal	Wilhelm (TUM-40)	Türkenlouis (TUM-45)
light output at 300K [compared to Boris]	84.0%	84.5%
detected light at mK [fraction of E_r]	1.62%	-
size [mm ³]	39.2x32.0x32.0	39.7x31.7x31.7
mass [g]	244.5	243.0
TES carrier [internal number]	WI-299/1	WI-426/1
transition temperatur T_C [mK]	20.2	17.3
total α activity [mBq/kg]	2.93 ± 0.35	-
light detector in run33	Michael	Oliver

Table 3.4: Properties and performance of the two prototype detectors which were installed in the CRESST setup of run33. The light output and the α -contamination of TUM-45 has not been measured at mK temperatures, but room-temperature measurements as well as comparable crystal-growth conditions and raw materials suggest a similar performance.

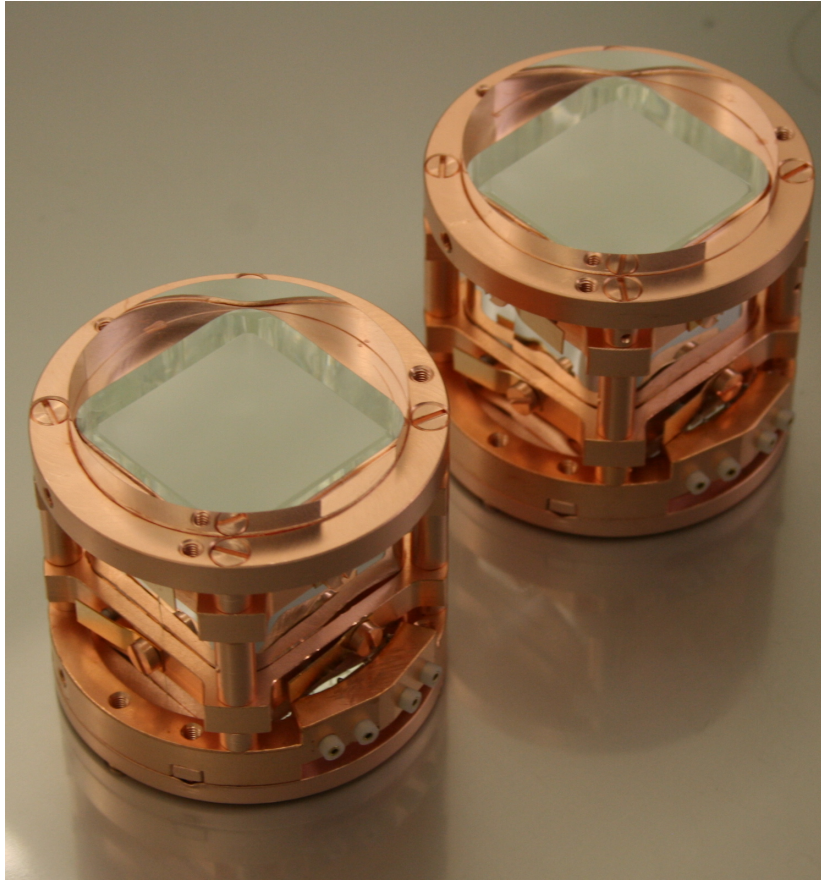


Figure 3.40: The two prototype modules based on CaWO_4 sticks containing the block-shaped crystals Wilhelm (TUM-40, right) and Türkenlouis (TUM-45, left) which were produced in the crystal laboratory of TUM [73]. The modules were equipped with light detectors and installed in the CRESST setup for the upcoming run33.

Chapter 4

Quenching Factor (QF) Measurements of CaWO₄

4.1 Definition of QFs and Relevance for the CRESST Experiment

The reduction of the relative light output for nuclear recoils compared to electron recoils in a given scintillator is referred to as (light) quenching. For CaWO₄ crystals used as detectors in the CRESST experiment this effect is observed for the intrinsic nuclei O, Ca and W as well as for particles interacting with the crystal from the outside (eg. α 's, ²⁰⁶Pb nuclei). Generally this quenching effect increases with the mass of the recoiling nucleus.

To describe this effect quantitatively the following parametrization is applied [27]. First of all, the electron recoil band is phenomenologically parametrized according to equation 3.3 in chapter 3.2.4 by

$$E_L = (p_0 \cdot E_r + p_1 \cdot E_r^2) \cdot \left(1 - p_2 \exp\left(-\frac{E_r}{p_3}\right)\right)$$

where E_r is the recoil energy in the phonon channel, E_L is the calibrated energy in the light channel (see chapter 3.2.1) and p_0 , p_1 , p_2 and p_3 are parameters determined by a maximum likelihood fit. This fit procedure which was developed and optimized within the CRESST collaboration is explained in detail in chapter 3.2.4. Commonly, CRESST data is illustrated in a so-called light-yield plot where the light yield

$$LY_\gamma(E_r) = \frac{E_L(E_r)}{E_r} = (p_0 + p_1 \cdot E_r) \cdot \underbrace{\left(1 - p_2 \exp\left(-\frac{E_r}{p_3}\right)\right)}_{\text{non-proportionality effect}} \quad (4.1)$$

is plotted versus the recoil energy E_r . A typical dataset is shown in figure 4.1 together with the 80% acceptance bounds (1.28-sigma) for the electron-recoil band. The corresponding fit results are presented in table 4.2 in chapter 4.8.2.

The Quenching Factor (QF) is defined as the light output of a nuclear recoil compared to an electron recoil of the same energy not accounting for the non-proportionality effect¹ in the

¹The exponential decrease of the relative light output of the electron-recoil band observed in a CaWO₄ crystal (in the CRESST collaboration) is referred to as non-proportionality effect. A qualitative explanation is given in chapter 4.2, however, the effect is not fully understood and varies between different CaWO₄ crystals [27].

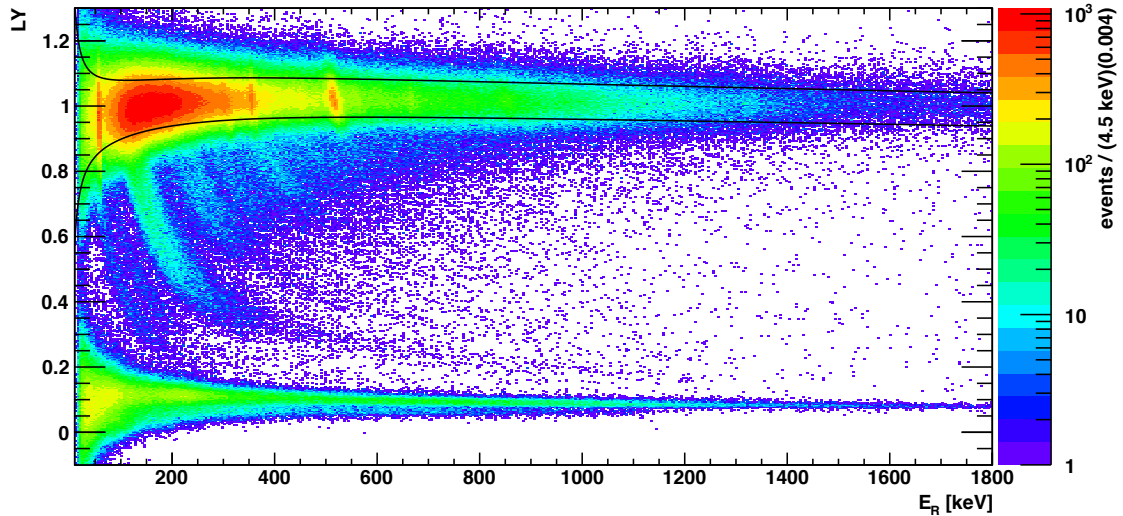


Figure 4.1: Two-dimensional histograms of the recoil energy-light yield (LY) plane of the data acquired during the Oct 2011 beamtime (50% of total data). The e^-/γ band is fitted by a maximum-likelihood fit (see chapter 3.2.4) following equation 4.1. The 80% acceptance bounds (1.28σ C.L.) of the electron-recoil band are depicted as full lines. At lower recoil energies, a decrease in light yield due to the non-proportionality effect is visible. At light yields of $\lesssim 0.2$ the nuclear-recoil bands arise. The curved bands in between are due to inelastic scattering on W (see chapter 4.7).

electron recoil band. This is illustrated in figure 4.2 and described by the following formula:

$$QF_x(E_r) = \frac{LY_x(E_r)}{LY_{\gamma,np}(E_r)} = \frac{LY_x(E_r)}{p_0 + p_1 \cdot E_r} \quad (4.2)$$

where $LY_x(E_r)$ is the mean of the light-yield contribution of the nuclear recoil band of the nucleus x , $LY_{\gamma,np}(E_r)$ the mean of the electron gamma band without considering the non-proportionality effect. This is the convention used in the CRESST collaboration [27] as the non-proportionality effect has so far not been observed for the nuclear recoil bands. This assumption, however, has to be proven in future dedicated experiments.

Precise knowledge of the quenching behaviour is of high relevance for the CRESST experiment:

- The reduced light output of nuclear recoils allows to discriminate the dominant electron/ γ background very efficiently (rejection power of up to $\sim 10^{-5}$).
- Neutron background which above the typical threshold of ≥ 5 keV is mainly visible as recoils on O can be discriminated from high-mass WIMP-induced nuclear recoils on W.
- The disentanglement of the nuclear-recoil band's composition (of O, Ca and W) especially at low energies ($\lesssim 100$ keV) is a prerequisite to exploit the full potential of the experiment, namely performing “WIMP-mass spectroscopy” in the future (see chapter 2.1).

An precise measurement of the QFs in the bulk material at the operational temperature of ~ 10 mK is mandatory for CRESST to reach its full potential as a multi-target experiment.

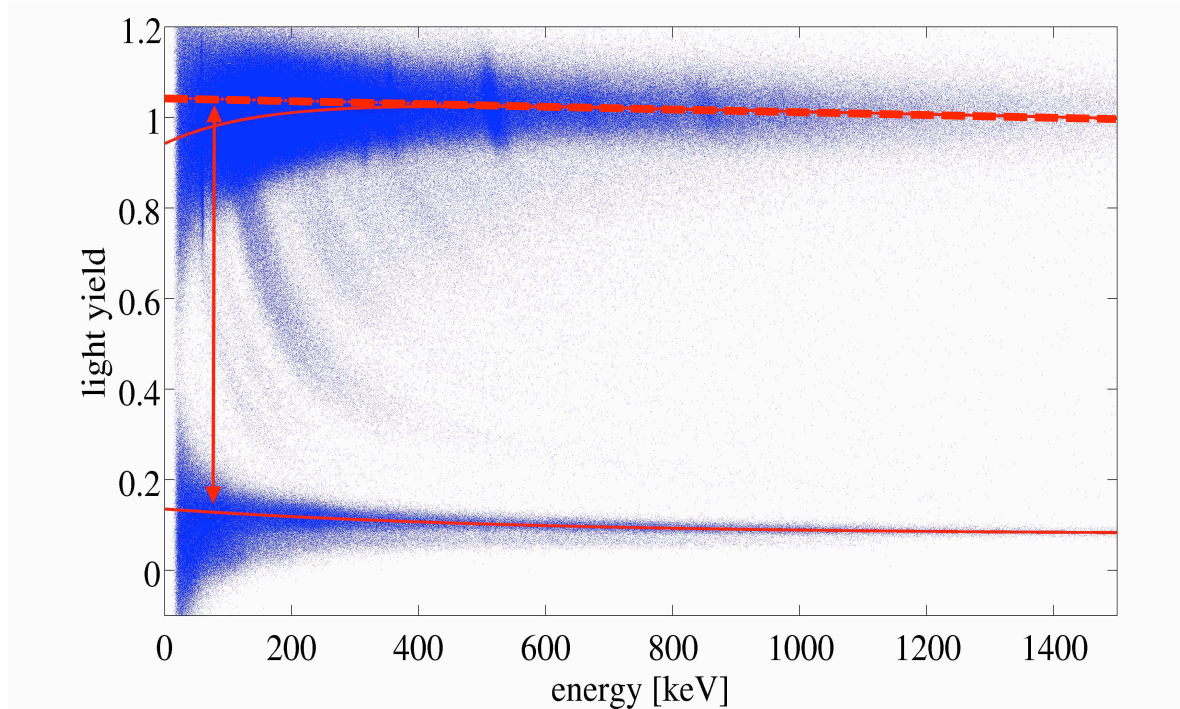


Figure 4.2: Definition of QFs illustrated in a typical light-yield plot: The mean of the electron-recoil band is indicated by a full line. The part of the parametrization which is not affected by the non-proportionality effect ($p_0 + p_1 \cdot E_r$) is shown by a dashed line. This effect is not completely understood and varies from crystal to crystal. The tilt of the electron recoil band (visible at higher energies) is supposed to be an effect of calibration. The mean of the light-yield distribution of the nuclear recoil bands (full line, here oxygen) relative to the dashed line is defined as the QF which is illustrated by a red arrow.

4.2 Phenomenological QF Model

Up to now, no theoretical model has been published which can fully explain the quenching mechanisms in inorganic scintillators as, e.g., CaWO_4 . Nevertheless, the long-standing approach of Birks [53] is widely used in physics to describe the scintillation processes in different kinds of scintillators phenomenologically. It is commonly known that the scintillation-light output of scintillating materials induced by highly ionizing particles (like ions) is lower compared to electrons of the same energy. This behaviour is usually quantified by Quenching Factors (QFs). For low stopping powers $\frac{dE}{dr}$ (as for electrons of energies $\gtrsim 100$ keV) the scintillation centers have neighbouring distances large enough that interactions between them can be neglected and, thus, the light output of electron recoils L_e per path length $\frac{dL_e}{dr}$ is proportional to the deposited energy E per path length r (stopping power) in the material:

$$\frac{dL_e}{dr} = S \frac{dE}{dr} \quad (4.3)$$

where S is a constant which accounts for the absolute scintillation efficiency [53]. On the other hand, highly ionizing particles with a high energy release such as heavy ions excite

most of the scintillation centers along their track. The scintillation-light output of heavy ions L_i saturates and is therefore proportional to the length of the track:

$$\frac{dL_i}{dr} = \text{const} \rightarrow L_i = A \cdot r \quad (4.4)$$

with A being a constant parameter which depends on the scintillating material and - as shown below - also to a certain extent on the kind of ionizing particle. The shorter the track length the higher the stopping power and thus typically the heavier the particle. The QF can thus be defined as

$$QF = \frac{L_i(E)}{L_e(E)} \quad (4.5)$$

and gets smaller for heavier particles².

Birks proposed a semi-empirical formula [53] to describe the scintillation mechanism in general, also between these limiting cases:

$$\frac{dL}{dr} = \frac{S \frac{dE}{dr}}{1 + kB \frac{dE}{dr}} \quad (4.6)$$

where S , k and B are material constants. In this picture, $S \frac{dE}{dr}$ accounts for the density of “excitons”³ and $B \frac{dE}{dr}$ for the density of impurities (e.g. damaged molecules) in the material. Generally, such impurities acting as traps for electrons, and, in addition, non-radiative “exciton-exciton” annihilations are supposed to influence the quenching. k is the fraction of these impurities which contribute to such a light-quenching effect, i.e. k is the “exciton”-capture probability of a damaged molecule (impurity) compared to an undamaged molecule. Usually, kB is empirically determined and treated as one single parameter, called *Birks factor*. In the extreme case of highly ionizing particles ($kB \frac{dE}{dr} \gg 1$) the light output L_i according to equation 4.4, is given by:

$$L_i = A \cdot r = \frac{S}{kB} \cdot r. \quad (4.7)$$

Using equation 4.7 and $L_e(E) = S \cdot E$, the QF can be written as [91]

$$QF = \frac{L_i(E)}{L_e(E)} \approx \frac{\frac{dL_i(E)}{dr}}{\frac{dL_e(E)}{dr}} \approx \frac{1}{kB \left(\frac{dE}{dr}\right)_i} \quad (4.8)$$

which is an approximation and is only valid for the limiting case of highly ionizing particles. Nevertheless, the following qualitative features of QFs can be derived:

- QFs are, in general, energy-dependent.
- The QF is the smaller the higher the stopping power for individual nuclei. This is also consistent with smaller QFs for heavier ionizing particles (see stopping powers of different nuclei, e.g., in [91]).
- Nuclear stopping powers typically decrease at low particle energies [91] which results in a rise of the QF towards lower energies.

²In the CRESST collaboration another normalization of the QF is chosen, see equation 4.2 in chapter 4.1.

³In Birks phenomenological model “excitons” are rather loosely defined as excited molecular states in a scintillator. For more details concerning “excitons” see [90].

More generally, the QF can be expressed by

$$Q_F = \frac{L_i(E)}{L_e(E)} = \frac{\int_0^E \frac{dE}{1+kB(\frac{dE}{dr})_i}}{\int_0^E \frac{dE}{1+kB(\frac{dE}{dr})_e}} \quad (4.9)$$

where L_i and L_e are derived by integration of equation 4.6. Since the parameter S cancels, the QF - according to the Birks model - only depends on the parameter kB .

This model can be fitted to experimental data to determine the Birks factor kB empirically. This has been performed with data - in the framework of the CRESST experiment - from dedicated QF measurements of O, Ca and W in CaWO_4 [91] and from CRESST data acquired during neutron calibration campaigns in run32 [68]. While in none of these attempts the data is well-described by the Birks model over the entire energy range, a general trend for the QFs, however can be extracted.

- Generally the energy-dependence of the QFs is the weaker the heavier the particle involved.
- Since the Birks model does not describe combined data of different kinds of incident particles (e.g. e^-/γ and α particles [68]) in one measurement, the results suggest that the Birks factor kB varies for different kind of interactions in the same scintillator. This is further confirmed by measurements with liquid scintillators (e.g. in the BOREXINO experiment [92]) in which kB differs for γ 's and protons by a factor of up to ~ 2 [93].
- Different samples of the same material yield variable Birks factors⁴.

The precision measurements of the O, Ca, and W QFs of CaWO_4 at mK temperatures (see chapter 4.9) performed within the present thesis showed, for the first time, an energy dependence of the QFs. This is phenomenologically predicted by the Birks model.

4.3 Previous QF Measurements

In this chapter, previous attempts within the CRESST collaboration to measure the QFs of CaWO_4 are briefly reviewed. Although considerable effort has been made, the QFs - in particular that of W - could not be measured with the required precision.

CRESST Neutron Calibration Campaigns: In every extensive Dark-Matter run of CRESST (such as run32) a dedicated neutron calibration campaign with an AmBe source was performed to study the response of every individual detector module to neutron-induced nuclear recoils. Due to the strong energy-degradation in the various layers of shielding surrounding the detector volume (see chapter 2.3) mainly O-scatters are observed at energies $\gtrsim 20$ keV. Above this energy, Ca and W are strongly suppressed for kinematic reasons, below, the overlap between the individual contributions does not allow to disentangle O, Ca and W. Nevertheless, these calibration campaigns have been used to determine the QF of O for every CRESST detector operated assuming constant, energy-independent quenching. Typically, the QF of O has been determined in the energy range of 100-300 keV in which

⁴A variation of the Birks factor for different CaWO_4 crystals can be seen, e.g., in the varying non-proportionality effect among detector modules operated in run32 of CRESST [27].

O completely dominates the recoil spectrum [25]. Light-yield plots of data acquired with detector modules operated in CRESST run32 during an AmBe neutron calibration campaign are shown in figure 4.31 in chapter 4.10.

First Steps at the Neutron Scattering Facility: In an early stage of the scattering facility at the MLL in Garching, neutron scattering experiments to measure the QFs of CaWO_4 at room temperature have been performed [94]. In principle, a triple-coincidence technique (see chapter 4.4) was performed to identify the kind of neutron-induced nuclear recoils, however, photomultipliers were used to measure the corresponding scintillation light of recoiling nuclei induced by fast neutrons (~ 11 MeV) produced by the accelerator. The room-temperature QFs of O and Ca at recoil energies of ~ 1 MeV and ~ 450 keV, respectively, could be measured with small statistical uncertainties [95]. The light output of W-recoils, however, was below the threshold of the photomultipliers.

In addition, as a first step towards the measurement of the QFs of CaWO_4 at mK temperatures [81, 79, 96] a CRESST-like detector module (see chapter 4.5) was irradiated with fast neutrons (~ 11 MeV) from the accelerator to study the continuous nuclear-recoil band (no coincidence techniques involved). In contrast to the neutron calibrations with an AmBe-source performed in CRESST, the nuclear-recoil spectrum of Ca (W) extends up to energies of ~ 1 MeV (~ 250 keV) which to a certain extent allows to fit the QFs directly by three Gaussians. The QFs of O and Ca could be determined with rather small statistical errors [81]. For W, however, the uncertainties were large ($\sim 50\%$). Parts of the calibration and the normalization of the QFs are not consistent with the convention used by the CRESST collaboration (see chapter 4.1 and, e.g., [27]) which complicates the comparability with other measurements.

Time-of-Flight Mass Spectrometry: At the Max-Planck-Institut für Physik in Munich (MPP) an experiment dedicated to the measurement of the QFs of ions interacting in scintillating crystals has been set up [97]. Thereby, different ions which are produced in a laser desorption/ionization source (LDI) and whose energies (typically ~ 18 keV) are selected by a time-of-flight mass spectrometer (ToF-MS) are shot onto a scintillating crystal (e.g. CaWO_4). The produced scintillation light of these (surface-only) events is detected by a photomultiplier coupled to the crystal.

Such experiments were performed for CaWO_4 with a variety of different ions (e.g. p, O, Ca, W, Pb) in several measurement campaigns [97, 98, 25], however, the results are not conclusive. Besides possible differences in the scintillation mechanisms between room temperature and the operational temperature of CRESST detectors (~ 10 mK) there are apparently systematic uncertainties which are not fully understood.

4.4 Working Principle of Quenching Factor Measurements

The aim of the neutron-scattering facility at the MLL (Maier-Leibnitz-Laboratorium) in Garching is to precisely measure the QFs of O, Ca, and W in the bulk of CaWO_4 at the operational temperature (~ 10 mK) of CRESST detectors.

As described in chapter 4.3, previous measurements failed to disentangle the composition of the nuclear-recoil band from data acquired with CRESST detector modules due to the finite resolution of the light detector and the corresponding significant overlap of the individual recoil bands (O, Ca and W). At low energies (< 100 keV), where - for kinematic reasons - most

of the W recoils are expected, the contributions of the three elements in CaWO_4 are highly correlated. This results in large errors for the QFs, in particular, for that of W. Therefore, an experiment which allows to separate individual contributions of recoiling nuclei has been set up and a measurement technique - the so-called **triple-coincidence technique** - has been developed [79, 96]. Furthermore the precise knowledge of the QFs (at a certain recoil energy) derived by this technique enables an **energy-dependent QF analysis** of the entire nuclear-recoil bands. The working principles of the measurement technique as well as the analysis which have been successfully performed in the framework of this thesis are explained in the following.

Triple-Coincidence Technique: Monoenergetic neutrons which are produced in the nuclear reaction $p(^{11}\text{B},n)^{11}\text{C}$ by a pulsed ion-beam from an accelerator are scattered off a CaWO_4 crystal operated as phonon detector in a CRESST-like detector module at mK temperatures. Neutrons which scatter elastically off the nuclei (O, Ca, W) deposit energy in the crystal depending on the mass of the recoiling nucleus. In addition, at fixed scattering angles an array of liquid-scintillator neutron detectors is installed to record the scattered neutrons. Therefore, one can search for (triple-) coincidences between:

- Neutron production (pulse from the accelerator)
- Energy deposition in the CaWO_4 crystal
- Neutron detection in a liquid scintillator detector

The kinematics of the scattering reaction are determined by the following parameters:

- scattering angle
- incident neutron energy
- deposited energy in CaWO_4 crystal (phonon detector)

With a fixed scattering angle, the incident neutron energy can be derived by a time-of-flight (ToF) measurement between neutron production and detection considering the energy deposition in the CaWO_4 crystal measured by the phonon detector. In this way, the recoiling nucleus can be identified unambiguously. The corresponding scintillation-light output of the CaWO_4 crystal is measured with a separate cryogenic light detector which consequently yields the QF of the identified type of nuclear recoil.

In figure 4.3, a schematic overview of the most important components of the neutron scattering facility is given and the main steps of the measurement technique are illustrated.

In practice, the experiment has been optimized for the separation of W recoils since the QF of W was not measured before at mK temperatures with the required precision. The QFs of O and Ca are accessible by a different measurement technique. For incident neutrons with a mean energy of ~ 11 MeV the elastic scattering cross-section of neutrons on W has a maximum at $\sim 80^\circ$ which can be derived from the differential spectrum shown in figure 4.4. The maximum at $\sim 45^\circ$ is not practicable since due to the finite opening angle of the neutron beam unscattered neutrons (direct hits in the neutron detectors) of lower energy mimic scattered neutrons of the considered energy and produce a non-tolerable background of accidental coincidences [96].

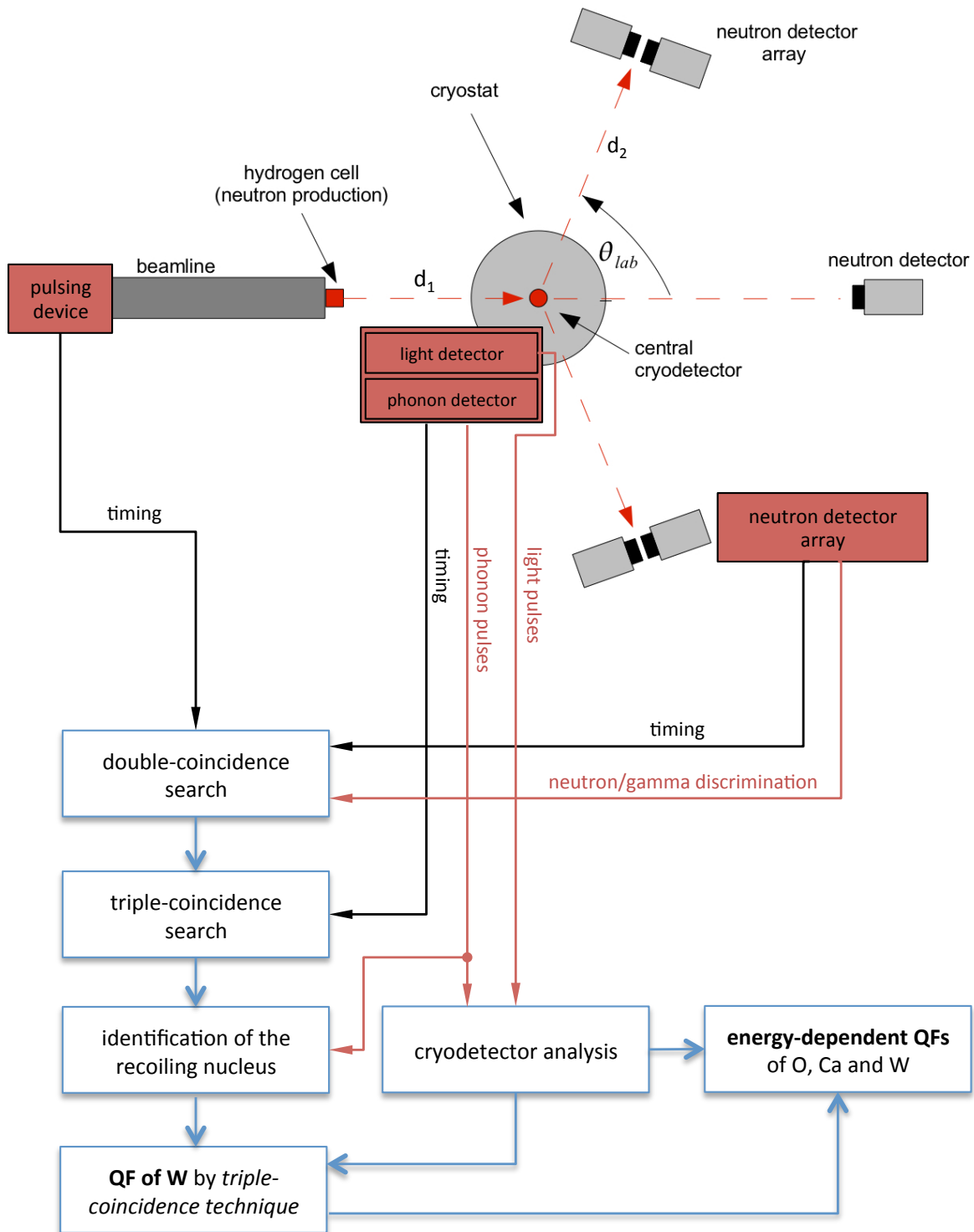


Figure 4.3: Schematic overview of the experimental setup of the neutron scattering facility at the MLL in Garching (grey) and an illustration of the main analysis steps for the measurement of the QFs as described in the text.

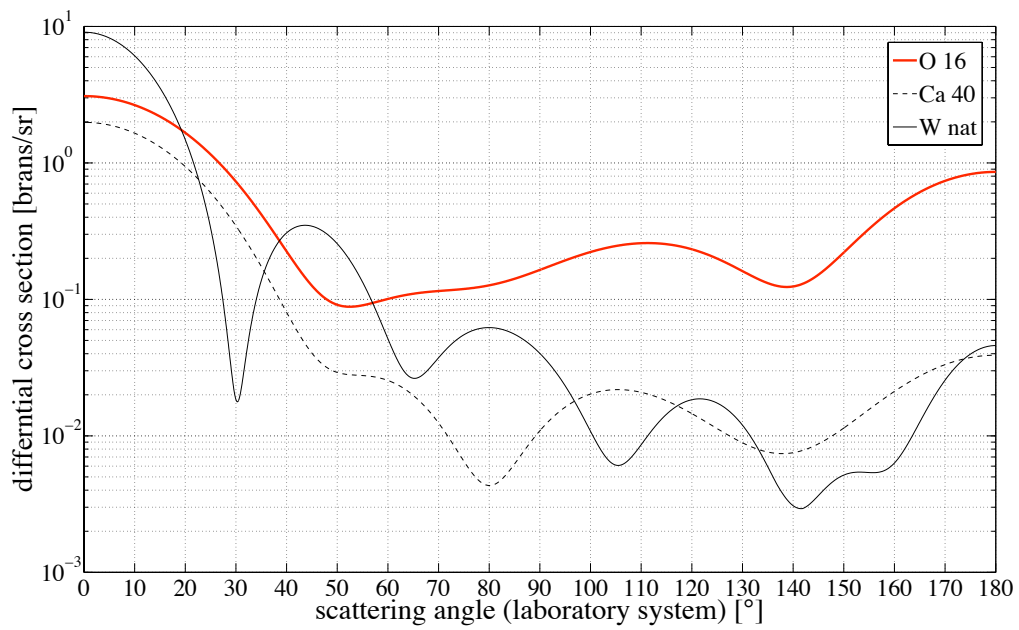


Figure 4.4: Differential elastic scattering cross-section of O, Ca and W for incident neutrons with an energy of 11 MeV plotted versus the scattering angle in the laboratory system. The isotope ratio of natural tungsten and the stoichiometric conditions in CaWO_4 are included in the calculation [96].

For elastic scattering, the recoil energy E_r of the nucleus x can be derived for a scattering angle Θ_{CM} in the center-of-mass system (CM) by

$$E_r(\Theta_{\text{CM}}) = 2E_n \frac{m_n \cdot m_x}{(m_n + m_x)^2} (1 - \cos(\Theta_{\text{CM}})) \quad (4.10)$$

with m_n , and m_x are the mass of the neutron, and of the recoiling nucleus x , respectively, and E_n is the incident neutron energy [96]. The scattering angle Θ_{CM} can be calculated from the scattering angle in the laboratory system Θ_{lab} by

$$\cos(\Theta_{\text{CM}}) = -k \sin(\Theta_{\text{lab}}) + \sqrt{1 - k \sin(\Theta_{\text{lab}})} \cdot \cos(\Theta_{\text{lab}}) \quad (4.11)$$

with the parameter $k = \frac{m_n}{m_x}$. This formula holds for reactions with $k < 1$ [94]. The recoil energies of O, Ca and W at the considered scattering angle of $\sim 80^\circ$ are listed in table 4.1.

Since not only neutrons with an energy of ~ 11 MeV but also neutrons with lower energies

recoiling nucleus	O	Ca	W
$E_r(80^\circ)$ [keV]	1088	447	98.4
$E_r(180^\circ)$ [keV]	2436	1047	237

Table 4.1: Recoil energies of O, Ca and W for incident neutrons with an energy of 11 MeV at a scattering angle of $\Theta_{\text{lab}} = 80^\circ$ and $\Theta_{\text{lab}} = 180^\circ$ (maximum energy transfer).

(see figure 4.5 in chapter 4.5.1) are produced, the determination of the incident neutron energy by ToF is important for background suppression. While the bunch width of the neutron pulses as well as the timing resolution of the neutron detectors is in the order of 2-3 ns, the timing of the phonon pulses in the cryodetector can only be determined with a resolution of $\sim 10\mu\text{s}$ [79] which is insufficient to resolve typical neutron ToF of ~ 50 ns. Therefore, at first only coincidences between neutron production and detection (so-called **double coincidences**) are considered. The neutrons are produced at a distance d_1 (~ 30 cm) from the CaWO_4 crystal where they - depending on the kind of recoiling nucleus - loose energy E_r . Thereafter, they are recorded by the neutron detectors ($\Theta_{\text{lab}} = 80^\circ$) at a distance d_2 (typically 1.5 m). The energy loss in the phonon detector E_r and the total ToF

$$t_{\text{ToF}} = \frac{d_1}{v_1} + \frac{d_2}{v_2} \quad (4.12)$$

where v_1 and v_2 are the neutron velocities before and after scattering, respectively, can be measured on an event-by-event basis. The velocity of the neutrons can be written as:

$$v = c \cdot \sqrt{1 - \frac{m_n c^2}{m_n c^2 + E_{\text{kin}}}} \quad (4.13)$$

with the neutron rest mass m_n and the kinetic energy E_{kin} of the neutron. The relation between the incident energy E_{in} of the neutron and t_{ToF} thus gives:

$$t_{\text{ToF}} = \frac{d_1}{c \cdot \sqrt{1 - \frac{m_n c^2}{m_n c^2 + E_{\text{in}}}}} + \frac{d_2}{c \cdot \sqrt{1 - \frac{m_n c^2}{m_n c^2 + E_{\text{in}} - E_r}}} \quad (4.14)$$

Typically, only double coincidences with a incident neutron energy > 7 MeV are considered as candidate events for triple coincidences since below the signal-to-background ratio suffers

significantly from parasitic scattering of low-energy neutrons on materials surrounding the CaWO_4 crystal. Double-coincident events which have, in addition, a coincident nuclear recoil in the cryodetector (timing resolution $\sim 10\mu\text{s}$) can be assigned to O, Ca or W by measuring the deposited energy in the phonon detector (see table 4.1). The events identified as W recoils allow to determine the QF of W at a recoil energy of $\sim 100\text{keV}$ (see chapter 4.8.3).

Energy-Dependent QF Analysis: This technique uses the entire nuclear-recoil spectrum of the three elements in CaWO_4 instead of separating a kinematically fixed sub-set of the data as done for the triple-coincidence technique. Incident neutrons with energies of $\sim 11\text{MeV}$ exhibit a continuous recoil spectrum (see equation 4.10) up to $\sim 2.4\text{MeV}$ for O recoils, up to $\sim 1.0\text{MeV}$ for Ca recoils and up to $\sim 230\text{keV}$ for W recoils. Other than in measurements with neutron sources, e.g., with an AmBe source [25], this measurements yield a significant amount of Ca and W scatters at energies $> 100\text{keV}$ where the resolution of the recoil bands is sufficient, and a direct fit of the light-yield (see chapter 4.1) distribution with three Gaussians is feasible. Nevertheless, without the precision measurement of the QF of W obtained by the triple-coincidence technique the fit does not converge over the entire nuclear-recoil band. This technique allows to describe the QFs of O and Ca with an energy-dependent parametrization which was possible for the first time within this thesis (see chapter 4.9).

4.5 Experimental Setup: The CRESST Scattering Facility

4.5.1 Accelerator Setup

The neutron scattering experiment is located at the tandem-accelerator facility of the Maier-Leibnitz-Laboratorium (MLL) in Garching. The accelerator is used to produce a pulsed monoenergetic neutron beam via the nuclear reaction:



This is achieved by accelerating ^{11}B ions up to an energy of $\sim 61\text{MeV}$ and by shooting the beam onto a cell (diameter: 1 cm, length: 3 cm) filled with pressurized hydrogen gas ($\sim 2\text{bar}$). The hydrogen cell is mounted at the end of the beamline, $\sim 30\text{cm}$ in front of the $^3\text{He}/^4\text{He}$ dilution refrigerator in which the CaWO_4 target crystal is installed. The cell is separated from the vacuum of the beamline by a $5\mu\text{m}$ thick molybdenum foil. Due to inverse kinematics a monoenergetic neutron beam of $\sim 11\text{MeV}$ focused into forward direction is produced. To allow a time-of-flight measurement to perform QF measurements by the triple-coincidence technique (see chapter 4.4) a bunched beam with a width of $\mathcal{O}(2\text{ns})$ is necessary. Therefore, the pulsing devices of the accelerator were renewed and optimized within this thesis. In appendix C, a detailed description of the tandem-accelerator setup, including the ion source, the neutron production, and - in particular - the pulsing devices is given.

At the present state, a pulse width of $\lesssim 2\text{ns}$ (FWHM) is achieved reproducibly for long-term measurements of several weeks. This was one of the main requirements for the success of the triple-coincidence measurement.

A typical neutron-energy spectrum recorded with an additional liquid-scintillator detector at a distance of $\sim 3\text{m}$ behind the hydrogen cell and a scattering angle of $\sim 0^\circ$ is shown in figure 4.5. Besides the dominant mononenergetic neutrons produced by the nuclear reaction at a

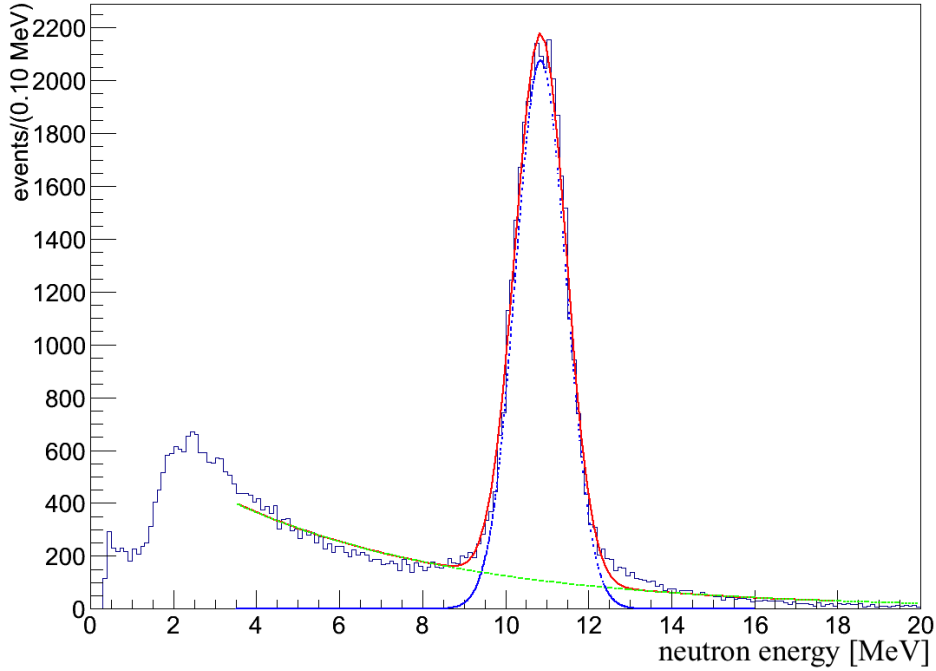


Figure 4.5: Neutron-energy spectrum recorded with a liquid-scintillator detector at a scattering angle of $\sim 0^\circ$. The peak of monoenergetic neutrons (blue) produced by the nuclear reaction $p(^{11}\text{B},n)^{11}\text{C}$ is found at a mean energy of 10.8 MeV and a 1σ width of 0.65 MeV. The spectrum of the background neutrons is approximated by an exponential (shown in green) with a “decay constant” of $\tau_{bg} = 4.73$ MeV. The combined spectrum is displayed in red.

mean energy of 10.8 MeV, a neutron background which exponentially decays towards higher energies can be observed. The latter is produced by the ^{11}B -beam being stopped at the end of the beamline by a Au-beamstopper (see appendix C).

4.5.2 Cryogenic Setup

CRESST-like Detectors: For the scattering experiment a dedicated CaWO_4 phonon detector with the following properties was developed [99]

- The CaWO_4 crystal of 5 mm in height and 20 mm in diameter ($m \approx 9.5$ g) called *cw520* is significantly smaller than a standard CRESST crystal (40 mm in height, ~ 40 mm in diameter, $m \approx 300$ g) to reduce the total event rate in the detector so that it becomes operational above ground. A background rate of only $\gtrsim 4$ Hz originating from natural radioactivity is observed in the setup at the MLL. The **size** is also crucial for the neutron scattering since a larger crystal would worsen the angular resolution. Multiple scattering of neutrons which could to a certain extent distort the QF measurements is reduced by a factor ~ 3 compared to standard CRESST-size detectors. Simple estimations suggest a total fraction of multiple neutron (11 MeV) scatters in CaWO_4 of $\sim 7\%$ [99]. A more sophisticated GEANT4 simulation [87] shows that most of the multiple scatters occur on O and thus have the same light yield as single O recoils. Mixed scatters (O-Ca, O-W, Ca-W) which show up between the individual nuclear recoil bands (O, Ca, W) in

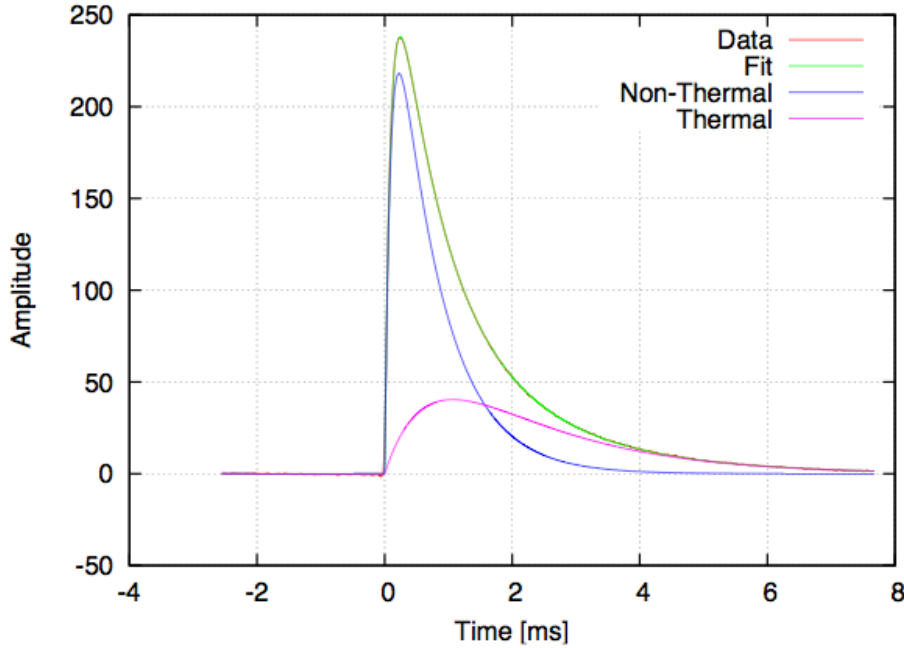


Figure 4.6: Fit of a template event of the CaWO_4 phonon detector *cw520* operated at the scattering facility. The template which is derived from electron-recoil events induced by a ^{55}Fe source at ~ 6 keV are fitted according to equation 2.6 in chapter 2.2.4. The data points (red) are not visible below the Fit (green). Picture from [??].

the light-yield plane are negligible in the considered energy range $\gtrsim 10$ keV.

- The **transition-edge sensor** (TES) which was evaporated onto the CaWO_4 crystal is optimized for high event rates in the detectors. A fast decay time of the pulses can be achieved by increasing the phonon collection area of the TES with Al phonon collectors. The sensor structure consists of 28 individual Ir/Au-TESs each connected to 10 Al-strips of $50 \times 250 \mu\text{m}^2$ acting as phonon collectors which establishes a total phonon collection area of 3.5 mm^2 [99]. As shown in figure 4.6, the thermal ($\tau_t = 1.7 \text{ ms}$) and non-thermal ($\tau_n = 0.7 \text{ ms}$) contributions to the pulse are sufficiently short to cope with trigger rates of up to $\sim 60 \text{ Hz}$ while a low detector threshold of $\sim 500 \text{ eV}$ (5σ) and a phonon-energy resolution of 0.66 keV on a 1σ C.L. at 59.5 keV (see chapter 4.7) were achieved. The temperature of the transition from the normal conducting to the superconducting state is $T_c \sim 60 \text{ mK}$ (width of transition curve: 2 mK).

The Si light detector originally developed for the scattering experiment [99] was replaced within this thesis by the light detector *Si448a* [100]. Like the phonon detector *cw520*, the Ir/Au-TES of the light detector is equipped with Al phonon collectors with a total collection area of $\sim 5.0 \text{ mm}^2$ [100]. The transition temperature is $T_c = 23.7 \text{ mK}$ and the 5σ detection threshold was determined with a ^{55}Fe source as $E_{5\sigma} = 83.0 \text{ eV}$. The exchange of the light detector together with the improvements concerning microphonics-induced noise at the setup (see below), the resolution of the light channel - a crucial parameter for the QF measurements

- has been enhanced significantly (see chapter 4.7).

Low-Mass Detector Housing: In an earlier stage of the scattering experiment, the detectors were housed in a massive copper holder [99] of ~ 200 g. Neutrons which scatter inelastically on the surrounding materials (e.g. the detector holder, the cryostat) and which are detected by the neutron detectors at a certain scattering angle eventually create γ 's (relaxation from excited states). If detected in the phonon detector they significantly contributed to the signal. An extensive study concerning these background contributions showed that only $\sim 19\%$ of all triple-coincidences acquired in a commissioning beamtime were nuclear recoil events induced by elastic scattering of neutrons [79].

Therefore, in this thesis an especially designed low-mass detector holder was developed and installed into the low-temperature setup. The basic structure consists of two copper rings (outer diameter: 40 mm, inner diameter: 35 mm, thickness 1 mm) connected by M1 brass screws on which the clamps holding the CaWO_4 crystal are attached (see figure 4.7 right-top). The three bottom clamps are made of teflon while the three top clamps are manufactured of bronze which still remains flexible at mK temperatures and can thus compensate contractions caused by temperature changes. The light detector is fixed on one copper ring by bronze clamps and the detectors are surrounded by the reflective and scintillating polymeric foil (VM2002) also used in the CRESST experiment (see figure 4.7 right-bottom). The module is connected by an ultra-light carbon tube (diameter ~ 24 mm, wall thickness: ~ 0.5 mm, length: ~ 30 cm) to the mixing chamber of the dilution refrigerator.

As will be presented in chapter 4.8.1, the identification of recoiling nuclei has become possible with an excellent signal-to-background ration of up to $\sim 28 : 1$ thanks to improvements in terms of mass-reduction.

^3He - ^4He Dilution Refrigerator: The CRESST like detector module is cooled to its operational temperature of ~ 20 mK by a dilution refrigerator of Oxford Instruments (KELVINOX400) [101] with a cooling power of $400\mu\text{W}$ at 100 mK and a base temperature of ~ 14 mK. Basic information about the working principle of dilution refrigerators is given in appendix D. To read out the cryogenic detectors, similarly to the CRESST experiment, SQUIDs were installed in the setup [79]. Two DC-SQUIDs (type *cs-blue*) manufactured by Supracon [65] are mounted on the 1K-plate of the cryostat and wired accordingly. Details about the functionality of SQUIDs are given in [55]. The TES of both detectors are biased by constant current sources with a typical current of $\sim 50\mu\text{A}$. At the low-temperature stage (~ 20 mK) a shunt resistor of $100\mu\Omega$ is connected in parallel to the TES which in turn is connected in series to the input coil of the SQUID (see figure 4.8). If a temperature rise in the cryogenic detector increases the resistance of the TES the magnetic flux in the superconducting coil decreases. The SQUID amplifies this change of the magnetic field and the corresponding signals are recorded by the data-acquisition system (see chapter 4.5.4).

At the low-temperature stage (mixing chamber, see appendix D) of the dilution refrigerator a temperature stabilization system was installed (PID controller, AVS-47 [79]). As the detectors cannot be stabilized by control pulses as done in the CRESST experiment due to the high event rate (up to ~ 60 Hz), both detectors which are thermally coupled to the mixing chamber by Cu-wires are kept at the same temperature level. The working point of the

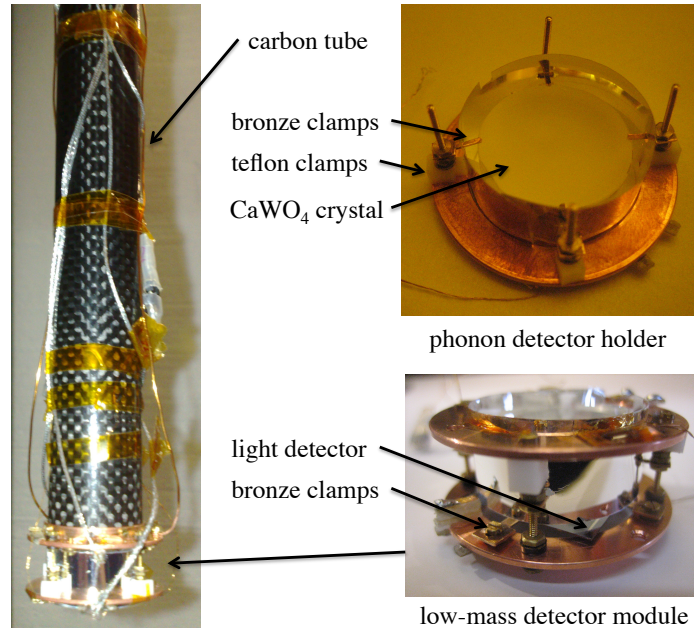


Figure 4.7: Pictures of the low-mass detector holder installed in the dilution refrigerator at the MLL. For details about the setup refer to the main text. Right: Low-mass detector holder with phonon and light detector. Left: Detector module mounted on the carbon tube which is connected to the mixing chamber.

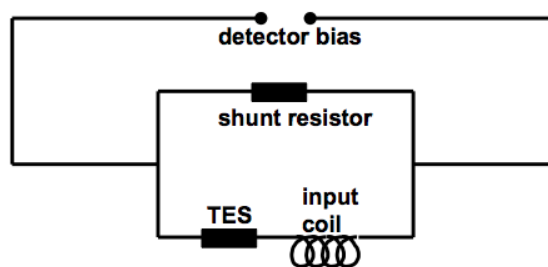


Figure 4.8: Wiring scheme of the TES readout. The (superconducting) input coil of the DC SQUID which is connected in series to the TES of the detector and in parallel to the shunt resistor ($R = 100\mu\Omega$) converts a resistance change of the TES - induced by a phonon signal in the cryogenic detector - into a change of the magnetic field. This in turn is amplified and converted into a electric signal by the SQUID and read out by the data-acquisition system described in chapter 4.5.4. Picture from [79].

individual detectors is adjusted by the bias current. Although, in general the sensitivity of a detector depends on the bias current, in the present case, the best performance in terms of long-term stability could be achieved in this operational mode. Furthermore, - as the light channel resolution is essential for the experiment - the temperature was adjusted such that the performance of the light detector was optimized. The cryostat is mounted on a steel structure (see figure 4.9) as the CaWO_4 target crystal must have the same height as the beamline (~ 1.5 m above ground).

The gas-handling system including pumps used for the circulation of the ^3He - ^4He mixture and for the operation of the pre-cooling system (1K-pot) of the cryostat (see appendix D) is installed on top of the steel structure on which the cryostat is mounted (see figure 4.9). Since the cryogenic detectors are very sensitive to mechanical distortions (micro-phonics), e.g., vibrations induced by the pumps which are transmitted to the cryostat via the steel structure affect the sensitivity of the measurement. Therefore, within this thesis extensive efforts have been made to mechanically decouple the pumps from the dilution refrigerator. A detailed description of these successful improvements is presented in [102].

4.5.3 Liquid-Scintillator Detectors

For the measurement of scattered neutrons, 40 liquid-scintillator detectors are installed at a distance of ~ 1.5 m from the CaWO_4 crystal in the cryostat. They are set up in two detector arrays as shown in figure 4.9. Each liquid-scintillator detector consists of a hexagonal container of 5.0 cm height and 9.1 cm inner diameter which is filled with the commercially available liquid organic scintillator (EJ-301 [96], former NE-213) optimized for pulse-shape discrimination between neutron- and γ -induced interactions. The perspex window of the container is optically coupled with silicone oil to a Phillips XP-3461-B photomultiplier which exhibits a timing resolution of 2-3 ns. EJ-301 has mainly three scintillation decay times, 3.16 ns, 32.3 ns, and 270 ns, of which the slow ones are enhanced for highly ionizing particles such as for recoiling protons induced by neutron scattering [96]. The ratio of the integration windows of the fast and the slow components of the pulse decay can be used to identify the kind of particle interaction in the scintillator. For the data-acquisition (ADC Sis3320, see chapter 4.5.4), this is realized by adjustable integration gates which are applied to the pulses. In figure 4.17 (see figure 4.8.1), a typical discrimination plot in which the ratio of the integration gates for fast and slow components are plotted against the pulse height, shows the strong neutron/ γ -discrimination capability of these devices.

4.5.4 Data Acquisition

For the neutron scattering facility a sophisticated data acquisition system is necessary as the signals from all detectors and the pulses from the accelerator have to be saved to enable an offline analysis which results in a large amount of data (~ 5 TB per week of beamtime). An online determination of the coincidences between neutron production, energy deposition and neutron detection is not possible via a hardware-coincidence circuit (e.g. with NIM electronics) as the time constants of the pulses in the cryodetector are in the order of 1-2 ms which is orders of magnitudes slower than the required resolution of ~ 2 ns for neutron time-of-flight measurements. Therefore, a VME-based data acquisition was chosen which is explained in great detail in [79]. Here, the VME modules used for the experiments performed in this thesis are briefly described:

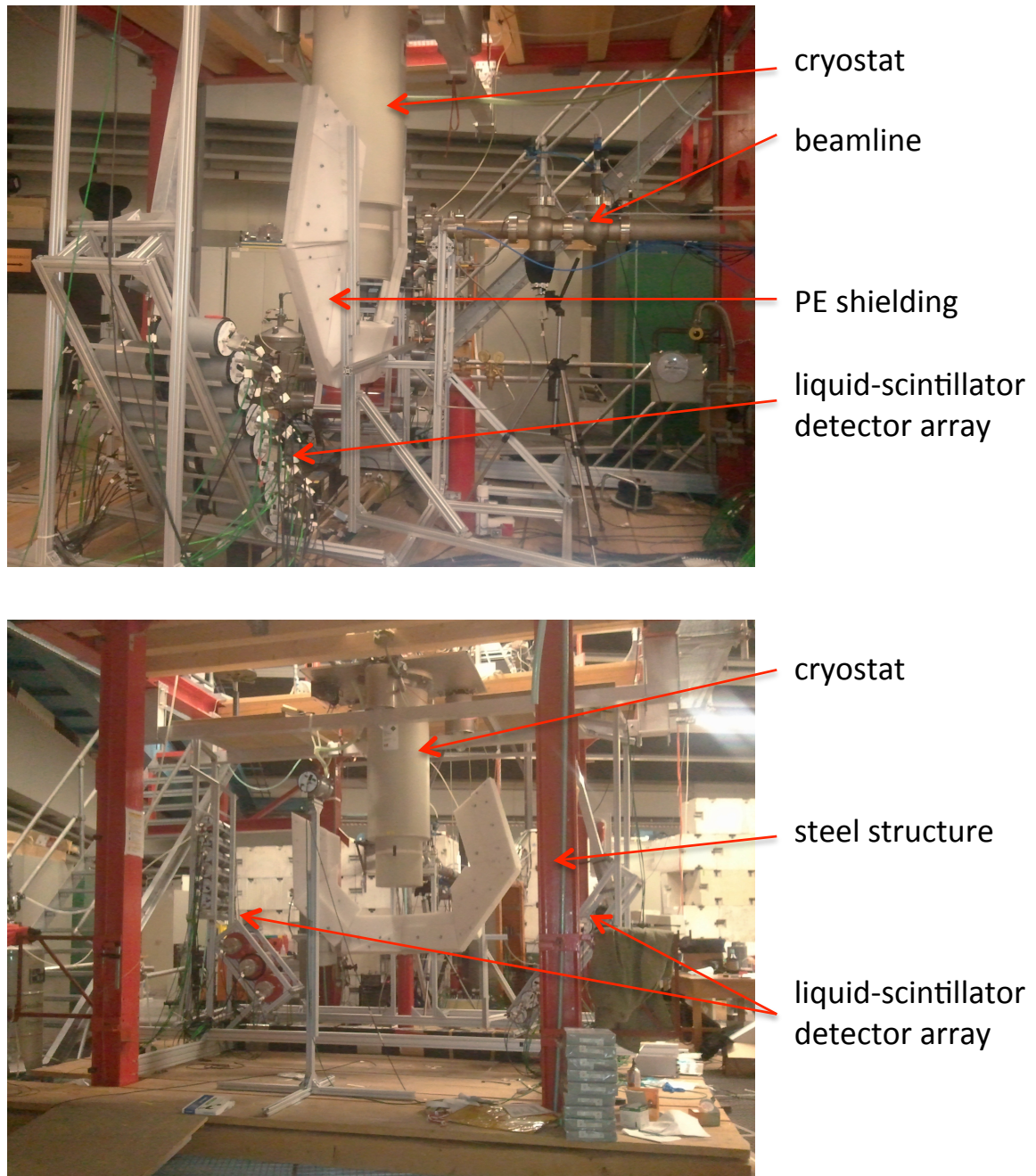


Figure 4.9: Pictures of the neutron scattering facility in hall 2 of the MLL in Garching.

- **Time to Digital Converter (CAEN v1190, 64 channels):** The timing signals of all detectors and of the accelerator pulses are recorded with a maximal resolution of 100 ps.
- **Constant Fraction Discriminator (CAEN v812, 16 channels):** All signals are fed through one of the 3 CFD modules and the corresponding trigger signals are transmitted to the TDC.
- **Analog to Digital Converter (Struck Sis3302, 8 channels):** This module is used to record the pulses from phonon and light detector with a maximum sample rate of 100 MHz and a 16 bit resolution. Although typical decay times of cryodetectors used here are ~ 1 ms, a high sampling rate and resolution is necessary to achieve a sufficient timing resolution (for the onset-determination algorithm, see chapter 4.6).
- **Analog to Digital Converter (Struck Sis3320, 8 channels):** Three modules are used to sample the pulses of the neutron detectors (maximum sample rate 250 MHz, resolution 12bit). It offers an alternative operation mode in which the pulses from the liquid-scintillator detectors are integrated on-board over adjustable time periods (so-called gates). An appropriate adjustment of these gates (up to 8 gates are available per channel) allows to establish a pulse-shape discrimination of proton and electron recoils in the scintillator. Using this feature only the results of the integration gates are saved which allows to reduce the amount of stored data significantly.

4.6 Data Analysis Overview

In this chapter an overview of the extensive data-analysis framework of the QF measurements is given. Figure 4.10 shows an illustration of the individual sections of the data analysis pipeline which are briefly described in the following.

Cryodetector Analysis: The pulses of the cryogenic phonon detector (CaWO_4) and of the light detector (Si) acquired with the ADC Sis3302 (see chapter 4.5.4) are analysed within this section in terms of deposited energy and scintillation light output, respectively. At first, the relevant parameters of the recorded pulses as, e.g., pulse height, peak position are calculated (more details in [79]). A truncated standard-event fit (see chapter 3.2.1) to derive the energy information and to compensate for non-linearities in the response of the detectors is applied to the pulses. Subsequently, valid pulses are selected by different cuts applied to the data (described in chapter 3.2.3). A dedicated stability cut excludes periods of unstable detector operation [79]. To correct drifts in the working points of both cryogenic detectors - which results in a variation of the pulse height - the peak position of a γ -calibration line (in this case the 59.5 keV line of ^{241}Am) was monitored with time and fitted with a polynomial. In addition, discrete changes of the working point are recognized by the algorithm and treated separately for drift correction. Individually, the subsets of the beamtime data are calibrated by the method presented in chapter 4.7.

Timing Operations: The timing signals of the detectors operated in the scattering experiment (cryodetectors, liquid-scintillator neutron detectors) as well as the signal of the pulsing devices of the accelerator are recorded by a TDC (see chapter 4.5.4). In order to assign the

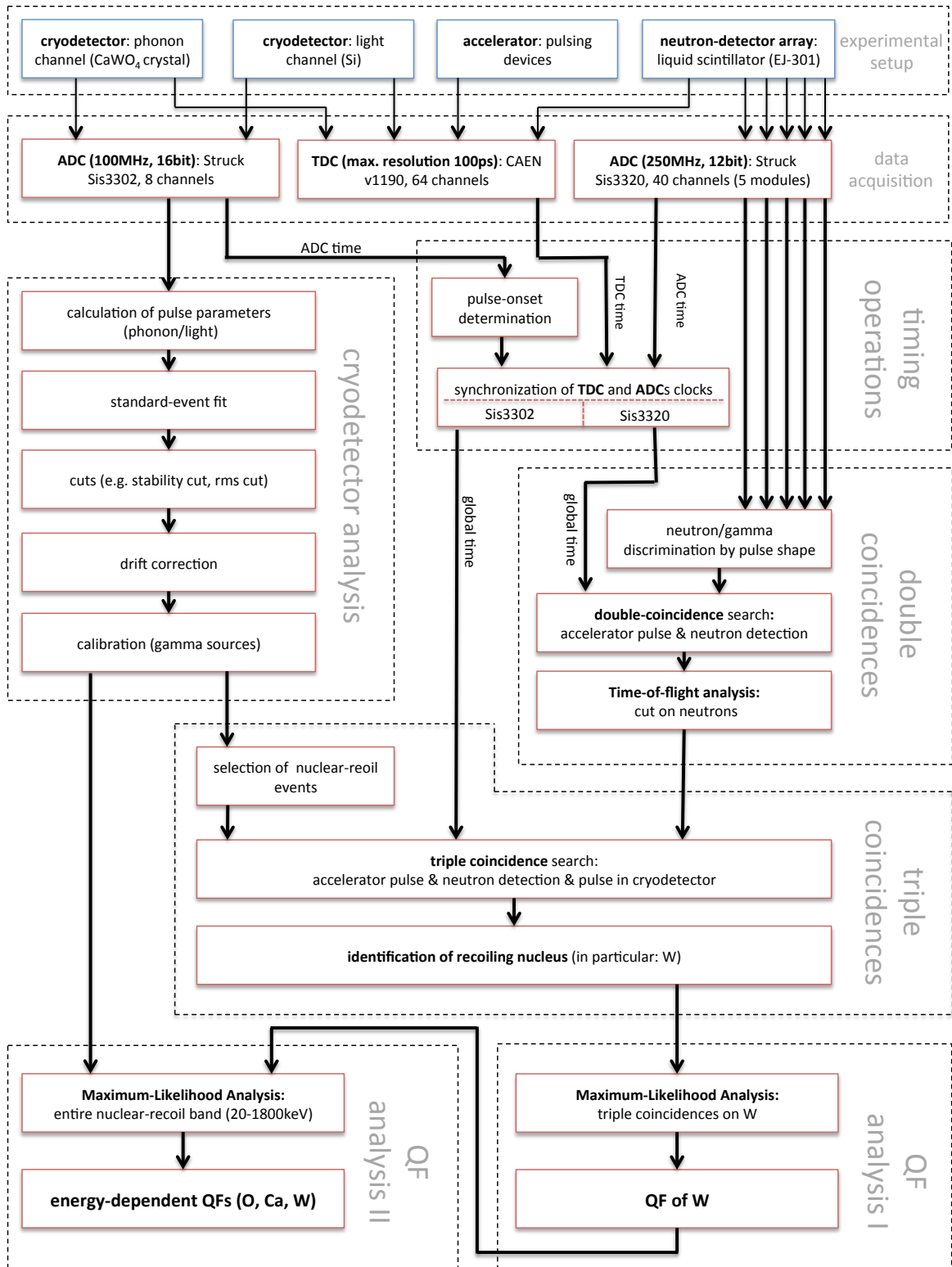


Figure 4.10: Overview of the main parts of the extensive data-analysis framework for the QF measurement performed at the neutron scattering facility. The individual sections are explained in the main text.

TDC signals to the simultaneously recorded ADC events - the individual data-acquisition modules have separate, freely adjustable clocks - a dedicated algorithm to synchronize the timestamps of the individual modules (TDC time, ADC time) was developed in [79]. Thereby, timestamps (global time) which are attached to every single event in the ADCs are introduced. Prior to the synchronization of the ADC Sis3302 which is used to record the pulses of the cryodetectors, the onset of the phonon pulses is determined by an especially developed algorithm [79]. It was optimized to achieve a timing resolution of the phonon channel of $\sim 10\mu\text{s}$ which can be seen by the width of the peak of real triple coincidences in figure 4.20 (chapter 4.8.1).

Double Coincidences: In this section, candidate events for neutron-induced nuclear recoils in the CaWO_4 crystals are selected. Neutron events recorded by the liquid-scintillator detectors can be discriminated from γ -induced electron recoils by pulse-shape discrimination (see chapter 4.5.3). This makes it possible to discard the dominant γ background which would significantly increase the signal-to-noise ratio. In the next step, coincidences between neutron production by the accelerator and detection at the fixed scattering angle of $\sim 80^\circ$ are determined (search margin of typically $\pm 1\mu\text{s}$). A typical time-of-flight plot in which the time difference between neutron production and detection of double-coincident events are put into a histogram is shown later in figure 4.16 (see chapter 4.8.1). The γ -peak can be used as reference to derive the time of neutron production which allows to perform a time-of-flight cut on neutrons.

Triple Coincidences: Other than the fast signals (timing resolutions $\sim 2\text{ns}$) used for the double-coincidence search, the onset of the phonon pulses can only be determined with an uncertainty of $\sim 10\mu\text{s}$. Therefore, in a search margin of typically $\pm 0.1\text{ms}$ around every double-coincident event the algorithm looks for corresponding nuclear-recoil events in the cryodetector. These triple-coincident events can be identified as O, Ca or W recoils after taking into account also the measured phonon energy deposited in the CaWO_4 target crystal. A detailed description of these analysis tools by means of beamtime data is given later in chapter 4.8.1.

QF Analysis I: In this section, the QF of W is determined by the triple-coincidence technique which is achieved by an extensive maximum-likelihood analysis developed in this thesis (see chapter 4.8.2).

QF Analysis II: Using the results of the QF of W derived by the triple-coincidence analysis an energy-dependent QF analysis of O, Ca and W of the entire nuclear recoil bands can be set up (see chapter 4.9.2). Therefore, a dedicated maximum-likelihood tool has been developed (see chapter 4.9.3).

4.7 Results of the Cryodetector Measurement

The center piece of the scattering experiment consists of a cryodetector module: A CaWO_4 crystal operated as phonon detector and a Si light detector in a CRESST-like detector module (see chapter 4.5). For the subsequent analysis steps the energy and timing information of the

events in those two cryogenic detectors have to be extracted. This chapter focuses on the determination of the energy spectra.

An overview of the steps for the analysis of the cryogenic detector used in this work are presented in chapter 4.6. Detailed explanations of the truncated standard event fit used to derive the energy information of every pulse and the standard cuts which are applied to the data are given in chapter 3.2.

During the beamtimes the following strategy was chosen to calibrate the cryogenic detectors:

- In dedicated calibration campaigns different γ -sources have been placed near the detector module to perform an energy calibration over a wide energy range (typically from 60 to 1300 keV) with high statistics. These campaigns usually took place at the beginning and at the end of a beamtime as well as in periods in which the accelerator had to be serviced.
- In periods in which the accelerator is available for the scattering experiment the detectors are exposed to a minimal γ -rate in order to gain maximal statistics of neutron-induced nuclear recoils. Nevertheless, to control the detector stability and possibly monitor drifts in the pulse height an ^{241}Am source (59.5 keV γ rays) was always present during all beamtimes. Additionally, ^{11}C produced by the ^{11}B beam in a nuclear reaction in the hydrogen cell constantly provides 511 keV γ 's for calibration purposes.

Typically, the detectors are stabilized in the most linear part of the transition from the superconducting to the normal conducting state which results in an almost linear response below the truncation limit of the standard event fit. The truncation excludes the non-linear parts above the limit from the fit. Thus the response of the detectors is usually close to linearity up to the MeV range. Nevertheless, to account for remaining non-linearities in the transition, a power-law function is commonly used for parametrization of the phonon detector [99].

$$E_r = a \cdot u^b \quad (4.16)$$

where E_r is the calibrated recoil energy and u is the pulse height in the phonon channel. The two parameters a and b have been determined in the Oct 2011 beamtime (this beamtime is exemplarily presented in the following) in a calibration measurement. The fit which is shown in figure 4.11 yields following values:

$$\begin{array}{l|l} a[\text{keV}] & 0.0835 \pm 0.0015 \\ b & 1.072 \pm 0.002 \end{array}$$

In figure 4.12 the calibrated phonon recoil spectrum is shown exhibiting an energy resolution of $\sigma = 0.66$ keV (1- σ C.L.) at 59.5 keV.

After a drift correction [96, 79] of the pulse height in the phonon channel performed with the 59.5 keV gamma line of ^{241}Am , the calibration - according to equation 4.16 - is applied to the total beamtime data. A spectrum including $\sim 50\%$ of the Oct 2011 beamtime data is shown in figure 4.13. It can be seen that compared to figure 4.12 the energy scale remains unchanged while the phonon resolution slightly suffers ($\sigma = 0.97$ keV (1- σ C.L.) at 59.5 keV) which is due to drifts in the transition curve that can only be corrected to a certain extent.

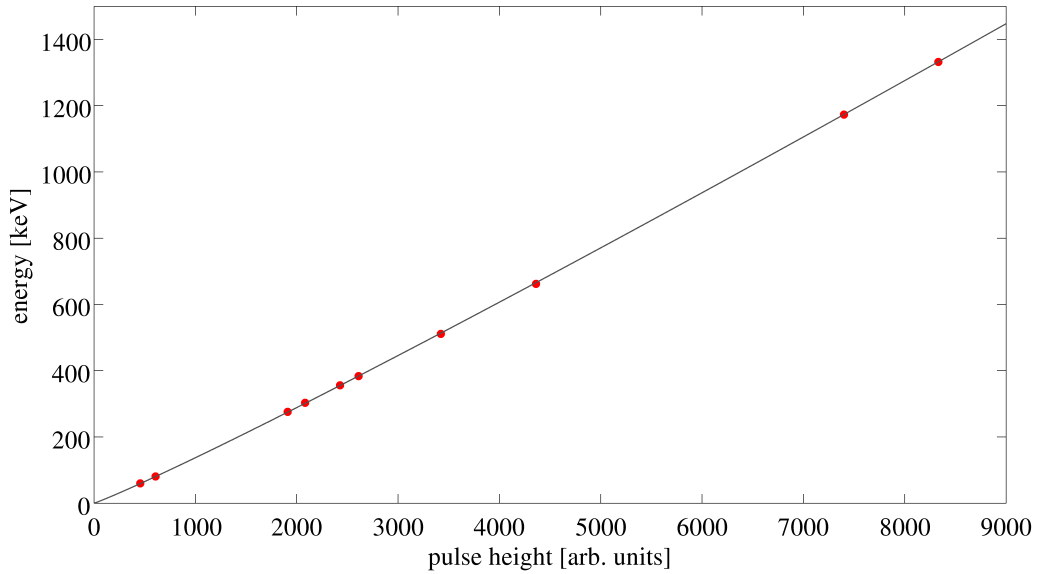


Figure 4.11: Calibration of the phonon channel with gamma sources during the Oct 2011 beamtime: The pulse height derived by a truncated standard-event fit is plotted versus the energy of the respective gamma lines. ^{241}Am , ^{133}Ba , ^{22}Na , ^{137}Cs , and ^{60}Co sources have been used (energies see figure 4.12). The statistical errors of the calibration points are negligible.

The performance of the phonon detector in terms of resolution and stability is by far sufficient for the projected measurements within this work.

For the light detector (LD) a different kind of calibration method was chosen as no direct characterization with sources is feasible. In the relevant energy range of a few keV, there is no suitable source available at present which would allow to check the linearity of the detector. The scintillation light produced in the CaWO_4 crystal is not practical for calibration at low energies ($\lesssim 100$ keV) because in this energy range the non-proportionality effect (see equation 4.1) which varies from crystal to crystal reduces the light yield (LY). The convention in the CRESST collaboration is such that the energy deposited in the LD by the scintillation light of a 122 keV electron recoil (^{57}Co) in the crystal is defined as 122 keVee (electron equivalent energy). The electron-recoil band is usually parametrized according to equation 4.1 (see chapter 4.1). The quadratic term therein (p_1) accounts for possible deviations from linearity which, however, cancels out and hence does not contribute to the Quenching Factor (see equation 4.2).

Figure 4.14 shows the data of the calibration measurement together with the full data set illustrated in a light-yield plot. The electron recoil bands of both measurements match nicely which shows the excellent long-term stability of the detector response of both detectors. In the full data set, the nuclear recoil bands are visible. Above ~ 300 keV two contributions due to O at $LY \sim 0.1$ and due to Ca at $LY \sim 0.05$ show up. At lower energies there is also a significant contribution of W at even lower LYs, however, due to the finite resolution of the light detector the bands can not be separated in this energy range. Above ~ 1 MeV - due to kinematics - only O recoils are expected from incident ~ 11 MeV neutrons (see

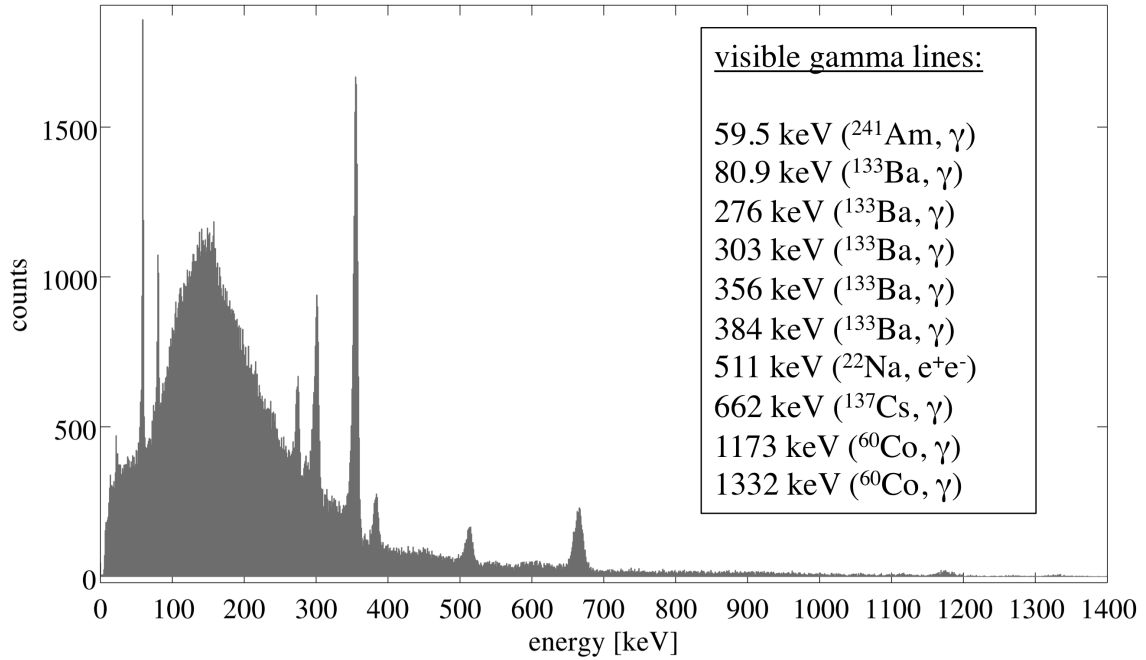


Figure 4.12: Phonon spectrum acquired in a calibration campaign during the Oct 2011 beam-time. ^{241}Am , ^{133}Ba , ^{22}Na , ^{137}Cs , and ^{60}Co sources have been used to calibrate the detector. The inset shows the energies of the γ lines.

chapter 4.4). Between the electron and the nuclear recoil bands there are contributions from inelastic scattering of neutrons on tungsten where the combination of a γ particle from the de-excitation of an excited W-energy level to the ground state⁵ and an elastic W-recoil is observed. Such events if displayed in the LY-energy plane are visible as curved bands below the electron-recoil band.

Reduction of the Sample Length As the statistics which can be acquired with the scattering experiment is limited by the maximum rate the cryogenic detectors can cope with (typical pulse decay times of $\mathcal{O}(1\text{ ms})$) a simulation has been set up to determine the optimal trigger rate of the phonon detector. The following conditions have to be fulfilled:

- In order to determine the onset of the pulse with the desired precision of $\sim 10\mu\text{s}$ the length of the pre-trigger must be free of pileup for at least 4 ms.
- The resolution of the light detector must not change significantly ($\mathcal{O}(1\%)$) due to the shortening of the sample length. As a good compromise, pulses are only used if the subsequent event takes place at least 3 ms after the trigger time.
- The post-trigger length must not be too short as at higher energies the pulse does not decay sufficiently below the truncation limit of the standard-event fit. The minimal

⁵The most prominent inelastic excitation levels of the relevant W isotopes cluster between 100 keV and 120 keV. There are further less pronounced levels of W at lower and higher energies. The lowest excited levels of Ca and O lie in the MeV range [79].

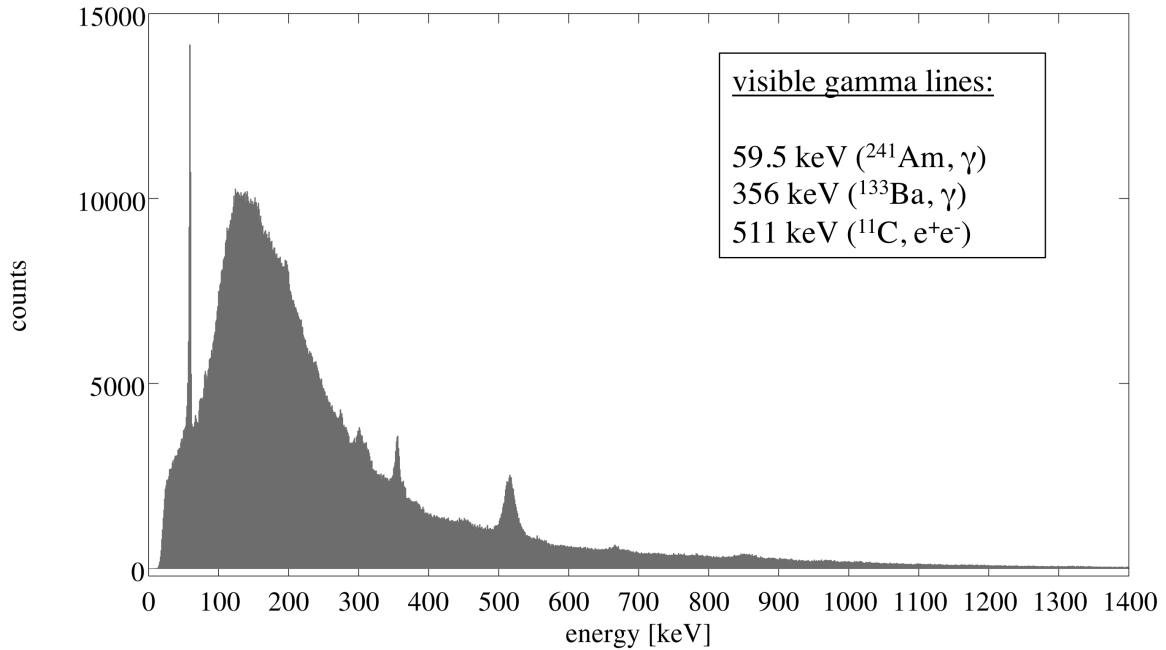


Figure 4.13: Phonon spectrum including $\sim 50\%$ of the Oct 2011 beamtime. A ²⁴¹Am source was always present during the beamtime in order to monitor the detector performance and to perform a drift correction of the pulse height. An additional cross check is the 511 keV gamma line originating from ¹¹C in the hydrogen cell (see chapter 4.5). The resolution of the ²⁴¹Am line at 59.5 keV for this data set is 0.97 keV ($1-\sigma$ C.L.).

length of the post-trigger thus depends on the maximum energy which is important for the experiment. For the triple-coincidence method optimized for the measurement of the tungsten QF a post-trigger of 7 ms is a good compromise (events up to an energy of ~ 500 keV can be analysed)

In figure 4.15 the results of a dedicated simulation are presented. With a post-trigger length of 7 ms a maximal usable rate of ~ 40 Hz can be achieved which is a factor of ~ 1.5 higher than that of the original setup. Half of the Oct 2011 beamtime and both beamtimes in 2012 have been performed with a reduced sample window as the main goal of the experiment was a precision measurement of the tungsten QF.

4.8 QF Measurements using the Triple Coincidence Technique

As reported in chapter 4.3, the QF of W was not measured before with the precision required for the CRESST experiment. In this chapter, the triple-coincidence technique explained in detail in chapter 4.4 is illustrated on the basis of a data set from the Oct 2011 beamtime whereas the results for the QF of W take into consideration the data of all beamtimes (Oct 2011, Feb 2012, Aug 2012). The experiment was optimized for the measurement of the QF of W as the other QFs (O, Ca) are easier to determine by other techniques (see chapter 4.9). Furthermore, it is shown in chapter 4.9 that the results for the QF of W obtained by the

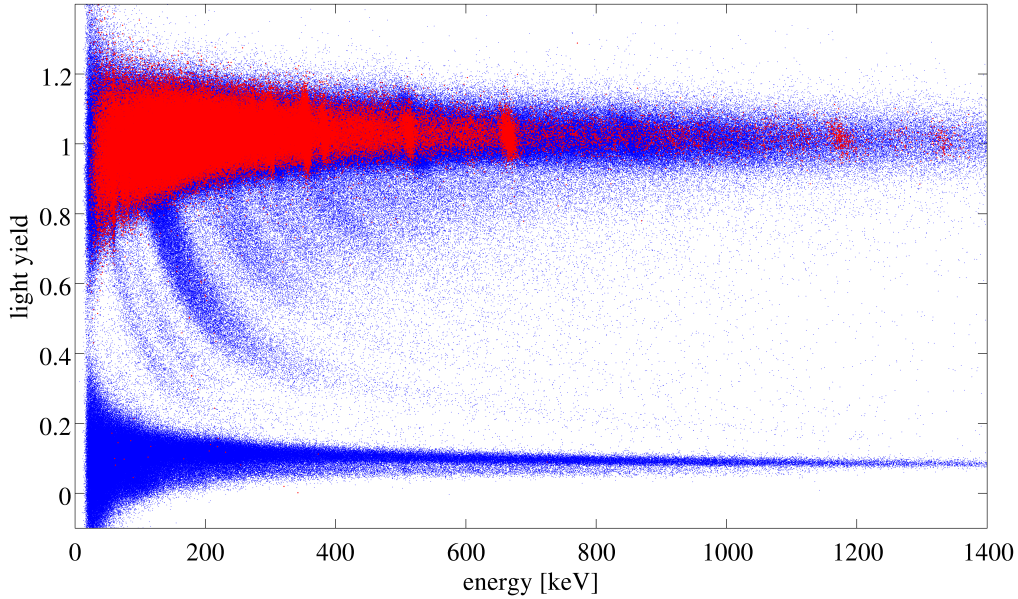


Figure 4.14: Comparison of light-yield plots of two periods of the Oct 2011 beamtime. A gamma calibration campaign (red) is plotted on top of the total data set. As described in more detail in the text, the calibration is extracted from an extensive calibration measurement and applied to the combined data set. The spectra are mapped with each other via the 59.5 keV gamma line of an ^{241}Am source which was always present during the measurement. The two spectra reflecting the two measuring periods are in nice agreement which shows the excellent long-term stability (\sim weeks) of the cryogenic light and phonon detectors. Between the nuclear recoil bands at $LY \sim 0.1$ and the electron recoil band curved bands due to inelastic scattering on W arise (see text).

triple-coincidence technique enable a more sophisticated new energy-dependent QF analysis for all elements of CaWO_4 .

4.8.1 Triple Coincidence Search

For the identification of the recoiling nucleus monoenergetic neutrons produced by a pulsed ^{11}B beam from the accelerator scatter off a CaWO_4 crystal operated as a CRESST-like phonon detector and are detected in liquid-scintillator neutron detectors at fixed scattering angles. The working principle of the experiment, the experimental setup and an overview of the complex analysis scheme are explained in chapters 4.4, 4.5 and 4.6. Here the results of the most important analysis steps are presented exemplarily for the Oct 2011 beamtime.

In a first step, one looks for coincidences between the production of neutrons by the pulsed beam of the accelerator and a neutron detection in the liquid-scintillator neutron detectors, the so-called *double coincidences*. This can be achieved with uncertainties of $\mathcal{O}(2\text{ns})$ for a typical neutron time-of-flight (ToF) of $\mathcal{O}(100\text{ns})$. The neutron detectors are placed at a distance of $\sim 1.5\text{m}$ from the cryostat at a scattering angle of 80° . Figure 4.16 shows a timing spectrum of double-coincident events. Two populations of events are visible: a gamma peak produced almost instantaneously by the ^{11}B bunch and a broad neutron population at longer

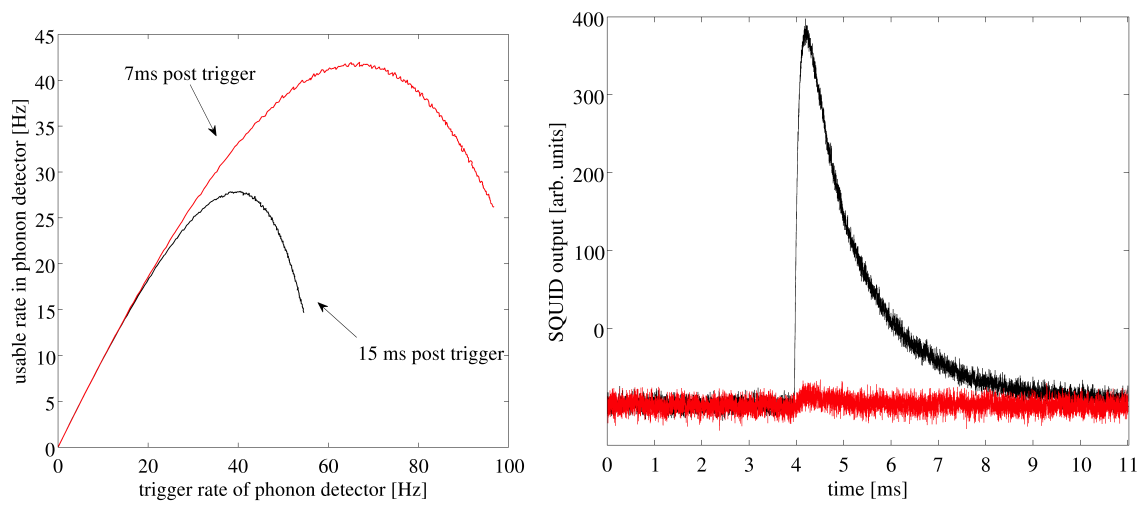


Figure 4.15: Left: Trigger rate of the phonon detector vs. rate in the phonon detector which can be used for analysis (usable rate). The condition for usable pulses is defined as follows: 4 ms before and 3 ms after each pulse must be free of pulses (to avoid pile-up). The results of Monte-Carlo simulations for a pre-trigger of 4 ms and a post-trigger of 7 ms and 15 ms, respectively, are shown. For a post-trigger of 7 ms the optimal trigger rate yields a gain in usable rate by a factor of ~ 1.5 . Right: Nuclear recoil event on oxygen at a recoil energy of ~ 100 keV (phonon pulse: black, light pulse: red). The reduced sample length of 11 ms has only a weak influence on the energy resolution ($\mathcal{O}(1\%)$). However, high-energy events ($\gtrsim 500$ keV) can not be fitted correctly as the pulse does not sufficiently decay below the truncation limit of the standard-event fit (see chapter 3.2.1).

ToFs. A rough cut on neutrons is applied here (between dashed lines).

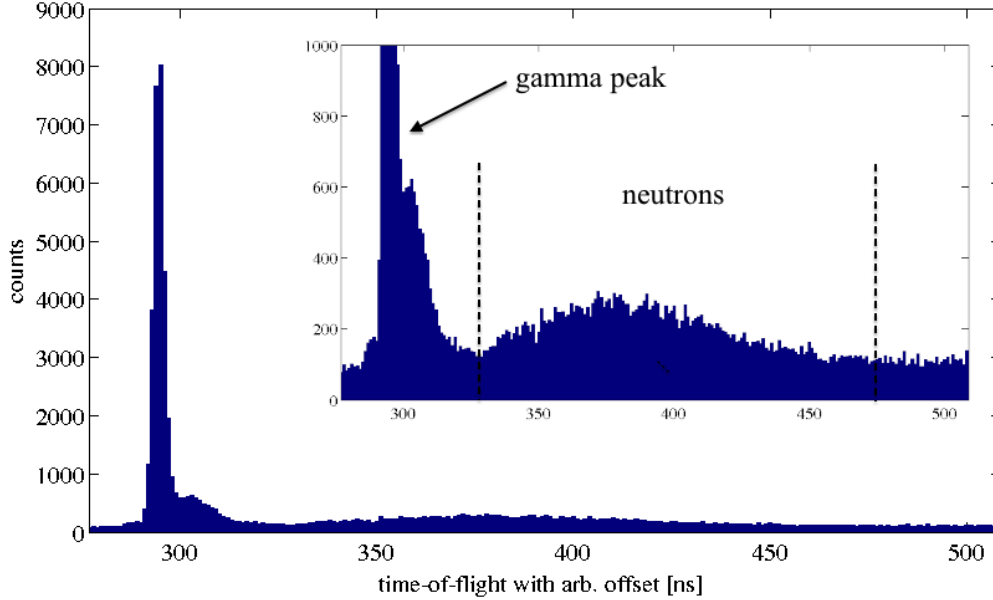


Figure 4.16: Time-of-flight plot of a typical liquid-scintillator detector placed at a fixed scattering angle of $\sim 80^\circ$. The gamma peak has an arbitrary offset due to cables and delays in the pulsing devices but can be used as a reference for the determination of the neutron time-of-flight. A rough cut on neutrons is applied (between dashed lines). The peak visible at ~ 310 ns is probably due to γ -rays that (Compton)-scatter off surrounding material (e.g. cryostat, steel structure) and thus reach the liquid-scintillator detector slightly after the direct γ -rays (prominent gamma peak).

The background in the timing plot is distributed uniformly in time (mainly γ 's) and can further be reduced by exploiting the neutron-gamma discrimination capability of the liquid scintillator detectors (see chapter 4.5.3). In figure 4.17 a discrimination plot of a typical neutron detector is shown.

The sum of double coincidences of all 40 neutron detectors constitute the data subset of candidate events for an additional search for coincident recoils in the cryodetector (triple coincidence). The algorithm searches for cryogenic pulses (timing resolution $\sim 10 \mu\text{s}$) in a time window of ± 0.1 ms around every candidate event. The result is shown in figure 4.18. From the total of ~ 40 million pulses recorded during this beamtime, ~ 400 000 pulses remain in the search window of which ~ 50 000 events are in the peak of real triple coincidences while the rest is accidental background distributed uniformly in time. To further reduce background and extract a "pure" signal of each recoiling nucleus (O, Ca, W), the following cuts are applied to the data:

- **Phonon-energy cut:** From kinematics the expected energy loss of the incident ~ 11 MeV neutrons on each element in the CaWO_4 crystal is known (see chapter 4.4). Depending on the resolution of the phonon detector and angular and spatial resolutions of the whole setup, acceptance bounds for O, Ca and W are defined for this cut.

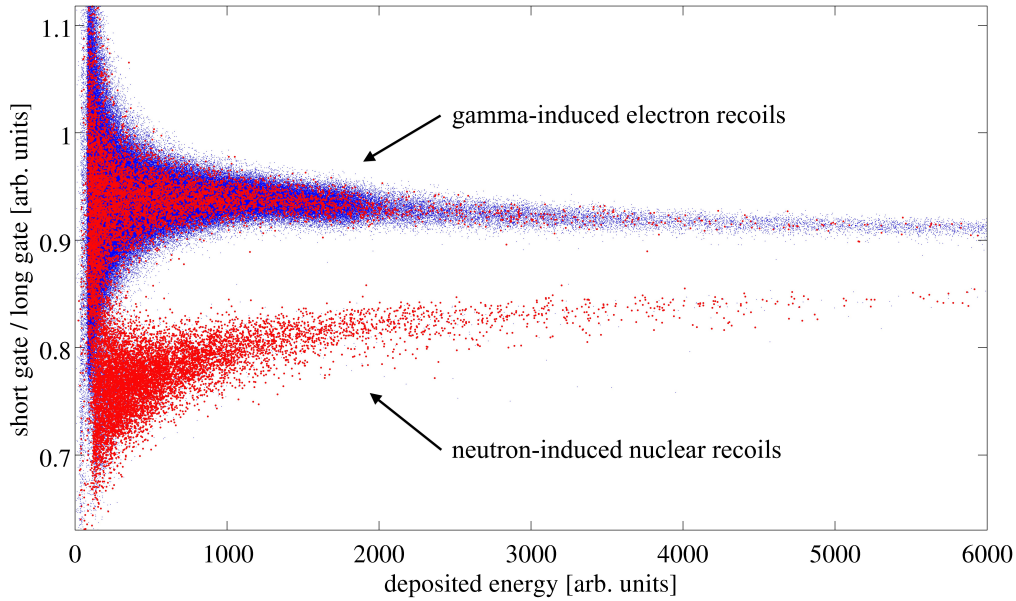


Figure 4.17: Typical discrimination plot of a liquid-scintillator detector. The deposited energy ($1 \text{ [arb. units]} \hat{=} 0.5 \text{ keV}$ deposition by an electron recoil) is plotted versus the ratio of the integration gates (short gate/long gate) applied to the photomultiplier pulses (see chapter 4.5.3). All events recorded are shown in blue while events tagged as neutron events with the correct ToF are highlighted in red. Two bands clearly arise due to the different kinds of incident particles. A cut on the neutron-induced nuclear recoils discriminates possible coincidences of neutrons which are produced by the pulsed ^{11}B beam from accidental background which is mainly constituted by γ -events that are uniformly distributed in time.

- **Nuclear-recoil cut:** Due to the quenching effect, nuclear-recoil events in the cryo-detector can clearly be discriminated from the dominant electron/ γ background above a threshold of $E_r \sim 20 \text{ keV}$ and thus in the entire region of interest for the following analysis.
- **Neutron-energy cut:** Besides the desired monoenergetic neutrons of $\sim 11 \text{ MeV}$ a low-energetic neutron background is produced which can scatter parasitically off the various parts of the setup and mimic triple coincidences. The incident neutron energy can be calculated using the ToF, the exact distances of the experimental setup and the measured energy loss in the phonon detector [79]. Events are accepted if their incident neutron energy is higher than 7 MeV .
- **Neutron-detector cut:** This cut tags valid liquid-scintillator detectors at a scattering angle of 80° . Detectors are excluded from the analysis, e.g., due to instabilities in the PMTs (see chapter 4.5.3). Figure 4.19 shows the accepted devices and their individual detection efficiencies.

The cuts mentioned above reduce the ratio of accidental background to real triple coincidences significantly as shown in figure 4.20. The ratios between O, Ca and W events agree well with the calculated expectations (see chapter 4.4). However, one has to mention that

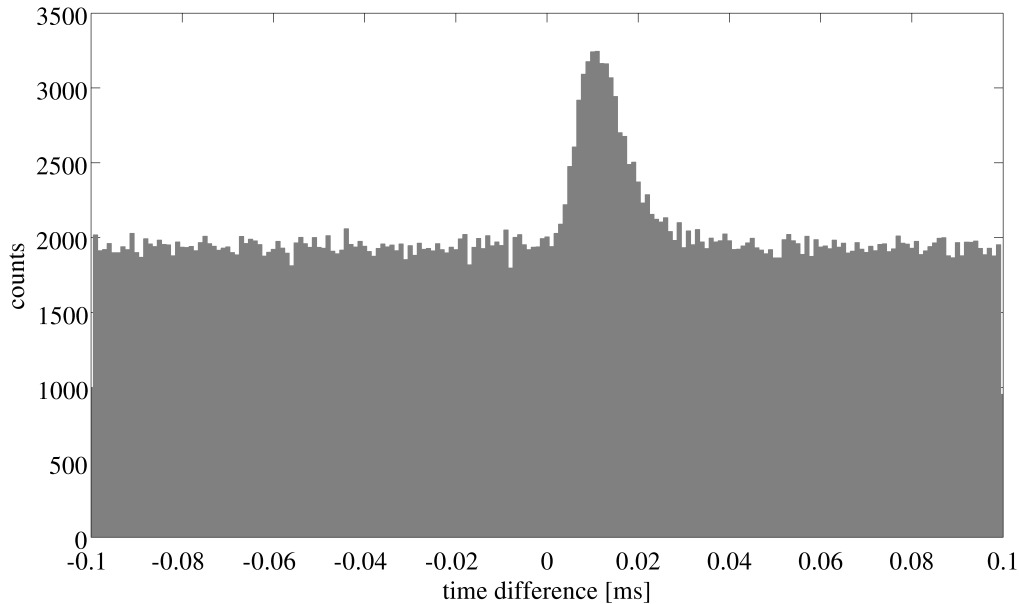


Figure 4.18: Timing spectrum of triple-coincident events from the Oct 2011 beamtime. The x-axis indicates the time difference Δt between double-coincident events (coincidence between accelerator pulse and neutron event in a liquid-scintillator detector) and the closest pulse (in time) in the cryodetector. Besides a constant background due to accidental coincidences distributed uniformly in time, a peak of real triple coincidences arises at $\Delta t \approx 0.015$. The constant offset is due to the onset determination algorithm and has no influence on the data analysis itself [79].

most of the original triple coincidences are due to inelastic scattering in the surrounding of the CaWO_4 detector (the corresponding γ is detected in the phonon detector) and due to low-energy neutron scattering.

To significantly improve the signal-to-background ratio an additional cut on the time distribution of the triple-coincidence search is performed.

- **Coincidence cut:** Only events which are found within $\pm 2\sigma$ around the peak of real triple coincidences in the timing spectrum are accepted. The cut is performed individually for every recoiling nucleus (O, Ca and W) as the peaks are slightly shifted with respect to each other due to an effect of the onset-search algorithm⁶ [79] of the phonon pulses (see figure 4.20).

In the following the focus lies on the identification of W recoils as the QF of O and Ca can be determined using a different method (see chapter 4.9). After all cuts, 92 tungsten recoil events within the Oct 2011 beamtime remain and are identified with an excellent signal-to-background ratio of $\sim 28:1$, see figure 4.21. In figure 4.22, a histogram of the light-yield distribution for recoil energies between 90 keV and 120 keV - and thus in the energy range

⁶The shift of the peaks with respect to each other is due to the onset-search algorithm which does not correct for the individual pulse height (constant fraction) but triggers at a certain threshold [79]. This effect does not affect the functionality of the experiment and the capability to identify the recoiling nucleus.

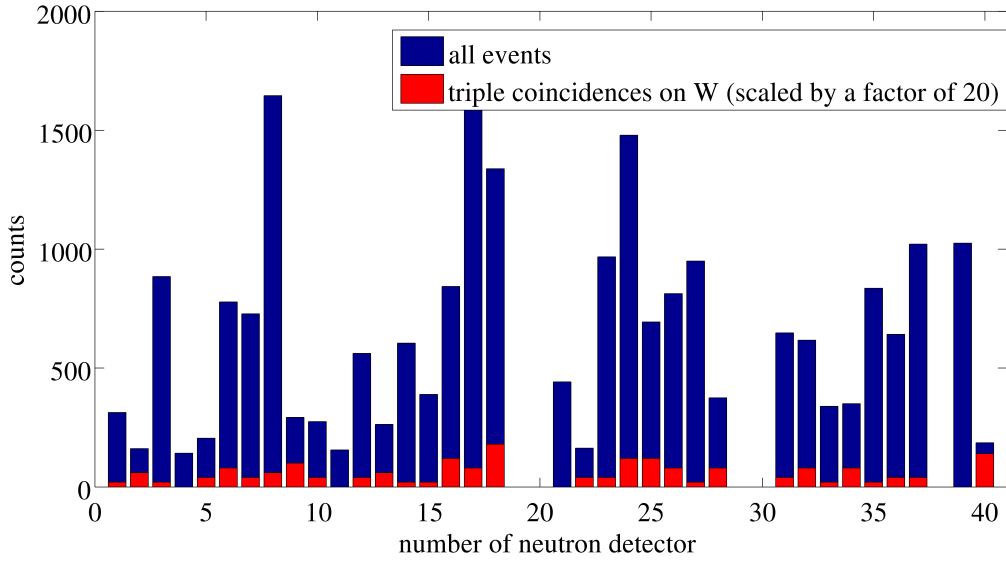


Figure 4.19: Number of detected double coincidences for every liquid-scintillator detector (detector identification number) placed at a fixed scattering angle of 80° . The number of counts is an indication for the efficiency of each detector as all devices have virtually the same distance to the CaWO_4 crystal (~ 1.5 m). In red the number of triple coincidences on tungsten (scaled up by a factor of ~ 20) are shown which are distributed equally within statistical accuracy considering these efficiencies.

in which W events identified with the triple-coincidence technique are expected - is shown. As expected the events identified as W events (red) lie at lower light yields $LY_W \sim 0.02$ compared to the mean of the nuclear-recoil bands (blue, centered at $LY \sim 0.1$) which are obtained from the full data set. In the light-yield plot shown in figure 4.23 the events of the full data set (blue) are plotted together with the triple-coincident W-events (red), however, without the phonon-energy cut applied. The clustering of the tungsten events at a recoil energy of ~ 100 keV at low light yields is a definitive proof that the experimental approach is correct.

4.8.2 Maximum-Likelihood-Analysis

For the analysis of the QF measurement based on the triple-coincidence technique, a dedicated maximum likelihood analysis framework was developed in this thesis and implemented in the *rooFit* analysis framework [103]. For the measurement of the QF of W a correlated maximum likelihood fit including the following data information has been set up:

- The **timing distribution** of the triple coincidences (e.g. shown in figure 4.21) is fitted by a Gaussian accounting for the peak of real coincidences on W and a constant describing the accidental background which is distributed uniformly in time. This fit (called: timing fit) determines the signal-to-background ratio $R_{S/B}$ and the number of identified triple coincident events on W (2σ around the peak).

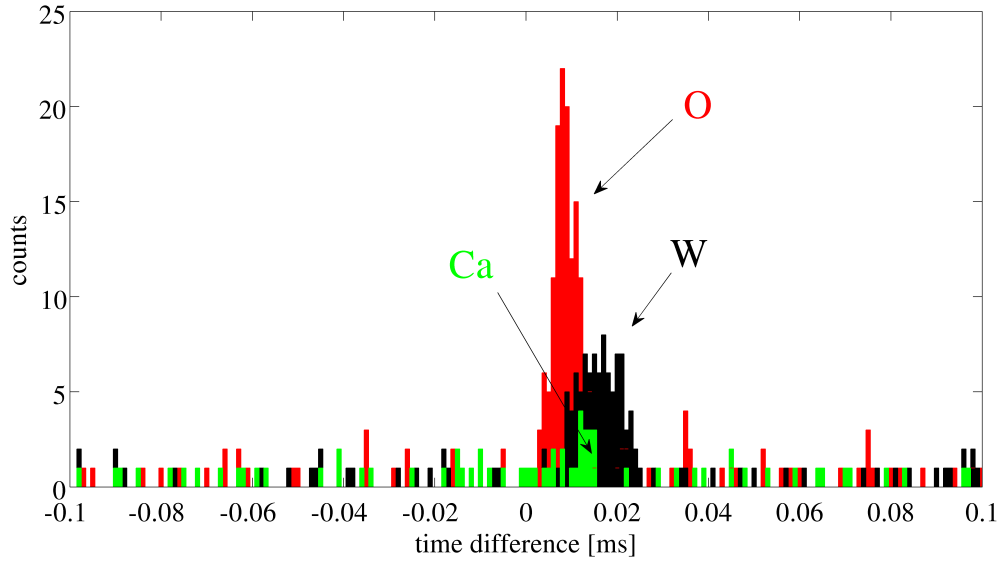


Figure 4.20: Time spectrum of triple coincident events of the Oct 2011 beamtime. The x-axis indicates the time difference Δt between double coincident events (coincidence between accelerator pulse and neutron detection in liquid-scintillator detectors) and the closest pulse (in time) in the cryodetector. Apart from cuts on the incident neutron energy via time-of-flight (neutron-energy cut) and the nuclear recoil band in the cryodetector (nuclear-recoil cut), there are cuts applied on the deposited energy in the cryodetector for each recoiling nucleus individually (phonon-energy cut). The expected recoil energies for an incident neutron energy of ~ 11 MeV and for a detection at a scattering angle of 80° are ~ 100 keV (W), ~ 450 keV (Ca) and ~ 1.1 MeV (O). Three peaks are visible above constant background which are shifted towards positive time differences depending on the pulse height. This effect is due to the onset-search algorithm which does not correct for the individual pulse height (constant fraction) but triggers at a certain threshold [?]

- The continuous light yield (LY) spectrum at the phonon energy of interest $E_r \sim 100$ keV, in the following called **“background” spectrum** which includes O, Ca, and W recoils, is converted into a probability density function (PDF)⁷ P_{bck} . This PDF is used to describe the light-yield distribution of the fraction of triple coincident events which is related to accidental background. The fraction is quantified by $R_{\text{S/B}}$ which is determined by the fit on the timing distribution. The PDF can well be reproduced by O, Ca and W recoils which shows that double scatters and other parasitic background play only a minor role (see chapter 4.9). Nevertheless, even such minor contributions are taken into account by the PDF.
- The **light-yield (LY) distribution** of the triple coincident events are fitted by a Gaussian (W contribution) and the PDF (“background” spectrum). Their ratio is determined by the timing fit. The mean of the Gaussian yields (according to equation

⁷The probability density function (PDF) is implemented as “Keys PDF” in RooFit [103] which models an arbitrary input dataset as a superposition of Gaussians, one for each data point. Thereby, each data point contributes with $1/N$ (number of counts N) to the total integral of the PDF. For further details see [104].

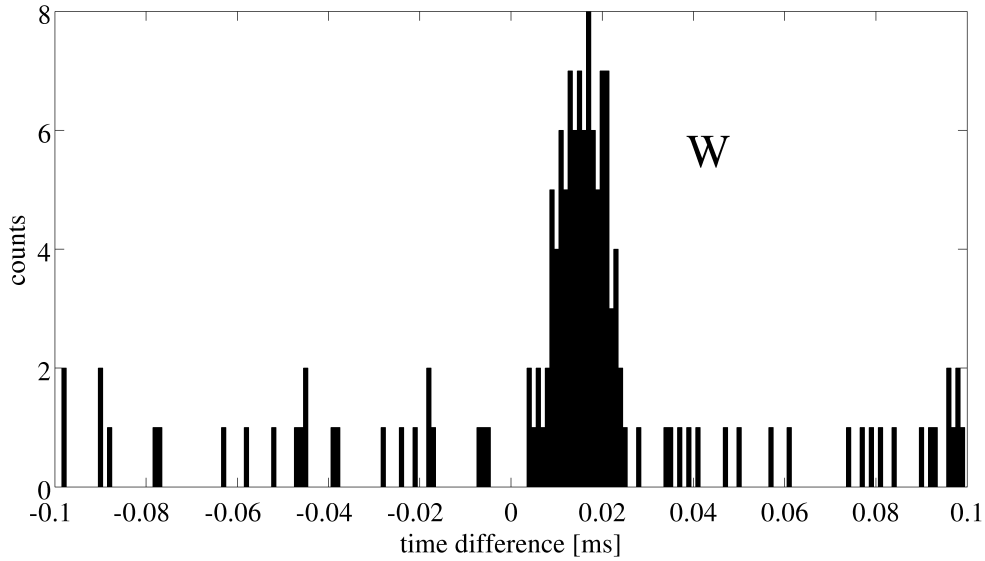


Figure 4.21: Time spectrum of triple-coincident events on tungsten from the Oct 2011 beam-time. The x-axis indicates the time difference Δt between double coincident events (coincidence between accelerator pulse and neutron detection in liquid-scintillator detectors) and the closest pulse (in time) in the cryodetector. In addition, cuts on the deposited energy in the phonon detector (phonon cut on tungsten events), the incident neutron energy via time-of-flight (neutron cut), and the nuclear recoil band in the cryodetector (NR cut) are applied to the data; see main text for details. Above a constant background due to accidental coincidences a significant peak of real triple coincidences at $\Delta t \approx 0$ is visible. The constant offset $\Delta t = 15.3\mu\text{s}$ and the width $\sigma_t = 4.8\mu\text{s}$ of the peak originate from uncertainties of the onset determination of the phonon pulses (see text). The fit shows that in case of this beamtime, tungsten events can be identified with an excellent signal-to-noise ratio of $R_{S/N} \approx 28.4$.

4.2) the QF of pure W recoils in CaWO_4 .

Both likelihood distributions, \mathcal{L}_t for the triple-coincidence times t_i and \mathcal{L}_{LY} for the triple-coincidence LY values LY_i selected as triple coincident events, are maximized simultaneously. \mathcal{L}_t and \mathcal{L}_{LY} are given by the following equations:

$$\mathcal{L}_t = \prod_i^{n_t} R_S \cdot \frac{1}{\sqrt{2\pi}\sigma_t} \exp\left(-\frac{(t_i - t_{\text{mean}})^2}{2\sigma_t^2}\right) + (1 - R_S) \cdot \frac{1}{\Delta t_{\text{plot}}} \quad (4.17)$$

where t_{mean} and σ_t are the mean time and the width of the timing peak, respectively, R_S is the ratio of the amplitudes of the Gaussian to the the accidental background, n_t is the number of events in the timing data set and Δt_{plot} is the total range of the timing spectrum (here $\Delta t_{\text{plot}} = 0.2\text{ ms}$). Furthermore, the following equation holds:

$$\mathcal{L}_{LY} = \prod_i^{n_{LY}} A_W \frac{1}{\sqrt{2\pi}\sigma_W(LY_W)} \cdot \exp\left(-\frac{(LY_i - LY_W)^2}{2\sigma_W(LY_W)^2}\right) + (1 - A_W) \cdot P_{\text{bck}}(LY_i) \quad (4.18)$$

where LY_W and σ_W are the mean and the width of the W peak, respectively. The relation $\sigma_W(LY_W)$ is determined by a separate likelihood fit which is applied to the electron-recoil

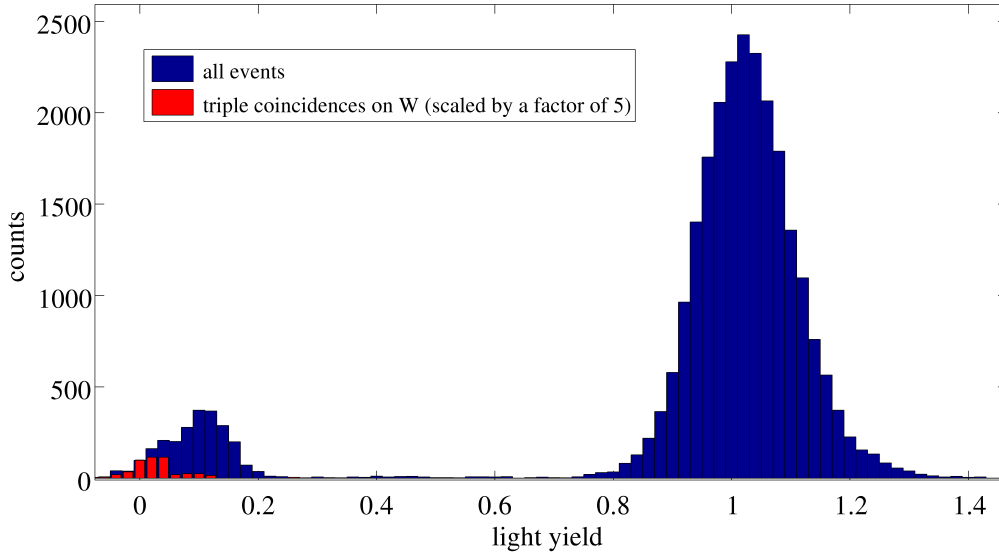


Figure 4.22: Light-yield histogram of the recoil-energy interval $90 \text{ keV} \leq E_r \leq 120 \text{ keV}$ for the full data set (blue) and the 92 events identified by the triple-coincidence method (red) centered at a light yield of ~ 0.02 . The electron-recoil band is visible at $LY \sim 1$ while the nuclear-recoil bands are centered at $LY \sim 0.1$. For illustration, the coincident events are scaled up by a factor of 5.

band of the combined beamtime data. The fit procedure according to equations 3.3 and 3.4 is presented in detail in chapter 3.2.4. The fit results are listed in table 4.2. P_{bck} is the PDF of the “background” spectrum and

$$n_{\text{acc}} = (1 - R_S) \frac{4\sigma_t}{\Delta t_{\text{plot}}} n_t \quad (4.19)$$

is the number of accidental background events within the $2\text{-}\sigma$ acceptance bounds ($4 \cdot \sigma_t$) of the timing fit. The fraction A_W of signal events which are inside the $2\text{-}\sigma$ acceptance bounds around the peak of real coincidences can then be calculated as

$$A_W = \frac{n_{LY} - n_{\text{acc}}}{n_{LY}} \quad (4.20)$$

where n_{LY} is the number of events in the LY data set.

The total likelihood function is thus the product of the single likelihood functions. Instead of maximizing the total function, the best fit - for technical reasons - is obtained by minimizing the negative logarithm:

$$\mathcal{L}_{\text{tot}} = -\ln(\mathcal{L}_{LY} \cdot \mathcal{L}_t). \quad (4.21)$$

The signal-to-background ratio can be obtained by the following equation:

$$R_{S/B} = \frac{A_W}{1 - A_W}. \quad (4.22)$$

The analysis framework was developed within the object-oriented program ROOT developed by CERN with the extension ROOFIT [103]. The statistical errors of all components of the

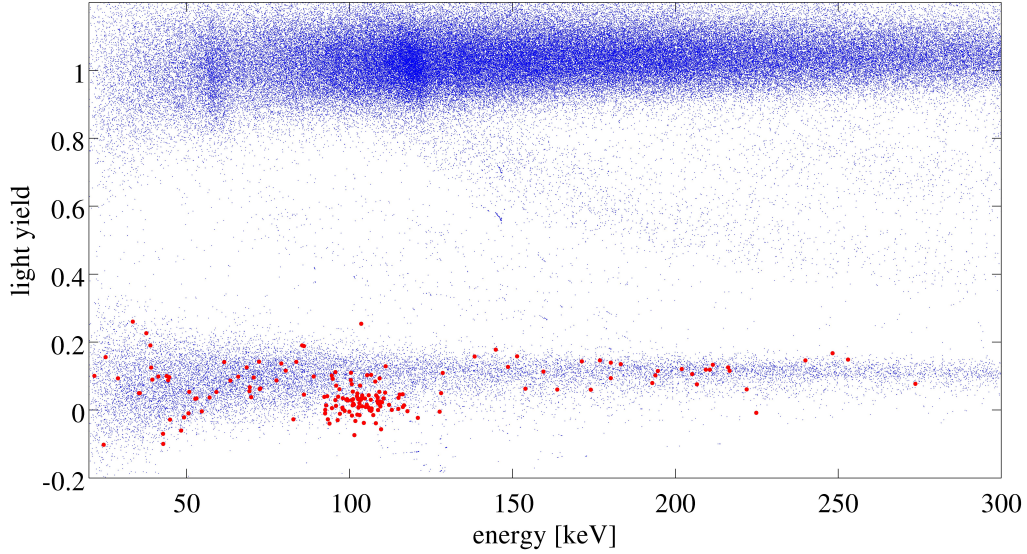


Figure 4.23: Lighth-yield plot of a data subset (426 227 events) acquired during the Oct 2011 beamtime. Highlighted (red) are triple-coincident events where cuts on the neutron energy, the nuclear recoil band and the triple coincidence time (2-sigma acceptance around peak) are applied, but the phonon energy has been left free. Around a phonon energy of 103.5 keV a clear accumulation of tungsten recoil events at lower light yields (~ 0.02) can be observed.

correlated maximum-likelihood fit are automatically included in the total statistical error of the free parameters.

parameter	combined beamtimes	Oct 2011
p_0	1.065	1.043
p_1	$-1.400 \cdot 10^{-5}$	$-3.001 \cdot 10^{-5}$
p_2	$6.935 \cdot 10^{-2}$	$9.691 \cdot 10^{-2}$
p_3	147.0	149.7
S_0	5.52 (f)	5.53 (f)
S_1	0.384	0.308
S_2	$1.88 \cdot 10^{-3}$	$1.43 \cdot 10^{-3}$

Table 4.2: Fit results according to equations 3.3 and 3.4 in chapter 3.2.4 for the electron recoil band of the combined data set used for the triple coincidence analysis (chapter 4.8) and of the data subset of the Oct 2011 beamtime used for the energy-dependent QF analysis (chapter 4.9). The errors are negligible for the QF analysis performed in the present thesis. (f) indicates that the parameter was fixed in the fit. The parameter S_0 was determined individually by the baseline noise.

4.8.3 Results for the QF of W

The neutron scattering facility at the MLL accelerator has been set up and optimized over years to measure particularly the QF of tungsten which has not been measured at mK temper-

atures in CaWO_4 before with the required precision. It was shown in chapter 4.8.1 exemplarily for the Oct 2011 beamtime that the triple-coincidence technique is fully functional and - due to the improvements performed in the present thesis - statistics are now sufficient to measure the QF of W with the required precision of $\sim 10\%$ within 2-3 weeks of beamtime. This technique allows to separate W recoil events - which in the considered energy range are not resolvable directly within the dominant O and Ca contributions - from the continuous nuclear recoil band.

Three successful beamtimes of ~ 1 week each (beamtime Oct 2011, beamtime Feb 2012, beamtime Aug 2012) have been performed in this thesis with the setup described in chapter 4.5. The functionality of the setup and the measurement technique presented in chapter 4.8.1 is the same for all three beamtimes, however, in Feb and Aug 2012 there have been hardware problems with the data acquisition which resulted in a lower signal-to-background ratio⁸.

The full data set of ~ 3 weeks of measuring time has been combined and 158 events are selected in the triple-coincidence acceptance window $t_{\text{mean}} \pm 2\sigma_t$. In figure 4.24, the total timing distribution (top right), the “background” spectrum (top left), and the total light-yield distribution (bottom) are shown. The data points in the histograms are depicted as black points with the corresponding (statistical) error bars. The maximum-likelihood-analysis described in detail in chapter 4.8.2 is applied to the total data set. The timing distribution is fitted by a Gaussian (black) and a constant (red). The ratio R_S of the amplitude of the Gaussian and the constant determines the fraction of accidental background events. The “background” spectrum is described by a PDF (see chapter 4.8.2) and used to account for the accidental background in the light-yield distribution (red). Therein the peak of real coincidences on W - of which the mean value actually determines the QF of W - is fitted by a Gaussian (black). All curves in figure 4.24 show the best fit of the (correlated) maximum-likelihood analysis. The results for the free parameters are summarized in table 4.3 together with the total statistical errors obtained by the correlated fit.

The QF of tungsten has been measured for the first time at mK temperatures and for

free parameter	best fit value
$t_{\text{mean}}[\text{ms}]$	0.0158 ± 0.0005
$\sigma_t[\text{ms}]$	0.0048 ± 0.0004
$R_{S/B}$	7.0 ± 0.6
LY_W	0.0208 ± 0.0024
QF_W	0.0196 ± 0.0022
$1/QF_W$	$51.0^{+6.5}_{-5.1}$

Table 4.3: Results of the correlated maximum-likelihood fit with 1σ errors derived with the MINOS algorithm (asymmetric errors included) [103]. t_{mean} is the position of the peak of triple-coincidences in the timing plot, σ_t is the width of the latter, $R_{S/B}$ is the signal-to-background ratio, LY_W is the mean of the LY distribution of the identified W-events, and QF_W is the final result for the QF of W.

⁸Due to a hardware failure in the VME controller (see chapter 4.5.4) the signal which is used to synchronize the TDC clock [79] could not be triggered correctly in the beamtimes Feb and Aug 2012. Therefore, a certain fraction ($\mathcal{O}(10\%)$) of the real triple coincidences had incorrect timestamps. These misidentified events do not lie in the peak of real coincidences but have random times. This effect increases the signal-to-background ratio, however, does not affect the functionality of the experiment. Studies to further investigate and solve these hardware problems for future experiments are ongoing [105].

recoil events distributed uniformly in the bulk of the CaWO_4 crystal with the projected precision of $\sim 10\%$ (1σ C.L.). The final result of the maximum likelihood analysis is $QF_W = 0.0196 \pm 0.0022$. Its more intuitive reciprocal value is $1/QF_W = 51.0_{-5.1}^{+6.5}$.

However, one has to consider that this value is related to the CaWO_4 crystal (cw520) used in the measurement presented here. As discussed in chapter 4.10, the QFs vary from crystal to crystal in the order of $\sim 10\%$. A model to describe this effect was developed in this thesis (see chapter 4.10).

4.9 Energy-Dependent QF Analysis of CaWO_4 at mK Temperatures

4.9.1 Independent Fits of the Nuclear Recoil Bands

Due to the finite resolution of the light detector the nuclear recoil bands strongly overlap especially at low energies (< 200 keV) and it was not possible to directly separate the individual contributions by O, Ca and W in earlier measurements. However, for the measurement presented here - due to the high recoil energies up to ~ 1800 keV, an improved cryogenic setup (e.g. resolution of light detector, long-term stability) and the enormous amount of statistics acquired during the beamtimes - the situation has changed. Above $E_r \sim 300$ keV where no W recoils are expected due to kinematics the contributions of O and Ca can be sufficiently separated.

To determine the QFs of O and Ca above 300 keV, the nuclear recoil band is cut into phonon-energy intervals of 20 keV from 300 keV to 1500 keV. The projection of every interval onto the light-yield (LY) plane is fitted by Gaussians. Below 1000 keV each slice is described by two Gaussians (O, Ca) and above 1000 keV only one Gaussian is used since (due to kinematics) only O recoils are expected in this energy range. The width of the Gaussians are correlated to the width of the e^-/γ band and to the QF according to equation 3.10 (see chapter 3.2.4 for details). This correlation reduces the number of free parameters and hence leads to a smaller error of the remaining parameters. In figure 4.25 the results of these individual fits (O and Ca) are shown together with the result of the QF of W measured by the triple coincidence technique (see chapter 4.8.3). In the considered energy region, the QFs of O and Ca can be determined with small errors ($\lesssim 5\%$) and an **energy dependence** could be observed for the first time.

4.9.2 Basic Considerations for a Energy-Dependent QF Analysis

It is clearly visible in figure 4.25 that the QF of O rises towards lower energies while this effect is much less pronounced for Ca recoils. The monotonic rise of the QFs towards lower recoil energies E_r is qualitatively compatible with phenomenological models addressing the mechanism of light quenching in CaWO_4 [53, 68, 90] (see chapter 4.2). Furthermore, these models predict that the energy-dependence is indeed reduced the higher the mass of the recoiling nucleus which is in nice agreement with the measurement. This shows that the data acquired within this work is not consistent with previous assumptions that the QFs are constant over the energy range considered in CRESST detector modules ($E_r \leq 300$) [25].

In chapter 4.9.3 a method is developed which allows to determine the QFs over the entire energy range. The maximum-likelihood analysis used to account for energy-dependent QFs over the entire nuclear-recoil band relies on the following assumptions:

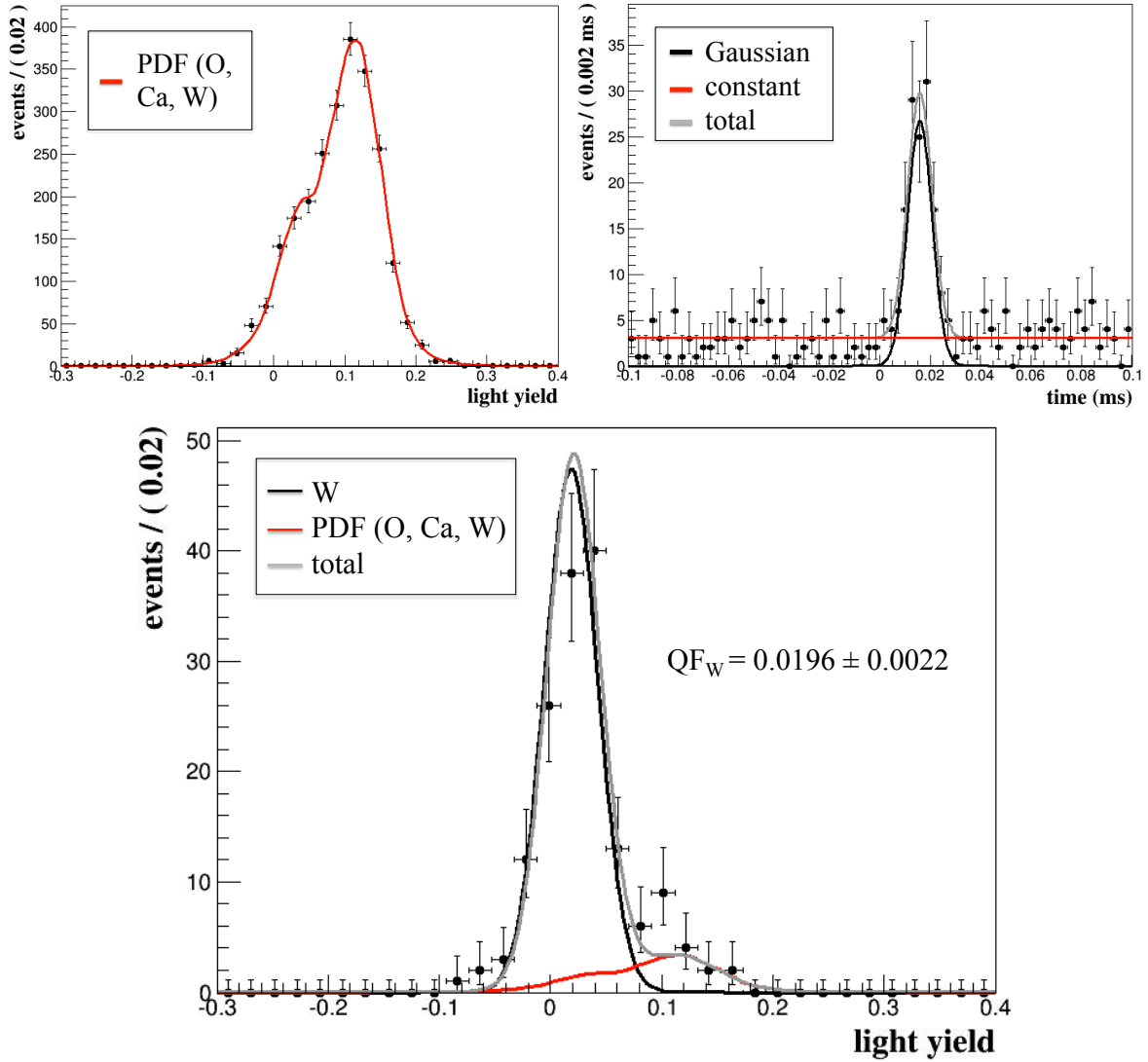


Figure 4.24: Final result of the tungsten QF in CaWO_4 measured at mK temperatures with the triple-coincidence technique. Shown are the results of the maximum-likelihood analysis including the following data information (see text): the “background” light-yield spectrum at $E_r \sim 100$ keV (top left) accounting for the light-yield distribution of the accidental coincidences along with the PDF (red) derived from the data, the timing spectrum of triple coincidences (top right) which is fitted by a Gaussian (black) and a constant (red), and the light-yield distribution of the triple-coincident recoil events (bottom) which is fitted by the PDF (red) accounting for the “background” and by a Gaussian (black) to account for the peak of real coincidences on W. In the data of three beamtimes (Oct 2011, Feb 2012, Aug 2012), a total of 158 triple coincident events are identified with a signal-to-background ratio of $R_{S/B} \approx 7.0$. At the investigated recoil energy of $E_r \approx 100$ keV the center of the W distribution is found at a light yield of $LY_W = 0.0208 \pm 0.0024$ which corresponds to a Quenching Factor of $QF_W = 0.0196 \pm 0.0022$. Its more intuitive reciprocal value is $1/QF_W = 51.0^{+6.5}_{-5.1}$.

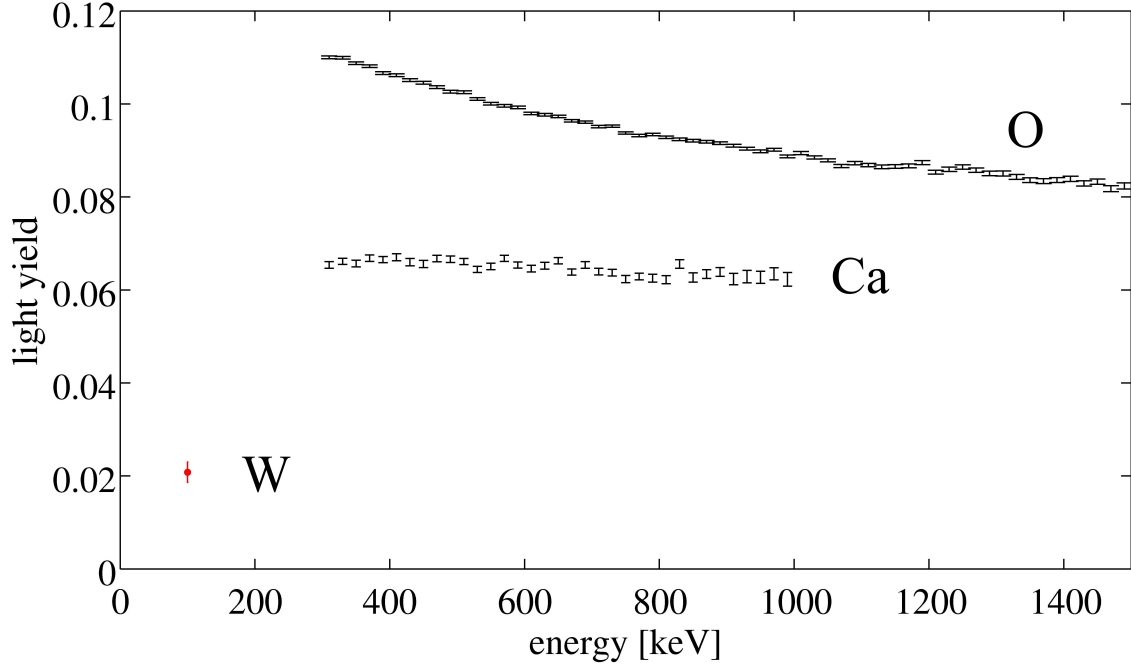


Figure 4.25: Results of individual Gaussian fits applied to the data acquired in the Oct 2011 beamtime for O and Ca above a recoil energy $E_r = 300$ keV. Above $E_r \sim 250$ keV no W recoil are expected anymore from incident ~ 11 MeV neutrons. For the same reason, above $E_r \sim 1000$ keV only O scatters are observed. The data is cut into bins of 20 keV each in the energy range of 300-1500 keV. For $E_r < 300$ keV the overlap of the individual nuclear-recoil bands is too high to fit the recoil bands individually. The results of the fits show that the QFs are energy dependent, clearly visible for O and less pronounced for Ca. The QF of W measured at ~ 100 keV with the extensive triple-coincidence measurement presented in chapter 4.8.3 is also shown (red error bar).

- According to equation 4.1 which phenomenologically describes the electron/gamma band, an **energy-dependent parametrization of the nuclear recoil bands** is proposed here:

$$LY_x(E_r) = LY_x^\infty \left(1 + f_x \cdot \exp\left(\frac{-E_r}{\lambda_x}\right) \right) \quad (4.23)$$

where $LY_x(E_r)$ is the mean of the corresponding nuclear recoil band of the nucleus x . The specific parameters, LY_x^∞ which is the mean of the corresponding light-yield distribution at $E_r = \infty$, f_x which accounts for the total strength of the energy dependence, and λ_x which is the scale of the energy dependence are introduced.

- As discussed above, the energy dependence should decrease the higher the mass of the recoiling nucleus. Therefore, in good approximation the **QF of W is assumed to be constant** over the considered energy range in which W recoils are expected (0-250 keV). The value of $QF_W = 0.0196 \pm 0.0022$ was determined with high precision by the triple-coincidence technique presented in chapter 4.8.3.

4.9.3 Correlated Likelihood Fit for the Energy-Dependent QF Analysis

Firstly as presented in chapter 3.2.4, the electron recoil band can be fitted (maximum-likelihood fit) by a Gaussian with an energy-dependent mean

$$E_L = (p_0 \cdot E_r + p_1 \cdot E_r^2) \cdot \left(1 - p_2 \exp\left(-\frac{E_r}{p_3}\right)\right)$$

and width

$$\sigma_\gamma(E_L) = \sqrt{S_0 + S_1 \cdot E_L + S_2 \cdot E_L^2}$$

with the parameters S_0 , S_1 , S_2 , p_0 , p_1 , p_2 , and p_3 . E_r and E_L are the calibrated energies in the phonon and the light detector, respectively. Reconsidering equation 4.1, for the light yield of the e^-/γ band the following relation holds:

$$LY_\gamma(E_r) = \frac{E_L(E_r)}{E_r} = (p_0 + p_1 \cdot E_r) \cdot \left(1 - p_2 \exp\left(-\frac{E_r}{p_3}\right)\right)$$

For the reduced light yield $LY_x(E_r)$ the width $\sigma_x^{LY}(E_r, LY_x(E_r))$ of the nuclear recoil band (in the light-yield plane) can be calculated:

$$\sigma_x^{LY}(E_r, LY_x(E_r)) = \sqrt{(\sigma_\gamma^{LY}(LY_x(E_r) \cdot E_r))^2 - (\sigma_{\gamma,P}/E_r)^2 + \sigma_{x,P}^2 \cdot (LY_x(E_r))^2} \quad (4.24)$$

with $\sigma_{\gamma,P}$ being the phonon resolution derived from the ²⁴¹Am γ -line at $E_r = 59.5$ keV (and approximated as a constant over the entire energy range) and $\sigma_{x,P}$ being the phonon resolution for the nuclear recoil band. In this particular case, also broadening effects of the light-yield resolution due to the energy binning ΔE_r in the phonon energy have to be considered. The phonon-energy resolution of the nuclear recoil bands is approximated by

$$\sigma_{x,P} \approx \sigma_\gamma^P + \frac{\Delta E_r}{2}. \quad (4.25)$$

According to equation 4.23, the energy dependence of the light-yield distribution of the individual nuclear-recoil bands is described by:

$$LY_x(E_r) = LY_x^\infty \left(1 + f_x \cdot \exp\left(\frac{-E_r}{\lambda_x}\right)\right).$$

To set up a correlated maximum likelihood fit the data acquired during the Oct 2011 beamtime (285 224 events) of the nuclear recoil band is cut (in the phonon energy plane) into bins of 10 keV up to 1000 keV, bins of 20 keV above 1000 keV and bins of 50 keV above 1400 keV up to the maximum energy of 1800 keV. Within each phonon-energy bin j of mean energy E_j , every event i with the light yield $LY_{i,j}$ has a likelihood contribution:

$$\mathcal{L}_{i,j}(E_j, LY_{i,j}) = \sum_{x=x_j} A_x(E_j) \cdot \frac{1}{\sqrt{2\pi} \sigma_x^{LY}(E_j, LY_x(E_j))} \cdot \exp\left(-\frac{(LY_{i,j} - LY_x(E_j))^2}{2 \sigma_x^{LY}(E_j, LY_x(E_j))^2}\right) \quad (4.26)$$

with $LY_x(E_j)$ being the mean of the light-yield distribution at the phonon energy E_j (see equation 4.23), $\sigma_x(E_j, LY_x(E_j))$ the 1-sigma width of the respective nuclear recoil band at a certain phonon energy, $A_x(E_j)$ the fraction of events of each type of recoiling nucleus

$$x_j = \begin{cases} \text{O,Ca,W} & \text{for all } j \mid E_j < 250 \text{ keV} \\ \text{O,Ca} & \text{for all } j \mid 250 \text{ keV} \leq E_j \leq 1050 \\ \text{O} & \text{for all } j \mid E_j > 1050 \text{ keV} \end{cases} \quad (4.27)$$

which contribute in the considered energy bin due to kinematics. The full likelihood function is then

$$\mathcal{L}_{\text{tot}} = -\ln \left(\prod_{j=1}^m \prod_{i=1}^{n_j} \mathcal{L}_{i,j}(E_j, LY_{i,j}) \right) \quad (4.28)$$

where m is the total number of bins with n_j events each. For technical reasons the product of the single likelihood functions is not maximized but the negative logarithm of it is minimized, the so-called log-likelihood minimization [86].

4.9.4 Results of the Energy-Dependent QF Analysis

The maximum-likelihood analysis developed in chapter 4.9.3 is applied to the well-calibrated data set of $\sim 50\%$ of the Oct 2011 beamtime (see chapter 4.7). All other data of the three beamtimes was recorded in a measurement mode which was optimized for the triple-coincidence method and can be calibrated only up to $E_r \sim 500$ keV.

The correlated fit converges over the entire energy range from 20 keV up to 1800 keV. Below ~ 20 keV there are unwanted effects due to the trigger threshold and above 1800 keV there are no events expected due to kinematics. It should be emphasised here that except for the two well-motivated assumptions - the (constant) value of the QF of W which was measured with high precision by the triple coincidence method within the same data set (chapter 4.8.3) and the energy-dependent parametrization of the QFs according to equation 4.23 - all parameters in particular the amplitudes of the individual Gaussians $A_x(E_j)$ are left free in the fit.

The results for the free parameters of the correlated fit which describes the means of the nuclear recoil bands according to equation 4.23 are presented in table 4.4.

Therein only statistical errors of the fit are included which due to high statistics in the

nucleus	LY_x^∞	f_x	λ_x
O	0.07908 ± 0.00002	0.7088 ± 0.0008	567.1 ± 0.9
Ca	0.05949 ± 0.00078	0.1887 ± 0.0022	801.3 ± 18.8
W	0.0208 ± 0.0022	-	-

Table 4.4: Results of the correlated fit to the nuclear-recoil data set of $\sim 50\%$ of the Oct 2011 beamtime. According to equation 4.23 these parameters determine the mean of the light-yield distribution of O and Ca over the whole energy range. The parametrization agrees nicely with the data and the fact that the energy dependence is reduced for heavier recoiling particles supports phenomenological models (see chapter 4.2) and justifies the procedure that the W contribution is kept constant in the fit. The value of LY_W has been measured with high precision by the triple coincidence method presented in chapter 4.8.3.

nuclear-recoil band are negligible compared to the systematic errors discussed below. In figure 4.26, two-dimensional histograms of the energy-LY plane of data acquired during the Oct 2011 beamtime (50% of total data) are presented. The 80%-acceptance bounds (1.28σ) of the three constituents of CaWO_4 derived from the results of the correlated fit are depicted: full lines for O, dashed lines for Ca and dashes-dotted lines for W. The 80%-acceptance bounds of the e^-/γ band (figure 4.26 top) are derived by an individual maximum-likelihood fit which is presented in chapter 3.2.4. The data nicely agrees with the fit results which is in particular visible for O which dominates the spectrum over a wide energy range. There is a feature in

the (nuclear-) recoil spectrum at ~ 220 keV due to a resonance in the neutron-scattering cross section on O [81] which is nicely enclosed by the acceptance bounds of O.

Histograms in the LY plane of selected energy intervals are shown in figure 4.27 together with the Gaussians for O (red), Ca (green) and W (black) according to the results of the correlated fit (see chapter 4.9.3). Over the entire energy range, the data is well-described by the parametrization chosen.

While statistical errors of the correlated fit are very small due to the high statistics in the data set (see table 4.4) the systematic errors have to be discussed in more detail:

- Systematic uncertainties due to the phonon-detector **calibration** are negligible as the phonon detector has been calibrated with various γ -sources up to ~ 1400 keV. Here, only statistical errors contribute. The light detector is calibrated with the 122 keV γ -line of ⁵⁷Co which is the convention for the CRESST experiments. Possible deviations from linearity are accounted for by the parameters p_0 and p_1 in equation 4.1 (chapter 4.1). A deviation from linearity at small light energies cannot be completely excluded but there are no signs for it in the presented data or in any comparable experiments with CRESST-like detectors.
- The **contribution of W** is kept constant over the whole energy range from 20 keV to 250 keV at the value measured by the triple-coincidence method. A possible energy dependence and a variation of the measured value could affect the O and Ca contribution. Therefore, the fit was repeated with LY_W changed inside its 1σ error bounds. The maximal deviation from the best fit is conservatively assumed as systematic uncertainty.
- **Different parametrizations**, e.g. a 1st-order (for Ca) or 2nd-order polynomial (for O) do not describe the data in the entire energy range. Nevertheless, a correlated fit assuming such a parametrization converges up to phonon energies of ~ 1000 keV and the deviations to the parametrization according to equation 4.23 (see chapter 4.9.2) are included in the error bars.
- As an additional cross-check, a correlated fit has been performed only in the region where the contributions of O and Ca can be directly separated (300 keV to 1800 keV). Deviations between an extrapolation to lower energies and the best fit of the total data set are also accounted for as systematic error.

The statistic and systematic uncertainties are combined linearly to derive the overall error⁹. In figure 4.28, the final energy-dependent light-yield distributions of O, Ca and W with statistical and systematic errors are shown (red error bars). Furthermore, the results of the individual Gaussian fits (O and Ca) above 300 keV which are discussed in chapter 4.9.2 and in which all parameters have been individually left free are also presented (black error bars). Both techniques are in perfect agreement with each other which confirms again the choice of the parametrization.

The Quenching Factor (QF) is calculated by combining equation 4.2 (see chapter 4.1) and

⁹The combination of the systematic error is not trivial here. Every single source of possible uncertainty was investigated very conservatively. Those investigations constituted rather extreme tests of the fit procedure and parametrization compared to a realistic quantification of the systematic error. Finally, the total systematic errors for every recoil energy was determined by the maximal deviation from the best fit value.

The statistical errors of the correlated fit are negligible (see table 4.4). Conservatively, the statistical errors obtained by the independent Gaussian fits (see section 4.9.1) are included.

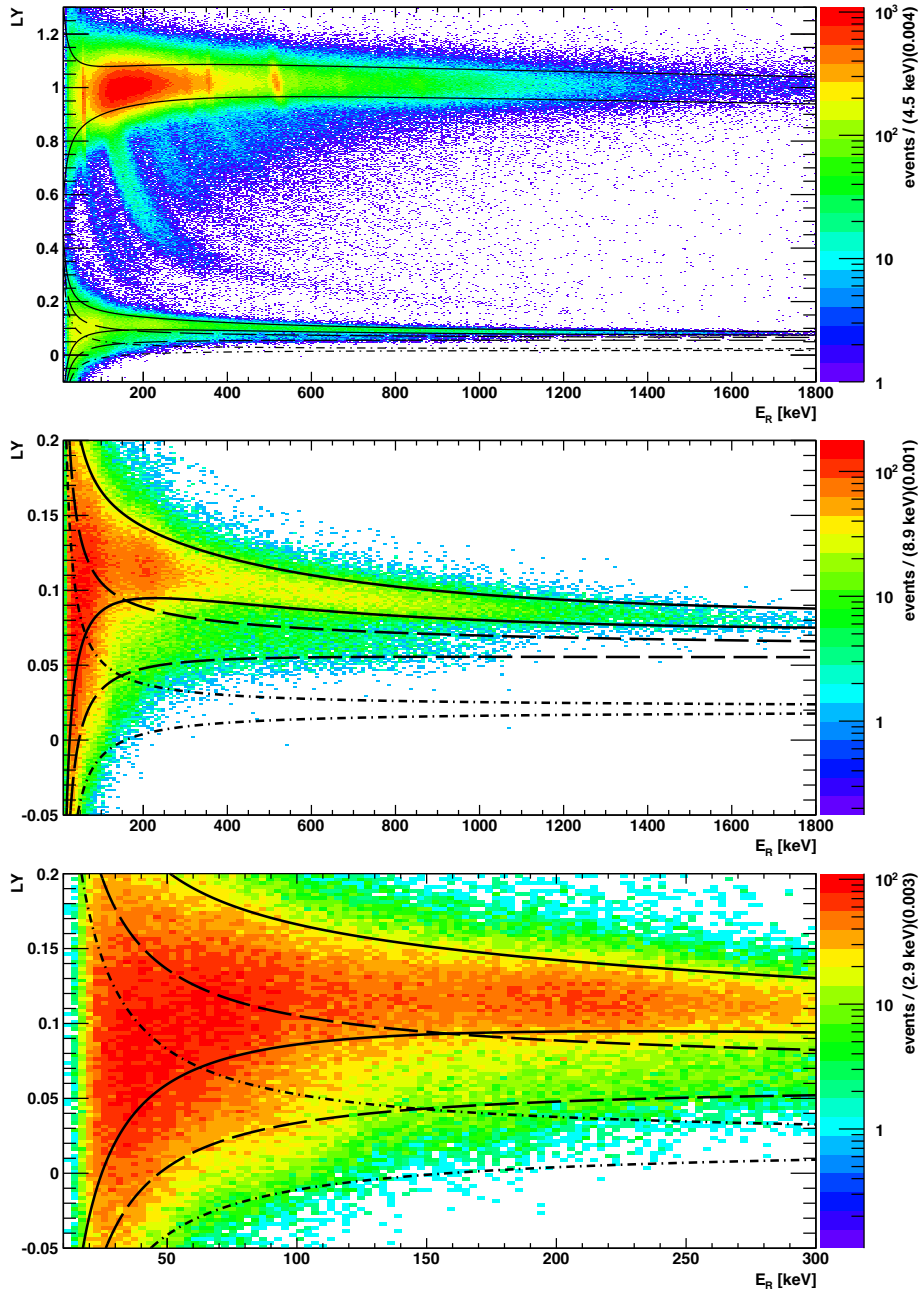


Figure 4.26: Two-dimensional histograms of the recoil energy- LY plane of the data acquired during the Oct 2011 beamtime (50% of the total data set, see text). The 80%-acceptance bounds (1.28σ) of the nuclear-recoil bands of O (full lines), Ca (dashed lines), and W (dashed-dotted lines) derived by the energy-dependent QF analysis and of the e^-/γ band (full lines, at $LY \sim 1$) are depicted. The middle and lower figures show zoomed-in regions for lower values of LY and recoil energy E_R . The feature in the (nuclear-) recoil spectrum at ~ 220 keV due to a resonance in the neutron-scattering cross section on O [81] is nicely enclosed by the acceptance bounds of O.

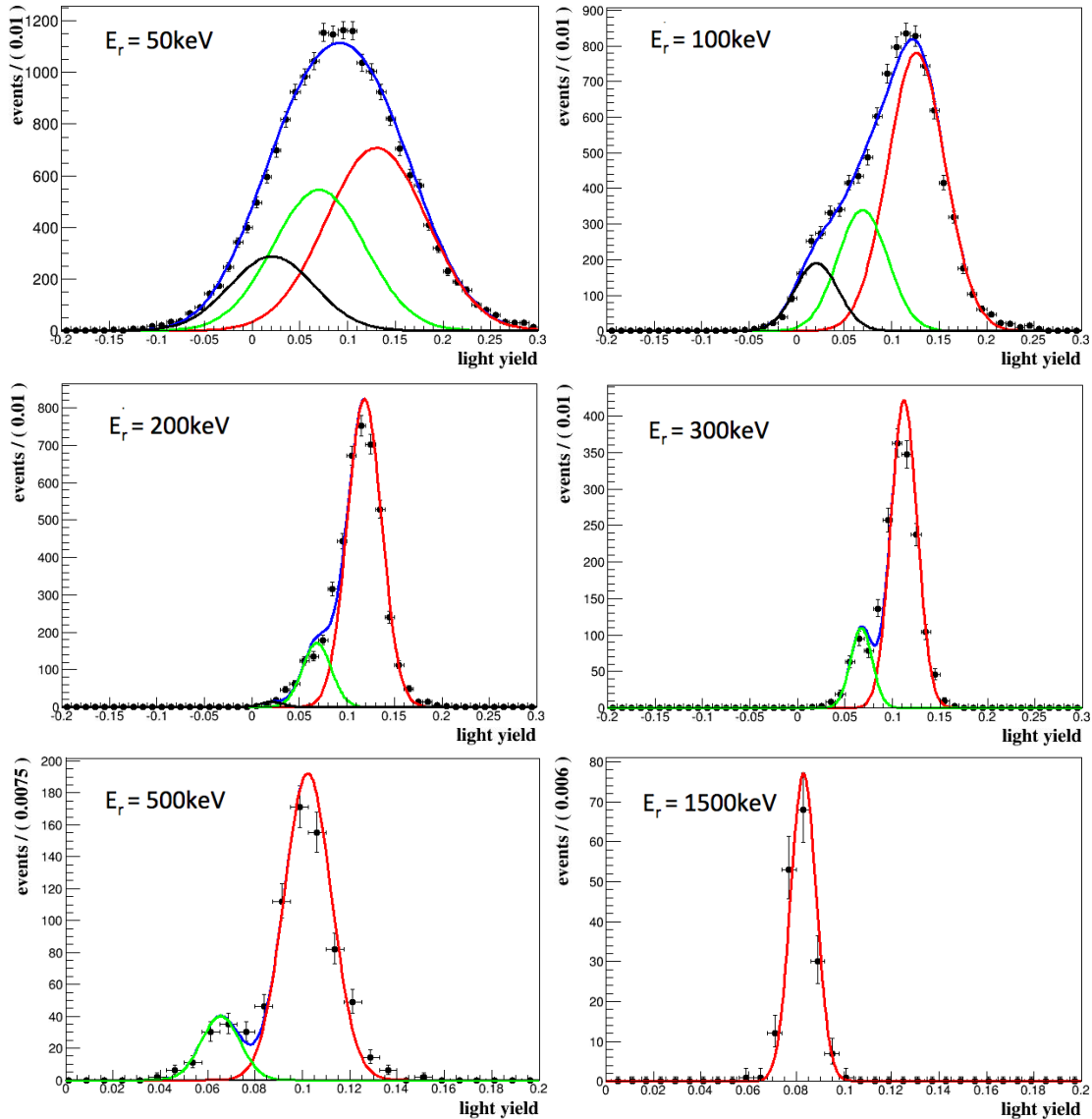


Figure 4.27: Selected light-yield histograms of the nuclear recoil bands (O, Ca and W) at different recoil energies E_r acquired during the Oct 2011 beamtime (50% of total data, see text). The intervals of 10 keV (20 keV to 1000 keV), intervals of 20 keV (above 1000 keV to 1400 keV) and intervals of 50 keV (above 1400 keV) are fitted by up to three Gaussians, one for oxygen (red) at a light yield of ~ 0.1 , one for calcium (green) at a light yield of ~ 0.06 - for kinematic reasons - only up to $E_r \sim 1000$ keV and one for tungsten (black) at a light yield of ~ 0.02 up to $E_r \sim 250$ keV. The total fit is shown in blue. The individual fits to the energy intervals are correlated by equation 4.23 (see chapter 4.9.2) which describes the light-yield distribution of the mean of each recoil band. The light-yield dependent widths of the Gaussians were derived from the electron recoil band (see equation 4.24). The nuclear recoil bands are well described by this parametrization over the entire energy range (up to 1800 keV).

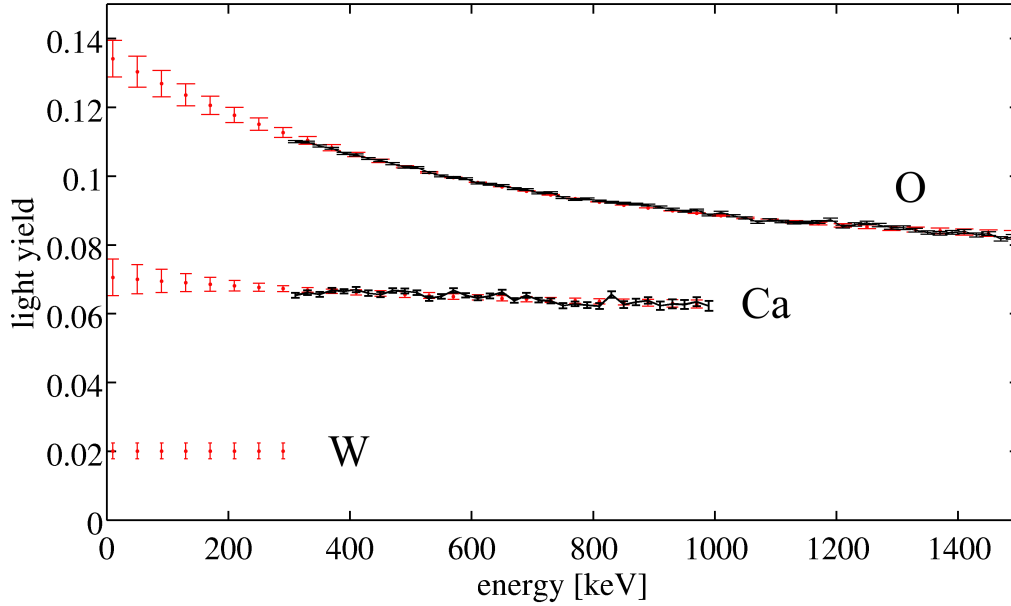


Figure 4.28: Results of the correlated fits of the nuclear recoil bands for O, Ca and W. The underlying data was acquired during the Oct 2011 beamtime (50% used for this analysis). The red points show the means of the three Gaussians together with the systematic and statistical errors of the fit, as described in detail in the text. Above 300 keV, the O and Ca distributions - there are no W recoils above ~ 250 keV - can be fitted without correlations with all parameters left free. In black the means and statistical errors of these fits (energy intervals of 20 keV each) are plotted and are in perfect agreement with the results of the correlated fit. This supports the choice of the parametrization (see equation 4.23) which describes the light-yield distributions.

the energy-dependent parametrization according to equation 4.23 (see chapter 4.9.2):

$$QF_x(E_r) = \frac{LY_x(E_r)}{LY_{\gamma,np}(E_r)} = \frac{LY_x^\infty(1 + f_x \cdot \exp(\frac{-E_r}{\lambda_x}))}{p_0 + p_1 \cdot E_r} \quad (4.29)$$

In table 4.5 the QFs of O, Ca and W are listed for selected energies and illustrated in a light-yield plot in figure 4.29 with the acceptance bounds based on the total 1-sigma errors. These values are valid for the measurement presented here with the crystal cw520. It is shown in chapter 4.10 that the QFs vary from crystal to crystal in the order of $\sim 10\%$. For a DM experiment this variation, however, can be compensated by a dedicated technique described in chapter 4.10.

4.10 Application of QFs to CRESST Detector Modules

In this chapter, the Quenching Factors (QFs) obtained in chapter 4.9 are applied to other CRESST detector modules, in particular those operated in run32. One basic question addresses the problem whether QFs are universally valid or vary from crystal to crystal. To investigate a possibly different quenching behaviour of different CaWO_4 crystals the QF

E_r [keV]	QF_O	QF_{Ca}	QF_W
10	0.1286 ± 0.0051	0.0677 ± 0.0051	0.0196 ± 0.0022
20	0.1277 ± 0.0049	0.0675 ± 0.0048	
30	0.1269 ± 0.0047	0.0674 ± 0.0046	
40	0.1260 ± 0.0045	0.0673 ± 0.0043	
100	0.1212 ± 0.0035	0.0667 ± 0.0030	
200	0.1142 ± 0.0022	0.0658 ± 0.0016	
300	0.1084 ± 0.0013	0.0650 ± 0.0004	-
500	0.0995 ± 0.0004	0.0637 ± 0.0008	-
1000	0.0875 ± 0.0006	0.0619 ± 0.0012	-
1500	0.0832 ± 0.0011	-	-

Table 4.5: Final QF results of the correlated fit presented in chapter 4.9 with combined statistical and systematic errors as measured in the scattering experiment with the crystal cw520. The QF of W has been determined within the same data set by the triple-coincidence method described in chapter 4.8.3. The QF of W has been assumed to be constant over the relevant energy range at the value derived with the precision measurement based on the triple-coincidence technique (see chapter 4.8.3).

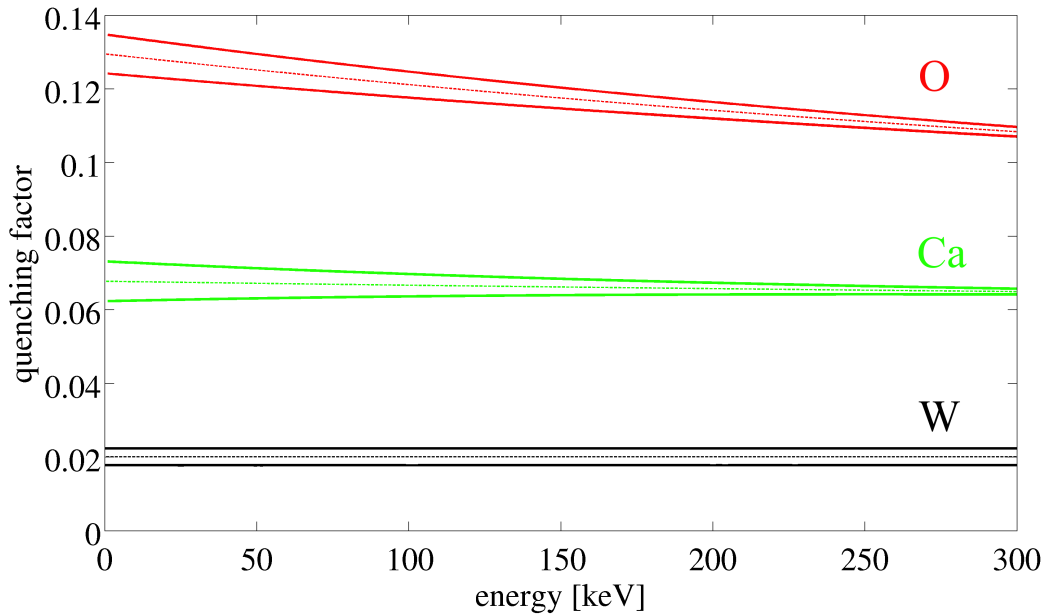


Figure 4.29: Final results for the QFs of O, Ca and W (dashed lines) derived by a correlated fit to the data of the Oct 2011 beamtime described in detail in the text. The QF of tungsten has been measured with the triple-coincidence technique (see chapter 4.8.3). The value of the QF of W was input and requirement for the convergence of the correlated fit. The acceptance bounds (full lines) include combined systematic and statistic (1-sigma) errors.

of oxygen is used as reference parameter. For every CRESST module, calibration data from AmBe neutron-calibration campaigns is available. Due to the shielding surrounding

the CRESST detector volume (see chapter 2.3) the neutron spectrum is highly degraded. Nuclear recoil events are typically observed only up to ~ 300 keV and are dominated by O scatters [25]. To compare the data of CRESST detector modules with the QF measurements performed in this thesis the nuclear-recoil bands are binned from 150 keV to 200 keV and the projection onto the light-yield axis is fitted by two Gaussians. For kinematic reasons oxygen recoils completely dominate over calcium (by a ratio of ~ 10) in this energy range in which there are typically no, or only a few, W scatters. Multiple scatters play only a minor role in this energy interval [87]. To quantify the differences of the QFs depending on the crystal one can define a detector-specific constant ϵ

$$\epsilon = \frac{QF_{\text{O}}^*(175\text{keV})}{QF_{\text{O}}(175\text{keV})} = \frac{LY_{\text{O}}^*(175\text{keV})}{LY_{\gamma,\text{np}}^*(175\text{keV}) \cdot QF_{\text{O}}(175\text{keV})} \quad (4.30)$$

where $QF_{\text{O}}^*(175\text{keV})$ and $LY_{\text{O}}^*(175\text{keV})$ are the QF and the mean of the light-yield distribution of oxygen between 150 and 200 keV of a certain detector to be calibrated (marked in the following by an asterisk *). $LY_{\gamma,\text{np}}^*(175\text{keV})$ is the mean of the electron recoil band not accounting for the non-proportionality effect (see equation 4.2). $QF_{\text{O}}(175\text{keV})$ is the QF of oxygen measured in this thesis with the setup described in chapter 4.5 and the technique presented in chapter 4.9. These parameters have been determined for the detector modules of CRESST run32 and the relevant values are listed in table 4.6. One can see that the QFs of the CRESST modules vary by $\sim 11\%$, whereas the QF measured in this work is $\sim 12\%$ higher than the CRESST modules' mean. They are thus incompatible with each other within statistic and systematic errors.

crystal	channel	$LY_{\text{O}}^*(175\text{keV})$	$LY_{\gamma,\text{np}}^*(175\text{keV})$	ϵ	$QF_{\text{O}}^*(175\text{keV})$
VK33	05	0.106 ± 0.001	1.040	0.88 ± 0.007	0.102 ± 0.001
Verena	20	0.116 ± 0.002	1.091	0.91 ± 0.017	0.106 ± 0.002
Maya	29	0.110 ± 0.001	1.074	0.88 ± 0.007	0.103 ± 0.001
Sabine	33	0.112 ± 0.001	1.119	0.86 ± 0.01	0.100 ± 0.001
Wibke	43	0.115 ± 0.001	1.136	0.87 ± 0.009	0.101 ± 0.001
K07	45	0.106 ± 0.001	1.075	0.85 ± 0.01	0.098 ± 0.001
Daisy	47	0.123 ± 0.003	1.128	0.94 ± 0.02	0.109 ± 0.002
Rita	51	0.100 ± 0.001	1.026	0.84 ± 0.006	0.098 ± 0.001
average				0.88 ± 0.04	0.102 ± 0.004
cw520	-	0.120 ± 0.002	1.038	1.00(def)	0.1159 ± 0.002

Table 4.6: Comparison of relevant parameters related to the quenching behaviour between detector modules operated in CRESST run32 and the detector used in this work (crystal cw520). The errors for $LY_{\gamma,\text{np}}^*(175\text{keV})$ are negligible compared to the other relevant values. For details see main text.

In the following, a possible correlation between the absolute light output of a CaWO_4 crystal and the respective QFs is investigated. Therefore, the scintillation capability of a crystal is quantified by the light output L of γ -ray interactions measured by a photomultiplier at room temperature compared to the reference crystal Boris [52]. The QF of O determined between 150 and 200 keV is plotted against the light output L in figure 4.30. In this plot, the eight detectors operated in run32 of CRESST (red) are compared with the crystal cw520

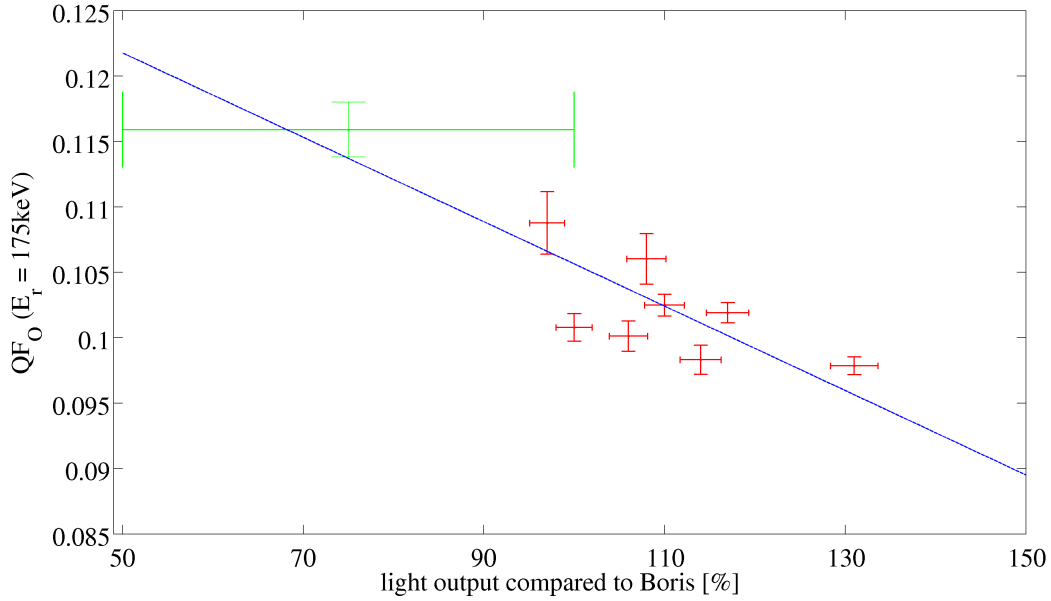


Figure 4.30: Correlation between light output of different crystals and their QF (here: QF of oxygen between 150 and 200 keV). The light output for the 8 crystals operated in run32 of CRESST (red) has been measured at 300K with a photomultiplier and normalized to the reference crystal Boris (Daisy: $L \sim 97\%$, Wibke: $L \sim 100\%$, Sabine: $L \sim 106\%$, Verena: $L \sim 108\%$, Maja: $L \sim 110\%$, K07: $L \sim 114\%$, VK33: $L \sim 117\%$, Rita: $L \sim 131\%$). The light output $L = 75 \pm 25\%$ of the crystal cw520 used in this work (green) can only be determined with rather large uncertainties as the crystal is rather small: 20 mm in diameter and 5 mm in height (cylindrical). Which light output a CRESST crystal (40 mm in diameter, 40 mm in height) of the same material would have can only be determined by simulations [52]. The blue line is the best (linear) fit of all eight detectors operated in run32. The mean dependence of the QF of O on the light output L (slope of the line) is: $\Delta QF_O(L) = (-2.3 \cdot 10^{-4} \pm 1.3 \cdot 10^{-4})/[\%]$. A clear tendency towards lower QFs for crystals with higher light output L is visible.

(green) used for the calibration measurement performed in this work (see table 4.6). The light output of the crystal cw520 (used in the scattering experiment) has been measured with a size of 20 mm in diameter and 5 mm in height (cylindrical). The light output a CRESST-size crystal (40 mm in height, 40mm in diameter) of the same material would have can only be estimated by Monte-Carlo simulations [52]. This results in rather large uncertainties for the (comparable) light output of this crystal: $L = 75 \pm 25\%$.

A significant correlation between L and $QF_O^*(175keV)$ is found: the higher the light output of the crystal and thus usually the lower the number of impurities in the crystal the lower is the measured QF. Taking into consideration all eight crystals operated in run32, the mean dependence of the QF of O on the light output L is

$$\Delta QF_O(L) = (-2.3 \cdot 10^{-4} \pm 1.3 \cdot 10^{-4})/[\%] \quad (4.31)$$

where L is given in units of [%] compared to the light output $L = 100\%$ of the reference crystal Boris. This result suggests that the origin of the varying QFs (from crystal to crystal)

is physical and not caused by systematics of the individual measurements. There are attempts [90] for a deeper understanding of the quenching mechanism of CaWO_4 using dedicated experiments to develop a model which extends the phenomenological model of Birks [53]. This extended model suggests a dependence of the QFs on the number of impurities which is usually inversely proportional to the light output of a crystal. The model still has to be further proven by future experiments.

Motivated by a possible physical origin of the varying QFs, a model to apply the measured QFs to other CRESST detector modules is proposed here. Therefore, the energy-dependent QFs are scaled by the crystal-specific constant ϵ :

$$QF_x^*(E_r) = \epsilon \cdot QF_x(E_r) \quad (4.32)$$

where $QF_x(E_r)$ and $QF_x^*(E_r)$ are the energy-dependent QFs of the nucleus x according to the detector used in this thesis and that of a detector which has to be calibrated, respectively. The light-yield distribution $LY_x^*(E_r)$ can be calculated accordingly:

$$\begin{aligned} LY_x^*(E_r) &= \epsilon \cdot LY_{\gamma, \text{np}}^*(E_r) \cdot QF_x(E_r) \\ &= \epsilon \cdot LY_x^\infty \left(1 + f_x \cdot \exp\left(\frac{-E_r}{\lambda_x}\right)\right). \end{aligned} \quad (4.33)$$

In table 4.7, the mean QFs of O, Ca and W averaged over the eight detector modules operated in run32 of CRESST in the region-of-interest for Dark Matter search (typically 12-40 keV) are listed.

In figure 4.31 the data of two detector modules used in run32 of CRESST (crystals Rita

E_r [keV]	QF_O	QF_{Ca}	QF_W
10	0.1132 ± 0.0042	0.0596 ± 0.0022	0.0172 ± 0.0022
20	0.1124 ± 0.0042	0.0595 ± 0.0022	
30	0.1117 ± 0.0041	0.0594 ± 0.0022	
40	0.1109 ± 0.0041	0.0593 ± 0.0022	

Table 4.7: Mean QFs averaged over the eight CRESST detector modules operated in run32. The QFs have been adapted to the individual crystals by scaling the QFs following equation 4.32. The QF of tungsten has been measured with the triple coincidence method presented in chapter 4.8.3 and scaled accordingly.

and Wibke) is shown together with the 80% acceptance bounds (1.28-sigma) for O, Ca and W recoils. The data was acquired during an neutron calibration campaign¹⁰. The acceptance bounds have been derived by applying the QFs discussed in chapter 4.9 using the method described above and a likelihood fit of every individual electron-recoil band in order to gain the width of the quenched bands (see equation 4.24 in chapter 4.9.3). For both, the crystal Rita (Ch51) which has the highest light output ($L = 131\%$) among all CRESST crystals and for Wibke (ch43) which is among the worst in terms of light output ($L = 100\%$) and resolution, data and prediction are in good agreement.

For the module Rita/Steven selected energy intervals were fitted by three Gaussians (O, Ca and W, see figure 4.32) with the energy-dependent QFs fixed by the parameters listed in table 4.4 (adapted for every individual detector). The individual amplitudes of the Gaussians

¹⁰An AmBe neutron source was placed inside the PE shielding of the CRESST setup (see chapter 2.3).

were left free. Due to low statistics and the strong overlap at low energies ($\lesssim 80$ keV) the contributions of Ca (green) and W (black) are highly correlated. Therefore, at low energies only the Gaussian corresponding to Ca has an influence, the amplitude of the Gaussian corresponding to W is set to zero by the fit. Down to energies of ~ 30 keV, the O contribution (red) dominates the nuclear-recoil bands and can well be fitted over the entire energy range. Thus, the description of the upper bound of the nuclear-recoil bands in the light-yield plane is a good check whether the energy-dependent parametrization is applicable to CRESST modules. As can be seen in figure 4.31, this actually is the case within the limited statistics. In particular, in the histogram at 20 keV in which the data points show a tail towards higher light yields the need of a higher QF of O (compared to the value at e.g. 200 keV) is clearly visible.

In conclusion, despite statistics being very low in the CRESST neutron calibration campaign, the data is well consistent with energy-dependent QFs as proposed within this thesis.

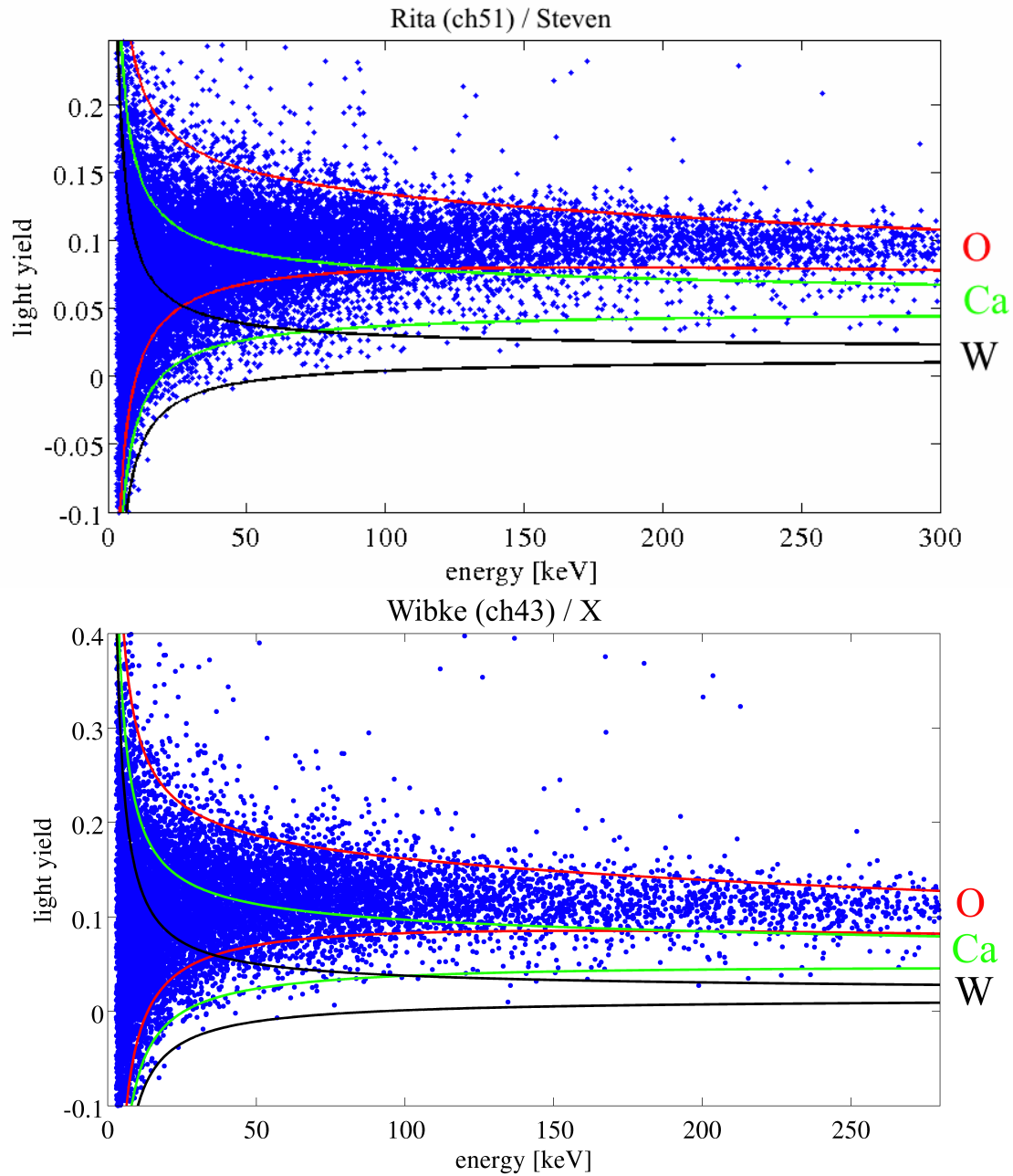


Figure 4.31: Light-yield plots of the nuclear recoil bands of two CRESST detector modules. The data was acquired in a neutron calibration campaign during run32. Shown are the 80% (1.28-sigma) acceptance bands of O, Ca and W which are derived from the QF measurements performed in this work (see chapter 4.9). This illustrates that the QF results obtained in the present thesis are consistent with CRESST data. Note: At lower ($\lesssim 30$ keV) recoil energies, Ca and W provide the dominant contributions to the nuclear recoil bands (see figure 4.32) which gives the misleading impression of a decreasing QF of O. The data is well consistent with energy dependent QFs as proposed in chapter 4.9, see also figure 4.32.

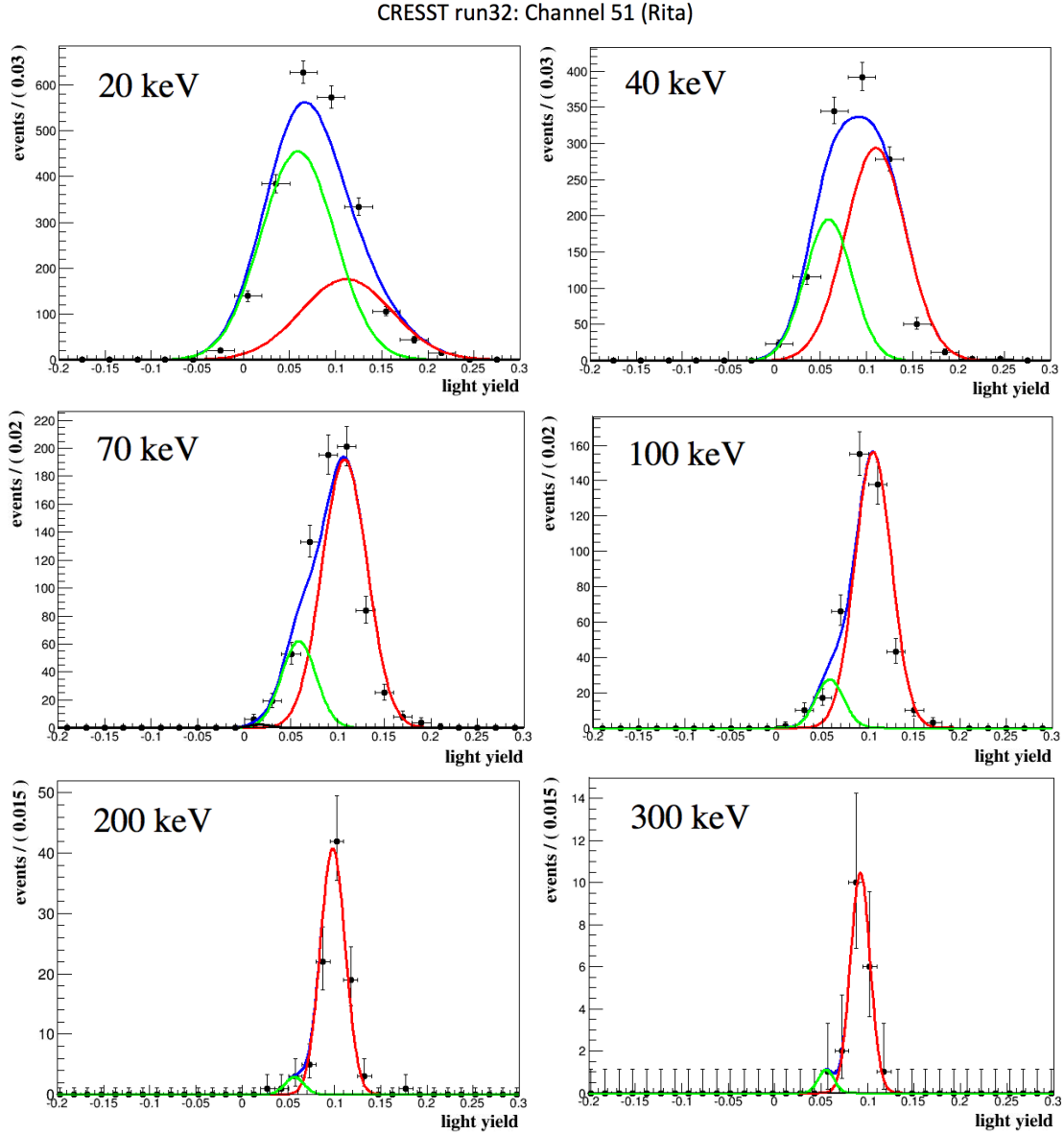


Figure 4.32: Selected light-yield histograms of data acquired in CRESST run32 with the module Rita/Steven during a neutron calibration campaign (ncal2). In each energy interval of 10 keV a Gaussian is fitted for each kind of recoiling nucleus using the energy-dependent QFs measured within this work. Despite very low statistics the bands are well described by O (red) and Ca (green) distributions according to equation 4.33. At low energies $\lesssim 70$ keV also W (black) plays a significant role, however, it cannot be fitted correctly due to low statistical significance and strong overlap with the Ca distribution. Despite low statistics, the upper edge of the O band is nicely described by the proposed energy-dependent parametrization of the QFs according to equation 4.23 (see chapter 4.9.2). The fits show that the energy-dependent QFs as presented in chapter 4.9 are well consistent with the data of a typical CRESST detector module over the entire energy range. In particular the histogram at 20 keV in which the data points show a tail towards higher light yields the need of a higher QF of O (compared to the value at e.g. 200 keV) is clearly visible.

Chapter 5

Summary and Outlook

The challenge of experiments which aim towards a direct detection of Dark Matter (DM) is to combine ultra-sensitive detector performance for the measurement of WIMP (Weakly Interacting Massive Particle)-induced low-energy recoil events ($\mathcal{O}(10\text{ keV})$), a large detector mass ($\mathcal{O}(10\text{-}100\text{ kg})$) and ultra-low background conditions to cope with the low-event rates that are expected for DM-particle interactions ($\mathcal{O}(\lesssim 10/\text{kg}/\text{year})$). Recently, a variety of these experiments with different measurement techniques and target elements, namely NaI in DAMA (Dark Matter search) [26], CaWO_4 in CRESST (Cryogenic Rare Event Search with Superconducting Thermometers) [25], Ge in CoGeNT [36] and Si in CDMS (Cold Dark Matter Search) [37], reported signal excesses above the known backgrounds which can be interpreted as hints for the existence of low-mass WIMPs (5-30 GeV). However, the XENON experiment [24] based on the liquid rare-gas Xe claims to mostly exclude this parameter space and to set the world-best limit on coherent spin-independent WIMP-nucleon scattering cross-section of $2 \cdot 10^{-45} \text{ cm}^2$ (at a WIMP mass of $\sim 55 \text{ GeV}$). Probably only a clear signature consistent with the A^2 -dependency of this cross-section among different target materials would allow to prove unambiguously the discovery of Dark Matter. The planned next-generation DM search experiments like XENON1T [47] and EURECA (European Underground Rare Event Calorimeter Array) [48, 49] which includes the CRESST and EDELWEISS (Experience pour DETecteur Les Wimps En Site Souterrain) [33] techniques have a good chance to reach this aim within the next decade.

The CRESST experiment which is located underground in the LNGS (Laboratori Nazionali del Gran Sasso) in central Italy uses scintillating CaWO_4 crystals as target material. The detector volume is shielded by layers of ultrapure Cu, Pb and polyethylene (PE) against ambient radioactivity and an active muon-veto reduces background induced by cosmic radiation. The CaWO_4 crystals - equipped with a tungsten transition-edge-sensor (TES) - are operated as phonon detectors which allow to measure the total energy deposition of a particle (phonon channel). The produced scintillation light is simultaneously detected by a separate cryogenic silicon-on-sapphire light detector. The part of the energy which is converted into scintillation light (called light yield LY) strongly depends on the kind of interacting particle. The unique feature of CRESST besides the capability to discriminate the dominant e^-/γ background at $LY = 1$ (per definition) is to identify - to a certain extend - the kind of recoiling nucleus with reduced light yield $LY \lesssim 0.1$. This effect of light quenching is the stronger the higher the mass of the recoiling nucleus. The light yield of particle interactions compared to elec-

tron recoils is quantified by Quenching Factors (QF). Their precise knowledge is of utmost importance for the Dark Matter analysis of CRESST as it allows to discriminate the mainly intrinsic e^-/γ background and ambient neutrons - for kinematic reasons dominantly visible as O scatters - from possible WIMP-induced W (and Ca) recoils at lower QFs. With CaWO_4 as target material, the composition due to O, Ca and W contributions of a possible DM signal can be determined and thus the A^2 dependence of the expected cross-section can be tested within a single experiment. In addition, this allows to determine the mass of a Dark Matter particle (WIMP-mass spectroscopy). Within this thesis, the QFs of all elements in CaWO_4 - in particular also that of the heavy element W ($A \approx 184$) - have been measured for the first time with the required precision at the operational temperature (~ 10 mK) of CRESST detectors in the region-of-interest (ROI) for DM search (typically 12-40 keV). In the latest experimental run of CRESST (run32) a signal excess above the known backgrounds was observed with high significance (4.7σ). Interpreted as interactions of DM particles, this would hint towards low-mass WIMPs in the order of 10-30 GeV. However, background contributions due to e^-/γ -induced recoils, ambient neutrons, α -particles and ^{206}Pb decays on surfaces surrounding the detectors (e.g., the bronze clamps holding the crystals) are rather high. The possibility that rare processes which are correlated to these known backgrounds could mimic the intriguing signal events have been controversially discussed. For the next CRESST run (run33), besides increasing the target mass to ~ 5 kg, the main aim is to significantly reduce the background level.

Within this thesis, studies and a series of measurements with novel CRESST-detector prototypes have been performed underground at the CRESST test cryostat in the LNGS. Recently, the crystal laboratory of the TU München has set up a production cycle for CaWO_4 crystals. The first TUM-grown crystal of the CRESST type, called Rudolph VI (TUM-27, 40mm x 40mm, cylindrical, ~ 300 g) was operated as cryogenic detector to study phonon properties, light output and radiopurity (α -contamination). Furthermore, the influence of roughening the crystal on the lateral surface was investigated in a second measurement. In both experimental runs in the test cryostat, the performance of the phonon detector was well consistent with that of commercial CaWO_4 crystals operated in the CRESST setup and an energy resolution of ~ 2 keV (at 122 keV) was reached. The additional roughening has no disadvantages concerning phonon properties, however, the fraction of detected scintillation light was increased from 1.09% to 1.31%. With the crystal TUM-27 a dedicated measurement was carried out to study a possible ^{222}Rn -implantation-induced ^{206}Pb -recoil background in CRESST. The non-scintillating bronze clamps of the standard CRESST holder are supposed to be the source of ^{206}Pb scatters by surface ^{210}Po α -decays part of which could be due to an exposition of the clamps to ^{222}Rn -contaminated air before mounting the detectors. Prior to the measurement in the test cryostat, a set of standard run32 bronze clamps has been exposed to a strong Rn source. The results of this study suggest that $\sim 28\%$ of the observed ^{206}Pb recoils at a recoil energy of ~ 103 keV in run32 are due to this process.

In order to avoid background from surface events completely, a novel fully-scintillating detector holder for block-shaped crystals was designed, realized and successfully tested within this thesis. A TUM-grown crystal ($32 \times 32 \times 40 \text{ mm}^3$, ~ 250 g) is held by sticks made of the same CaWO_4 material (diameter ~ 3 mm) which together with a scintillating polymeric foil establish a fully scintillating detector housing. Surface-decay events of which the recoiling nucleus hits the target crystal feature a corresponding α -particle which simultaneously produces scintillation light in the fully scintillating coverage of the detector housing. Thereby, these (low light-yield) events are shifted out of the ROI. After extensive tests concerning the influence of

the CaWO_4 sticks on the phonon properties, the light output, and sensitivity as Dark Matter detector, it was shown that this novel detector design is fully functional and no surface-decay induced nuclear recoils are expected in typical exposures used in CRESST DM-search runs (~ 100 kg-days per module). In addition, the light output of the block-shaped crystal Wilhelm I (TUM-40) which in terms of crystal quality and growth conditions is comparable to the cylindrically shaped TUM-27 is enhanced by 48% in the cryogenic measurement. A dedicated α -analysis of the TUM-grown crystals TUM-27 and TUM-40 showed a total α -contamination (1.5-7 MeV) of ~ 3 mBq/kg well competitive with the best commercially available CaWO_4 crystals. A detailed view on the individual α -lines shows that the spectrum is completely dominated by ^{230}Th (4.7 MeV) and ^{210}Po (5.3 MeV) decays. It can be deduced that the ^{238}U -chain is broken and an additional ^{210}Po contamination must significantly contribute.

Within this thesis, two detector modules based on CaWO_4 sticks with TUM-grown block-shaped crystals (TUM-40 and TUM-45) were realized and implemented into the CRESST setup for the upcoming experimental run (run33). The full veto against surface events on the crystal's surface and the surfaces surrounding the crystal established with this promising detector design should significantly reduce the background level in CRESST compared to run32 and prove the competitiveness of the light-phonon technique in the field of direct DM search.

For run33 of CRESST, a new production cycle for ultra-pure bronze used for the clamps of the standard CRESST detector holders should reduce α and ^{206}Pb backgrounds by at least one order of magnitude. A new clean room at the LNGS in which the detectors can be assembled under Rn-filtered air flow from a purifier was installed to minimize the Rn-induced background which - as was shown in this thesis - could have played an important role in run32. An additionally installed PE shielding around the inner detector volume should further degrade ambient neutrons. In total, 18 detector modules with a total target mass of ~ 5 kg will be integrated in the CRESST setup which allows to reach a net exposure of ~ 2 ton-days within a measuring time of two years. In case of the existence of low-mass WIMPs this improved experimental setup would undoubtedly either confirm the DM hypothesis with high statistical confidence or otherwise strengthen the limit for spin-independent WIMP-nucleon cross-section $\sim 10^{-45}$ cm² at a WIMP mass of ~ 65 GeV (estimation assuming improved background conditions).

For the measurement of bulk QFs of CaWO_4 in a CRESST-like detector module, at the accelerator of the MLL (Maier-Leibnitz-Laboratorium) in Garching a dedicated neutron-scattering facility was expanded and significantly improved within this thesis. Monoenergetic neutrons of ~ 11 MeV are produced by a pulsed ^{11}B beam in a nuclear reaction and - due to inverse kinematics - are predominantly emitted into forward direction. The pulsing devices of the accelerator were renewed and optimized to achieve the required bunch width of ~ 2 ns which allows a time-of-flight (ToF) measurement. After being scattered off the CaWO_4 crystal (~ 30 g) which is operated as a phonon detector in a dilution refrigerator, the neutrons are recorded in an array of liquid-scintillator detectors at fixed scattering angles. Thereby, kinematics are fixed and the measurement of the ToF as well as the energy loss in the CaWO_4 crystal enable an identification of the recoiling nucleus (O, Ca or W). Once identified by this so-called triple-coincidence technique, the scintillation-light output of the corresponding nuclear recoils can be measured on an event-by-event basis by the Si light detector. With sufficient statistics, this method allows to directly determine the QFs. Both cryogenic detectors are housed in an especially designed low-mass holder to avoid parasitic scattering of neutrons in the vicinity of the target crystal. In addition, the TESs and the data

acquisition were optimized such that the cryogenic detectors could be operated in a mode in which they could cope with an event rate of up to ~ 100 Hz. These improvements were the break-through for the experiment in terms of signal-to-background ratio and statistics. In ~ 3 weeks of beamtime performed in the framework of this thesis, the experiment was running in a setup which was optimized for the measurement of the QF of W at a scattering angle of $\sim 80^\circ$. Thus for W recoils a recoil energy of ~ 100 keV is expected. A sufficient number of 158 W-recoils with a signal-to-background ratio of $\sim 7:1$ were separated out of the initial ~ 100 million pulses acquired by the cryodetectors. The complex data-analysis framework developed to process the enormous amount of data ($\mathcal{O}(10$ TB)) from the cryodetectors, the liquid scintillator detectors, and the timing signals of the pulsing devices, was extended by a dedicated maximum-likelihood tool for the final analysis of the QF of W. Timing, energy and light-yield information of the identified W recoils as well as the known background light-yield distribution of the nuclear recoil bands were included in a correlated maximum-likelihood fit. The best fit yields the QF of W at a recoil energy of 100 keV: $QF_W = 0.0196 \pm 0.0022$. This is the first measurement of the QF of W in CaWO_4 under realistic measurement conditions, at mK temperatures and - because neutrons are used as probes - for events uniformly distributed in the crystal's bulk. The errors are $\sim 10\%$ on a 1σ confidence level which matches the original objective of this experiment.

The precise measurement of the QF of W is the crucial input parameter for a complete energy-dependent analysis of the entire nuclear-recoil band. In a well-calibrated data sub-set of the Oct 2011 beamtime (400 000 pulses), the continuous light-yield contributions of O and Ca above a recoil energy of 300 keV in which for kinematic reasons no W recoils are expected, can be directly fitted by two Gaussians. This was individually done for recoil-energy intervals of 10-50 keV up to energies of 1500 keV above which statistics gets insufficient. A significant energy-dependence of the QF of O and - less-pronounced - for Ca has been observed. This observation is in agreement with qualitative predictions from, e.g., the semi-empirical description based on the Birks theory, which, however, has not been observed before in CaWO_4 crystals operated as CRESST detectors. Prediction and observation further motivate the assumption that for heavy nuclei like W the energy-dependence is negligible. To analyse the entire nuclear-recoil bands extended for recoil energies < 300 keV and > 1500 keV, a correlated maximum-likelihood fit was developed which includes an energy-dependent parametrization of the O (and Ca) QFs and the QF of W. In this fit, the QF of W obtained in the precision measurement by the triple-coincidence technique was used and kept constant in the considered energy range of W recoils (up to ~ 250 keV). In analogy to the electron-recoil band, the QFs are parametrized with a constant and an exponential rise (for the electron-recoil band: exponential decay) towards lower QFs. Except for these assumptions, all parameters are left free in the fit. The fit converges over the entire nuclear-recoil band above the energy threshold of ~ 20 keV up to 1800 keV and yields the QFs with unprecedented accuracy. E.g., at a recoil energy of 100 keV, for the QFs holds: $QF_O = 0.1212 \pm 0.0035$, $QF_{Ca} = 0.0667 \pm 0.0030$ and $QF_W = 0.0196 \pm 0.0022$. Towards the analysis threshold of 20 keV the QF of O (Ca) rises by $\sim 6.1\%$ ($\sim 1.5\%$).

In order to proof the applicability of the energy-dependent QF results to other CaWO_4 crystals, the eight CRESST detector modules operated in the latest experimental run (run32) were studied in the framework of this thesis. For every module, data from an AmBe neutron-calibration campaign is available which provides nuclear-recoil events up to an energy of ~ 300 keV. From this data it is not possible to derive the QFs of Ca and W, however, it allows to determine the QF of O at an energy of 150-200 keV with small uncertainties ($\sim 1\%$).

Among the considered CRESST crystals a variation of the QF of $\sim 11\%$ was observed. A significant correlation between the QF and the scintillation capability of different CaWO_4 crystals was found. The higher the absolute light output of a crystal (and thus the lower the number of impurities) the lower are the QFs. The precision measurements of the QFs performed within this thesis at the MLL allow to nicely describe the CRESST data from the neutron calibration campaigns with energy-dependent QFs. The mean QFs averaged over the eight CRESST modules considered are $QF_{\text{O}}^{\text{cresst}} = 0.1124 \pm 0.0042$, $QF_{\text{Ca}}^{\text{cresst}} = 0.0595 \pm 0.0022$ and $QF_{\text{W}}^{\text{cresst}} = 0.0172 \pm 0.0022$ at a recoil energy of 20 keV.

Previously, the QF of O has been derived by neutron-calibration campaigns of CRESST at energies > 100 keV assuming constant quenching over the entire energy range. The QFs of Ca and W were not accessible in this way and have been taken from independent experiments with rather large systematic errors. The results of this thesis show that the previously assumed constant QFs are only an approximation and that the energy-dependent parametrization has to be integrated into the CRESST analysis framework. This will - to a certain extend - influence the DM results of run32 which have to be reanalysed and will be of utmost importance for the future.

In the view of the planned “multi-material” experiment EURECA, the fully operational scattering facility at the MLL allows to determine the QFs of alternative target crystals within 2-3 weeks of beamtime. In particular, considering the recent results of the CDMS experiment, target materials with low A suited for the detection of low-mass WIMPs (e.g. Ti-doped Al_2O_3) could become important for the future of cryogenic direct Dark Matter experiments.

Appendix A

Background Gamma Lines

Selected gamma lines which can be observed in low-background experiments such as the measurements performed within the present thesis in the test cryostat at Gran Sasso (see chapter 3) are listed in table A.1. Along with the individual mother nucleus, the production mechanism and the affiliation to a natural decay chain (^{238}U , Th) is indicated.

energy [keV]	emitting nucleus	production mechanism
72.8	Pb $K_{\alpha 2}$	radiation, μ
72.8	Pb $K_{\alpha 2}$	radiation, μ
75.0	Pb $K_{\alpha 1}$	radiation, μ
84.5	Pb $K_{\beta 3}$	radiation, μ
84.9	Pb $K_{\beta 1}$	radiation, μ
87.3	Pb $K_{\beta 2}$	radiation, μ
92.4	$^{234}\text{Th} \xrightarrow{\beta^-} ^{234}\text{Pa}$	primordial, ^{238}U -chain
92.8	$^{234}\text{Th} \xrightarrow{\beta^-} ^{234}\text{Pa}$	primordial, ^{238}U -chain
93.3	$^{228}\text{Ac} \xrightarrow{\beta^-} ^{228}\text{Th}$	primordial, Th-chain
186.2	$^{226}\text{Ra} \xrightarrow{\alpha} ^{222}\text{Rn}$	primordial, ^{238}U -chain
238.6	$^{212}\text{Pb} \xrightarrow{\beta^-} ^{212}\text{Bi}$	primordial, Th-chain
242.0	$^{214}\text{Pb} \xrightarrow{\beta^-} ^{214}\text{Bi}$	primordial, ^{238}U -chain
295.2	$^{214}\text{Pb} \xrightarrow{\beta^-} ^{214}\text{Bi}$	primordial, ^{238}U -chain
300.1	$^{212}\text{Pb} \xrightarrow{\beta^-} ^{212}\text{Bi}$	primordial, Th-chain
338.3	$^{228}\text{Ac} \xrightarrow{\beta^-} ^{228}\text{Th}$	primordial, Th-chain
351.9	$^{214}\text{Pb} \xrightarrow{\beta^-} ^{214}\text{Bi}$	primordial, ^{238}U -chain
463.0	$^{228}\text{Ac} \xrightarrow{\beta^-} ^{228}\text{Th}$	primordial, Th-chain
510.7	$^{208}\text{Tl} \xrightarrow{\beta^-} ^{208}\text{Pb}$	primordial, Th-chain
511.0	e^+	pair production, β^+ , μ
583.1	$^{208}\text{Tl} \xrightarrow{\beta^-} ^{208}\text{Pb}$	primordial, Th-chain
609.3	$^{214}\text{Bi} \xrightarrow{\beta^-} ^{214}\text{Po}$	primordial, ^{238}U -chain
661.7	$^{137}\text{Cs} \xrightarrow{\beta^-} ^{137\text{m}}\text{Ba}$	anthropogenic
665.5	$^{214}\text{Bi} \xrightarrow{\beta^-} ^{214}\text{Po}$	primordial, ^{238}U -chain

energy [keV]	emitting nucleus	production mechanism
727.2	$^{212}\text{Bi} \xrightarrow{\beta^-} ^{212}\text{Po}$	primordial, Th-chain
768.4	$^{214}\text{Bi} \xrightarrow{\beta^-} ^{214}\text{Po}$	primordial, ^{238}U -chain
785.4	$^{212}\text{Bi} \xrightarrow{\beta^-} ^{212}\text{Po}$	primordial, Th-chain
785.9	$^{214}\text{Pb} \xrightarrow{\beta^-} ^{214}\text{Bi}$	primordial, ^{238}U -chain
794.9	$^{228}\text{Ac} \xrightarrow{\beta^-} ^{228}\text{Th}$	primordial, Th-chain
860.4	$^{208}\text{Tl} \xrightarrow{\beta^-} ^{208}\text{Pb}$	primordial, Th-chain
911.1	$^{228}\text{Ac} \xrightarrow{\beta^-} ^{228}\text{Th}$	primordial, Th-chain
964.6	$^{228}\text{Ac} \xrightarrow{\beta^-} ^{228}\text{Th}$	primordial, Th-chain
969.1	$^{228}\text{Ac} \xrightarrow{\beta^-} ^{228}\text{Th}$	primordial, Th-chain
1001.0	$^{234\text{m}}\text{Pa} \xrightarrow{\beta^-} ^{234}\text{U}$	primordial, ^{238}U -chain
1120.3	$^{214}\text{Bi} \xrightarrow{\beta^-} ^{214}\text{Po}$	primordial, ^{238}U -chain
1173.2	$^{60}\text{Co} \xrightarrow{\beta^-} ^{60}\text{Ni}$	anthropogenic
1238.1	$^{214}\text{Bi} \xrightarrow{\beta^-} ^{214}\text{Po}$	primordial, ^{238}U -chain
1332.5	$^{60}\text{Co} \xrightarrow{\beta^-} ^{60}\text{Ni}$	anthropogenic
1377.7	$^{214}\text{Bi} \xrightarrow{\beta^-} ^{214}\text{Po}$	primordial, ^{238}U -chain
1401.5	$^{214}\text{Bi} \xrightarrow{\beta^-} ^{214}\text{Po}$	primordial, ^{238}U -chain
1408.0	$^{214}\text{Bi} \xrightarrow{\beta^-} ^{214}\text{Po}$	primordial, ^{238}U -chain
1460.8	$^{40}\text{K} \xrightarrow{\beta^+, \text{EC}} ^{40}\text{Ar}$	primordial
1495.9	$^{228}\text{Bi} \xrightarrow{\beta^-} ^{228}\text{Th}$	primordial, Th-chain
1509.2	$^{214}\text{Bi} \xrightarrow{\beta^-} ^{214}\text{Po}$	primordial, ^{238}U -chain
1587.9	$^{228}\text{Ac} \xrightarrow{\beta^-} ^{228}\text{Th}$	primordial, Th-chain
1620.6	$^{212}\text{Bi} \xrightarrow{\beta^-} ^{212}\text{Po}$	primordial, Th-chain

energy [keV]	emitting nucleus	production mechanism
1630.6	$^{228}\text{Ac} \xrightarrow{\beta^-} ^{228}\text{Th}$	primordial, Th-chain
1661.3	$^{214}\text{Bi} \xrightarrow{\beta^-} ^{214}\text{Po}$	primordial, ^{238}U -chain
1729.6	$^{214}\text{Bi} \xrightarrow{\beta^-} ^{214}\text{Po}$	primordial, ^{238}U -chain
1764.5	$^{214}\text{Bi} \xrightarrow{\beta^-} ^{214}\text{Po}$	primordial, ^{238}U -chain
1847.4	$^{214}\text{Bi} \xrightarrow{\beta^-} ^{214}\text{Po}$	primordial, ^{238}U -chain
2118.5	$^{214}\text{Bi} \xrightarrow{\beta^-} ^{214}\text{Po}$	primordial, ^{238}U -chain
2204.2	$^{214}\text{Bi} \xrightarrow{\beta^-} ^{214}\text{Po}$	primordial, ^{238}U -chain
2447.8	$^{214}\text{Bi} \xrightarrow{\beta^-} ^{214}\text{Po}$	primordial, ^{238}U -chain
2614.5	$^{208}\text{Tl} \xrightarrow{\beta^-} ^{208}\text{Pb}$	primordial, Th-chain

Table A.1: Selected gamma lines which can be observed in low-background experiments such as the measurements performed within the present thesis in the test cryostat at Gran Sasso (see chapter 3). The gamma lines are sorted by energy (in units of keV). The emitting nucleus, the production mechanism and a possible affiliation to a natural decay chain are also listed. μ indicates muon-induced X-ray emission. Values from [106, 107].

Appendix B

Technical Drawings of Novel Detector Holder

In the following technical drawings of the copper and CaWO_4 parts of the novel phonon-detector holder (discussed in detail in chapter 3.5) are shown. Figure B.1 shows the fully assembled module while drawings of the individual parts are presented in figures B.2 to B.11. The scale of the drawings is 2:1 (or the value depicted in the individual draft) if scaled up to DIN-A4 paper size.

- All copper parts including the screws (mostly M3) are made of ultrapure NOSV [57] copper as commonly used for the CRESST experiment (see chapter 2.2.1).
- The bronze clamps are machined from ultrapure raw materials as used for the standard design in run33 of CRESST (see chapter 2.5). The dimensions of the clamps for the side CaWO_4 sticks are: $5\text{ mm} \times 20\text{ mm} \times 0.3\text{ mm}$. The dimensions of the clamp for the bottom CaWO_4 stick which is fixed on the “Klemmblock” (see figure B.5) are: $3\text{ mm} \times 17\text{ mm} \times 0.3\text{ mm}$. The clamps have holes to be assembled on the copper structure by copper screws and are bent slightly to adapt them to the individual length of the CaWO_4 sticks.
- The reflective and scintillating foil (VM2002) is glued (with Araldite) onto the inner surfaces of the copper structure. To provide an optimal matching of the holes (for the CaWO_4 side-sticks) of foil and “Stäbchenring”, small pieces of the foil ($5\text{ mm} \times 5\text{ mm}$) with a hole (diameter: 2.7 mm) in the center are first glued onto the copper structure. The main foil ($146\text{ mm} \times 47\text{ mm}$) equipped with larger holes ($4\text{ mm} \times 6\text{ mm}$) is then glued on top. The overlap assures a total coverage of the detector housing by the foil while the holes therein are aligned optimally.

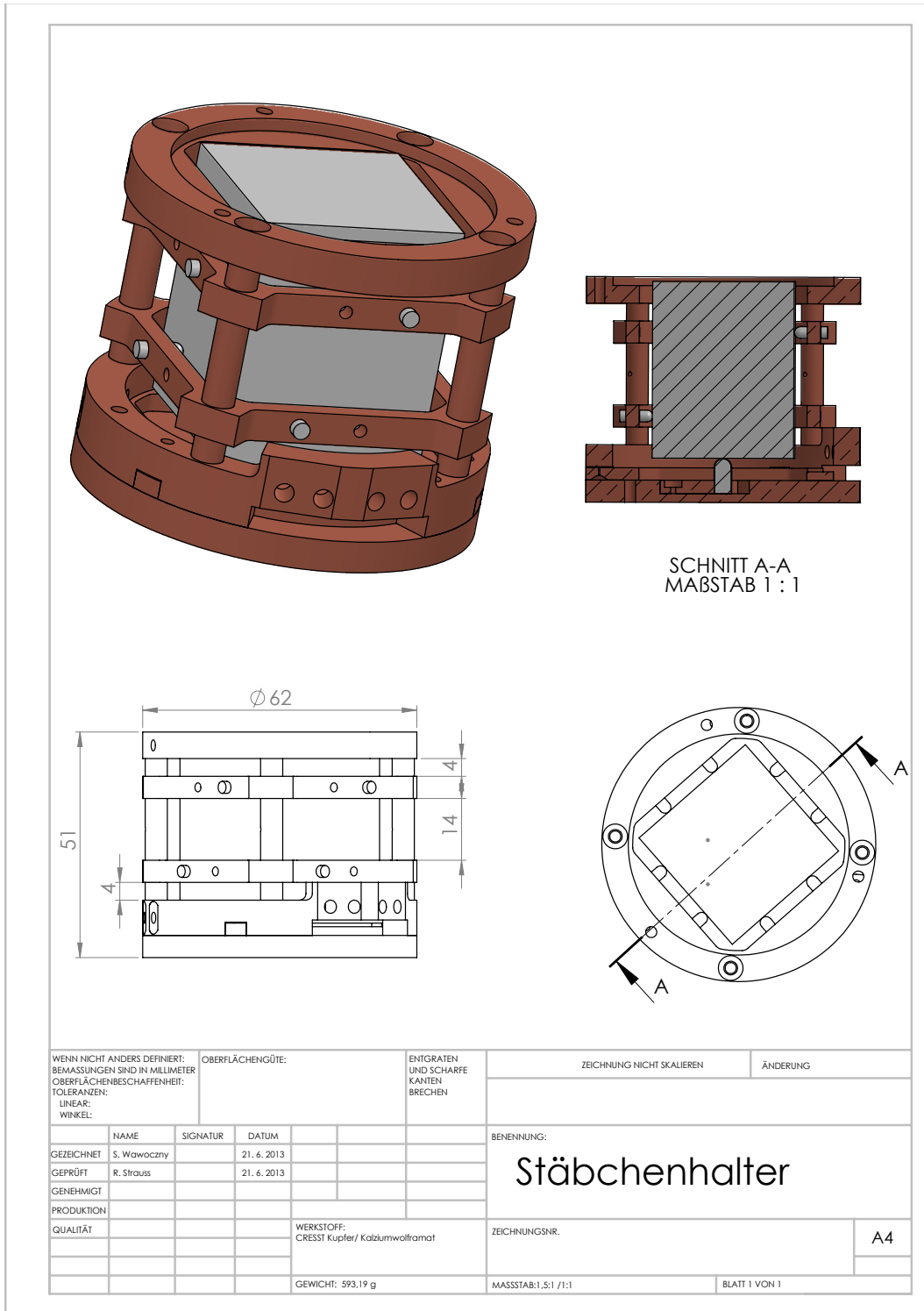


Figure B.1: Technical drawing of the novel phonon-detector holder based on CaWO_4 sticks. The bronze clamps which press the side CaWO_4 sticks onto the crystal and the scintillating foil are not shown.

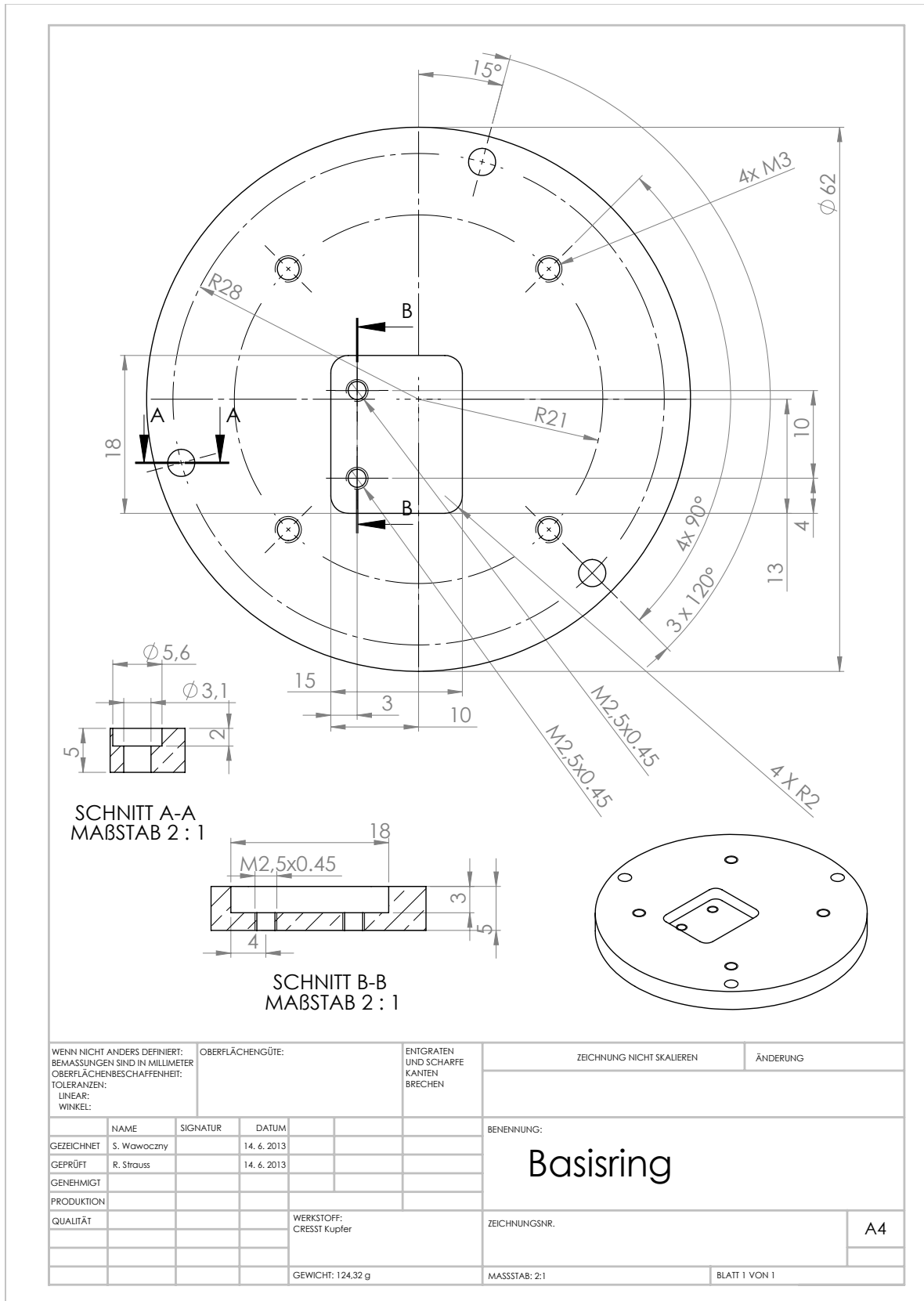


Figure B.2: Technical drawing of the “Basisring”.

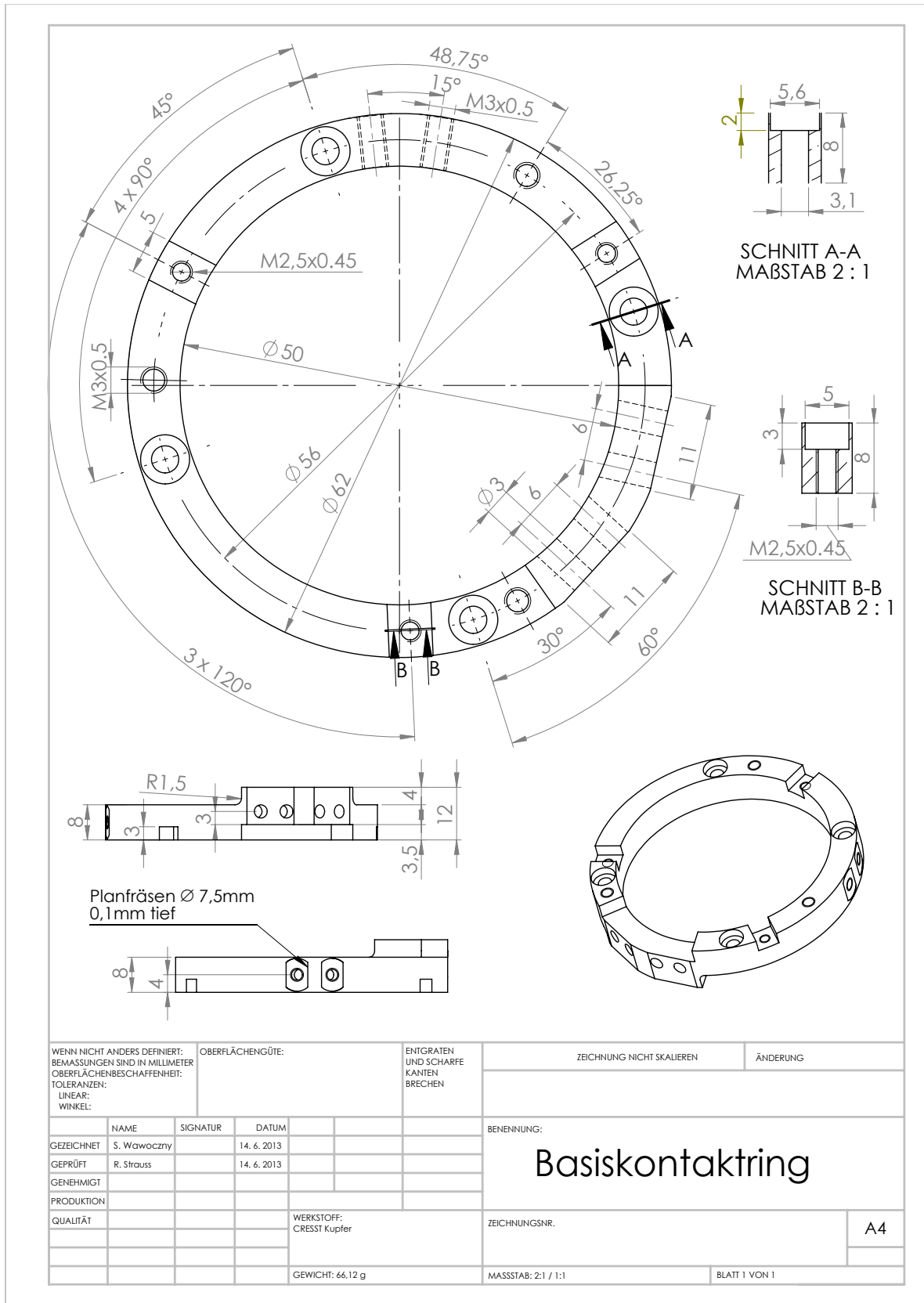


Figure B.3: Technical drawing of the “Basiskontakttring”.

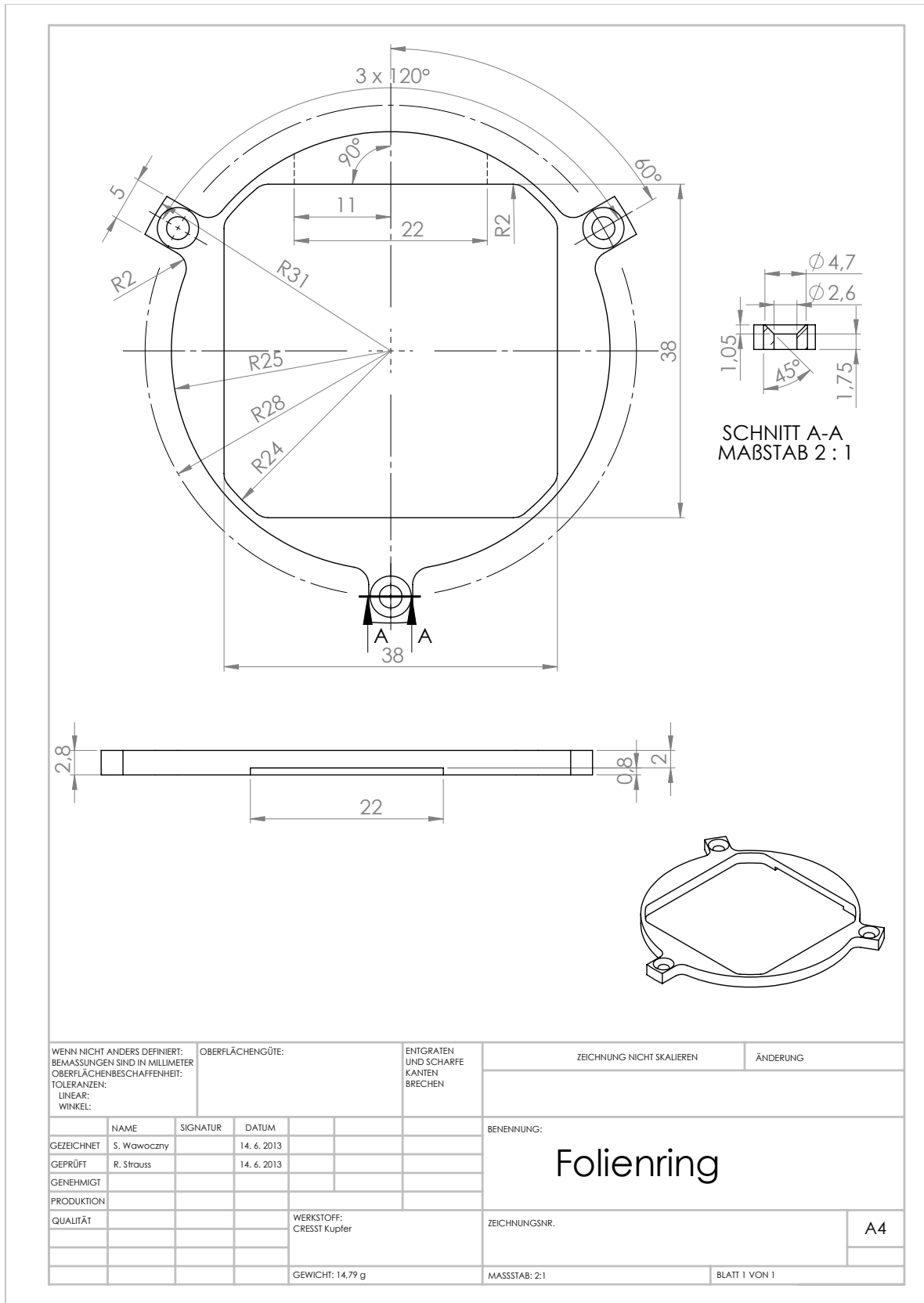


Figure B.4: Technical drawing of the “Folienring”.

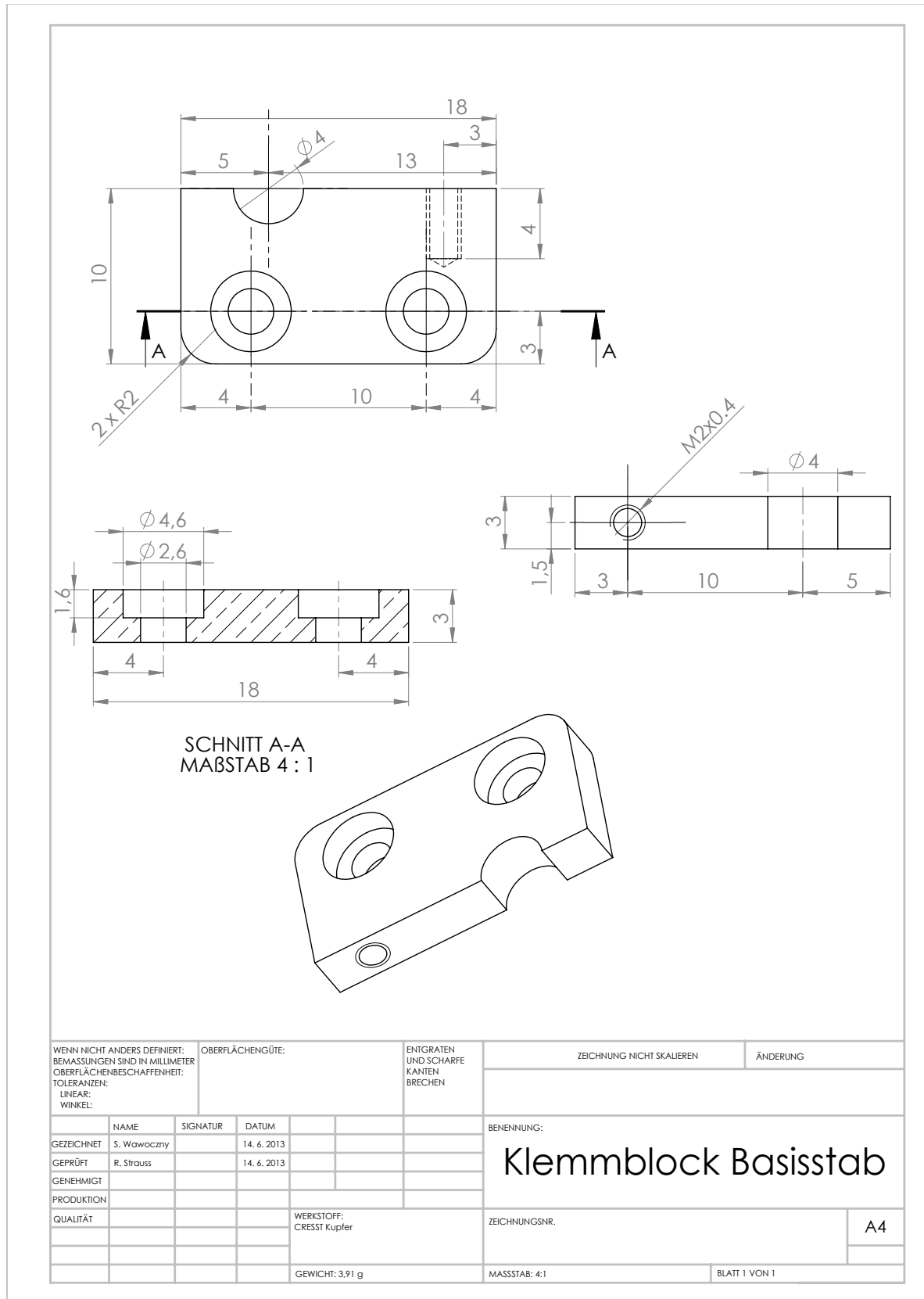


Figure B.5: Technical drawing of the additional piece of copper holding the bottom CaWO_4 stick (called “Klemmblock”). It is embedded in the “Basisring” and fixed by M2.5 screws.

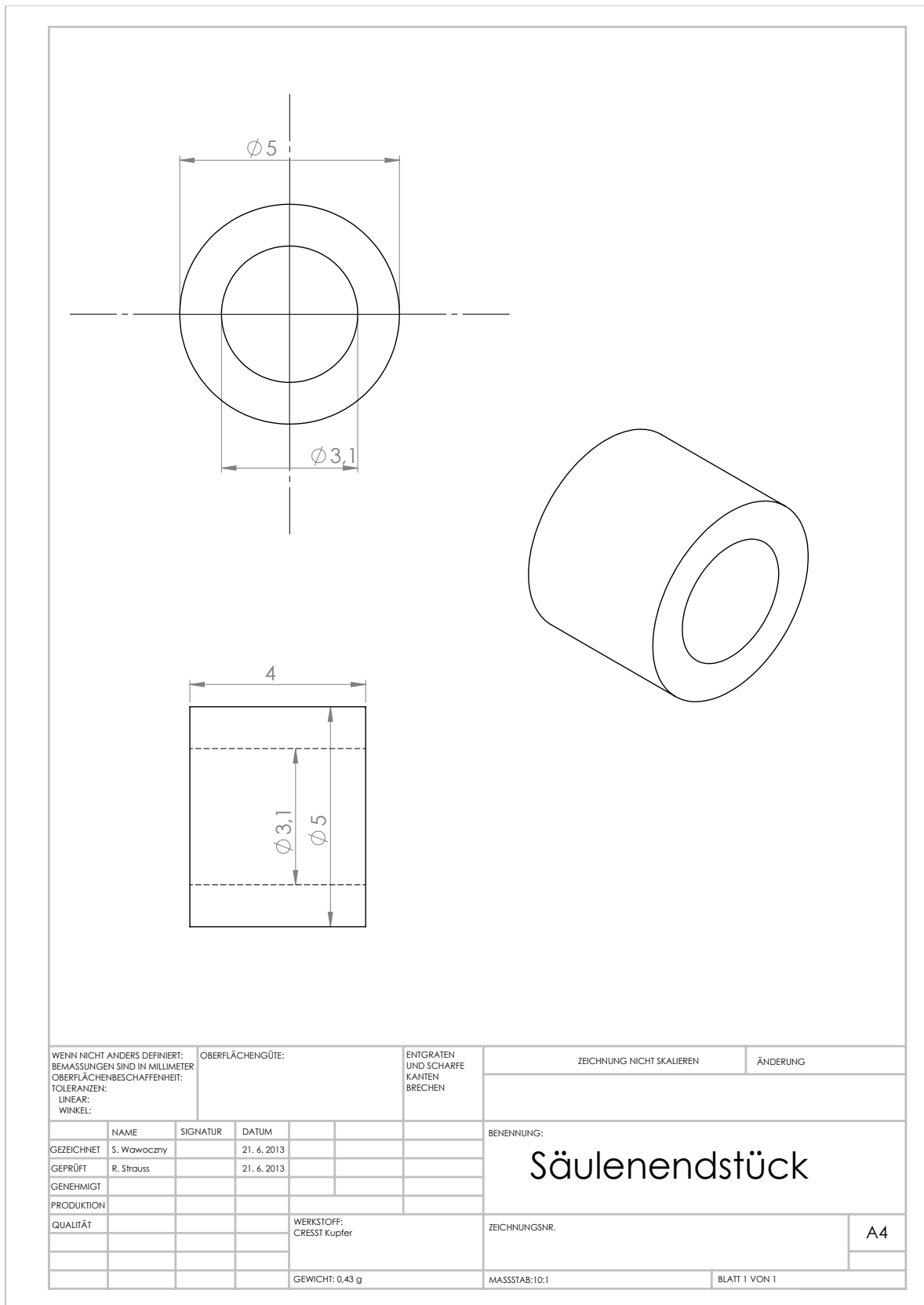


Figure B.6: Technical drawing of the post connecting the copper rings according to figure B.1.

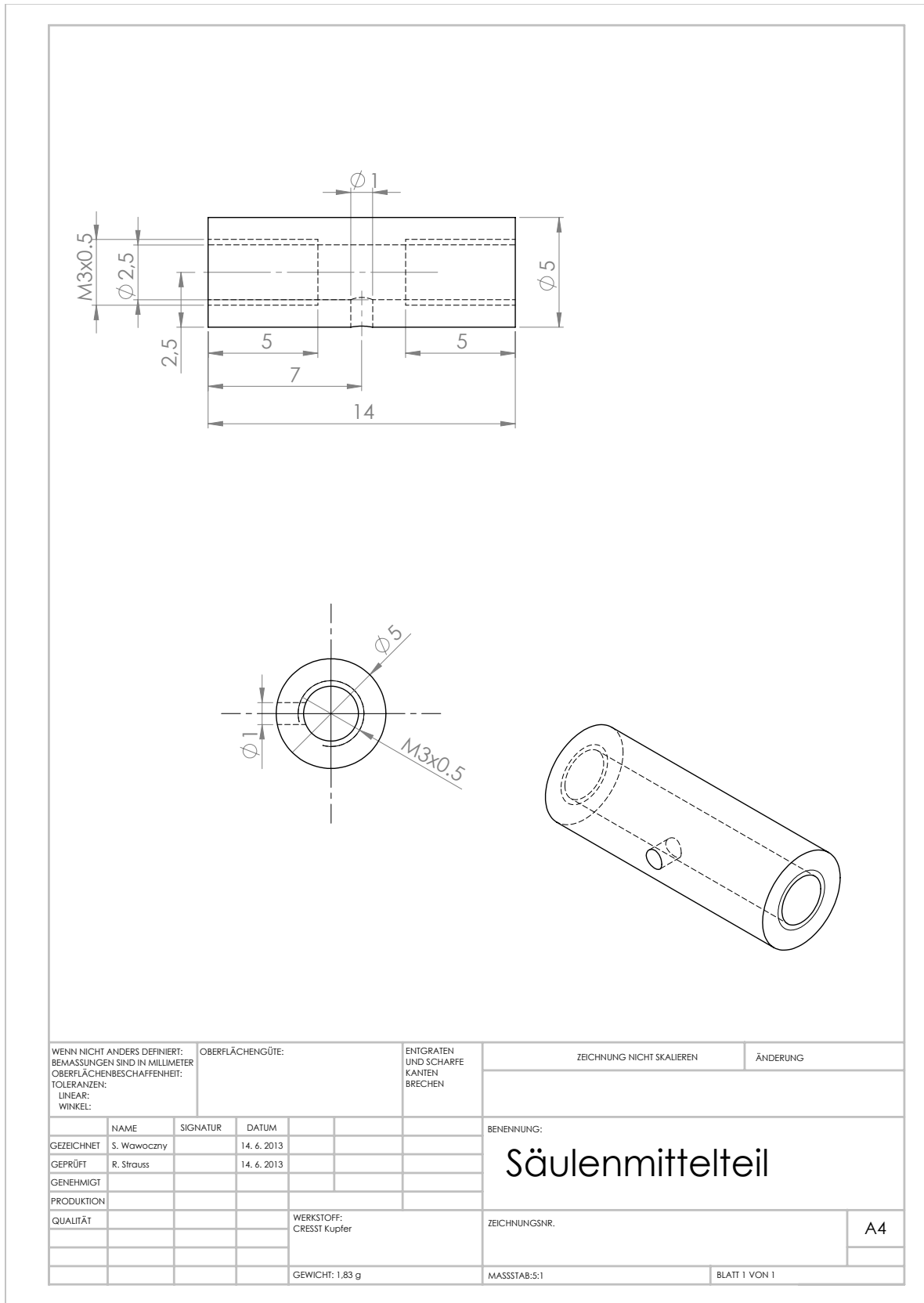


Figure B.7: Technical drawing of the post connecting the copper rings according to figure B.1.

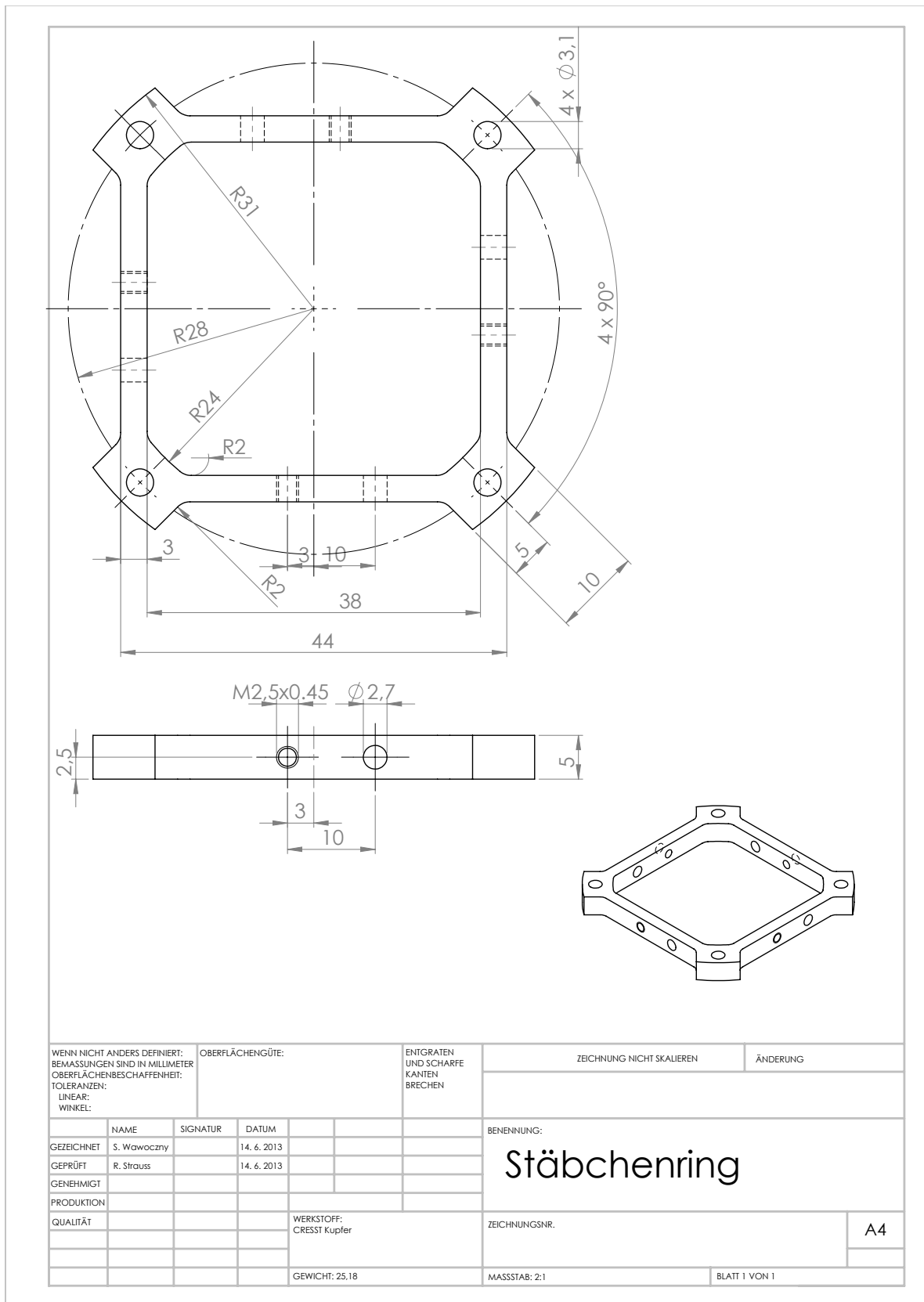


Figure B.8: Technical drawing of the "Stäbchenring".

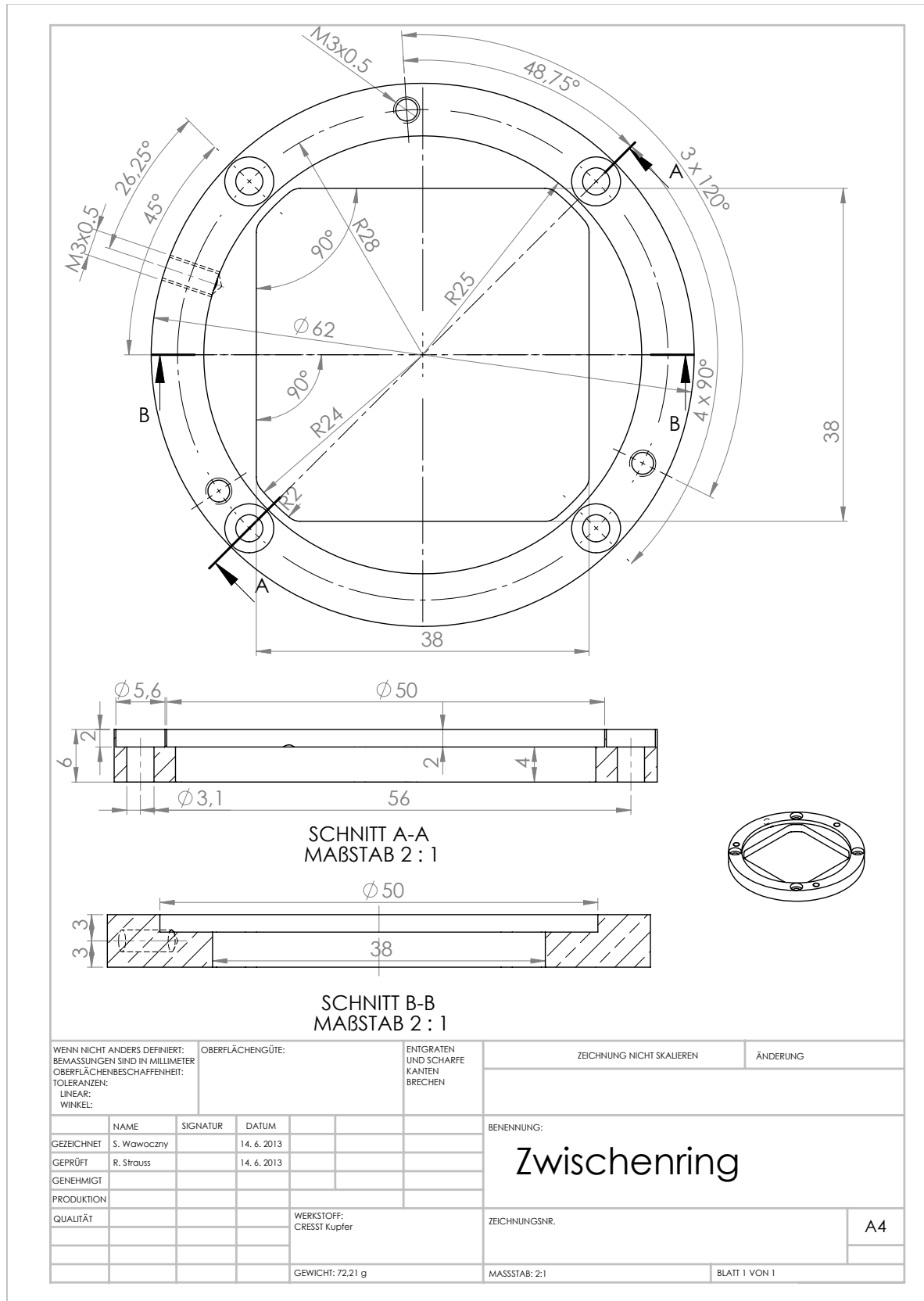


Figure B.9: Technical drawing of the “Zwischenring”.

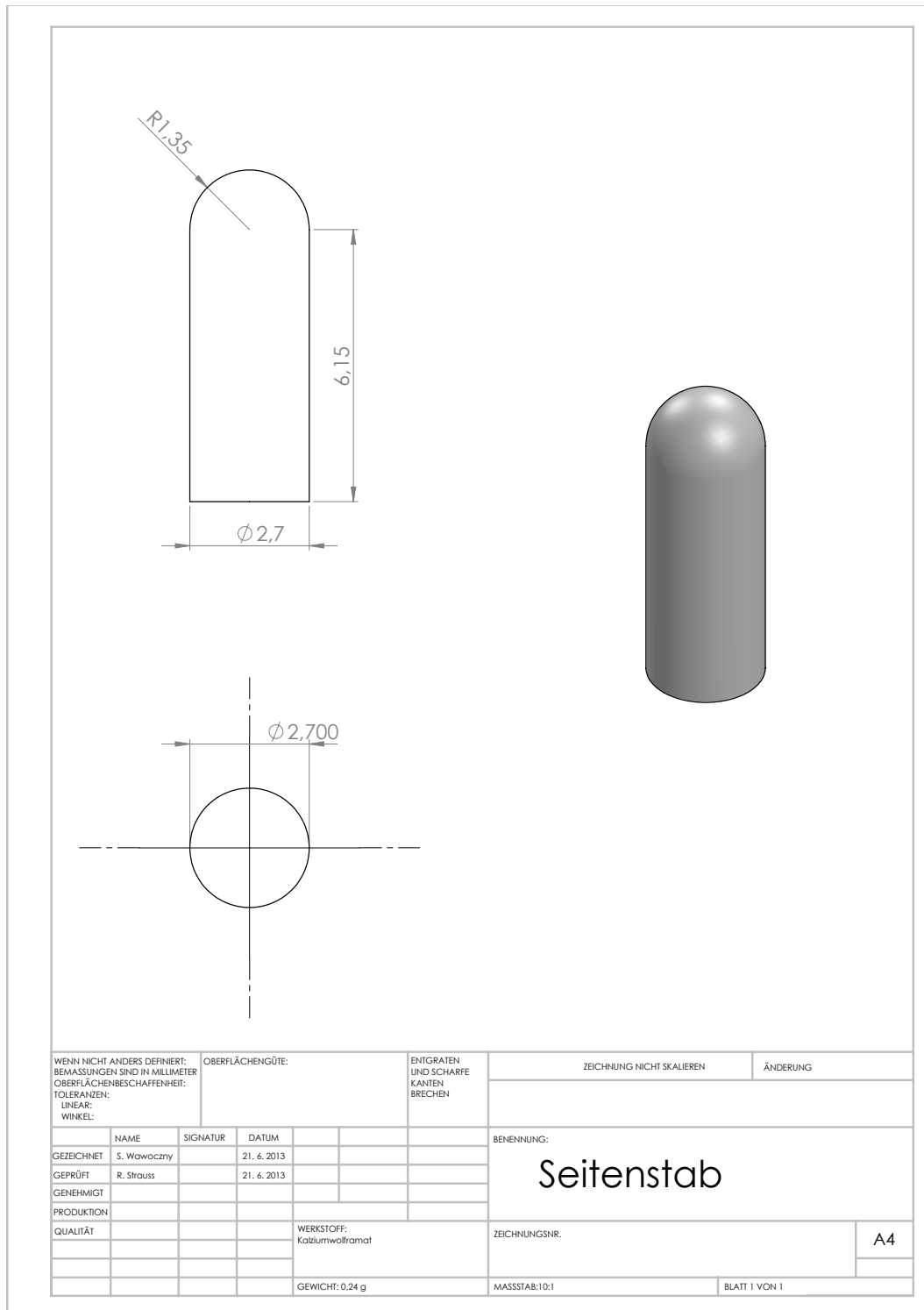


Figure B.10: Technical drawing of a side CaWO_4 stick. The tip surface is polished spherically. The bottom surface and parts of the lateral surface (3 mm in height from the bottom surface) are coated with ultrapure Al (thickness: 20 nm).

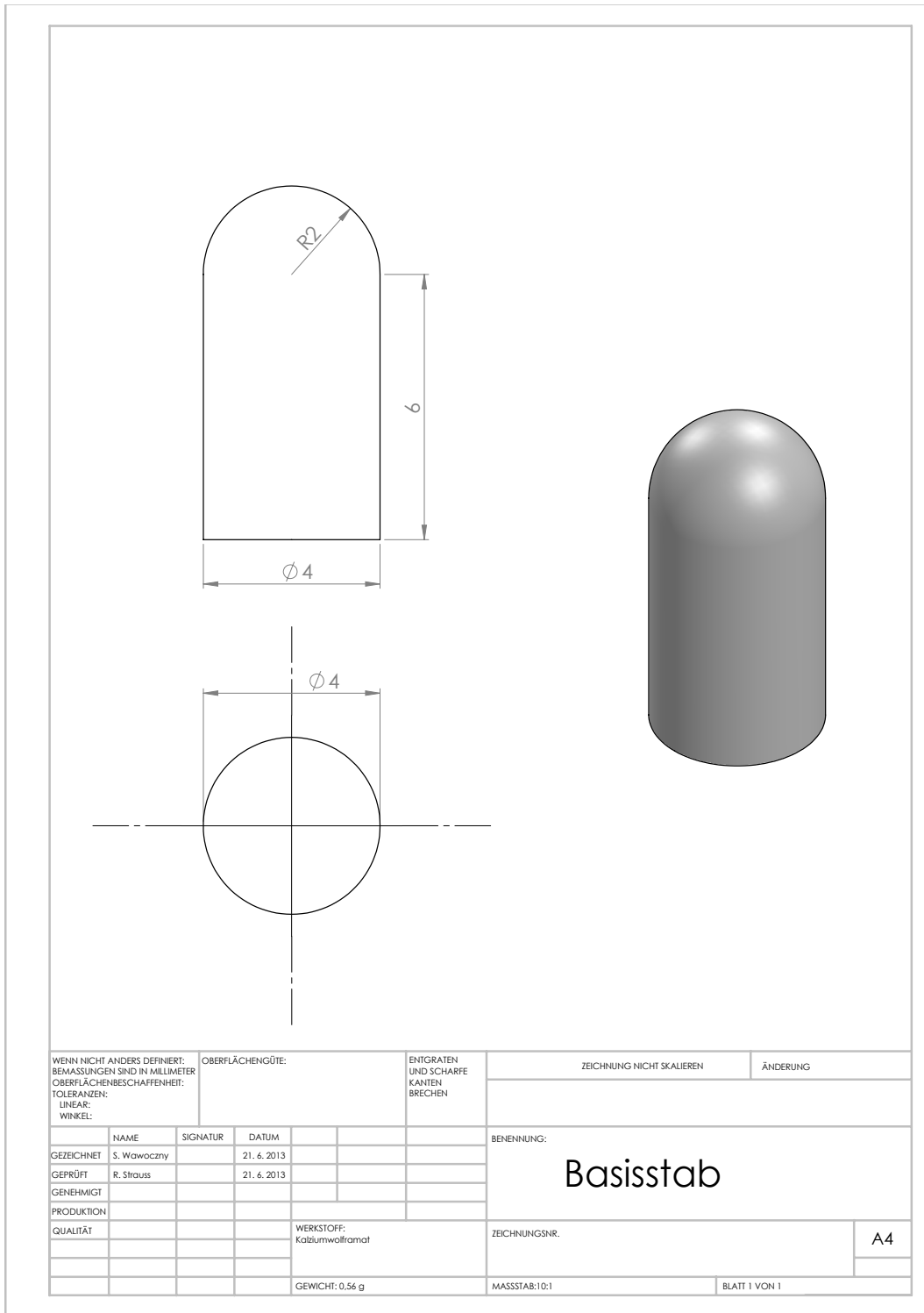


Figure B.11: Technical drawing of the bottom CaWO_4 stick. The tip surface is polished spherically. The bottom surface and parts of the lateral surface (3 mm in height from the bottom surface) are coated with ultrapure Al drawing of a side CaWO_4 stick. The tip surface is polished spherically. The bottom surface and parts of the lateral surface (3 mm in height from the bottom surface) are coated with ultrapure Al (thickness: 20 nm).

Appendix C

The MLL Accelerator as a Neutron Source

Appendix C is a direct copy of pages 47-52 in [96] published by the author of the present thesis.

The neutron scattering facility is placed in Hall 2 at the accelerator of the MLL (Maier Leibnitz Laboratorium) in Garching. Figure C.1 shows a top view of the accelerator facility. Several important components of this setup are described in the following sections.

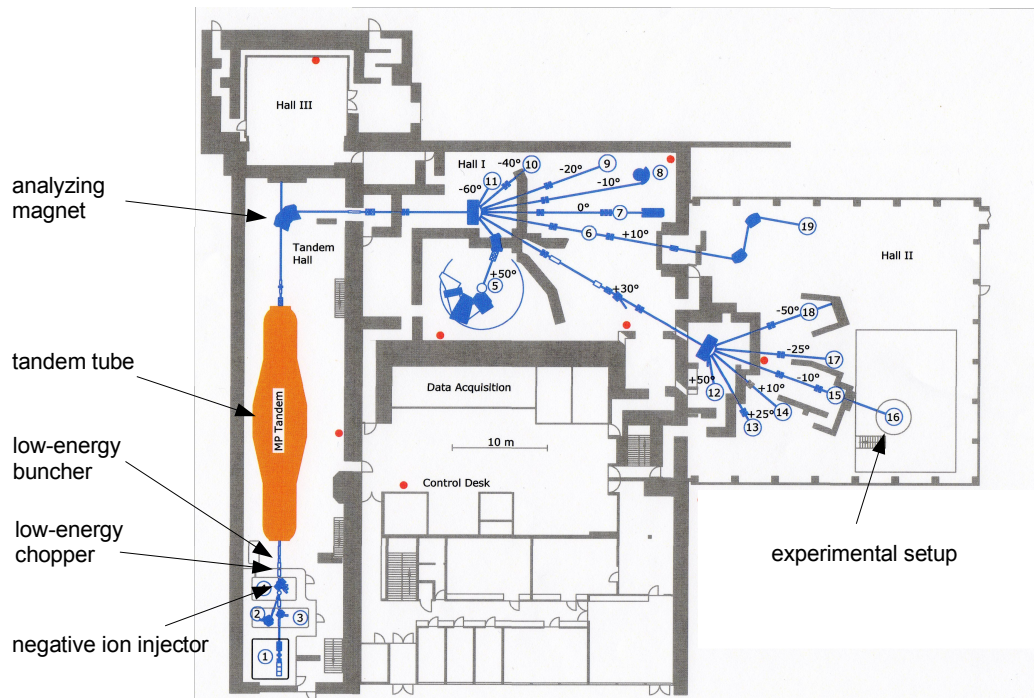


Figure C.1: Top view of the MLL accelerator facility in Garching. Relevant components are indicated. The setup described in this thesis is located in hall II.

C.1 Ion Production and Acceleration

The accelerator laboratory is equipped with a negative-ion injector (figure C.2) that allows to use a wide range of ions [108]. A solid cone-shaped source is placed in an evacuated vessel, where a heater produces neutral Cs vapour, which deposits on the surface of the source as well as on an ionizer. The ionizer is heated to 1400° and, by applying an electric voltage (U_2), Cs^+ ions are generated and finally sputtered onto the source. There they knock out target atoms (in our case ^{11}B) from the source. Since the ^{11}B atoms have to pass a few layers of evaporated neutral Cs atoms, they easily pick up an electron from the loosely bound outermost electron shell of the Cs atoms. In this manner B^- ions are produced and preaccelerated by the extraction voltage U_1 .

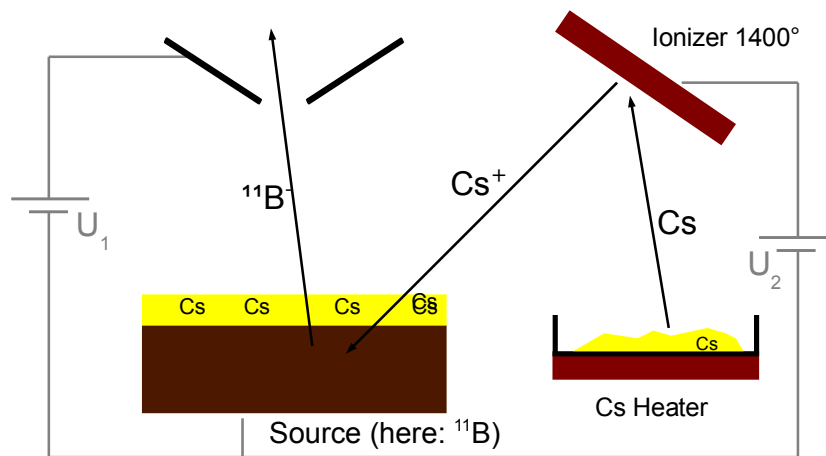


Figure C.2: Working principle of the negative ion injector. Evaporated Cs atoms are ionized and sputtered onto a solid target of choice, where they knock out negatively charged target ions (in our case ^{11}B). A more detailed description is given in the text.

After passing the low-energy pulsing devices (described in section C.2) the beam is injected into the tandem accelerator tube, where the maximum acceleration voltage of ~ 15 MV can be used twice. Due to a stripper foil in the middle of the tank, electrons of the negative ions are stripped off and the generated positive ions traverse the same potential difference (15MV) again.

The beam usually consists of ions with different charge numbers and thus of miscellaneous energies. With the analyzing 90° magnet the desired energy and charge state (here $^{11}\text{B}^{+5}$, means that all electrons of ^{11}B are stripped off) can be selected and focused into the beamline in order to be guided to the experiment.

C.2 Pulsed Ion Beam

The Time-of-Flight (ToF) measurement requires extremely sharp bunches of the beam (width $\sim 2\text{-}3$ ns), for which different devices of the accelerator are used and need to be properly adjusted. The so-called low-energy buncher is used to compress the continuous beam periodically into packages. This is achieved by a saw tooth voltage applied between the hollow buncher tubes, which enclose the beam. The principle is shown in figure C.3.

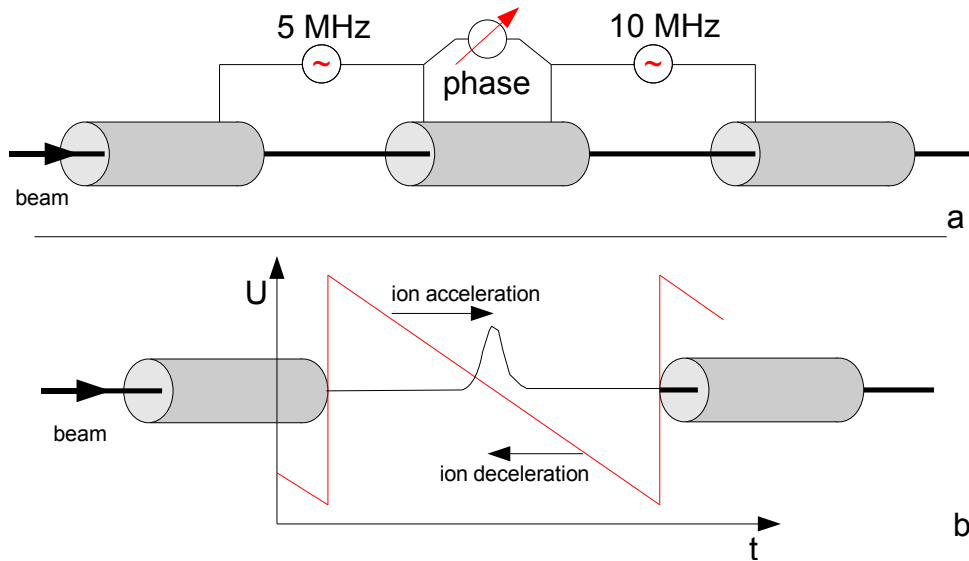


Figure C.3: Scheme of the low-energy buncher: (a) principle of the actually used setup with two applied sine-shaped voltages, (b) functional principle of an ideal saw tooth voltage (U) between the buncher tubes.

By applying a saw-tooth-voltage in the gap between the two tubes early arriving ions are decelerated, late arriving ions are accelerated, thus a periodic accumulation of ions is generated. Since a clean and stable saw-tooth voltage at the desired frequency of 5 MHz is difficult to generate, two sine waves of 5 MHz and 10 MHz, respectively, are applied at two separated gaps of the bunch tubes. By adjusting the phase between them one can obtain an approximately saw-tooth shaped voltage. Because of this approximation, along with a sharp peak periodically appearing every 100 ns, a background intensity (± 20 ns around the peak) remains, which is depicted in figure C.4a.

For this reason a low-energy chopper is installed in front of the buncher, to cut away parts of the beam, before it reaches the buncher. As shown in figure C.5 the Chopper simply consists of a capacitor with an applied AC voltage, which wiggles the beam over an aperture. Regulating the amplitude of the voltage and the phase with respect to the buncher, the cut region (hatched area in figure C.4a) can be adjusted at will. As can be seen in figure C.4b, a pattern with sharp peaks remains.

The buncher produces a logical signal for every bunch in order to have a timing information, that is required for the coincident measurement.

C.3 Neutron Production

To produce neutrons in the MeV regime, the reaction $p(^{11}\text{B},n)^{11}\text{C}$ was chosen [109]. This nuclear reaction takes place in a cell (inner diameter: ~ 1 cm, length ~ 3 cm) placed at the end flange of the beamline at a distance of ~ 30 cm from the cryodetector. The hydrogen gas at a pressure of 2 bar in the cell is separated from the vacuum in the beamline by a $5 \mu\text{m}$ thick molybdenum foil that can stand the pressure difference of ~ 3 bar and allows the high energetic ^{11}B beam to pass with an average energy loss of 4.9 MeV [94]. The hydrogen cell

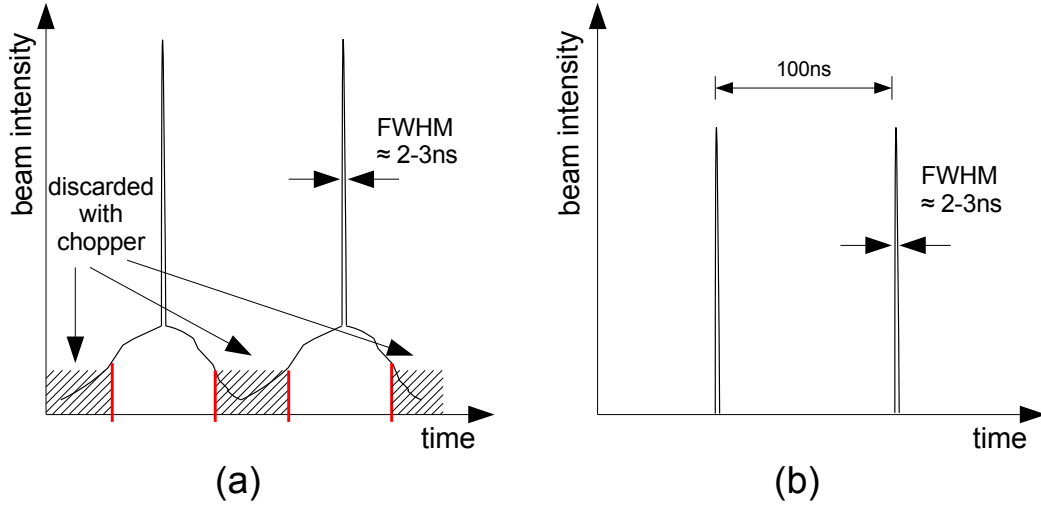


Figure C.4: Schematics of typical beam structures. (a) shows a pattern using only the Buncher, whereas in figure (b) the chopper/buncher ensemble is turned on and properly adjusted. The hatched areas confined by red vertical lines indicate the part of the beam that is discarded by the Chopper.

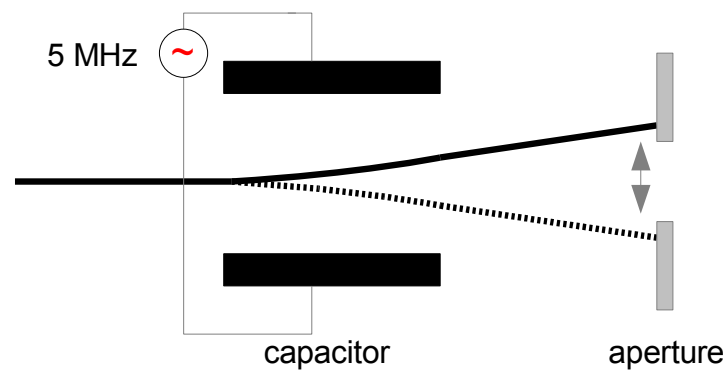


Figure C.5: Working principle of the low-energy chopper. An AC voltage is applied on the capacitor, that wiggles the beam over the aperture. Further details are given in the text.

can be filled and evacuated by a system of transfer tubes.

The energy of the ^{11}B beam is adjusted in such way that a maximum event rate is achieved without reaching the energy of the first excited state of the daughter nucleus (^{11}C), which would lead to lower-energy neutrons (figure C.6). A ^{11}B beam of an energy of 55.4 MeV is found to be the optimal value, leading to a resonant production of 11 MeV neutrons. Due to a large center of mass (CM) velocity the induced neutron beam is collimated in forward direction (inverse kinematics). Because not all ^{11}B ions are interacting with the H_2 gas, a Au beam-stop is installed at the end of the cell. Reactions in this gold disc produce a background of neutrons of lower energies, but for ^{197}Au this background has been shown to be smallest [110].

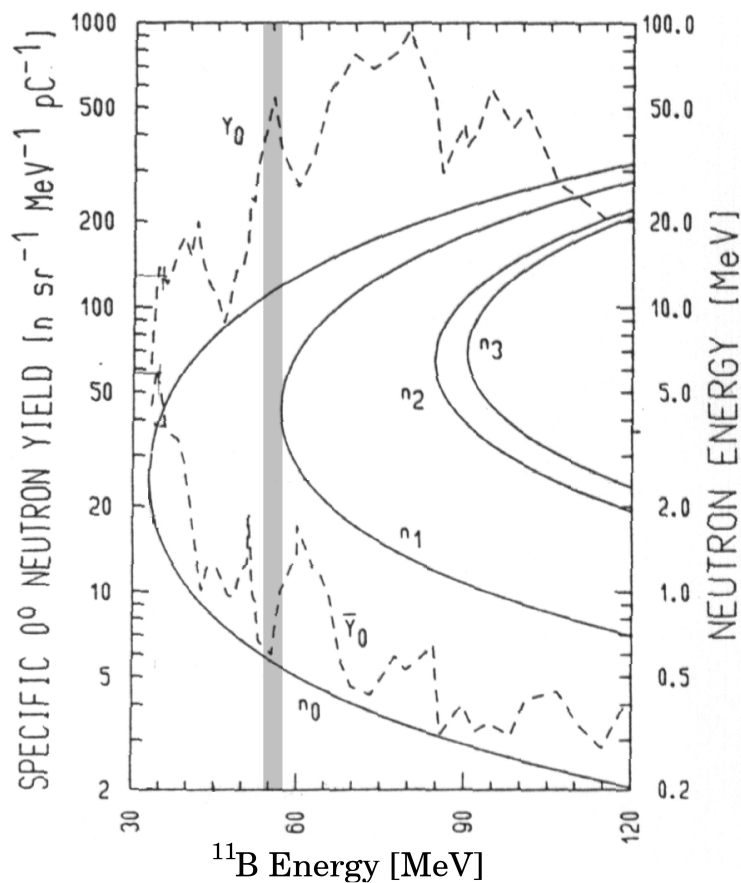


Figure C.6: Specific 0° neutron yield and neutron energy versus the incident ^{11}B energy for the nuclear reaction $p(^{11}\text{B},n)^{11}\text{C}$. The grey vertical line indicates the ^{11}B energy used in this experiment (55.4 MeV). n_0 indicates the line of elastic scattering, whereas n_1, n_2, \dots indicate the lines of inelastic scattering leading to the first, second excited state of ^{11}C . Y_0 and \bar{Y}_0 is the yield of the high-energy branch and the low-energy branch of the n_0 reaction, respectively [109].

The total acceleration voltage is stabilized at 10.2 MV resulting in a beam energy of 61.5 MeV while losses [94] in the Mo-window (4.9 MeV) and the hydrogen cell itself (1.3 MeV)

lead to the desired resonance energy.

C.4 Mounting of the Cell and Beam-Monitoring System

During the commissioning beamtimes it appeared to be quite a challenge to hit the target cell properly, thus several mounting and monitoring devices have been installed within this work, both to stabilize the beam at the right position and to control the shape of the beam itself.

The end of the beamline was supported by a variable aluminium profile system (item-profiles [111]) to avoid vibrations of the setup, for example, when filling the hydrogen cell. In order to check the shape of the beam at about one metre distance from the hydrogen cell, a removable quartz screen was installed. When hit by an ion beam, the quartz scintillates and thus reflects the actual beam shape. The screen is mounted together with a mirror, so that the scintillation light of the quartz can be observed through a glass window by a CCD camera (Figure C.7a). The quartz/mirror ensemble can be moved in and out of the beam by a pneumatic lifter. Using the various quadrupole magnets in the beamline, the beam shape can be optimized, preferably to a circular shape. Elliptical beam shapes not only hit the hydrogen volume, but also the material surrounding it, leading to a parasitic neutron background.

At the hydrogen cell itself, two electrodes can be used to measure the current of the beam. Maximizing the current (figure C.7b) on the Au beamstop while minimizing it on the ring-shaped aperture in front of the cell can be obtained by adjusting X and Y dipole magnets.

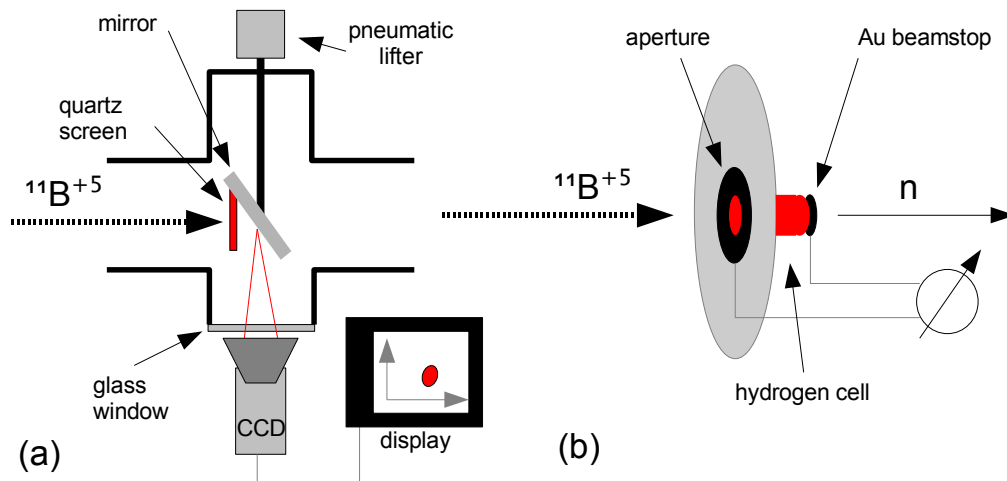


Figure C.7: (a) The camera setup to monitor the $^{11}\text{B}+5$ beam. (b) Schematic view of the hydrogen cell with its electrodes (aperture, Au beamstop) to measure the beam current.

Appendix D

Cryogenic Setup of the Scattering Facility

Appendix D is a direct copy of pages 52-54 in [96] published by the author of the present thesis.

To cool the CRESST-like detector to its operating temperature of $\sim 20\text{mK}$ a ${}^3\text{He}$ - ${}^4\text{He}$ dilution refrigerator (KELVINOX400, cooling power of $400\mu\text{W}$ at 100mK) with a base temperature of $\sim 10\text{mK}$ is used [79, 112]. Despite the complexity of this kind of refrigerator and the big effort to install the cryostat in the beamline of the accelerator, it represents the most convenient way to obtain the required mK-temperatures and necessary cooling power. In the following we will give a brief description of the working principle of a ${}^3\text{He}$ - ${}^4\text{He}$ dilution refrigerator, for further details see [63].

In order to obtain temperatures in the temperature regime $< 0.1\text{K}$, evaporation cooling that uses the latent heat of evaporation while pumping on a cryogenic liquid (e.g. ${}^3\text{He}$, ${}^4\text{He}$), is not sufficient. As can be seen in figure D.1 a minimum temperature of $\sim 0.3\text{K}$ can be reached by reducing the vapour pressure of ${}^3\text{He}$ due to the exponential decrease of the cooling power ($Q \propto \exp -\frac{1}{T}$). Pumping on ${}^4\text{He}$ results in a limit of $\sim 1\text{K}$.

To reach even lower temperatures another cooling method is applied, namely the enthalpy of mixing two quantum liquids. This can be realized by using a mixture of ${}^3\text{He}$ and ${}^4\text{He}$ below its lambda point at $T=0.867\text{K}$, where the mixture separates into a ${}^3\text{He}$ -rich and a ${}^3\text{He}$ -poor phase (see figure D.1). The finite solubility of ${}^3\text{He}$ in ${}^4\text{He}$ (6.6% @ $T=0\text{K}$) is crucial for the cooling mechanism. If ${}^3\text{He}$ is removed from the ${}^3\text{He}$ -poor phase, ${}^3\text{He}$ atoms will pass the phase boundary to maintain the minimum solubility. Since the enthalpy of ${}^3\text{He}$ in the dilute phase is larger than in the concentrated phase, each ${}^3\text{He}$ atom passing the phase boundary is cooling the system. As one can see in figure D.1 left the temperature dependence of the cooling power is weaker and is maintained down to the mK range.

The technical solution of this cooling mechanism is shown in figure D.2 . Since a continuous cooling is required, the mixture is circulated in a closed cycle with pumps, that are placed outside the cryostat at room temperature. The mixture is precooled by a ${}^4\text{He}$ evaporation stage (the so-called 1K-pot), where the mixture condenses. The ${}^3\text{He}$ is continuously removed in the so-called still by pumping which as a welcome side-effect leads to the cooling of the system by ${}^3\text{He}$ -evaporation. The phase boundary occurs in the mixing-chamber, the coldest part of the cryostat, to which the detector module is thermally coupled. Temperature differences

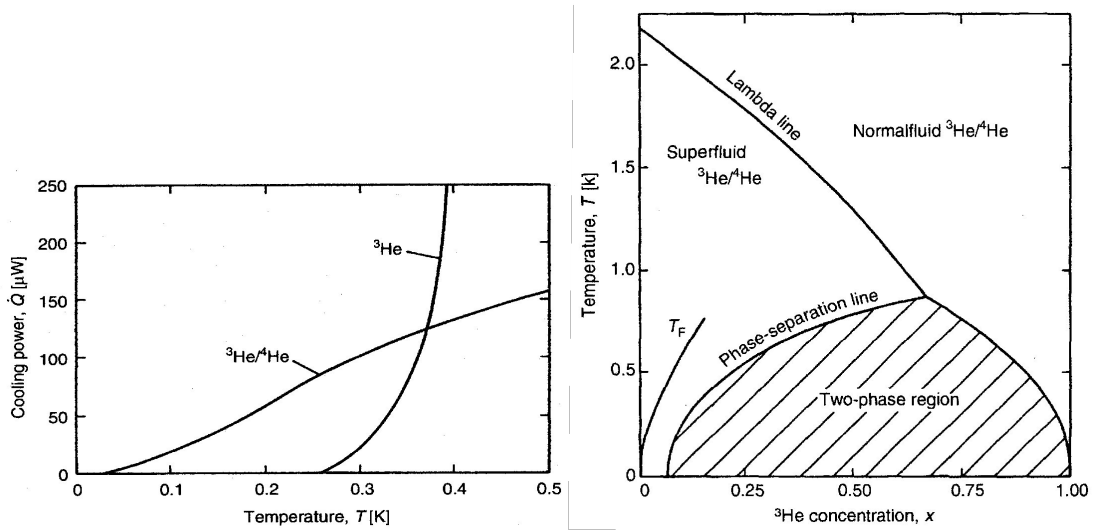


Figure D.1: The left panel indicates the cooling power of the ${}^3\text{He}$ evaporation and the dilution cooling of a ${}^3\text{He}$ - ${}^4\text{He}$ mixture plotted against the temperature. The right plot shows the phase diagram of a ${}^3\text{He}$ - ${}^4\text{He}$ mixture at saturated vapour pressure. Below the lambda point ($T=0.867\text{K}$) the mixture separates into two phases. The finite solubility of ${}^3\text{He}$ in the mK range is of utmost importance to reach mK temperatures (see text) [63].

between the downstreaming and upstreaming gas/liquid are compensated by heat exchangers (see figure D.2).

Since the scattering experiment requires a minimum amount of material around the detector module to avoid parasitic neutron scattering, a dedicated slim He-dewar was designed and installed (see figure 4.9 in chapter 4.5) [112].

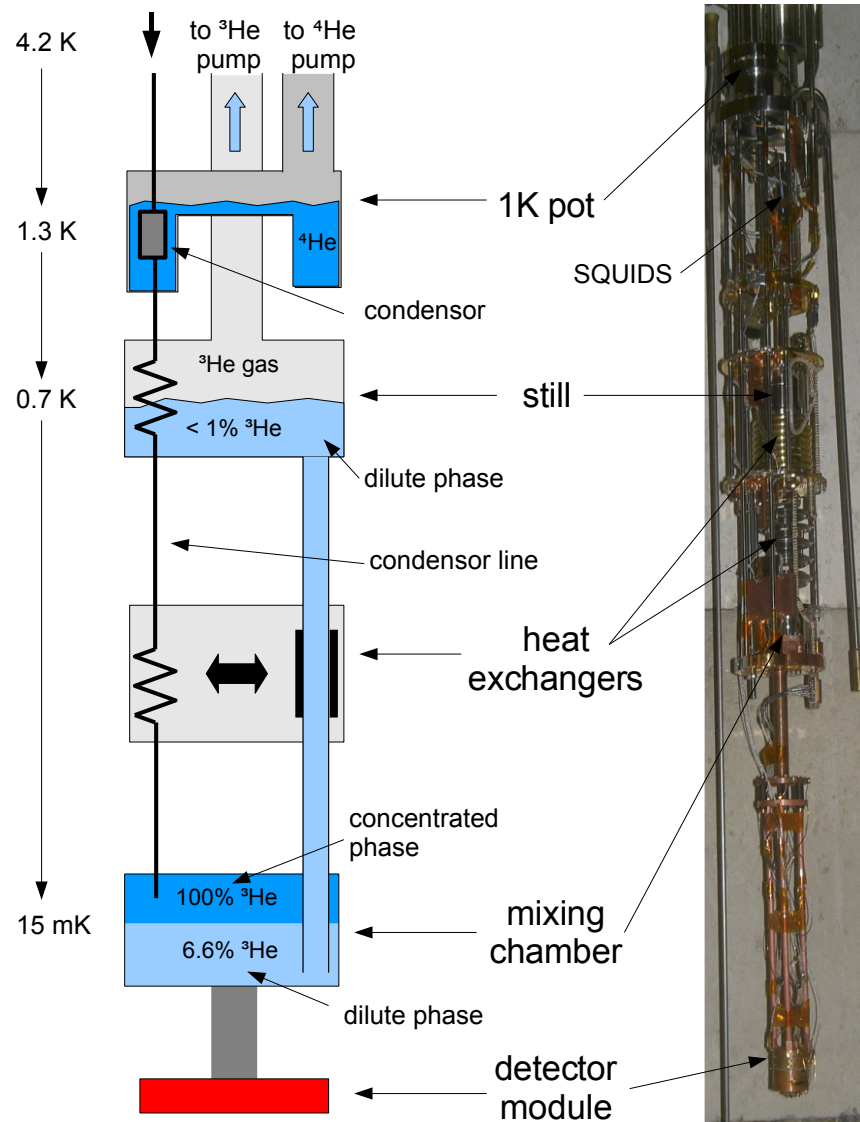


Figure D.2: The main components of a ^3He - ^4He dilution refrigerator are shown schematically (left) and indicated on a picture of the cryostat used for the Quenching-Factor measurements (right). The working principle of a dilution refrigerator is explained in the text.

Bibliography

- [1] K. G. Begeman, A. H. Broeils, and R. H. Sanders, “Extended Rotation Curves of Spiral Galaxies: Dark Haloes and Modified Dynamics,” *MNRAS* **249** no. 523, (1991) .
- [2] G. Bertone, D. Hooper, and J. Silk, “Particle dark matter: Evidence, candidates and constraints,” *Phys.Rept.* **405** (2005) 279–390, [arXiv:hep-ph/0404175](#) [hep-ph].
- [3] F. Zwicky, “Die Rotverschiebung von extragalaktischen Nebeln,” *Helv. Phys. Acta* **6** (1993) 110.
- [4] D. Clowe, M. Bradac, A. H. Gonzalez, M. Markevitch, S. W. Randall, *et al.*, “A direct empirical proof of the existence of dark matter,” *Astrophys.J.* **648** (2006) L109–L113, [arXiv:astro-ph/0608407](#) [astro-ph].
- [5] A. A. Penzias and R. W. Wilson, “A Measurement of Excess Antenna Temperature at 4080-Mc/s,” *Astrophys.J.* **142** (1965) 419–421.
- [6] **Planck** Collaboration, P. Ade *et al.*, “Planck 2013 results. I. Overview of products and scientific results,” [arXiv:1303.5062](#) [astro-ph.CO].
- [7] D. Fixsen, E. Cheng, D. Cottingham, R. Eplee, R. Isaacman, *et al.*, “Cosmic microwave background dipole spectrum measured by the COBE FIRAS,” *Astrophys.J.* **420** (1994) 445.
- [8] **WMAP** Collaboration, C. Bennett *et al.*, “Nine-Year Wilkinson Microwave Anisotropy Probe (WMAP) Observations: Final Maps and Results,” [arXiv:1212.5225](#) [astro-ph.CO].
- [9] L. Bergström and A. Goobar, *Cosmology and Particle Astrophysics*. Springer Praxis Books / Astronomy and Planetary Sciences, 2006.
- [10] **Particle Data Group** Collaboration, K. Nakamura *et al.*, “Review of particle physics,” *J.Phys.* **G37** (2010) 075021.
- [11] L. Bergstrom, “Dark Matter Evidence, Particle Physics Candidates and Detection Methods,” *Annalen Phys.* **524** (2012) 479–496, [arXiv:1205.4882](#) [astro-ph.HE].
- [12] C. Weinheimer, “The Neutrino mass direct measurements,” [arXiv:hep-ex/0306057](#) [hep-ex].
- [13] J. R. Bond, G. Efstathiou, and J. Silk, “Massive neutrinos and the large-scale structure of the universe,” *Phys. Rev. Lett.* **45** (Dec, 1980) 1980–1984. <http://link.aps.org/doi/10.1103/PhysRevLett.45.1980>.

- [14] G. R. Blumenthal, S. Faber, R. Flores, and J. R. Primack, “Contraction of Dark Matter Galactic Halos Due to Baryonic Infall,” *Astrophys.J.* **301** (1986) 27.
- [15] E. Kolb and . Michael Turner, *The Early Universe*. Frontiers in physics. Westview Press, 1994. <http://books.google.com/books?id=Qwijr-HsvMMC>.
- [16] G. Jungman, M. Kamionkowski, and K. Griest, “Supersymmetric dark matter,” *Phys.Rept.* **267** (1996) 195–373, [arXiv:hep-ph/9506380](https://arxiv.org/abs/hep-ph/9506380) [hep-ph].
- [17] **ATLAS** Collaboration, G. Aad *et al.*, “The ATLAS Experiment at the CERN Large Hadron Collider,” *JINST* **3** (2008) S08003.
- [18] **CMS** Collaboration, S. Chatrchyan *et al.*, “Observation of a new boson at a mass of 125 GeV with the CMS experiment at the LHC,” *Phys.Lett.* **B716** (2012) 30–61, [arXiv:1207.7235](https://arxiv.org/abs/1207.7235) [hep-ex].
- [19] F. Halzen and D. Hooper, “The Indirect Search for Dark Matter with IceCube,” *New J.Phys.* **11** (2009) 105019, [arXiv:0910.4513](https://arxiv.org/abs/0910.4513) [astro-ph.HE].
- [20] J. Lewin and P. Smith, “Review of mathematics, numerical factors, and corrections for dark matter experiments based on elastic nuclear recoil,” *Astropart.Phys.* **6** (1996) 87–112.
- [21] F. Donato, N. Fornengo, and S. Scopel, “Effects of galactic dark halo rotation on WIMP direct detection,” *Astropart.Phys.* **9** (1998) 247–260, [arXiv:hep-ph/9803295](https://arxiv.org/abs/hep-ph/9803295) [hep-ph].
- [22] R. H. Helm, “Inelastic and elastic scattering of 187-meV electrons from selected even-even nuclei,” *Phys. Rev.* **104** (Dec, 1956) 1466–1475. <http://link.aps.org/doi/10.1103/PhysRev.104.1466>.
- [23] R. Lang, *Search for Dark Matter with the CRESST Experiment*. PhD thesis, TU München, 2008.
- [24] **XENON100** Collaboration, E. Aprile *et al.*, “Dark Matter Results from 225 Live Days of XENON100 Data,” *Phys.Rev.Lett.* **109** (2012) 181301, [arXiv:1207.5988](https://arxiv.org/abs/1207.5988) [astro-ph.CO].
- [25] G. Angloher, M. Bauer, I. Bavykina, A. Bento, C. Bucci, C. Ciemniak, G. Deuter, F. Feilitzsch, D. Hauff, P. Huff, C. Isaila, J. Jochum, M. Kiefer, M. Kimmerle, J.-C. Lanfranchi, F. Petricca, S. Pfister, W. Potzel, F. Pröbst, F. Reindl, S. Roth, K. Rottler, C. Sailer, K. Schäffner, J. Schmaler, S. Scholl, W. Seidel, M. Sivers, L. Stodolsky, C. Strandhagen, R. Strauß, A. Tanzke, I. Usherov, S. Wawoczny, M. Willers, and A. Zöller, “Results from 730 kg days of the CRESST-II Dark Matter search,” *The European Physical Journal C* **72** no. 4, (2012) 1–22. <http://dx.doi.org/10.1140/epjc/s10052-012-1971-8>.
- [26] **DAMA, LIBRA** Collaboration, R. Bernabei *et al.*, “New results from DAMA/LIBRA,” *Eur.Phys.J.* **C67** (2010) 39–49, [arXiv:1002.1028](https://arxiv.org/abs/1002.1028) [astro-ph.GA].
- [27] J. Schmaler, *The CRESST Dark Matter Search – New Analysis Methods and Recent Results*. PhD thesis, TU München, 2010.

- [28] G. Bertone, *Particle Dark Matter*. Cambridge University Press, 2010.
- [29] **KIMS** Collaboration, H. Lee *et al.*, “Limits on WIMP-nucleon cross section with CsI(Tl) crystal detectors,” *Phys.Rev.Lett.* **99** (2007) 091301, [arXiv:0704.0423](#) [astro-ph].
- [30] J. Cherwinka, R. Co, D. Cowen, D. Grant, F. Halzen, *et al.*, “A Search for the Dark Matter Annual Modulation in South Pole Ice,” *Astropart.Phys.* **35** (2012) 749–754, [arXiv:1106.1156](#) [astro-ph.HE].
- [31] **IceCube** Collaboration, S. Odrowski, “Recent results from the IceCube neutrino telescope,” *Acta Phys.Polon.Supp.* **6** (2013) 687–693.
- [32] **XENON10** Collaboration, J. Angle *et al.*, “A search for light dark matter in XENON10 data,” *Phys.Rev.Lett.* **107** (2011) 051301, [arXiv:1104.3088](#) [astro-ph.CO].
- [33] **EDELWEISS** Collaboration, E. Armengaud *et al.*, “Final results of the EDELWEISS-II WIMP search using a 4-kg array of cryogenic germanium detectors with interleaved electrodes,” *Phys.Lett.* **B702** (2011) 329–335, [arXiv:1103.4070](#) [astro-ph.CO].
- [34] **CDMS-II** Collaboration, Z. Ahmed *et al.*, “Dark Matter Search Results from the CDMS II Experiment,” *Science* **327** (2010) 1619–1621, [arXiv:0912.3592](#) [astro-ph.CO].
- [35] **CDMS-II** Collaboration, Z. Ahmed *et al.*, “Results from a Low-Energy Analysis of the CDMS II Germanium Data,” *Phys.Rev.Lett.* **106** (2011) 131302, [arXiv:1011.2482](#) [astro-ph.CO].
- [36] **CoGeNT** Collaboration, C. Aalseth *et al.*, “CoGeNT: A Search for Low-Mass Dark Matter using p-type Point Contact Germanium Detectors,” [arXiv:1208.5737](#) [astro-ph.CO].
- [37] **CDMS** Collaboration, R. Agnese *et al.*, “Dark Matter Search Results Using the Silicon Detectors of CDMS II,” *Phys.Rev.Lett.* (2013) , [arXiv:1304.4279](#) [hep-ex].
- [38] J. P. Filippini. PhD thesis, University of California, Berkeley, 2008.
- [39] **EDELWEISS** Collaboration, E. Armengaud *et al.*, “A search for low-mass WIMPs with EDELWEISS-II heat-and-ionization detectors,” *Phys.Rev.* **D86** (2012) 051701, [arXiv:1207.1815](#) [astro-ph.CO].
- [40] S. Ahlen, F. Avignone, R. Brodzinski, A. Drukier, G. Gelmini, *et al.*, “Limits on Cold Dark Matter Candidates from an Ultralow Background Germanium Spectrometer,” *Phys.Lett.* **B195** (1987) 603–608.
- [41] D. O. Caldwell, B. Magnusson, M. S. Witherell, A. Da Silva, B. Sadoulet, *et al.*, “Searching for the cosmion by scattering in Si detectors,” *Phys.Rev.Lett.* **65** (1990) 1305–1308.

- [42] **CoGeNT** Collaboration, C. Aalseth *et al.*, “Results from a Search for Light-Mass Dark Matter with a P-type Point Contact Germanium Detector,” *Phys.Rev.Lett.* **106** (2011) 131301, [arXiv:1002.4703](#) [[astro-ph.CO](#)].
- [43] C. Aalseth, P. Barbeau, J. Colaresi, J. Collar, J. Diaz Leon, *et al.*, “Search for an Annual Modulation in a P-type Point Contact Germanium Dark Matter Detector,” *Phys.Rev.Lett.* **107** (2011) 141301, [arXiv:1106.0650](#) [[astro-ph.CO](#)].
- [44] **LUX** Collaboration, D. Akerib *et al.*, “The Large Underground Xenon (LUX) Experiment,” *Nucl.Instrum.Meth.* **A704** (2013) 111–126, [arXiv:1211.3788](#) [[physics.ins-det](#)].
- [45] **DEAP** Collaboration, M. Boulay, “DEAP-3600 Dark Matter Search at SNOLAB,” *J.Phys.Conf.Ser.* **375** (2012) 012027, [arXiv:1203.0604](#) [[astro-ph.IM](#)].
- [46] **DarkSide** Collaboration, A. Wright, “The DarkSide Program at LNGS,” [arXiv:1109.2979](#) [[physics.ins-det](#)].
- [47] **XENON1T** Collaboration, E. Aprile, “The XENON1T Dark Matter Search Experiment,” [arXiv:1206.6288](#) [[astro-ph.IM](#)].
- [48] H. Kraus, M. Bauer, I. Bavykina, A. Benoit, J. Blumer, *et al.*, “EURECA: The European future of dark matter searches with cryogenic detectors,” *Nucl.Phys.Proc.Suppl.* **173** (2007) 168–171.
- [49] H. Kraus, E. Armengaud, C. Augier, M. Bauer, N. Bechtold, *et al.*, “EURECA,” *PoS IDM2010* (2011) 109.
- [50] A. Gutlein, C. Ciemniak, F. von Feilitzsch, N. Haag, M. Hofmann, *et al.*, “Solar and atmospheric neutrinos: Background sources for the direct dark matter search,” *Astropart.Phys.* **34** (2010) 90–96, [arXiv:1003.5530](#) [[hep-ph](#)].
- [51] M. Sivers, C. Ciemniak, A. Erb, F. Feilitzsch, A. Gutlein, *et al.*, “Influence of Annealing on the Optical and Scintillation Properties of CaWO₄ Single Crystals,” [arXiv:1206.1588](#) [[physics.optics](#)].
- [52] M. v. Sivers, *PhD thesis (in preparation)*. PhD thesis, TU München.
- [53] J. Birks, *The Theory and Practice of Scintillation Counting*. Pergamon Press, 1964. <http://books.google.com/books?id=OR1RAAAAMAAJ>.
- [54] M. Kiefer, G. Angloher, M. Bauer, I. Bavykina, A. Bento, *et al.*, “Composite CaWO₄ Detectors for the CRESST-II Experiment,” [arXiv:0912.0170](#) [[astro-ph.IM](#)].
- [55] R. C. Jaklevic, J. Lambe, A. H. Silver, and J. E. Mercereau, “Quantum interference effects in josephson tunneling,” *Phys. Rev. Lett.* **12** (Feb, 1964) 159–160. <http://link.aps.org/doi/10.1103/PhysRevLett.12.159>.
- [56] P. Huff, *The Detector Parameters Determining the Sensitivity of the CRESST-II Experiment*. PhD thesis, TU München, 2010.
- [57] “NA CAST - Die Marke für Stranggussprodukte.”

- [58] F. Pröbst, M. Frank, S. Cooper, P. Colling, D. Dummer, P. Ferger, G. Forster, A. Nucciotti, W. Seidel, and L. Stodolsky, “Model for cryogenic particle detectors with superconducting phase transition thermometers,” *Journal of Low Temperature Physics* **100** no. 1-2, (1995) 69–104. <http://dx.doi.org/10.1007/BF00753837>.
- [59] M. Gluyas, F. D. Hughes, and B. W. James, “The elastic constants of calcium tungstate, 42-300 k,” *Journal of Physics D: Applied Physics* **6** no. 17, (1973) 2025. <http://stacks.iop.org/0022-3727/6/i=17/a=309>.
- [60] **MACRO** Collaboration, M. Ambrosio *et al.*, “Measurement of the energy spectrum of underground muons at Gran Sasso with a transition radiation detector,” *Astropart.Phys.* **10** (1999) 11–20, [arXiv:hep-ex/9807009](https://arxiv.org/abs/hep-ex/9807009) [hep-ex].
- [61] C. Arpesella, “Background measurements at gran sasso laboratory,” *Nuclear Physics B - Proceedings Supplements* **28** no. 1, (1992) 420 – 424. <http://www.sciencedirect.com/science/article/pii/0920563292902079>.
- [62] A. Alessandrello, C. Arpesella, C. Brofferio, C. Bucci, C. Cattadori, O. Cremonesi, E. Fiorini, A. Giuliani, S. Latorre, A. Nucciotti, E. Orvini, M. Pavan, S. Parmeggiano, M. Perego, G. Pessina, S. Pirro, E. Previtali, B. Romualdi, A. Rotilio, E. Tatananni, and L. Zanotti, “Measurements of internal radioactive contamination in samples of roman lead to be used in experiments on rare events,” *Nuclear Instruments and Methods in Physics Research Section B: Beam Interactions with Materials and Atoms* **142** no. 1–2, (1998) 163 – 172. <http://www.sciencedirect.com/science/article/pii/S0168583X98002791>.
- [63] F. Pobell, *Matter and methods at low temperatures*. Springer textbook. Springer-Verlag, 1992. <http://books.google.com/books?id=grrvAAAAMAAJ>.
- [64] S. Pfister, *Suche nach Dunkler Materie mit dem CRESST-II-Experiment*. PhD thesis, TU München, 2010.
- [65] “Supracon AG.” <http://www.supracon.com/de/squid.html>.
- [66] S. Henry, N. Bazin, H. Kraus, B. Majorovits, M. Malek, *et al.*, “The 66-channel SQUID readout for CRESST II,” *JINST* **2** (2007) P11003.
- [67] S. Scholl, *Neutron Background Simulations for the CRESST Experiment*. PhD thesis, Universität Tübingen, 2011.
- [68] K. Schäffner, (*to be published*). PhD thesis, TU München, 2013.
- [69] M. Kuzniak, M. Boulay, and T. Pollmann, “Surface roughness interpretation of 730 kg days CRESST-II results,” *Astropart.Phys.* **36** (2012) 77–82, [arXiv:1203.1576](https://arxiv.org/abs/1203.1576) [astro-ph.IM].
- [70] “RWTH Aachen.” http://www.imm.rwth-aachen.de/home_page_2008/html/welcome.htm.
- [71] F. Alessandria, E. Andreotti, R. Ardito, C. Arnaboldi, I. Avignone, F.T., *et al.*, “Sensitivity of CUORE to Neutrinoless Double-Beta Decay,” [arXiv:1109.0494](https://arxiv.org/abs/1109.0494) [nucl-ex].

- [72] M. A. Spivack, "Parylene thin films for radiation applications," *Review of Scientific Instruments* **41** no. 11, (1970) 1614–1616.
- [73] A. Erb and J.-C. Lanfranchi, "Growth of high-purity scintillating CaWO_4 single crystals for the low-temperature direct dark matter search experiments CRESST-II and EURECA," *CrystEngComm* **15** (2013) 2301–2304.
<http://dx.doi.org/10.1039/C2CE26554K>.
- [74] C. Kister, (*in preparation*). PhD thesis, TU München.
- [75] F. Reindl, "private communication," 2013.
- [76] "Leiden Cryogenics." <http://www.leidencryogenics.com/>.
- [77] "Applied Physics." <http://www.appliedphysics.com/about>.
- [78] F. Reindl, "Analysis of CRESST Dark Matter Search Data," Diploma Thesis, TU München, 2011.
- [79] C. Ciemniak, *Setup of a Neutron Scattering Facility for the Measurement of Scintillation Light Quenching Factors of Low-Temperature Detectors Used in the Direct Dark Matter Search Experiments CRESST and EURECA*. PhD thesis, TU München, 2011.
- [80] C. Arnaboldi, J. Beeman, O. Cremonesi, L. Gironi, M. Pavan, G. Pessina, S. Pirro, and E. Previtali, "Cdwo4 scintillating bolometer for double beta decay: Light and heat anticorrelation, light yield and quenching factors," *Astroparticle Physics* **34** no. 3, (2010) 143 – 150.
<http://www.sciencedirect.com/science/article/pii/S0927650510001210>.
- [81] C. Coppi, *Quenching-Factor Measurements for Cryogenic Dark Matter Detectors*. PhD thesis, TU München, 2009.
- [82] F. Pröbst, "private communication," 2013.
- [83] A. Zoeller, (*in preparation*). PhD thesis, TU München.
- [84] R. Lang, G. Angloher, M. Bauer, I. Bavykina, A. Bento, *et al.*, "Scintillator Non-Proportionality and Gamma Quenching in CaWO_4 ," [arXiv:0910.4414](https://arxiv.org/abs/0910.4414) [nucl-ex].
- [85] M. v. Sivers, "Optimizing Detectors for Dark Matter Search," Diploma Thesis, TU München, 2010.
- [86] G. Cowan, *Statistical Data Analysis*. Oxford Science Publications. Oxford University Press on Demand, 1998. <http://books.google.com/books?id=ff8ZyW0nLJAC>.
- [87] S. Scholl, "private communication."
- [88] J. Astrom, F. Probst, P. Di Stefano, L. Stodolsky, J. Timonen, *et al.*, "Fracture processes studied in CRESST," *Nucl.Instrum.Meth.* **A559** (2006) 754–756.

- [89] A. Münster, “Absolute α -Radioactivity Determination of Scintillating CaWO_4 Crystals for Direct Dark Matter Search,” Diploma Thesis, TU München, 2012.
- [90] S. Roth, (*in preparation*). PhD thesis, TU München, 2013.
- [91] V. Tretyak, “Semi-empirical calculation of quenching factors for ions in scintillators,” *Astroparticle Physics* **33** no. 1, (2010) 40 – 53.
<http://www.sciencedirect.com/science/article/pii/S0927650509001650>.
- [92] **Borexino** Collaboration, C. Arpesella *et al.*, “First real time detection of Be-7 solar neutrinos by Borexino,” *Phys.Lett.* **B658** (2008) 101–108, arXiv:0708.2251 [astro-ph].
- [93] M. Wurm, “private communication.”
- [94] T. Jagemann, *Measurement of the Scintillation Light Quenching for Nuclear Recoils induced by Neutron Scattering in Detectors for Dark Matter Particles*. PhD thesis, TU München, 2004.
- [95] T. Jagemann, F. von Feilitzsch, H. Hagn, J. Jochum, W. Potzel, *et al.*, “Measurement of nuclear recoil quenching factors in CaWO_4 ,” *Astropart.Phys.* **26** (2006) 269–281.
- [96] R. Strauss, “Quenching Factor Measurements of CaWO_4 at mK Temperatures by Neutron Scattering for the Dark Matter Experiments CRESST and EURECA,” Diploma Thesis, TU München, 2010.
- [97] J. Ninkovic, P. Christ, G. Angloher, D. Hauff, P. Huff, *et al.*, “New technique for the measurement of the scintillation efficiency of nuclear recoils,” *Nucl.Instrum.Meth.* **A564** (2006) 567–578, arXiv:astro-ph/0604094 [astro-ph].
- [98] I. Bavykina, P. Christ, P. Huff, J. Ninkovic, F. Proebst, *et al.*, “Interpretation of Light-Quenching Factor Measurements,” *Astropart.Phys.* **28** (2007) 489–493, arXiv:0707.0766 [physics.ins-det].
- [99] W. Westphal, “Development and Characterization of Cryogenic Detectors for the CRESST Experiment.” 2008.
- [100] M. Stark, *Detektoren mit effizienter und schneller Phononensammlung für das CRESST-Experiment*. PhD thesis, TU München, 2005.
- [101] “Oxford instruments.” <http://www.oxford-instruments.com/>.
- [102] S. Wawoczny, “Optimierung des Experimentellen Aufbaus zur Messung der Quenching Faktoren von CRESST/EURECA - Tieftemperaturdetektoren,” Diploma Thesis, TU München, 2011.
- [103] W. Verkerke and D. P. Kirkby, “The RooFit toolkit for data modeling,” *eConf* **C0303241** (2003) MOLT007, arXiv:physics/0306116 [physics].
- [104] K. S. Cranmer, “Kernel estimation in high-energy physics,” *Comput.Phys.Commun.* **136** (2001) 198–207, arXiv:hep-ex/0011057 [hep-ex].

- [105] S. Wawoczny, (*in preparation*). PhD thesis, TU München.
- [106] M. Hofmann, “Low-Background Gamma Spectroscopy for the Neutrino Oscillation Experiment Double-CHOOZ,” Diploma Thesis, TU München, 2007.
- [107] R. B. Firestone, C. M. Baglin, and S. Chu, *Table of isotopes*. No. Bd. 4. Wiley, 1999.
- [108] W. Carli, “private communication,” 2009.
- [109] M. Drogg, “Novel monoenergetic neutron sources for energies between 2.5 and 25.7 mev,” *Nuclear Instruments and Methods in Physics Research Section A: Accelerators, Spectrometers, Detectors and Associated Equipment* **254** no. 2, (1987) 466 – 468. <http://www.sciencedirect.com/science/article/pii/0168900287907017>.
- [110] W. V. Witsch and J. Willaschek, “High-pressure gas target for the production of intense fast-neutron beams,” *Nuclear Instruments and Methods* **138** no. 1, (1976) 13 – 17. <http://www.sciencedirect.com/science/article/pii/0029554X76901464>.
- [111] “item Industrietechnik GmbH ,” 2013. <http://www.item24.com/>.
- [112] J.-C. Lanfranchi, C. Ciemniak, C. Coppi, F. von Feilitzsch, A. Gütlein, H. Hagn, C. Isaila, J. Jochum, M. Kimmerle, S. Pfister, W. Potzel, W. Rau, S. Roth, K. Rottler, C. Sailer, S. Scholl, I. Usherov, and W. Westphal, “Neutron scattering facility for characterization of {CRESST} and {EURECA} detectors at mk temperatures,” *Optical Materials* **31** no. 10, (2009) 1405 – 1409. <http://www.sciencedirect.com/science/article/pii/S0925346708002796>.

Acknowledgements

In erster Linie möchte ich Herrn Prof. Dr. Franz von Feilitzsch für die Überlassung dieses interessanten und vielseitigen Themas im Rahmen des CRESST Experiments danken. Für die Aufnahme bei E15, das freundliche Umfeld und das Vertrauen zum selbständigen wissenschaftlichen Arbeiten bin ich zutiefst dankbar. Ich habe sein überaus großes Interesse an meiner Arbeit immer sehr geschätzt und mich sehr gefreut, dass er mit Wohlwollen bereit war meine Arbeit über seine Pensionierung hinaus zu betreuen. Ich danke meinem Doktorvater für die unzähligen Diskussionen über Physik und seinen Rat in allen Fragen des Lebens.

Dem Lehrstuhlinhaber von E15, Herrn Prof. Dr. Stefan Schönert, danke ich für die vielen interessanten physikalischen Diskussionen. Seine Faszination für die Astroteilchenphysik ist dabei oft auf mich überggesprungen.

Die Unterstützung von Herrn Prof. Dr. Lothar Oberauer war ein sehr wichtiger Baustein zum Erfolg meiner Doktorarbeit. Sein konstantes Interesse an meinen Experimenten und der Physik im Allgemeinen haben mich ständig motiviert.

Ein besonders großer Dank gilt meinem direkten Betreuer, Dr. Jean-Côme Lanfranchi. Er war es, der von Anfang an mich geglaubt, mich bei E15 integriert und in jederlei Hinsicht unterstützt hat. Die CRESST Gruppe bei E15 und die Zusammenarbeit innerhalb der Kollaboration wäre ohne sein großes Engagement nicht auf dem hohen Niveau, auf das es in den letzten Jahren gelangt ist. In den 3.5 Jahren meiner Doktorarbeit war er mein erster Anlaufpunkt und sein großes Vertrauen in meine Arbeit habe ich immer sehr geschätzt. Darüberhinaus habe ich - nicht nur auf unseren unzähligen gemeinsamen Dienstreisen - viel von ihm gelernt, unter anderen von seiner Fähigkeit wissenschaftliche Themen darzustellen und an Andere weiterzugeben. Nicht zuletzt hat er meine oft finanziell kostspieligen Projekte am Gran Sasso immer ohne zu zögern unterstützt. Über die tiefe Freundschaft, die sich aus unserer gemeinsamen Zeit bei E15 entwickelt hat, bin ich sehr dankbar. "Thank you so much for everything, Sir!" 😊

Ohne die vielen Diskussionen mit Dr. Walter Potzel, sein physikalisches Verständnis, sein schier unbegrenztes Fachwissen und nicht zuletzt seine große Erfahrung wäre diese Arbeit undenkbar. Er war während meiner Zeit bei E15 immer für mich da und allzeit bereit zu helfen, sei es im Labor oder am Schreibtisch. Ich bedanke mich für die unzähligen Stunden, die er mit der Korrektur und Diskussion dieser Arbeit verbracht hat, einen Großteil davon in seiner Freizeit. Seine grenzenlose Freude an der Physik haben mich stets motiviert.

Dr. Franz Pröbst vom Max-Planck-Institut für Physik in München habe ich einen Großteil meiner Arbeit zu verdanken. Sein tiefes Detailwissen in jedem Bereich des CRESST-Experiments, seine große Hilfsbereitschaft und seinen unermüdlichen Einsatz wusste ich besonders in den letzten 1.5 Jahren meiner Arbeit sehr zu schätzen, als ich intensiv am Gran Sasso und am CRESST-Experiment selbst gearbeitet habe. Danke auch für das Vertrauen in mein Projekt von der ersten Minute an. Unsere gemeinsamen Aufenthalte am Gran Sasso habe ich

immer sehr genossen.

Dr. Christian Ciemniak hat den Grundstein für den Erfolg der Quenchingfaktor-Messungen am Beschleuniger des Maier-Leibnitz-Laboratorium gelegt. Ohne seine experimentelle Erfahrung sowie die Vorarbeit für das Streuexperiment und die Analysesoftware wäre diese Arbeit unmöglich gewesen. Unsere gemeinsame Arbeit am Beschleuniger während meiner Diplomarbeit und zu Anfang meiner Doktorarbeit haben mir sehr viel für mein wissenschaftliches Leben gebracht. Danke für die Unterstützung über die aktive Wissenschaftszeit hinaus.

Ohne Karoline Schöffner wären meine Projekte am Gran Sasso schlicht nicht möglich gewesen. Sie war es, die den Testkryostaten aufgebaut und in monatelanger Arbeit optimiert hat. Damit wurde die Grundlage für eine neue Art von Detektor-R&D geschaffen. Danke auch für den unermüdlichen Einsatz (im wahrsten Sinne des Wortes!) für den neuen CRESST-Run, insbesondere in den letzten Monaten ihrer Doktorarbeit. Die vielen schönen Momente am Gran Sasso nicht zuletzt bei "unserer kleinen italienischen Familie" werden mir immer in Erinnerung bleiben.

Ich danke Moritz v. Sivers, Andrea Münster und Stephan Wawoczny für die sehr gute Zusammenarbeit, ohne die die neu entwickelten CRESST-Detektormodule niemals realisierbar gewesen wären. Danke auch für das sehr hilfreiche Korrekturlesen dieser Arbeit.

Stephan Wawoczny danke ich außerdem für die jahrelange Unterstützung am Streuexperiment. Ohne seine Mithilfe wäre das Experiment nicht auf dem jetzigen Niveau. Ich hoffe sehr, dass er es in Zukunft weiter betreiben wird.

Bei der CRESST Gruppe der Uni Tübingen, allen voran bei Christof Sailer und Igor Usherov, bedanke ich mich für die rege Zusammenarbeit am Streuexperiment, die vielen Nachtschichten am Beschleuniger und die schönen Momente am Gran Sasso.

Darüberhinaus, danke an alle, die sich die Nächte am MLL um die Ohren geschlagen haben. Über 1500 h Nachtschicht sprechen für sich!

An dieser Stelle möchte ich mich bei meinen Operateurskollegen am Beschleuniger - unter der Leitung von Walter Carli - Peter Ring, Wolfgang Hagn, Sigi Korschatz und Georg Anachorlis für die sehr gute Zusammenarbeit und die Unterstützung für das Streuexperiment bedanken, sowie beim Werkstatt-Team um Fritz Haftlmeier und Schorsch Obermaier. Die angenehme Atmosphäre am MLL und die vielen schönen Momente werde ich nicht vergessen.

Ein besonderer Dank geht an meinen Bürokollegen Domenikus Hellgartner, der mich nicht nur stets bei guter Laune gehalten hat, sondern auch sein umfassendes Wissen über Fitmethoden und Statistik mit mir geteilt hat. Seine Mithilfe war entscheidend für die energieabhängige Analyse der Quenching Faktoren.

Ich bedanke mich bei Dr. Sebastian Pfister, der mir nicht nur zu Beginn meiner Arbeit die Welt des Gran Sasso gezeigt hat, sondern immer wieder wichtige Impulse für meine Arbeit gegeben hat. Nicht zuletzt bedanke ich mich für die schönen Momente in Italien, auf dem Rad oder an der Kletterwand.

Außerdem bedanke ich mich bei Sabine Roth, Andreas Zöller, Dr. Achim Gütlein, Michael Willers and Marc Wüstrich für die vielen Diskussionen und die nette Atmosphäre in der Kryogruppe bei E15.

Bei Florian Reindl und Clemens Kister vom MPI bedanke ich mich für die vielen interessanten Diskussionen über CRESST und die sehr angenehmen Aufenthalte am Gran Sasso. Und natürlich beim Rest der MPI Gruppe, allen voran bei Dr. Federika Petricca, Dr. Wolfgang Seidel und Dieter Hauff für die nette Zusammenarbeit und die Unterstützung meiner Arbeit.

Ein großer Dank an Dr. Gode Angloher für die aufschlussreichen Diskussionen über Physik

und den Sinn des Lebens. Seine Herangehensweise an die Dinge und seine Faszination für die Forschung motivieren mich jedesmal aufs Neue.

Vorrei ringraziare tantissimo Marco Guetti del LNGS per il suo supporto al CRESST in generale e soprattutto nei miei esperimenti al Gran Sasso. Per mesi(!) ha sorvegliato il test-cryostat durante le mie misure, giorno e notte! Grazie anche per gli innumerevoli giri in bici e le magnifiche passeggiate in montagna.

Ein besonderer Dank gilt Hermann Hagn, der mir immer bereitwillig in elektronischen Fragen zur Seite stand und ohne den ein störungsfreies Messen unmöglich gewesen wäre. Seine Erfahrung gepaart mit unglaublichem Fachwissen und großer Einsatzbereitschaft sowie seine radioastronomischen Experimente sind eine große Bereicherung für den Lehrstuhl. Persönlich danke ich ihm für seine freundschaftliche Art und nicht zuletzt für das Reparieren des einen oder anderen historischen Röhrengeräts.

Außerdem danke ich dem Werkstatt-Team von E15 rund um Harald Hess, die viele mechanische Arbeiten am Experiment durchgeführt und neue Ideen eingebracht haben. Das neue CRESST-Modul wäre ohne Harrys Einsatz undenkbar. Nicht vergessen werde ich diverse Wiesen und Kneipenbesuche mit ihm.

Durch Norbert Gärtner habe ich mich im Labor stets sehr sicher gefühlt. Danke auch für die Unterstützung am Experiment.

Ein besonderer Dank an Maria Bremberger für ihre überaus wichtige Arbeit. Sie hat es nicht versäumt auch mal auf den Tisch zu hauen, wenn die "lieben Physiker" es mal wieder nicht so genau genommen haben. Persönlich danke ich ihr für ihre Unterstützung während meiner Arbeit und die ein oder andere Reisekostenabrechnung.

Grazie a Giannina, Sara, Serena, Silvia, Sandro e Pietro per i momenti bellissimi a Ornano Grande. Siete diventati veramente come una seconda famiglia per me! Senza le bellissime serate, la vostra compagnia e soprattutto la caprese da morire, questo lavoro e la tesi non sarebbero mai stati possibili. Tanti baci e a presto!

Ich bin sehr froh, dass Andi es weitgehend verkraftet hat, öfter als gewohnt auf seinen Kletterpartner verzichten zu müssen.

Ich entschuldige mich bei all meinen Freunden und Verwandten, denen ich in den letzten Monaten oft absagen musste.

Meine Mitbewohner Doris und Hubert haben es über sich ergehen lassen, dass ich des öfteren die überaus strengen ☺ Koch- und Putzpläne unserer kleinen Kommune nicht einhalten konnte. Danke für die wunderschöne Zeit mit euch!

Ich danke der besten Oma aller Zeiten!

Ganz besonders danke ich meinen Eltern! Ohne sie wäre diese Arbeit undenkbar. Meine Eltern haben mich mein ganzes Leben bedingungslos unterstützt und mir vertraut, egal welchen Weg ich einschlagen wollte. Der Legostein war mein erstes kleines Labor, nicht nur für das bin ich meinen Eltern unendlich dankbar. Ich kann mich an ihre Worte in der 7. Klasse erinnern: "Physik wird dir mal Spass machen!" Wie recht sie schon damals hatten, sie haben sowieso in den meisten Fällen recht behalten. Überflüssig zu erwähnen, dass sie mir finanziell immer unter die Arme gegriffen haben, was Schule und Studium erst ermöglicht hat. Danke für alles!

Anni, du hast das letzte Jahr zur schönsten Zeit meines Lebens gemacht! Noch mehr freue mich auf alles was jetzt kommt...